Coupling biological, interior and atmosphere models to infer habitability and biosignatures

Antonin Affholder

Thèse de Doctorat
Sorbonne Université

Sciences de la nature et de l'Homme : évolution et écologie

Laboratoire d'Écologie-Évolution Mathématique, École Normale Supérieure
Institut de Mécanique Céleste et de Calcul des Éphémérides, Observatoire de Paris

Coupling biological, interior and atmosphere models to infer habitability and biosignatures

Par Antonin Affholder

Dirigée par

Pr. Régis Ferrière
Dr. Stéphane Mazevet

Composition du Jury

Pr. Christophe Sotin	*Rapporteur*	Dr. Nancy Y Kiang	*Examinatrice*
Dr. Purificación López García	*Rapportrice*	Pr. Ludovic Jullien	*Examinateur*

May, 2022

Abstract

Is Earth's ability to harbor life, habitability, a rare or unique occurrence in the Universe? What are remotely detectable signs of a biosphere, or biosignatures? These profound questions, once philosophical debates, may enter the realm of empirical science as the exploration of the solar system goes on with increasing ambition and means, as thousands of exoplanets have been detected in the past twenty-five years, and as upcoming ground and space telescopes might enable the characterization of their atmospheres. In this thesis, we leverage recent progress in theoretical and quantitative ecosystem science to present not only a biologist's take on the meaning of habitability, but also the means of quantitative inference of habitability and biosignatures, as well as a path towards the assessment of astrobiological hypothesis on the exoplanet population level.

Part I lays out the physiological modeling basis for energy-limited organisms and estimates model parameter values using published data to explore adaptation of micro organisms to temperature under the model's hypotheses. Second, Part II uses the modeling developed in Part I to assess the habitability and biosignatures of Saturn's icy moon Enceladus. Last, Part III couples this model to atmospheric, climate and geochemical modeling to predict patterns in exoplanet atmospheric composition versus orbital radius under various scenarios, thus paving the way to conceptualize exoplanet population level signatures of habitability and biosignatures.

Résumé

La capacité de la Terre à abriter la vie, autrement dit son habitabilité, est-elle rare ou même unique ? Que pourraient être des manifestations observables à distance, ou biosignatures, associées à l'existence d'une biosphère ? Ces questions fondamentales pourraient passer des débats philosophiques à une science basée sur la donnée, alors que l'exploration du système solaire se poursuis et s'amplifie ; ainsi que des milliers d'exoplanètes sont découvertes et que de nouveaux télescopes plus puissants sont mis en service dans l'espace comme au sol. Dans cette thèse, nous mobilisons des outils quantitatifs de la théorie des écosystèmes afin de donner non seulement un point de vue écosystémique au concept de l'habitabilité, mais également de concevoir les bases d'un moyen d'inférence quantitative de l'habitabilité et des biosignatures.

La Partie I décrit un modèle de croissance microbienne limitée par l'accès à l'énergie chimique, estime la valeur des paramètres du modèle en utilisant des données publiées et explore l'adaptation des organismes à la température dans le contexte de ce modèle. La Partie II applique le modèle développé en partie I pour inférer quantitativement l'habitabilité et les potentielles biosignatures d'Encelade, une lune de glace de Saturne. Enfin, la Partie III couple ce modèle à des modèles d'atmosphère, de climat et de géochimie afin de simuler les corrélations entre la composition atmosphérique d'exoplanètes et leur situation autour de leur étoile sous différents scénarios. Ces travaux permettent de considérer les signatures d'habitabilité et les biosignatures au niveau de populations d'exoplanètes.

Acknowledgments

Thanks to all members of the jury for accepting to review this work: Nancy, Ludovic, Puri and Christophe.

My gratitude goes to all my friends, colleagues and my family, let the pleasure of having them in my life accompany me in my journey across the Atlantic. You have all been at my side, in one way or another, in these past few years and you have made this adventure a fun and pleasant one.

I express particular thanks to my mentors in those early years of my research experience. This thesis is the fruit of the co-supervision by a theoretical ecologist and an astronomer, Régis Ferrière and Stéphane Mazevet. Working with them both has been a true experience of interdisciplinary science in the making, and for that I am grateful. Of course, their contribution to this PhD extends far beyond scientific guidance. I admire their curiosity, enthusiasm and creativity, which made this PhD much more than scientific work, but also a pleasant human experience. I must also address very special thanks to François Guyot, who although not an official advisor of this thesis would deserve to be cited as such. His encyclopedic knowledge and endless enthusiasm have kept me motivated and creative during these past few years.

Thanks to Boris Sauterey, closely collaborating with you during the past few years has been a pleasure and I have learned a lot working with you. Thanks to Daniel Apai and his team, Alex, Kevin and now Martin for welcoming me and for the inspiration and supervision that were instrumental to part III of this thesis. I would also like to take the chance to thank Christian Lorenzi, dean of science at ENS during my masters and the beginning of my PhD, who showed great interest for our projects and encouraged us all to undertake this ambitious work. Many thanks also to Morgane Thomas-Chollier, my tutor at ENS, for her kind words, her encouragements, and her precious advice. Thanks also for teaching me how to teach, my experience at the biology department as a teaching assistant has been a great thanks to you, but also thanks to Pierre, Andréa, Anne, Barbara, Lucie and others. Thank you to my colleagues from IBENS; Eric, Silvia, Mathieu, Philippe,

Contents

Appendices 239

Introduction

La thèse que je défendrai ici, c'est que la biosphère ne con-
tient pas une classe prévisible d'objets ou de phénomènes,
mais constitue un événement particulier, compatible certes
avec les premiers principes, mais non *déductible* de ces
principes. Donc essentiellement imprévisible.

–Jacques Monod, *Le Hasard et la Nécessité*, 1970

O PPORTUNITIES GRANTED TO SCIENCE by past, current and future exploration of extraterrestrial environments seem endless. In 1971, during the third moon walk of mission Apollo 15, the American astronaut David Scott simultaneously drops a hammer and a feather from his hands. Despite having significantly different masses, both objects touch the lunar surface at virtually the same time. This result, that might appear counter intuitive, was predicted nearly four centuries earlier by Italian astronomer Galileo Galilei. When first proposed, this prediction –or hypothesis–, was met with skepticism, as experiments showed different fall duration for objects of different mass. But, Galileo argued, these results were due to the resistance of air, and to test his hypothesis, one would have to experiment in vacuum. Fortunately, mankind did not have to wait to reach the lunar surface to provide support for Galileo's prediction. Low air pressure chambers were constructed in the late 17th century, and a guinea (gold coin) raced a feather only to come *ex aequo* every time[1], just as predicted by theory.

This story, among many others that also involve Galileo, offers an example of how the scientific method has at least as much to do with refuting hypotheses than it has with adhering to a paradigm and exploring its descriptive or predictive power[2]. Thus, the way paradigms, or in other words our general interpretation framework (Thomas Kuhn's *disciplinary matrix*), can change is an essential characteristic to what science and the scientific method are.

Commander David Scott about to drop a hammer and a feather on the lunar surface. (NASA)

Maybe one opportunity that stands out as characteristic to the exploration of space is discovery, or absence thereof extraterrestrial life. Assessing whether life (as we know it or not) is a common occurrence in the universe, is sure to hold an immense potential for redefining the way we perceive Earth's position in the universe as a life-bearing planet, and the position of its biosphere as a manifestation, perhaps a singular one, of what we call life. In this introduction, I will attempt to summarize the history of past scientific transitions, in both astronomy and biology, relevant to the conceptualization of extraterrestrial life. In doing so, I hope to set the context in which we stand today, at a turning point in theoretical and observational developments, that make us hopeful to significantly advance our understanding of where the Earth stands in the apparent diversity of worlds that populate our galactic neighborhood.

I then consider methodological constrains that weigh on the possibility of conceptualizing habitability and biosignatures from the

point we currently stand at in the historical context of astrobiology. In particular, the search for extraterrestrial life suffers from the seemingly insurmountable obstacle that we are limited by the possibility that our knowledge of the Earth's biosphere misleads us in that it may be a uniquely "exotic" manifestation of life. These methodological considerations address this apparent issue, and show that this obstacle actually invites us to design a modeling framework taking the Earth as a template and use it as a starting point for a theoretical understanding of habitability and biosignatures. The new framework should also provide us with a practical tool to turn astrobiological hypotheses into quantitative predictions helpful to interpret existing data on extraterrestrial environments and design future missions.

Historical context

The copernican revolution

Perhaps the most studied example of a paradigm shift in science turns out to be of interest for the present dissertation. The proposition by Nicolaus Copernicus, formulated in the first half of the 16th century, that Earth was not at the center of the Universe but revolving around the Sun, ushered the possibility that Earth was only one world among many others. As pointed out in Imre Lakatos's *Falsification and the Methodology of Scientific Research Programmes*[3], Copernicus's proposition did not at first explain the apparent motion of planets in a simpler (however vaguely "simpler" is defined) way than the Ptolemaic model did; and until Galileo came up almost a century later with the concept of inertial reference frames, experiments would seem to refute Earth's rotation and motion. Yet, eminent scientists such as Giordano Bruno, Johannes Kepler and Galileo adhered to Copernicus's view *before* such theoretical developments were proposed. But Copernicus's proposition is not just a physical model, it is also of course the postulate that Earth's place in the Universe is not exceptional (a view that is sometimes called the mediocrity or Copernican principle). Or rather, that we should not assume that the situation of the Earth in the universe is exceptional.[a] And it may have been that these scientists glimpsed at

---

a. This remark is an important one, as it indicates not what we should assume, but what we should not. Which leaves a vast liberty of what we can assume.

the potential that such a paradigm could offer [b] and that was what decided them to entertain the idea.

The Copernican principle can boil down at least to the methodological assumption that physical laws applicable on Earth are also applicable elsewhere (and thus that they are universal). But whether this implies that the Earth as a planet harboring life is a generic occurrence in the universe is an entirely different question, although the nuance between the assumption of Earth's *mediocrity* and the speculation of its *genericity* has not always been clear.

Giordano Bruno proposed early on (in his *De l'infinito universo et mondi*, 1584) that the universe is infinite (not heliocentric, and thus stars are not fixed like Copernicus initially described them to be), that stars were objects similar to the Sun and that they had planets orbiting around them. Moreover, he claimed that other worlds around other stars would be inhabited like ours is, and he was later sentenced for defending his views against the church. In a brilliant demonstration of a shift of perspective, Johannes Kepler hypothesizes in his *Epitome Astronomiae Copernicanae* how a distant observer would see the Earth in the sky of their planet. He proposes that from afar, the Earth would not be distinguishable from the comparatively brighter Sun, and that the observer would see the Sun appearing as a simple bright dot. In other words, that the Sun would appear to that distant observer just like stars appear to the Earth-based observers. [c] Given that, what would indicate that the stars we see in the night sky do not also have worlds orbiting around them, and that we just cannot see them because we are so far away from them?

One world among many. Figure M, in Johannes Kepler's *Epitome Astronomiae Copernicanae*, 1635 (BNU, Université de Strasbourg)

A parallel with the history of biology

Even if as early as during the antiquity, thinkers like Epicurus and later Lucretius proposed the idea known as the plurality of worlds, it might be Kepler and Bruno who birthed astrobiology as a scientific discipline, specifically because they operated this shift of perspective consisting of posing as an observer positioned outside of the Earth. For a long period of time, the field of astrobiology

---

b. In other words, subjective criteria rather than a predefined and consistent hypothetical scientific method [4]

c. to the exception of the modern observer that disposes of large aperture telescopes and coronographs, which allow them to perform direct imagery of exoplanets.

has been the endeavour of astronomers and astrophysicists, interested in the formation of planets, the means by which they could be detected as well as the observation of the solar system. But there is a long history of progress in biology that has considerably enriched the hypotheses made by astronomers, such as the discovery of microbial organisms: their apparent ubiquity[5] and unsuspected diversity[6], the refutation of their spontaneous generation[7], considerations on the age of the Earth and its biosphere as well as the conditions required for it to have appeared[8], as well as the discovery of microbes dwelling in inhospitable places such as off-axis hydrothermal vents[9].

While Galileo, Kepler, Bruno and others were caught up in their own scientific revolution and having trouble with the catholic church, another one was brewing, with conceptual consequences that could be just as deep. The progress in optics did not only profit to astronomers. It is often overlooked how the conception of microscopes followed closely the one of telescopes, and that while distant worlds revealed themselves, so did the microscopic one. The first published report of observations through a microscope is given by Robert Hooke in his *Micrographia* (1665)[10].

Only a few years later, Antony Van Leeuwenhoek's discovery of microbes (*animalcules*) by observation through the microscope is published[5]. Soon after Leeuwenhoek's observations, Robert Hooke replicated them, and so did Christian Huygens. In fact, Huygens and Leeuwenhoek were among the first participants in the biogenesis versus spontaneous generation debate, siding against spontaneous generation (letter from Huygens to Leeuwenhoek on October 20, 1692). This question became the object of an important controversy in 1859, which was ended by Louis Pasteur showing that after sterilization, a sealed flask containing growth medium remained sterile[d].

This scientific milestone has some deep consequences on astrobiology. It provides an example of how an environment can be habitable but lifeless. In the flask of Pasteur's experiment, all the ingredients for microbes to grow were present, but no population was since there was no initial microbe from which it could have grown. If spontaneous generation is refuted, it implies that there

Observ. XVIII. of the Schematisme or Texture of Cork, and of the Cells and Pores of some other such frothy Bodies. *Micrographia*, R. Hooke, 1665. (Source `gallica.bnf.fr` / BnF)

Le 1ʳ Aoust. Je pris de la surface de l'eau de pluie que j'avois mis 6 jours auparavant dans une petite fiole. *Oeuvres complètes, tome XIII*, C. Huygens, 1916. (Source `gallica.bnf.fr` / BnF)

---

d. The story is actually much more complex than that. Pasteur's experiment had flaws and it is as much for historical reasons than scientific ones that it was remembered as the refutation of spontaneous generation.

could have been a single shared origin to all life on Earth. There-fore, the astrobiologist looking for habitable environments outside of Earth is reliant on the consideration -additional to habitability- that life could have emerged and did not entirely die out[11]. There must indeed have been, at some point during Earth's history, a transition between the non-living and the living, between the abi-otic and the biotic. How life emerged from abiotic processes is an event called *abiogenesis*.

The subject of abiogenesis is therefore essential to astrobiology, as identifying conditions in which organic molecules with the poten-tial to become self replicative and assemble themselves in a network displaying the characteristics of life: a metabolism, the capacity to evolve through natural selection, the definition of barrier sep-arating an interior medium from the environment and the means to perform and maintain these characteristics autonomously. De-spite considerable progress since the famed Miller-Urey experiment that showed how amino acids can be spontaneously generated in an early Earth atmosphere analogue[12], how life emerged on Earth is still unknown and continues to raise chemical, theoretical and philosophical questions about how these characteristics have been able to emerge spontaneously[13–15].

On the other hand, the advent of sequencing techniques has al-lowed to dive deeper in time that ever before and demonstrate that all known life on Earth shares a common ancestor, as well as shed light on what could have been the earliest organisms present on Earth. These discoveries suggest that early life relied on chemi-cal reactions with a low energy yield to grow, among which one stands out as the possible earliest catabolic reaction: methano-genesis[16,17]. Incidentally, the discovery of methane producing mi-croorganisms is also historically connected to how microbiolobiol-ogy came to be an environmental science. Louis Pasteur was fo-cused on the relation of microbes to our health, that of silk worms and to the conservation and production of wine. In doing so, he led the discovery of the metabolic diversity of the microbial world, but it is Béchamp, his student who provided the first experimen-tal indication that methane could be produced biotically[18], after a long-standing interest of the scientific community for environmen-tal methane production, for instance by Bunsen or Volta as early as 1776 who discovered that "flammable" air was produced in marsh sediments.

The relatively late discovery of the diversity of microbial

metabolisms, and methane production in particular (methanogenesis), can be explained by how alien those organisms are to us. Not only are they invisible to the naked eye, but anaerobic metabolisms (called fermentations at the time of Pasteur[e]) are found in anoxic environments. Also because traditional classification techniques, based on observable morphological characteristics, fail to apprehend the phylogenetic relations of microbes, their natural history remained widely unknown until the late 20th century. In 1977, Carl Woese and George Fox discovered using recently made available molecular techniques that methane producing "bacteria" were forming a group as distinct from other Bacteria as from Eukaryotes[6]. Woese and Fox called these organisms Archaeabacteria (and later Archaea), based on the apparent antiquity of their methanogenic metabolism and adaptation to environments presumably dominating the Archean Earth. Shortly before that, in 1967, Lynn Margulis had proposed what is now a widely accepted hypothesis; that the eukaryotic cell originates from endosymbiosis between prokaryotic cells[19].

Together, these discoveries have prompted us to reconsider our place in Earth's biosphere. The metabolism on which we rely, respiration, is only possible because some two billion and some years ago, some microbes found a way to use sunlight and water as a food source instead of low-energy chemical reactions. There are slightly more (30%-120%) microbial cells (mainly Bacteria) in the human body than there are human cells[20]. Despite Archaea and Bacteria making up less biomass than Eukaryotes[21], their antiquity, apparent ubiquity and their predominant role in Earth's biogeochemical cycles throughout most of its geological history[22–24] make us wonder, similarly to how Kepler reflected on how the Earth could appear from a distant observer, if a similar distant observer that would look at indirect signs of the Earth's biosphere would not be more likely to see the footprint of its microbial component than the one of the multicellular biosphere we are used to see and interact with every day.

---

e. we now know anaerobic metabolisms that are not fermentations

Methodological road map to infer habitability and biosignatures

We are severely limited in our ability to explore other worlds. They are separated from us by vast distances; even reaching the surface of nearby Mars is not a small endeavor, and no human has yet set foot on another planet. Our other neighbor Venus, has an atmosphere so dense and a surface so warm, that even landing a robotic probe at its surface has only been achieved a few times [f] during the era of the soviet union's space exploration program, and never again since. The Cassini/Huygens mission, led by NASA, performed an in depth exploration of the Saturnian system, dropped the Huygens lander on the surface of Titan and performed several fly-bys of Enceladus. Even though the Cassini/Huygens mission considerably increased our understanding of both these worlds, the mission is now retired (the Cassini probe disintegrated in Saturn's atmosphere in 2017), and many questions remain. Other than the very partial knowledge we have of Mars, Venus, Enceladus and Titan, very little is known of or about other solar system bodies potentially relevant to the search for extraterrestrial life, such as the moons of Uranus[25], Jupiter's moon Europa[26,27], or even asteroid Ceres[28].

Almost three decades ago, the existence of exoplanet, speculated by Kepler and others, has been confirmed by the detection of 51 Pegasi-b by Didier Queloz and Michel Mayor[29]. Since then, more than 5,000 other exoplanets have been discovered, using a variety of methods, some of them indirectly deducing the existence of a planet from a star's change in luminosity when eclipses occur ("transits"), or the Doppler change in its received emission spectrum ("radial velocity" method), and some of them directly (direct imaging method).

Facing such an abundance of extraterrestrial worlds, we can only hope that there might be at least one that harbors life. The enormous cost in time and money of exploring solar system bodies and of characterizing distant extrasolar worlds [g] make it more likely that

---

f. The probes that have landed on the surface only managed to transmit data for a few hours before failing.

g. Exploring them in the sense of sending probes like those used in the solar system is out of the question in any relevant timescale as they are separated

we find indirect rather than direct evidence of life in the next couple of decades (and even that could be extremely unlikely). The notion of biosignature is pervasive in the field of astrobiology, but it has no clear and consensual definition in the context of inferring the existence of an extraterrestrial biosphere[h]. Perhaps, a biosignature is best described as a collection of observable features that can be coherently explained by the assumption of a biosphere rather than by abiotic processes alone. This constitutes a central argument of this manuscript as the concept of biosignature is not commonly understood as an *explanatory system* that consistently explains observations rather than a specific and unique footprint pertaining to a single quantity derived from observations. But even measuring relevant observable features, such as the composition of an atmosphere or an ocean comes at a great observational cost, and worlds that have these observable features must first be identified.

Such worlds, that are situated in a context that makes us think that they could be suitable for a biosphere to exist are called *habitable*, and constitute candidates for the search of biosignatures. Commonly, the Habitable Zone (HZ) corresponds to the range of orbital distances at which the light received from the host star is sufficient to sustain a liquid water ocean at the surface, but low enough to prevent its evaporation[32,33]. This is also a characteristic that is expected to be deduced from indirect evidence, albeit based on data more easily gathered than the observables that might carry biosignatures. For example, the existence of an internal source of heat or sufficient insolation might point towards the possibility that a body of liquid water can exist and be sustained through time.

The concepts of habitability and biosignatures both require us to have an *a priori* idea of what type of environment are good candidates to harbor life and what molecular signal in observable quantities would be considered a biosignature. Furthermore, it has been stressed that in order to perform inference of biosignatures, there must be theoretical framework capable of producing *quantitative* predictions pertaining to potential biosignatures[34]. In other words, any definition of biosignatures and habitability relies on making assumptions on a biosphere: the environments that are suitable to it

_____

from us by distances measured in light years.

h. It is remarkable that the entry for the term biosignature in the Encyclopedia of Astrobiology[30] points to the entry for "biogenicity" as the uniquely biotic origin of chemical or morphological features in the geological record[31]

and the footprint the biosphere leaves in the observable features of the considered world, such as its atmospheric composition.

Given that, we are facing a conundrum: how can we look for extraterrestrial life, that might be very different from the Earth's, when our understanding of what makes an environment suitable for life and how life changes its environment in ways that could be observed from astronomical distances is centered around the only biosphere currently known to us? It might be possible to entirely encompass the concepts of biosignatures and habitability in using so-called *first principles*, *ie* deducing from physical and chemical laws the set of conditions that make life possible and the way life interacts with its environment. Such a strategy is expected to fail at describing the Earth's biosphere as a complex network of interactions between its components, the current shape of which could be entirely conditional on a particular sequence of events [35].

The same argument about the Earth's biosphere being conditional on a particular set of events could also be interpreted as one against using the Earth's biosphere as a template to find extraterrestrial life. We thus seem to be facing an impossible choice: a first principle approach cannot be tested against the particular case of the Earth's biosphere and thus might be inefficient in predicting biosignatures and habitability, and the extrapolation of our empirical knowledge of Earth's biosphere to extraterrestrial bodies might be too restrictive to capture biosignatures of different biospheres.

Some authors have focused on identifying fundamental characteristics of life that would enable the identification of so-called *agnostic biosignatures*, as they supposedly do not rely on the assumption of a particular biosphere, of particular metabolisms, or of particular biological interactions or rates. The existence of an agnostic biosignature usually supposes the existence of fundamental defining characteristics that can be deduced from fundamental laws of physics and chemistry, expected to be shared by all life, terrestrial or extraterrestrial. In the context of biosignatures, it often assumed that such a universal feature relates to thermodynamics [36–38] or information theory [39]. But there exists some exceptions that focus on other properties. For instance, life on Earth's ocean is observed to display a particular pattern in the ratio of the different constitutive elements C, H, O, N and P [40], and approaches to biosignatures based on stoichiometric ratios have been proposed [41].

The identification of such a biosignature could be of limited scope, firstly because their universal nature as well as their ability to only refer to processes that we would comfortably call life (a counter example would be simple dissipative autocatalytic or self oscillating chemical systems[42]) remain to be proven. Second, it would be preferable if the identification of a biosignature could point towards a representation of the life at its origin, that we can ideally replace in the context of life on Earth. So-called disequilibrium biosignatures, pertaining to a global measure of out-of thermodynamical equilibrium state[36] require observables that can be as difficult to obtain as those pertaining to "gnostic" biosignatures, such as the atmospheric composition. Lastly, it could be useful that mechanical modeling taking Earth-like life as a template serves to constrain higher level agnostic biosignatures. In other words, the potential existence of agnostic biosignatures actually stresses the need for a modeling framework that simulates variation around the Earth's biosphere in order to explore the robustness of the concept of agnostic biosignatures.

It remains that Earth's biosphere might be unique in the Universe and that a framework using it as a template could miss out most or all relevant biosignatures. At the scale of the solar system, there is evidence that suggests that the Earth's biosphere as we know it today could be a rare, perhaps unique occurrence. So far, our neighboring terrestrial planets Mars and Venus do not appear to have or have had in the past a biosphere comparable to the Earth's and have followed geological and climate trajectories very different from that of the Earth. Numerical simulations of the solar system dynamics also point that Earth's orbit and obliquity to being remarkably stable over its geological history compared to Mars, or to what it could have been if it were not for the stabilizing effect of the Moon[43,44].

Together, these elements make the case that habitability on the long term could be rare, and thus that the complex life (*e.g* multicellular) that was able to evolve on Earth over billions of years might also be rare. However, these elements do not contradict the possibility that life resembling Earth's early microbial ecosystems in their metabolisms and environments might be a frequent occurrence. In fact, a modeling framework based on Earth-like life could be useful to test whether Earth-like microbial life is a common occurrence in the Universe. Especially since early ecosystems on Earth do not seem to have relied on particularly improbable

12

metabolisms and that Earth's life is composed of elements that are commonly found in most of the solar system bodies that have been explored.

Lastly, the advent of powerful observation tools make it plausible that a relatively large number of terrestrial exoplanets, and a moderate number of "Earth-like" planets can be characterized with unprecedented insight into their surface conditions in the relatively near future. So-called Earth-like planets refer to exoplanets that have a mass and density similar to the Earth's and that orbit a Sun-like star in the habitable zone. The potential for abundant data has resulted in the growing interest for understanding the notion of biosignature as *contextual* itself[34,45,46]. In this case, the stellar or planetary context does not only define potentially interesting candidates to screen for a hypothetically unambiguous biosignature, but also opens the possibility for atmospheric features to constitute evidence in favor of an extant biosphere in a given context but not in another.

From these methodological arguments and the current scientific and technological context emerges the need for a modeling framework that leverages quantitative ecosystem science, geochemical and geophysical modeling all together in order to (i) ground the concept of habitability in our understanding of what makes Earth habitable and what constitutes a habitable environment to Earth-like life, (ii) predict biosignatures of the Earth's biosphere, and the early-Earth biosphere in particular, (iii) explore variations around the case of the Earth as a planet set in a particular planetary context, with respect to habitability and biosignatures and (iv) reflect upon the detectability of such biosignatures given the instruments that are currently available or under development.

In this thesis, I contribute to build such a framework by defining a theoretical yet empirically grounded model of microbial growth and unraveling how it imposes conditions on the design of geochemical global models that must be coupled to it in order to operate the transition from the scale of the environment to that of the planetary context and potentially observable biosignatures. This work spans a wide range of different processes and theoretical tools, from ecosystem and evolution to photochemical reactions in the atmosphere or mineral alteration at the surface. Yet, it is not my purpose here to provide a framework that exhaustively models every possible chemical and physical process in an *in silico* replication of a

planet, but rather to navigate the *inherent* and essential complexity of the climate system of biological population and try to identify the part of it that is irreducible to the assessment of habitability and biosignatures. Second, while this work is mostly theoretical, it is about making it possible to ground the hypothesis of an extraterrestrial biosphere in our quantitative understanding of that of the Earth as well as it is about considering future or current data on exoplanets and Enceladus in the solar system and their ability to reject or corroborate astrobiological hypotheses.

Outline

The conventional articulation between the concepts of biosignatures and habitability is that the context of a planet, such as its orbital distance, sets its potential habitability and makes it an interesting candidate to screen for biosignatures. In part I of this manuscript (composed of chapters 1 and 2), I take the opposite route and describe a theoretical approach to habitability that takes the dynamics of a biological population in a particular environment as a starting point to build a metric of habitability from the bottom up, where the planetary context helps shaping a candidate environment on which *viability* is assessed, relative to a particular organism defined by functional traits. Conversely, linking the larger scale of the planetary context to the smaller one of the potentially viable environment serves the purpose of scaling up from the potentially *inhabited* environment to global process and observable biosignatures.

In chapter 1, I describe a model suited to estimate the growth rate of microbes that rely on low-energy yield reactions as their source of energy, such as those that made up the early Earth's biosphere, methanogens in particular. This model is based on thermodynamical and thermokinetic semi-empirical modeling of energy-yielding and energy-consuming reactions in the cell which results in the expression of the minimally required available energy for growth as a function of parameters relating to functional traits.

Next, in chapter 2, I examine how adaptation resulting from natural selection could affect the values of these parameters in natural populations. In particular, I examine how the relation between traits pertaining to the kinetics of functional reactions and the kinetics of the denaturation of functional molecules could explain the existence of any upper temperature limit for life from a theoretical

evolution standpoint. Then, I estimate the values of the parameters of the model of microbial growth using available data for various organisms growing at different temperatures in order to derive trends and discuss them from the perspective of the adaptation to environmental temperature. In doing so, I propose that the obtained set of parameter values could serve to define a set of *a priori* plausible combinations of parameters to use to assess the habitability of an environment.

Part II (chapters 3 and 2) concerns the application of the aforementioned model to assess the habitability and biosignatures of Saturn's moon Enceladus. Enceladus is thought to have a global ocean at the bottom of which may exist hydrothermal circulation similar to that occurring in Earth's seafloor hydrothermal vents inhabited by methanogenic Archaea and is therefore considered as a prime candidate for the search of extraterrestrial life. Moreover, Enceladus's ocean sprays out of cracks in the icy surface, producing a plume of gases and particles from oceanic origin that can and have been sampled by the Cassini mission. The case of Enceladus is therefore uniquely situated at the intersection of disposing of a candidate environment for habitability related to a candidate type of organism and presenting observables in the form of the space plume's composition. In chapter 3, we use the quantitative modeling developed in chapter 1 to simulate the abundance of key volatile chemical species in the space plume under the hypotheses that a population of methanogenic microbes similar to those present in Earth's hydrothermal vents is present or absent. The simulated plume compositions are then used to constrain the plausibility of biotic methane production in light of the measurements of the space plume's composition by the Cassini spacecraft. We find that the observed quantity of methane in the plume is a likely outcome from the simulations of biotic methane production but not of abiotic production from mineral alteration hydrothermal reactions.

Chapter 4 considers the characteristics of this hypothetical biosphere in the context of future exploration missions set out to gather evidence for or against its existence. In particular, we constrain the size and productivity of a methanogenic population inhabiting the putative hydrothermal environment in Enceladus's ocean. Particularly, we stress how the rigorous distinction between these quantities is important in considering the potential presence of cells or organic molecules in the plume; population size, or standing biomass refers to a quantity local to the potentially habitable environment,

while productivity measures the biomass that potentially escapes this environment and could constitute biosignatures in the observable plume. We also highlight that the measured abundance of methane in the plume can serve as additional information to further refine estimates of standing biomass and biomass production of a hypothetical population of methanogens. In doing so, we propose what abundances of organic molecules (that could be in principle produced biotically or abiotically) found in the plume would constitute a potential biosignature consistent with the previously measured abundance of methane. We find that missions currently under development for further analysis of Enceladus's plume might meet the requirements for assessing such biosignatures, despite the hypothetical biosphere found to be relatively small.

Lastly, part III (chapters 5 and 6) focuses on assessing the habitability and biosignatures of Earth-like extrasolar planets in the context of currently developing observational means that render plausible the characterization of their atmospheres. Chapter 5 provides an in-depth description of geophysical and atmospheric process that shape the surface conditions of a terrestrial planet set in a context similar to that of the Earth regarding its host star, orbital distance, mass and composition. Specifically, we show how these processes that together constitute a complex system can and should be coupled together in order to form a theoretical framework suited for assessing habitability and biosignatures using the type of modeling described in part I. The scaffolding of such a coupled framework is a tedious and technical endeavor, in which several obstacles are identified, but it ultimately leads to a "working version" of a numerical tool able to simulate the evolution of the atmosphere of Earth-like planets in various stellar context and under several scenarios of surface processes, in particular the presence or absence of a geological carbon cycle relying on the alteration of continental crust.

Chapter 6 uses this tool to predict trends in the expected atmospheric composition of terrestrial planets in relation with the incident flux of stellar radiation and with planetary age for different scenarios of planetary interior convection regime and of presence or absence of a methanogenic biosphere. We explore how different scenarios of volcanic outgassing and continental weathering affect the surface conditions and therefore effective habitability of planets within the habitable zone and how they are associated with different expected trends in their abundance of atmospheric CO_2

versus their orbital distance to the host star (or the received stellar flux of stellar radiation). We also demonstrate how the biological modeling developed in chapter 1 coupled with the geochemical modeling in chapter 5 can be used to predict the same type of trends that would be expected if terrestrial planets in the habitable zone had a methanogenic biosphere. Lastly, we elaborate on a statistical framework to prospectively design observation missions so that such trends can be assessed with sufficient statistical power.

Part I.

The biology of habitability: theoretical insights

Habitability and viability

WHAT MAKES AN ENVIRONMENT HABITABLE? Habitability as a concept is rarely defined and is vaguely understood as a property relative to the ability for life to exist[47]. In the context of astrobiology, habitability often refers to the habitable zone concept[32,33], that relates the astronomical context (orbital parameters of a planet) to surface conditions (temperature). This concept is thus built upon the working assumption that the stability of liquid water on the surface of a planet is a good starting point to permit the existence of suitable habitats (or viable environments). Here, I propose building a conceptualization of habitability up from the smaller scale, that is the viability of an environment. Moreover, I will restrict the analyses here to microbial life alone, leaving aside considerations of complex multicellular organisms. As I am interested in performing inference of habitability, a quantitative criterion for viability needs to be established, and thus some formal definitions need to be introduced.

First, let the viability of a population in an environment be the unitary component of habitability. Second, this yet undefined *viability* has to be a binary property[48]: a population is viable or it is not. In essence, this definition of habitability is the representation of an experiment in which an organism is brought to an environment and an observer assesses whether it grows or not. By choice, this definition does not concern itself with the conditions for life to emerge, but simply with those that allow a predefined organism to grow into a population, similar to the concept of the Grinnellian niche in ecology[49]. This choice and the limitations it introduces to inferring biosignatures are discussed in the conclusions of this thesis. Because carrying out such a contamination experiment on a distant world is challenging and counter productive[a], biological modeling is particularly warranted, additionally to physical and chemical modeling. An environment, denoted by E, refers here

---

a. due to the concern of contamination `https://sma.nasa.gov/sma-disciplines/planetary-protection`

to a set of physical and chemical quantities, as well as a description of their fluxes and interactions (*e.g.* the temperature and the abundance and dynamics of a potential resource). In particular, we assume here that the environment of interest is an open system, exchanging mass and energy with its surroundings. As such, the considered environment is potentially connected to global processes or observable quantities. A microbial population is quantified by the concentrations of cells or biomass in E, respectively denoted by N and B. The growth dynamics of a particular population depend on the value of physiological parameters such as nutrient uptake rate, the rate at which functional molecules in the cell decay, and most importantly the type of resource this population consumes. Together, the value of these parameters define a particular type of organism that I call here a functional type (noted by the subscript i), loosely following the terminology used in biogeochemistry referring to groups of organisms that participate differently to biogeochemical cycles (*e.g* diatoms are linked to the silica cycle and coccolithophorides to the carbonate cycle)[50].

The assumptions defining the criterion of habitability are summarized formally in the following definition.

Definition 0.1 (i-habitability, viability)**.** Let N_i be the number or density of microbial cells of functional type i in an open environment E_j. E_j is habitable to i (*i-habitable*) if and only if the *per capita* growth rate of an initially rare population is positive, or

$$\left(\frac{1}{N_i} \frac{dN_i}{dt}(E_j) \right)_{N_i=0} > 0 \qquad (0.1)$$

This criterion corresponds to the initial viability of the functional type i in environment E_j, and thus it may be practical to define this part of habitability as the *viability*. This logical operator is hereafter denoted by $H_i(E_j)$, or sometimes H if the context permits it. It is equal to 1 if the condition above is met, and 0 otherwise.

Such a criterion can be understood as a measure in the mathematical sense, which is a nice property as it allows Bayesian inference[b].

---

b. An example of the viability criterion being used to construct a probability measure is given in Chapter 3

An interesting property that immediately follows from the assumptions in definition 0.1 is that at the population steady-state (if there exists one), the apparent environment at equilibrium with the population [c] is at the limit of viability.

Proposition 0.1 (apparent uninhabitability of an inhabited environment)**.** Let E_j be an environment and E_j^* its value when the system composed of the environment and population i is at steady-state. Then
$$H_i(E_j^*) = 0$$
Proof is immediately obtained from the definition of the steady-state $d_t N = 0$.

In other words, a population spends the (limiting) resource in its environment to the point it can no longer grow, and thus the environment apparently has a scarcity of this resource. The consequence of this observation is that one cannot assess the habitability of a potentially inhabited environment *a posteriori* but has to apply this viability criterion in a representation of the environment constructed *a priori* based on contextual evidence of physical and chemical processes. One should keep this in mind when proceeding with inference of the habitability of extraterrestrial environments.

As a concrete example, one may consider the following equation[51]

$$\frac{dN}{dt} = N(v_{max}\frac{S}{a + S} - d) \tag{0.2}$$

where population N uptakes resource S following Monod kinetics with maximum rate (effectively the maximum resource conversion rate) v_{max}, half-saturation constant a and dies with constant rate d. In this very simple toy model, the criterion in definition 0.1 translates into

$$H(S) = 1 \iff S > \frac{ad}{v_{max} - d}, \quad v_{max} > d \quad . \tag{0.3}$$

This value is generally referred to as the break-even concentration[51]. In other words, a cell brought to an environment that has a nutrient concentration greater than this value will start to grow into a population, whereas if S is lower than this value, the cells will on average die before dividing.

---

c. Here, equilibrium refers to a steady-state rather than the thermodynamical equilibrium. In general, I use the word equilibrium to refer to this ecological steady-state.

An additional assumption underlying definition 0.1 is that the considered environment is an open system in which the microbial population remains, exchanging matter and energy with a surrounding larger scale environment or a neighboring one. This assumption is essential as a closed system has only ever one fixed point which is the population going extinct after having consumed all the initial stock of resource (if it could grow initially)[d]. In our toy model, it translates to S being renewed or continuously provided to the system at a certain rate. Of course, the openness of a system is mostly dependent on the considered scale in time and space chosen to describe it, thus highlighting the importance of carefully defining the environment to consider as potentially habitable.

The general class of models describing the consumption of resource by a population in an open environment is the chemostat[51]. Classically in this model, fresh medium where resource is at concentration S_0 is supplied at a certain rate F, equal to the removal rate. In the chemostat, the dynamics of a resource S in the chamber follows :

$$\frac{dS}{dt} = D(S_0 - S) - N\frac{v_{max}}{\gamma}\frac{S}{a+S} \tag{0.4}$$

The chemostat environment as a bioreactor.

where $D = F/V$ is the chemostat's dilution rate (with V the volume) and γ the yield constant corresponds to the efficiency of the conversion of S into biomass or cells. The yield is often taken as constant in the simple chemostat models, which is not the case in most of the work presented in this thesis except for the toy model used in this introduction. In the N, S plane (figure 0.1), this model has fixed points

$$\left\{\frac{dN}{dt}, \frac{dS}{dt}\right\} = \{0,0\} \iff \{N, S\} = \left\{ \begin{array}{l} \{0, S_0\} \\ \{\gamma\frac{D}{d}(S_0 - \frac{ad}{v_{max}-d}), \frac{ad}{v_{max}-d}\} \end{array} \right. \tag{0.5}$$

In the classical model, the death rate equals the dilution rate $D = d$, as removal of medium from the chemostat is assumed to correspond to removal of biomass if it is in suspension, which simplifies the system. Regardless of this assumption, it can be shown that the system is guaranteed to converge nicely if the concentration of nutrient in the supply fluid (S_0) is greater than the "break-even" concentration (equation 0.3). The steady-state population size depends on

---

d. Growth experiments are often carried out in isolated systems, where there is no constant supply of nutrients. In these experiments, the population reaches a so-called stationary phase that precedes the population die out. The stationary state or fixed point discussed here is not this stationary phase.

the environmental parameters D and S_0 and is sometimes referred to as the carrying capacity of the system. The term carrying capacity is pervasive in ecology and conservation biology, but is also criticized for incorporating disparate concepts[52]. Another way of looking at the carrying capacity is to consider its so-called intrinsic component, the value of S at the non zero population steady state $S^* = ad/(v_{max} - d)$ (break-even concentration). As shown previously, this value sets the minimal requirement on S_0 for population growth, but also measures how pessimized (or degraded) an environment the strain can tolerate. In the context of habitability, it is interesting to note that this intrinsic component of the carrying capacity, or pessimization ability is maximized in models of evolution where the environmental condition is 1-dimensional such as it is here the case[53]. The reader is encouraged to consult *The Theory of the Chemostat* by H. Smith and P. Waltman[51], where an in depth analysis of the dynamical properties of the model is presented. The chemostat model serves as the basis for modeling the environments in the different projects described in this thesis.

Figure 0.1.: Phase portrait of the (dimensionless) model of the chemostat. The red dot is the stable resting point, and the yellow dot is the metastable resting point $N = 0$.

By extension of definition 0.1, habitability can be measured over a set of different classes of organisms $\{N_i\}$ with $i \in \{1, \cdots, n\}$ and over a set of different environments $\{E_j\}$ with $j \in \{1, \cdots, n'\}$. There is however an important remark to be made. In Earth's ecosystems, organisms can have a variety of impacts on their environment that can be of physical (mechanical) or chemical nature. Globally relevant examples of mechanical interactions include bioturbation (biological reworking of soils and sediments), for example by termites (the most striking instance is perhaps the 230,000 km^2 network of interconnected mounds found in Northeastern Brazil[54]), or by earth worms which was suggested by Charles Darwin as an important soil process[55] and later confirmed as playing a key role in ecology, evolution and biogeochemistry[56]. Moreovoer, organisms also have direct interactions between each other such as predation or symbiosis. As a consequence, an organism of a new functional type emerging in an inhabited environment does so in an environment that is partly composed of other functional types and that is also defined by the biological action (mechanical or chemical) to some potentially extreme extent (the emergence of oxygenic photosynthesis dramatically changed the atmosphere and surface oxidation state, as well as the climate[24]). Therefore, one must note that any naive application of definition 0.1 to several functional types that would not account for these complex interactions is at risk of miss-

ing an essential characteristic of the biosphere as being itself part of what makes a world habitable and for how long. In this first model development, I only consider one functional type and explore the formalism of habitability introduced here as evaluated on a variety of environments. A preliminary work on the analytical intuitions of multi-species ecosystem's habitability is in Appendix B.1.

From these generic considerations on habitability, the work of a modeler interested in practical applications of this criterion should be geared towards carefully examining what relevant biological modeling to use, and in particular what sets the limits of viability. In the next chapter, I present a biological model that I think is suited for candidate organisms that might inhabit a variety of environments that are relevant to the search of extraterrestrial life. This model is based on energy balance in the cell and focuses on situations where resource uptake yields low amounts of energy.

Chapter 1.

Designing a thermodynamical model for chemo-autotrophs

> What is the characteristic feature of life? When is a piece of matter said to be alive? When it goes on 'doing something', moving, exchanging material with its environment, and so forth, and that for a much longer period than we would expect of an inanimate piece of matter to 'keep going' under similar circumstances.
>
> –Erwin Schrödinger, *What Is Life*, 1944

ORGANISMS on Earth always consume some resource, be it to acquire energy (*e.g.* through oxidation of reduced carbon in organic molecules) or to assemble functional polymers (using nitrogen, phosphate, carbon, oxygen and hydrogen as building blocks). The chemical reactions responsible for these interactions are called *catabolism* and *anabolism* respectively; together they form the *metabolism*. Therefore, the relationship between a functional type i and the environment E_j is at least tied to the metabolic activity of i, as the metabolic type sets chemical solutes that are consumed by the population and its size together with the physiology of the individuals set the rate at which these solutes are consumed. While a large number of environmental variables have the potential to prevent viability, such as ionizing radiation, extreme pH or salinity, they are observed to effectively prevent the existence of an ecosystem when they are found in combination[57–59]. But building a model accounting for every possible variable is neither useful nor required.

Early metabolisms on Earth were very different from those we know today. The early Earth's atmosphere was most likely reduc-

ing, and remained so until the emergence of oxygenic photosynthesis, at least 1,500 million years after the Earth formed, and at least 1,000 million years after the origin of life[16,60,61]. Photosynthetic organisms are not limited in the energy they acquire as sunlight is readily available to them, and thus the question of their viability shifts to the availability of nutrients such as nitrogen or iron if they use chlorophyl as a pigment. The transition to an oxygen rich atmosphere also permits respiration as an energy acquisition reaction. The oxidation of one mol of glucose with oxygen (aerobic respiration) yields about 3,000 kJ of Gibbs free energy. In comparison, methanogenesis which is likely one of the earliest metabolism to appear on Earth (equation 1.1)

$$H_2 + \frac{1}{4}CO_2 \longrightarrow \frac{1}{4}CH_4 + \frac{1}{2}H_2O \tag{1.1}$$
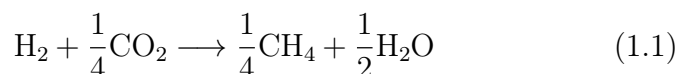
yields about 33 kJ Gibbs free energy in standard conditions, and the full anaerobic fermentation of one mole glucose into methane and carbon dioxide in standard conditions is of the order of 100 kJ[62]. For comparison, the energy dissipated to produce one mole of biomass (in carbon equivalent) is at least 230 kJ for heterotrophs and 900 kJ for autotrophs[62]. Thus, in the anaerobic conditions that have dominated on Earth for more than a third of its existence, deviation from standard conditions can have important consequences on the ability for both heterotrophs and autotrophs to acquire energy through the catabolic reaction. Furthermore, most extraterrestrial environments seen as candidate for habitability also seem lacking strong oxidants usable by living organisms[27,63–66]. Anaerobic conditions thus seem like an interesting first target to build a biological model for, and that energy availability might be a necessary aspect to account for.

But catabolic energy is not the only requirement for growth. This energy has to be converted into biomass, which requires anabolic nutrients (nitrogen and phosphorus). Biogeochemical models for Earth's ecosystem usually focus on the availability of a so-called *limiting* nutrient in order to estimate biomass stocks and production. In Earth's surface oceans, the limiting nutrient is always anabolic nutrient (such as nitrogen) since photons are available in virtually infinite quantity. The concept of a limiting nutrient from an empirical stand point is a nutrient that triggers growth in a settled population (a bloom), *e.g* iron[67]. In Earth's oceans, plankton is composed of approximately five times less nitrogen than carbon, and twenty times less phosphorus[68]. Assuming that this ratio

holds for the autotrophic Archaea that perform methanogenesis, and assuming standard conditions, for every one mole of hydrogen reacted, 1/120 moles of nitrogen are required (and 1/3000 of phosphorus). Additionally, biological fixation of N_2 may have originated early on[69]. For these elements to prevent growth at all, they would have to be so rare that they are virtually nonexistent. But anabolic nutrients do not seem to be rare in the candidate habitable environments known to date. Phosphate and nitrogen are both found in martian meteorites[70] and expected to be available in Enceladus's ocean[71].

For these reasons, the "follow the energy" approach to habitability has been suggested[72–74]. Looking at habitability through the constraint of energy rather than nutrient limitation also allows to neatly incorporate viability-limiting factors other than the availability of catabolic or anabolic molecules. Temperature, along with pH, pressure or salinity may impact the energy requirements of the cell. Among these factors, temperature is an essential one (and might also be easier to take into account). Indeed, temperature independently from other factors might constitute a hard limit on life on Earth, as no organism is known to grow above 122 °C[75].

In this chapter, I focus on energy flow in the cell (and therefore both on thermodynamics and kinetics) in order to capture the energy limitations that are likely to determine the viability of anaerobic, autotrophic populations such as methanogenic Archaea, and allow temperature limits to emerge. This model builds on a rich body of work on cellular energetics and thermodynamics that stems from environmental science and industrial biotechnology[62,76–79].

1.1. Energy balance in the cell

Building cell components requires energy and matter, which are obtained by the cell in its environment through catabolism and anabolism. The catabolic reaction is the reaction through which the cell acquires energy from its environment. This reaction holds some potential energy, that I note E_c (J mol^{-1}) for now, and occurs at a certain biomass-specific rate, accelerated by enzymes, noted q_{cat} (mol s^{-1} mol$_c^{-1}$, where mol$_c$ counts biomass in moles of carbon). The product $P_c = q_{cat} \times E_c$ therefore corresponds to a flux of energy acquired by the cell.

Electron exchanges that occur during the catabolic reaction are coupled to anabolic processes generally through intermediaries, for example to reduce inorganic carbon. In essence, this coupling corresponds to a transfer of energy from the catabolic reaction to the anabolic reactions. While anabolic reactions are as diverse as the functional molecules that make up the cell, I assume here for simplicity that a single rate can be defined for a generic biomolecule. This assumption corresponds to a single essential biomolecule having a slower synthesis rate than the others, or that the sum of all anabolic processes can be averaged to a single theoretical reaction. In order to quantify the amount of biomolecules that can be synthesized per time unit, the following energy balance equation is used

$$P_c + P_a = 0 \qquad (1.2)$$

where $P_a = q_{ana} \times E_a$ with q_{ana} (mol s^{-1} mol$_c^{-1}$) is the biomass-specific rate of the anabolic reaction, and E_a describes the energetic cost including dissipation and losses from building one mole of the theoretical biomolecule (J mol^{-1}).

But not all anabolic synthesis goes to increase the cellular stock of biomolecules. Functional molecules undergo irreversible changes, such as denaturation, and thus need to be replaced. The energy balance defined in equation 1.2 is not an actual representation of the energy conservation inside the cell, it just denotes the conservation of energy during the coupling of the catabolic reaction with anabolic processes. The cell itself is not a closed system, and there is no reason to believe *a priori* that energy must be conserved. And therefore, the energy content inside the cell changes when the cell grows or dies. This energy content is increased when new functional biomolecules are synthesized and diminished when these molecules (or rather their function) are lost to irreversible processes. Here, we are not as interested in accounting for the energy represented by all the biomolecules in any state they could find themselves, but what energy a functional molecule represents to the cell. Thus, I allow myself to equate the energy of a fully functional biomolecule with the catabolic energy it costs the cell to build it. Therefore, the change in functional molecule energy $B_c \times E_a$, where B_c denotes the cellular biomass (mol$_c$), inside the cell follows

$$\frac{d(B_c E_a)}{dt} = B_c(P_a - q_m \times E_a) \qquad (1.3)$$

where q_m is the rate of biomolecule functionality loss.

This description of the energetics of microbial growth has been proposed and used (albeit with a different formalism) in the industrial biotechnology literature for about three decades[62,78,79]. In general, the biomolecule function loss term is called the maintenance energy rate (noted e_m), as it corresponds to the minimal amount of energy that needs to be acquired from the catabolism in order to maintain cellular integrity. It has been proposed in the context of habitability that a minimal energy threshold to enable growth could be identified and assimilated to habitability[72,73,80]. These studies therefore propose that the assessment of the thermodynamical state of an environment and its comparison with the minimal energy yield requirement could serve as a measure of habitability.

But I argue that in order to infer habitability and define it rigorously as an energy-related barrier, a more detailed model must be built. First, an environment where the catabolic energy yield is close to the limit could be simply at equilibrium with an existing population, as suggested by proposition 0.1. Second, the existence of an energy yield threshold seems in apparent contradiction with the dynamical nature of biological processes. In other words, what does it matter that the potential energy of the catabolic reaction is low, if this reaction can be accelerated to compensate? Here, I show that using formalism from the maintenance energy, as well as the modeling of the kinetics of cellular processes can be used to connect a hypothetical population with geochemical cycles. Second, it permits to clearly define the possibility of an energy yield threshold for the growth of organisms that operate close to thermodynamic equilibrium (in other words that have low yield catabolic reactions), accounting for the adaptive constrains that weigh on the kinetics of functional biomolecules.

1.1.1. Catabolic energy yield

Catabolism is the set of reactions the a cell uses to harvest the energy needed for maintenance and the synthesis of complex organic molecules (cellular growth). Catabolism can be written for 1 mol of electron donor (eD) as:
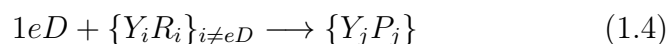
$$1eD + \{Y_i R_i\}_{i \neq eD} \longrightarrow \{Y_j P_j\} \tag{1.4}$$

where $\{R_i\}$ are the reactants, $\{P_j\}$ the products and $\{Y_{i,j}\}$ their stoichiometry (counted negative for reactants and positive for products). The catabolic reaction is usually *spontaneous*, meaning that

it has negative Gibbs free energy $\Delta_r G < 0$, hence the represented direction of reaction in equation (1.4).

The Gibbs free energy is computed from the environmental conditions through the Nernst equation

$$\Delta_r G_{cat} = \Delta_r G_{0,cat} + RT \ln(Q_{cat}) \qquad (1.5)$$

Often, the standard reaction Gibbs free energy as a function of temperature is approximated by

$$\Delta_r G_{0,cat} = \Delta_r G_{0,S,cat} \frac{T}{T_S} + \Delta_r H_{0,S,cat} \frac{T_S - T}{T_S} \qquad (1.6)$$

assuming $\Delta_r S_0(T) = \Delta_r S_{0,S}$. $\Delta_r G_{0,S,cat}$ and $\Delta_r H_{0,S,cat}$ are respectively the standard free energy and enthalpy of the reaction at standard room temperature $T_S = 298K$ and can be found in standard data tables (*e.g.* in the *CRC Handbook of Chemistry and Physics*[81]). The perfect gas constant is $R = 8.314$ J mol^{-1} K^{-1} and Q_{cat} is the catabolic reaction quotient:

$$Q_{cat} = \prod_i a_i^{Y_i} \approx \prod_i C_i^{Y_i} \qquad (1.7)$$

in a single aqueous phase, with a_i being the activity of i. Under the assumption of the ideal solution, the activities are commonly approximated by their molar concentrations C_i. In this thesis, I will make this assumption, and neglect second order effects on the activities of the solutes, even that of salinity, in order to focus on a clear formalism of how the catabolic energy interacts with biological requirements in defining a limit to microbial growth.

An important concept in this model, and in the terminology of bioenergetics, is the catabolic energy yield. Usually, the growth yield, or catabolic growth yield refers to the amount of new biomass that is synthesized when the population consumes one mole of resource. Specifically to bioenergetics, the catabolic energy yield corresponds to the amount of biomass synthesized per unit of energy acquired through the catabolic reaction. Kleerebezem and Van Loosdrecht (2010)[62] propose three methods to estimate this energy yield in a model, one of them referred to as the Gibbs energy dissipation method. In this approach, the catabolic yield is calculated by dividing the Gibbs free energy of the catabolic reaction by the enregy cost of building one mole of biomass (including

dissipation, see subsection 1.1.3 below). We adopt this methodology, and let this yield quantity emerge from the model. Rewriting equation 1.3 (assuming that E_a is constant over time) gives

$$\frac{dB_c}{dt} = B_c(\lambda q_{cat} - q_m) \tag{1.8}$$

where

$$\lambda = -\Delta_r G_{cat}/E_a \quad , \tag{1.9}$$

keeping in mind that $P_a = -P_c = -q_{cat} \times \Delta_r G_{cat}$. In essence, we have here the backbone of the model that will be used throughout this thesis, but it is essential that the rates q_{cat} and q_m are described in a way that is amenable to empirical estimation, and be used in a flexible manner since the model should be applicable to settings that are potentially not habitable.

1.1.2. Catabolic rate

Even spontaneous reactions may never occur, if their kinetics are infinitely slow. For the reaction to occur, an energy barrier has to be overcome. The energy source providing the means to overcome this barrier corresponds to the collisions of molecules induced by the thermal excitation of the system. A common empirical law describing the rate of an elementary reaction (in which no intermediate product is formed) as a function of the system's temperature and the reaction's activation energy (the energy barrier) is the Arrhenius law

$$k = Ae^{-\frac{\Delta E_a}{RT}} \tag{1.10}$$

where T is the absolute temperature (K), E_a is the activation energy of the considered reaction (in J mol^{-1}), and A is called the pre-exponential factor (in units of s^{-1}), often expressed as $A = k_b T/h$ with k_b the Boltzman constant and h the Planck constant. A fundamental property of living organisms is that they synthesize enzymes that significantly lower the activation energy of reactions so that they may occur at higher rates and that the potential energy they hold can be used.

But catabolic reactions are rarely if ever composed of a single elementary reaction. Nevertheless, it is not an uncommon assumption to model biological rates using the Arrhenius law, even at the scale of different species in different environments to which they

are adapted[77,82,83]. Using a single Arrhenius law to model biological rates would hold true to the exact application domain of the law if there was one elementary reaction that controls the kinetics of the modeled process. In the case of several species adapted to different environments, the law would hold true if the protein controlling the rate was conserved across the different groups. But despite that we might expect that rate controlling enzymes and especially their sensitivity to temperature is adaptive, Arrhenius-like functions have been fitted with some success to the growth rate of plankton as a function of seawater temperature[82], and so was the resting metabolic rate, or maintenance energy rate[77,78].

Here, I will make the assumption that the Arrhenius law describes sufficiently well the sensitivity of both the catabolic rate and the rate of protein denaturation. I will also assume that the parameters of these laws, in particular the activation energy, relate to some extent to protein function. The activation energy of the catabolic reaction might reflect the ability of the rate controlling enzyme to perform its function, and the activation energy of maintenance (denaturation) reflects the thermoresistance of functional proteins. This adaptive aspect will be explored in the next chapter. Here, I will describe the modeling of both the catabolic and the maintenance rate as if we were interested in modeling the growth of a particular organism, for now ignoring considerations of adaptation.

A general model of enzyme kinetic activity q_e (mol s^{-1} mol$_e^{-1}$, where mol$_e$ quantifies the enzyme abundance) as a function of temperature was derived in Daniel et al. (2010)[84] and validated experimentally. In their framework, q_e is determined by the abundance of activated enzymes E_{act}. Higher temperature accelerates the catabolic reaction, but also the conversion of activated enzymes to a deactivated state E_{inact} and irreversible denaturation into E_{den}.

$$E_{act} \rightleftharpoons E_{inact} \longrightarrow E_{den} \tag{1.11}$$

where E here denotes the enzyme abundance. The kinetics of the catabolic reaction and enzyme conversion are modeled using Arrhenius and equilibrium laws:

$$\begin{aligned} q_e &= \frac{k_{cat}}{1+K_{eq}} &&\text{with} \\ k_{cat} &= \frac{k_b}{h}Te^{-\frac{\Delta G_{acat}}{RT}} &&\text{and} \\ K_{eq} &= e^{\Delta H_{eq}\left(\frac{1}{T_{eq}}-\frac{1}{T}\right)} \end{aligned} \tag{1.12}$$

where k_b is the Boltzmann constant, h is the Planck constant, and ΔG_{acat}, ΔH_{eq} and T_{eq} are parameters governing q_e (respectively the activation energy of the activated enzyme activity, the equilibrium enthalpy and temperature of enzyme deactivation). Daniel et al. (2010)[84] estimated these parameters for different enzymes by fitting their model to laboratory experiments.

The quantity q_e expresses the catabolic rate per mole of catabolic enzyme. In order to define a biomass specific rate $q_{cat} \propto \tau q_e$ (and not enzyme specific) the scaling parameter τ, the number of catabolic enzyme per mole of cellular biomass, is introduced. Information on the value of this parameter is found in section 1.2.1.

1.1.3. Anabolism and maintenance energy

Some of the energy provided by the catabolism goes to the maintenance of the cell. An empirical relationship between the cell maintenance energy rate and temperature was established in Tijhuis et al. (1993)[78]:

$$
\begin{aligned}
e_m &= 84 * e^{\frac{69400}{R}(\frac{1}{T_S} - \frac{1}{T})} \\
q_m &= \frac{e_m}{E_a}
\end{aligned}
\tag{1.13}
$$

where $T_S = 298$ K and T is the absolute temperature. When $\lambda q_{cat} < q_m$, the cell decays and eventually dies. While in most of this thesis this empirical relationship to temperature is used, in the next chapter, I will use a simple Arrhenius law to describe the rate of temperature sensitive irreversible loss of function such as protein denaturation. One may note that the empirical relationship derived in Tijhuis et al. (1993)[78] described above dates from 1993, and to my knowledge, not much attention has been devoted since then to improve or challenge these estimates. Despite that, this relationship is widely used in astrobiology[63,72,74]. Therefore, empirical work to provide new estimates and a better understanding at the molecular level of the effective maintenance energy is warranted.

The leftover catabolic energy, after fulfilling maintenance requirements, goes to fueling net synthesis of biomass. The anabolic reaction is rarely spontaneous and often requires more energy than one mole of the catabolic reaction alone may provide. In effect, the cell is able to store energy in the form of ATP (or proton gradients in the shorter time scale) until enough is available to fuel an

anabolic reaction. The rate at which the anabolism runs is much lower than the catabolic reaction rate (one can compare catabolism to a small gear that drives the larger gear of anabolism). Furthermore, the Gibbs free energy, as calculated for the catabolic reaction describes the amount of the usable chemical energy change when the reaction occurs, not the energy required for a non spontaneous reaction to occur. Kleerebezem and Van Loosdrecht (2010)[62] uses a generic chemical composition of biomass that is useful to compute the Gibbs free energy change associated with the synthesis of one mole of biomass ($\Delta_r G_{ana}$). To this energy is added the cost of the dissipation that occurs during metabolism. An empirical relationship between characteristics of the metabolism and the amount of dissipated energy (ΔG_{diss}) is reported in the same study:

$$\Delta G_{diss} = 200 + 18(6 - NoC)^{1.8} + exp\left[((-0.2 - \gamma)^{2.16})(3.6 + 0.4 NoC)\right] \tag{1.14}$$

where NoC is the carbon chain length in the carbon source and γ is the oxidation state of carbon in the carbon source. This dissipation of energy is much larger than ΔG_{ana} for autotrophs, and I therefore make the convenient assumption that $E_a = \Delta G_{diss} + \Delta G_{ana} \approx \Delta G_{diss}$.

1.2. Single-species population dynamics

The basis of this model is that we link internal cell dynamics with population dynamics. We thus define the population (N) growth rate (r) as a function of the internal state B_c (internal biomass quantity of cells, assumed to be equal for all individuals in the population). The description of the mean field value of B_c does not exactly follow equation 1.8 as it is affected by cellular division. Rigorously, equation 1.8 describes only the net production of biomass by anabolism:

$$q_{growth} = \lambda q_{cat} - q_m \tag{1.15}$$

But the cellular biomass B_c in a population where cell divide follows

$$\frac{dB_c}{dt} = B_c(q_{growth} - r(B_c)) \tag{1.16}$$

where r is the division rate, assumed to be a function of the abundance of cellular biomass. It can be shown that the division rate is equal to the specific change in the mean field value of B_c, see proof B.2.

Then, the differential equation for the population dynamics writes

$$\frac{dN}{dt} = (r(B_c) - d)N \qquad (1.17)$$

where d denotes a death rate independent of maintenance.

The quasi-steady-state approximation (QSS) can be used to simplify the system :

$$\begin{aligned} \frac{dB_c}{dt} &= 0 \\ \Rightarrow \quad r(B_c^*) &= q_{growth} \end{aligned} \qquad (1.18)$$

where B^* denotes the steady-state of B. Equation 1.17 becomes

$$\frac{dN}{dt} = (q_{growth} - d)N \quad . \qquad (1.19)$$

1.2.1. Active biomass proportion estimation

In chapter 3, I estimate τ to be of the order of $2 \cdot 10^{-5}$ for a population of methanogens fitting data in Taubner et al. (2018)[85]. Gillooly et al. (2001)[77] reported the mass-specific resting metabolic rate as a function of temperature for a wide range of organisms, but not for thermophiles. We compared results of our modelling of q_{cat} for a thermophilic enzyme using $\tau = 2 \cdot 10^{-5}$ to the temperature-dependence of metabolism reported in Gillooly et al. (2001)[77] and obtained a rate at optimal temperature (75 °C) that corresponds to the lower values found for unicellular organisms ($\log B_0 \approx -6$, with the mass-normalized resting metabolic rate B_0 in $W/g^{3/4}$).

1.2.2. Steady-state thermodynamic state of the system

As the population grows, the energy intake rate *per capita* diminishes, because of lower availability of catabolic substrates and lower catabolic Gibbs free energy as the system is drawn closer to thermodynamic equilibrium. Here, I explore the non equilibrium thermodynamic state of the system at the population steady-state, assuming that growth stops because of the decreasing catabolic reaction Gibbs free energy. The system in equation 1.19 can be solved for steady-state following:

$$\begin{aligned} q_{growth} &= d \\ \Leftrightarrow \quad \Delta_r G_{cat}^* &= E_a \times \frac{q_m + d}{q_{cat}} \\ \Leftrightarrow \quad \ln Q^* &= \ln K_{cat} - \frac{E_a}{RT} \frac{q_m + d}{q_{cat}} \end{aligned} \qquad (1.20)$$

where K_{cat} is the catabolic reaction equilibrium constant and the superscript (*) denotes the steady-state value. In effect, the assumption of energy yield limitation translates into setting the catabolic rate at its theoretical maximum value. For example, q_{cat} might contain a Monod function of the limiting substrate concentration, *e.g* $q_{cat}(S) = \tau q_e S/(a + S)$, with a the half saturation constant. The assumption of growth being limited by energy yield rather than substrate availability corresponds to $S >> a, q_{cat}(S) \approx \tau q_e$.

By analogy with classical chemistry notations, equation 1.20 can be rewritten to express the out of equilibrium steady-state as

$$\text{pQ}^* = \text{pK}_{cat} + \frac{1}{\ln(10)} \frac{E_a}{RT} \frac{q_m + d}{q_{cat}} \tag{1.21}$$

where $\text{pX} = -\log_{10} \text{X}$.

It should be noted that if the initial condition is $Q > Q^*$, the initial growth rate is negative and the population and the population goes extinct. Also, this steady-state only exists when Q is allowed to admit a steady-state by equations governing the concentrations, that is when the system is open. If the system is closed and the microbial population only has access to a (short-term) finite resource, it will deplete it and die out. In an open system, fluxes of catabolic substrates correspond to a flux of chemical disequilibrium. Using chemostat dynamics for the catabolic substrates yields:

$$\frac{dC_i}{dt} = D(C_i^0 - C_i) + Y_i q_{cat} N B_c \tag{1.22}$$

where C_i is the concentration of the catabolic substrate i and Y_i its stoichiometry in the catabolic reaction, C_i^0 is its concentration in the supplied fresh medium. If the only chemical reaction occurring in the reactor is the catabolic reaction performed by the population, $\partial C_i \partial [e_D] = Y_i$ where $[e_D]$ is the concentration of the electron donor, with convention $Y_{eD} = -1$. The steady-state concentrations can therefore be expressed as a function of the electron donor concentration at steady-state $[e_D]^*$

$$C_i^* = C_i^0 + Y_i([e_D]^0 - [e_D]^*) \tag{1.23}$$

In combination with

$$\prod_i (C_i^*)^{Y_i} = Q^* \tag{1.24}$$

replacing Q^* with its expression derived in equation 1.20, and C_i^* using equation 1.23, the concentrations at steady-state can be numerically solved and subsequently the population size using equation 1.22. An example of this procedure is given in part II of this thesis.

In effect, we obtained a criterion satisfying the requirements of definition 0.1, and thus a binary measure of habitability focused on the energy yield value of the catabolic reaction. Thus, provided suitable values for the parameters governing enzyme activities, maintenance kinetics and the catabolic enzyme fraction τ, one is able to assess whether an environment is in sufficient thermodynamic disequilibrium to allow a population of energy-limited chemoautotrophs to grow. While the values of these parameters are empirically constrained to some extent, it is deeply unsatisfying that a criterion of habitability neglects the defining ability of life to adapt to its environment. These parameters relate (admittedly loosely) to phenotypic characteristics, or traits. For instance, equation 1.12 describes the kinetic factor of the catabolic reaction as a function of temperature and the enzyme properties. The rate of the catabolic reaction depends on its activation energy ΔG_{acat}, that relates (inversely) to the ability of the catabolic enzyme(s) to accelerate the catabolic reaction, and the amount of active enzymes at a given time depends on the equilibrium enthalpy of the reversible enzyme deactivation reaction ΔH_{eq}, which correlates with the ability of the enzyme to retain its function when temperature increases. The model is focused around calculating the kinetics of energy intake from catabolism and energy spending requirements from maintenance, and temperature emerges naturally as a major environmental factor from the physical modeling of these kinetics. In order to assess habitability, one has to consider at least how temperature affects the viability of a population. All species known on Earth are affected by temperature in their ability to survive and all microbes are observed to display an optimal and a maximal temperature for growth (*e.g* Rosso et al., 1993[86]), and no species has been observed to grow above ca. 120 °C [75]. These temperatures, called cardinal temperatures, are identifiable to parameters of the model and will serve as a description of the phenotype of a microbe in the temperature space in the next chapter, as well as later in part II of this thesis. Astrobiologically relevant extraterrestrial bodies, and environments in general, have temperatures spanning a wide interval of temperatures. The atmosphere of Venus varies vertically

from 750 K to 180 K at 100 km[87,88], the ocean of Enceladus has temperatures ranging from 273 K to more that 360 K[89] and the temperature below the surface of the early Mars could have ranged from $\approx$ 270 K at the surface to $\approx$ 450 K at 10 km depth[90].

But how do we go from there to actually link the parameters in the model to phenotypic traits possibly under selection for the adaptation to temperature? Or, what region of the parameter space (the values that the different parameters can take) can we explore in order to test habitability based on the ability and inability of Earth life to adapt to different temperatures? The question of defining the parameter space that can be explored by evolution, even for adaptation to temperature alone, is a vast and complex one. There is a large body of literature that is focused on the molecular basis to adaptation of proteins to higher temperatures[91,92], but little has been done in theoretical ecological and evolutionary modeling on the subject. For instance, Corkrey et al. (2016)[93] propose a method to fit kinetic parameter representative of functional properties of adaptive enzymes, and Thomas et al. (2012)[94] use a model of adaptation to assess the effect of adaptation on ecosystem-level temperature-sensitive rates but uses an empirical model that admits no phenotypical interpretation of this adaptation. In the next chapter, I will present exploratory work using the theory of adaptive dynamics[53] to discuss the evolutionary constrains that might bear on the adaptation to temperature. In particular I will explore how the activation energy required for a protein to perform its function could interplay with the activation energy required for loss of function to occur to explain the existence of an upper limit to viable temperatures. Second, I identify patterns in the values of these parameters retrieved by fitting the model to published temperature growth curves and discuss their relation to constrains on adaptation.

Chapter 2.

Adaptation to higher temperatures as a trade-off between enzyme affinity and thermoresistance

H OW THE ENVIRONMENTAL TEMPERATURE influences biological rates is a major scientific question, spanning multiple fields from biogeochemistry[82,94] to biotechnology[78], food science[95] and medicine. There exists a wide variety of models describing the sensitivity of the growth rate of microorganisms to temperature[83,96]. Some of these models are described as empirical (*e.g* Ratkowsky et al., 1982[97]), and other as mechanistic, or general mechanistic models (such as master reaction models[98], or modified Arrhenius models[76]). While these models focus on the description of the growth rate of a particular species with respect to temperature, another class of models –often empirical– aims to describe the metabolic rate at the scale of ecosystems, such as the well-known Eppley curve[82]. Often times, ecosystem-scale models of temperature resort to parameterized, empirical models of so-called temperature growth curves (the growth rate as a function of temperature) rather than mechanistic models[77,82,94,97]. While these models are able to provide good insight into the potential evolution of temperature adaptation patterns, as well as the importance of the environment's temperature as an environmental constraint on evolution, they rely on a vague (but practical) definition of adaptative traits, *e.g* optimal temperature[94]. On the other hand, other models, thermodynamically grounded, make use of master-reaction models (MRMs), that precisely describe an enzyme's properties, but fail to relate to ecologically relevant traits[93,99].

Here, I aim to build up from a simpler model of energy balance in the cell, inspired by the Hinshelwood model[76] and bioenergetics of microbial growth[62,79]. The model uses fewer parameters, but these parameters can be related to (i) physiological ecologically relevant traits regarding enzymatic rates; and (ii) a "coarse grain" description of maintenance requirements. This simpler model allows for analytical work and easier inference of the parameters than models with more complicated expressions and more parameters[83,96]. This model is centered around the energetic cost of biomass and the temperature-sensitive kinetics of biomass alteration and catabolic reaction to compute the growth rate. The activation energies of the catabolic reaction and the loss-of-function reaction both relate to protein flexibility (conformational changes are needed to perform function but rigidity might prevent denaturation). As a consequence, estimating parameters of this model against growth rates of various organisms allows to discuss thermal adaptation strategies and constraints which may in turn provide insight into linking temperature with ecosystem productivity. In this chapter, I briefly explore how adaptation can interplay with the ecology of energy yield limited ecosystems. Second, I fit the model on a database of temperature growth curves for various organisms and discuss the possibility of a trade-off between enzyme activity and enzyme thermoresistance. These results help to contextualize the application of the bioenergetics model in part II of this thesis.

2.1. Thermal properties of the model

Here, I use a version of the general model from chapter 1 where the description of the catabolic rate is simplified to adopt the formalism of the Hinshelwood model[76,83]. For consistency with classical notations of kinetic rates denoted by k, we rewrite equation 1.15 as

$$k_g = -\frac{E_c}{E_a}\tau \times k_c - k_m \tag{2.1}$$

Note that the scaling factor τ corresponds, like it does in the previous chapter, to the fraction of biomass that is enzymatically active in catabolism. Consistently with the previous chapter, we also note the *catabolic energy yield* as $\lambda = -\frac{\Delta_r G_{cat}}{E_a}$ [62]. The rates k_c and k_m do not describe phenomena of the same scale: we assume that all biomolecules are subject to denaturation but that only a part of biomolecules take part in accelerating the catabolic reaction, thus

k_c is multiplied by the scaling factor τ.

$$\tau = \frac{X_e}{X} < 1 \qquad (2.2)$$

where X (mol$_C$) is the amount of biomolecules in the cell and X_e (mol$_e$) the amount of catabolic enzymes in the cell.

Following Hinshelwood (1946)[76], we express the specific rates k_c and k_m as Arrhenius laws of activation $E_{a,c}$ and $E_{a,m}$ respectively. We assume that both these Arrhenius functions have the same pre-exponential factor A, the difference in catabolic and maintenance kinetics being captured by the catabolic yield and enzymatic investment scaling terms λ and τ. We thus rewrite equation 2.1 into our full model of biomass growth:

$$k_g = \lambda \tau A e^{-\frac{E_{a,c}}{RT}} - A e^{-\frac{E_{a,m}}{RT}} \qquad (2.3)$$

where $R = 8.314$ J K^{-1} is the perfect gas constant and T (K) is the temperature of the ectothermic organism's media. In this version of the model, the catabolic rate no longer follows the model of enzyme deactivation of Daniel et al. (2010)[84]. Whichever model is more accurate is not trivial. Indeed, the catabolic enzyme deactivation model accounts for a lower fraction of the enzyme being in the active state at higher temperatures, but an organism could compensate by producing more catabolic enzymes, which could translate into a lower fraction of active biomass τ, or equivalently a higher maintenance (inactive enzymes are functionally dead molecules, even if the reaction is reversible when the temperature is kept constant). While k_g is the specific biomass net production rate, it is equal to the growth rate of the microbial population under the assumption that the interior of the cell is at stationary state. We thus use the expression of k_g as a proxy for the specific growth rate μ.

Here, I focus on the effect of temperature on the kinetics of the catabolic reaction and the maintenance processes, therefore I neglect the effect of temperature on the catabolic energy yield (hence the catabolic energy yield λ is independent of temperature). From equation 2.3, the expression of cardinal temperatures T_{max} (maximum temperature of growth) and T_{opt} (temperature of maximal growth) is found

Figure 2.1.: Temperature growth curve simulated from the model.

$$\begin{cases} T_{opt} & = & \frac{E_{a,c}-E_{a,m}}{R(\ln(\lambda\tau)+\ln\frac{E_{a,c}}{E_{a,m}})} \\ T_{max} & = & \frac{E_{a,c}-E_{a,m}}{R\ln(\lambda\tau)} \end{cases} \qquad (2.4)$$

43

Note that $\tau < 1$ by definition, and although $\lambda < 1$ is not necessarily true, it seems unlikely that the product $\lambda\tau$ is greater than 1 since $\Delta_r G_{cat}$ would need to be orders of magnitude greater than the building cost of biomass E_a. Thus, on the condition that $E_{a,c} < E_{a,m}$ (catabolic reaction being faster than the denaturation processes), T_{max} and T_{opt} are effectively positive.

In essence, this limit formally captures a common hypothesis for existence of an upper temperature limit of life; that at higher temperatures, the denaturation kinetics of one or few essential biomolecules becomes so fast (or virtually instantaneous) that constructive cellular processes simply cannot keep up. But the model introduced here suggests the existence of another limit, which is that the upper temperature limit might be partly contextual to the type of environments that can exist. Indeed, equation 2.4 shows that T_{max} depends on the value of λ which linearly scales with the catabolic reaction Gibbs free energy (see equation 1.9). In environments where the catabolic reaction is closer to chemical equilibrium, the effective upper temperature limit would be lower. Second, equation 2.4 emerges from equation 2.3 where it is assumed that catabolic substrate availability is not limiting. Explicitly including substrate availability in catabolic energy intake rate leads to possibly even lower maximum growth temperature (see Appendix B.3). The equation 2.4 does not suggest that an absolute limit independent of any other factor exists as $\lim_{\lambda\tau\to\infty} T_{max} = \infty$. As a consequence, even if there exists an absolute limit, not captured by the model, it might never be reached because of the limited range of environments existing on Earth, setting a maximum value for λ.

2.2. Adaptation of a single metabolism to temperature

It is a common assumption that either a strain is adapted to its optimal growth temperature (as defined in the previous section), or that in an environment at a given temperature, the strain with the highest growth rate at this temperature is selected (regardless if this is its optimal temperature or not)[82]. But these assumptions rely on a loose definition of fitness. Fitness is a particularly difficult concept to define as an absolute property, but to circumvent this problem, a definition of fitness as the ability for a mutant to invade an environment in which a resident strain is at steady state

was proposed and called *invasion fitness*[100–102]. Adaptive dynamics modeling has been developed for the study of ecosystems under this ecological definition of fitness. Here, I use the adaptive dynamics framework to reexamine the bioenergetic model developed in chapter 1.

An adaptive dynamics analysis is built upon (i) the expression of the abundance of a shared resource at the steady-state with a resident population characterized by a particular value of a functional trait r and (ii) the derivation of the per capita growth rate of an initially rare mutant m in the environment set by the resident steady-state. This second quantity is the invasion fitness. In the case of microbes for which the substrate energy yield rather than the substrate availability is limiting, the carrying capacity is governed on the one hand by the theoretical steady-state value of the chemical potential energy $\Delta_r G_{cat}^*$ determined by parameters τ, E_a, $E_{a,c}$ and $E_{a,m}$ and on the other hand by the fluxes of catabolic substrates.

Let us assume, following the formalism of adaptive dynamics, that a resident population (denoted by the subscript r, with trait value x_r) exists and sets the Gibbs free energy at steady state $\Delta_r G_{cat}^*(x_r)$ (or equivalently $Q_{cat}^*(x_r)$). The invasion fitness of a mutant (denoted by subscript m) is defined as

$$s(x_r, x_m) = \frac{1}{N_m}\frac{dN_m}{dt}\Bigg|_{\substack{\Delta_r G_{cat}=\Delta_r G_{cat}^*(x_r)\\N_m=0}} \qquad (2.5)$$

where the variables x_r and x_m represent the value of the considered trait in the resident and mutant populations respectively. For now, this trait abstractly refers to a physiological parameter affecting population growth but will later explicitly refer to a parameter of the model. In the present case, this equation translates into

$$s(x_r, x_m) = k_g(\Delta_r G_{cat} = \Delta_r G_{cat}^*(x_r)) \quad . \qquad (2.6)$$

This invasion fitness corresponds to the per capita growth rate of an initially rare mutant, and thus its positivity indicates that the mutant might invade and replace the resident population. Upon examination of equations 2.3 and 1.20, it can be shown that the condition for invasion fitness to be positive is

$$s(x_r, x_m) > 0 \iff \Delta_r G_{cat}^*(x_m) > \Delta_r G_{cat}^*(x_r) \qquad (2.7)$$

or in other words, that the mutant can tolerate conditions closer to the equilibrium than the resident. This result is expected from adaptive dynamics theory, when the environment is described by a single variable in the growth equation[53]. The adaptive dynamics framework defines the evolutionary singularity (ES) as the value X of the trait(s) such that

$$\left.\frac{\partial s}{\partial x_m}\right|_{x_m=x_r=X} = 0 \quad .\tag{2.8}$$

This evolutionary singularity X corresponds to the value of the adaptive trait at which a resident population with $x_r = X$ cannot be invaded by an initially rare mutant with a slightly different trait value x_m.

Here, such a singularity exists if the expected steady-state catabolic reaction Gibbs free energy as a function of the trait value x, $\Delta_r G_{cat}^*(x)$ admits an extremum at $x = X$, as $\Delta_r G_{cat}^{*'}(X) = 0 \iff \partial_m s(X, X) = 0$. It can be shown further that this singularity is stable and attractive (resp. unstable and repelling) if this extremum is a global maximum (resp. global minimum), as $\Delta_r G_{cat}^{*''}(X) < 0 \iff \partial_{x_r}\partial_{x_m} s(X, X) < 0$ and $\partial_{x_m}^2 s(X, X) < 0$. The reader is directed to Diekmann et al. (2004)[53] for details on the conditions for attractivity and stability of the ES. But $\Delta_r G_{cat}$ is a function of several parameters, each of them could be interpreted as an adaptive trait, and they might not be evolving independently from one another.

An example of an adaptive trait could be the activation energy of the loss of function reaction $E_{a,m}$, as it sets the kinetics of the maintenance reaction and relates to the rigidity of biomolecules. But increasing a protein's rigidity might also increase the activation energy of the reaction of the protein's function on top of the activation energy of the loss-of-function reaction. In a sense, this corresponds to a trade-off where lowering the rate of maintenance is made at the cost of also lowering the rate of constructive reactions in the cell. Such a trade-off has been suggested, *e.g* by Daniel (1996)[103], and the adaptive dynamics framework allows to translate this hypothesis into predictions of patterns in the values of $E_{a,c}$ and $E_{a,m}$. One might expect evolution to simply select proteins to maintain the same level of flexibility at different environmental temperatures at which the organisms are adapted. In other words, that $A \exp(-E_{a,c}/RT_e)$ and $A \exp(-E_{a,m}/RT_e)$ are constant with T_e the temperature of the environment the species are adapted to. This would imply that the difference $E_{a,m} - E_{a,c}$ is constant. In the
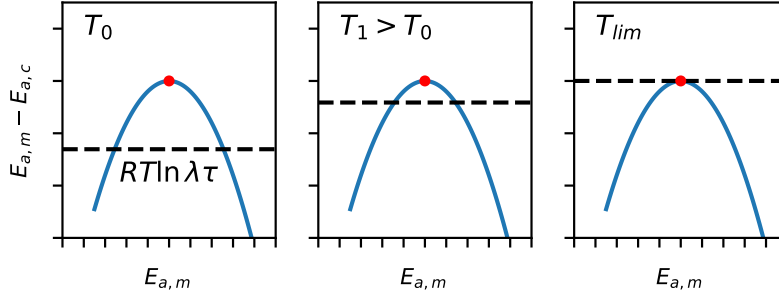
Figure 2.2. | Evolutionary singularity in the trait trade-off space. The dashed line corresponds to the minimal value of $E_{a,m} - E_{a,c}$ for growth to occur. The red dot is the maximum of $E_{a,m} - E_{a,c}$ at $E_{a,m} = X$, which is also the convergent stable evolutionary strategy. In this illustration, a quadratic function is used for f. The top panel is at a low temperature denoted by T_0, and the middle panel at a arbitrarily higher temperature $T_1 > T_0$, showing that if a global optimum exists, the survivable dispersion around it shrinks with increasing temperature.. The bottom panel shows the case where the temperature is set higher so that the maximum of $E_{a,m} - E_{a,m}$ is exactly equal to $RT_{lim} \ln \lambda \tau$, hence T_{lim} being the maximum temperature at which an organism can adapt.

next section, we will see that this does not appear to be the case. Here, I explore the adaptive dynamics of the system in the case of the maintenance activation energy $E_{a,m}$ being the only adaptive trait, and the catabolic reaction activation energy being positively correlated to $E_{a,m}$. All other parameters are assumed to remain constant. These patterns can then be confronted to estimates of these values for naturally occurring or laboratory populations, as presented in the next section of this chapter.

Before defining a trade-off function more precisely, let us express the value of $\Delta_r G_{cat}^*$ as a function of $E_{a,c}$ and $E_{a,m}$. Using equation 1.20, assuming that the mortality is only due to maintenance, and using the modified per capita growth rate in equation 2.1 yields

$$\Delta_r G_{cat}^{*r} = -\frac{E_a}{\tau} \exp\left(\frac{E_{a,c}^r - E_{a,m}^r}{RT}\right) \tag{2.9}$$

or equivalently

$$\ln Q^{*r} = \ln K_{cat} - \frac{E_a}{RT}\frac{1}{\tau} \exp\left(\frac{E_{a,c}^r - E_{a,m}^r}{RT}\right) \qquad . \tag{2.10}$$

Therefore, the per capita growth rate of mutant defined by $\{E_{a,c}^m, E_{a,m}^m\}$ follows

$$k_g^m(Q^{*r}) = A\left[\exp\left(\frac{E_{a,c}^r - E_{a,m}^r - E_{a,c}^m}{RT}\right) - \exp\left(-\frac{E_{a,m}^m}{RT}\right)\right] \qquad . \tag{2.11}$$

47

And in effect, the mutant can invade if $k_g^m(Q^{*r}) > 0$, or

$$E_{a,m}^m - E_{a,c}^m > E_{a,m}^r - E_{a,c}^r \qquad (2.12)$$

which corresponds to selection maximizing the difference $E_{a,m} - E_{a,c}$.

The assumption of a trade-off between $E_{a,c}$ and $E_{a,m}$ translates into the possibility of defining a function $f : E_{a,m} \mapsto E_{a,c}$. Solving equation 2.8 with $s(x_r, x_m) = k_g^m(Q^{*r})$ (equation 2.11) shows that there exist an evolutionary singularity, that we note as X a particular value of $E_{a,m}$, if

$$\frac{d}{dx}(f(x) - x)|_{x=X} = 0 \iff f'(X) = 1 \qquad (2.13)$$

Furthermore, this singularity is stable and attractive (ESS) if

$$f''(X) > 0 \qquad (2.14)$$

and unstable repelling if $f''(X) < 0$. That is, in the case of a convex trade-off between $E_{a,c}$ and $E_{a,m}$, there exists a value of $E_{a,m}$ that maximizes (potentially locally) the difference $E_{a,m} - E_{a,c}$, independently of the temperature. This implies that the ESS also maximizes T_{max}, as equation 2.4 shows that T_{max} scale with the difference $E_{a,m} - E_{a,c}$.

Under the additional assumptions that f'' is monotonic, the ESS is unique. The case of f'' not being monotonic allows the existence of multiple values of X for which $f'(X) = 1$, and thus multiple evolutionary singularities, some of them stable and some of them unstable. In such cases, it is also possible that an ESS does not correspond to a global maximum of $E_{a,m} - E_{a,c}$, and so that selection locks the evolving population in an apparently sub-optimal value of $E_{a,c}$ and $E_{a,m}$. When multiple ESS exist, the one towards which a population effectively converges is determined by the initial trait value in the population (assuming that mutations have a small phenotypic effect).

Additionally, equation 2.1 shows that

$$k_g > 0 \iff E_{a,m} - E_{a,c} > -RT \ln \lambda\tau \qquad (2.15)$$

so that if X is a global maximum of $X - f(X)$, then there is a stable and attractive evolutionary singularity, which is furthermore

independent of temperature as long as $E_{a,m}$ and $E_{a,c}$ are independent of temperature and the selective pressure on converging to this equilibrium increases with temperature. In other words, at lower temperatures, the strategy $E_{a,m} = X$ is optimal but deviation from it are viable, whereas at higher temperatures, only trait values close to the optimum are viable. Thus, if these activation energies are to be in trade-offs with other traits, or that the invasion fitness is dominated by other processes in usual conditions, the trait value $E_{a,m}$ could be expected to be found dispersed around the maximum at lower temperature and closer to the optimum when temperature becomes a strong selective pressure. Another consequence of X being a global maximum of $X - f(X)$ is that there exists a maximum theoretical maximum growth temperature T_{lim} when $E_{a,m} = X$. Using equation 2.15, this maximum temperature of adaptation is

$$T_{lim} = \frac{f(X) - X}{R \ln \lambda \tau} \tag{2.16}$$

Second, one can also show that if f satisfies the conditions for a convex tradeoff and $f'(X) = 1$, the derivative of $T_{max} - T_{opt}$ evaluated at X is negative:

$$\frac{d}{dE_{a,m}}(T_{max} - T_{opt})|_{E_{a,m}=X} = -\frac{(X - f(X))^2}{RXf(X)(\ln(\frac{X}{f(X)}) - \ln \lambda \tau)^2} < 0 \quad . \tag{2.17}$$

Therefore, it could be that in the vicinity of the ESS $E_{a,m} = X$, the span $T_{max} - T_{opt}$ is decreasing.

One could translate the hypothesis of a positive convex trade-off between $E_{a,c}$ and $E_{a,m}$ into a prediction that there exist an optimal value of $\{E_{a,c}, E_{a,m}\}$, independent of temperature, and that the dispersion of the observed values of these parameters around this optimum is expected to decrease with temperature. The hypothesis of a convex trade-off functions seems more natural as it expresses the impossibility of ever increasing returns on increasing $E_{a,m}$. Indeed, if f is concave, the singularity is unstable, and the framework predicts that $E_{a,m}$ is minimized (until the minimum possible value is reached) in the region where $f'(E_{a,m}) < 1$ and increased to infinity elsewhere (effectively, until it reaches a value where the model is no longer valid). Whichever of these regimes is followed depends on the initial value of $E_{a,m}$ in the ecosystem. These parameters interpreted as traits relate to the growth rate of a strain as a function of temperature. Therefore, so-called temperature growth curves,

measures of growth rates at different temperatures, are useful to estimate the values of the model parameters, $E_{a,c}$ and $E_{a,m}$ in particular. It would be ideal that databases containing such growth curves would also include the temperatures at which the organisms are found in natural settings (as a proxy of the temperature they are adapted to). Ideally, this database would also be composed of organisms sharing the same metabolism, as the present framework assumes that the coupling between catabolism and anabolism λ is constant, as well as the pre-exponential factor A. Thomas et al. (2012)[94] compiled such a database, unfortunately restricted to mesophilic plankton, and thus not suited to tackle the question of the upper temperature limit to life. The exact temperature at which extremophiles are found could be difficult to obtain, especially in the case of hydrothermal vent inhabiting organisms for which sampling is difficult. To our knowledge, this ideal database containing temperature growth curves of thermophiles as well as their environmental temperature does not exist. In the next section, we use a database compiled by Corkrey et al. (2016)[93] that contains temperature growth curves including thermophiles and hyperthermophiles but not their environmental temperature. We use this database to estimate values of $E_{a,c}$ and $E_{a,m}$ for different species growing at different temperatures to examine the possibility and meaning of a correlation between them.

2.3. Inferring parameter values from growth data

Here, inference of model parameters is performed on a data set published by Corkrey et al. (2016)[93], consisting in measured growth rates at different temperatures for 1627 strains of ectothermic Eukaryotes, Bacteria and Archaea. From this dataset, only experiments with 5 or more data points and at least two measured growth rates above the temperature optimum, and for which the fit of an empirical model (CTMI, see below) yielded physically sound parameters are selected, thus resulting in a subset of 327 strains.

Following recommendations in Grimaud et al. (2017)[96], a first fit is made using the empirical Cardinal Temperature Model with Inflexion (CTMI)[86] on the growth rate versus temperature data for a strain :

$$\begin{cases} \mu(T) &= \mu_{opt}\Phi(T) & \text{if } T_{min} \leq T \leq T_{max} \\ \mu(T) &= 0 & \text{else} \end{cases} \tag{2.18}$$

with

$\Phi(T) =$

$$\frac{(T - T_{max})(T - T_{min})^2}{(T_{opt} - T_{min})[(T_{opt} - T_{min})(T - T_{opt}) - (T_{opt} - T_{max})(T_{opt} + T_{min} - 2T)]}$$
(2.19)

under the condition (Bernard and Rémond, 2012 [104])

$$T_{opt} > \frac{T_{max} + T_{min}}{2}$$

so that Φ is positive. Fitting the CTMI is done using standard least mean square otpimization with Levenberg-Marquardt algorithm implemented in python's SciPy package [105]. In doing so, estimates of the cardinal temperatures T_{opt} and T_{max} as well as the maximal growth rate μ_{opt} are obtained.

The parameters of a simpler version of the model described in equation 2.3 have previously been described as being difficult to estimate from fitting the model to the data [83,86,96]. This is mainly due to intrinsic correlation between the parameters, resulting in convergence failures of traditional optimization approaches. Here, we combine estimates of cardinal temperatures and growth rate, as well as the data series $\{T_i, \mu_i\}_j$ (where j is the studied strain) to fit the parameters of equation 2.3 through an Approximate Bayesian Computation - Sequential Monte Carlo (ABC-SMC) procedure implemented in python's pyABC package [106]. Doing so allows to bypass the need for an explicitly-defined likelihood and thus the use of a combination of growth data ($\{T_i, \mu_i\}_j$) and cardinal quantities ($\{T_{opt}, T_{max}, \mu_{opt}\}_j$). Standard approaches such as Monte-Carlo Markov chains (MCMC) require the definition of a tractable likelihood $P(\{T_i, \mu_i\}_j | \theta_j)$ (where θ_j is the vector containing parameter values), which may be challenging (and even impossible) when using quantities that are themselves point estimates ($\{T_{opt}, T_{max}, \mu_{opt}\}_j$). Note that parameters λ and τ cannot be estimated independently, as they are fully correlated (see equations 2.3 and 2.4), thus the product $\lambda \times \tau$ is inferred instead as one single parameter.

ABC-SMC parameter inference, while being likelihood-free, requires the definition of a distance function, which is here con-

structed rather arbitrarily to allow convergence:

$$d(\tilde{\mu}_\theta, \hat{\mu}) = \frac{1}{3} \left((|\ln \tilde{\mu}_{opt} - \ln \mu_{opt}| + \frac{\tilde{\mu}_{opt} - \mu_{opt}}{\bar{\mu}})/2 \right.$$

$$\left. + |\tilde{T}_{max} - T_{max}| + |\tilde{T}_{opt} - T_{opt}| + \sum_i \frac{|\tilde{\mu}_i - \mu_i|}{\bar{\mu}} \right) \quad (2.20)$$

In this equation, $\tilde{\mu}_\theta$ is the vector of simulated growth rates with parameters θ and μ is the vector of the observed growth rates. $\tilde{\mu}_{opt}$, $\tilde{T}_{opt}$, $\tilde{T}_{max}$ are model's cardinal points using θ as parameters. μ_{opt}, T_{opt}, T_{max} are the CTMI μ_{opt}, T_{max}, T_{opt} fitted on the data μ. $\bar{\mu}$ is the mean of the observed μ. This distance function gives more weight to cardinal points than the actual data points, which should help render identifiable parameters $\lambda\tau$, $E_{a,m}$ and $E_{a,c}$ (since these cardinal points correspond to three equations, equation 2.4 and one for $k_g(T_{opt})$).

ABC-SMC parameter inference was performed for each of the 327 selected strains using the same prior distribution (reported in table 2.1). ABC-SMC runs were carried out in parallel on 12 cpu-cores, using pyABC. For each ABC-SMC step, we set the goal of accepted particles (parameter vector proposal) to 50. Stopping conditions for the inference were that the mean distance of accepted particles is less than 0.5 or the 101 step is reached or the run exceeds 15 minutes. After running inference on the 327 candidates, those that yielded final mean distance greater than 3 were discarded, thus thinning down the inference data set to 317 strains.

Using ABC-SMC for inference requires having an *a priori* range of credible values for the parameters of the model. Conveniently, these values can be somewhat constrained. For example, enzyme activity experiments in Daniel et al. (2010)[84] constrain the activation energy for enzyme activity below 70 kJ mol^{-1}. The empirical estimate of the maintenance energy in Tijhuis et al. (1993)[78] has an Arrhenius-like form with activation energy also around this value, while others report values of the activation energy of protein denaturation greater than $\approx$ 130 kJ mol^{-1} [107] and estimates in Daniel et al. (2010)[84] are also around 130 kJ mol^{-1}. The values of A and $\lambda\tau$ can also be constrained from fitting the CTMI model on the data combined with equations 2.4 and also fitting a line to the data when $T < T_{opt}$ in the $\ln k_g \propto 1/T$ space. Not all experiments compiled in Corkrey et al. (2016)[93] have sufficient data to do so, but a ballpark estimate is obtained and used as a prior. Another route is to use

Table 2.1. | **Prior distribution used for ABC-SMC inference of model parameters.**

Parameter	A	$\lambda\tau$	$E_{a,c}$	$E_{a,m}$
Units	s^{-1}	-	kJ mol^{-1}	kJ mol^{-1}
Distribution	$\ln U$	$\ln U$	U	U
Range	$[12, 14]$	$[-8, -4]$	$[45, 90]$	$[80, 210]$

$A = k_b T/h$, which is of the order of 10^{12} s^{-1} at room temperature, roughly of the same order of what is obtained by fitting data at low temperatures. Note that here, inference is performed assuming that A is independent of temperature for convenience. This assumption affects how the model fits the data at low temperatures but not the cardinal temperatures (see equation 2.4) The parameters λ and τ also can be constrained from other sources, for example autotrophic hydrogenotrophs have $\lambda \approx 0.03$ (see chapter 1) and $\tau \approx 2 \times 10^{-5}$ (see chapter 3). The adopted priors are summarized in table 2.1.

2.4. Results

Simulated growth rates based on parameter values inferred using ABC-SMC are shown in figures B.1 and B.2 of the Appendix for a selection of 24 species, all Archaea and thermophilic or hyperthermophilic. The fit quality is variable, but the cardinal temperatures are well retrieved, as confirmed by looking at the residuals in Appendix figure B.3. The maximum growth rate on the other hand is poorly estimated in a large fraction of cases. It is often estimated more than 5% different than what the CTMI predicted (29% for the complete dataset, 27% of Archaea, 39% of Bacteria and 6% of Eukaryotes). Fitting a Hinshelwood type model such as ours to growth curves is challenging, even with the intermediary step of using the CTMI model to extract cardinal temperatures and use them for inference, as noted by previous authors[86,96]. The fit quality is noticeably poorer for growth rates at temperatures lower than the optimum (figures B.1 and B.2), which may suggest that the Hinshelwood type model used here is not best suited for this $T < T_{opt}$ regime. Therefore, examination of the parameter point estimates should be done with caution, taking into account the uncertainty estimated by the ABC-SMC method.

The inference shows correlation between $E_{a,c}$ and $E_{a,m}$ (figure 2.3). Linear regressions result in correlation coefficients $r = 0.96$ for
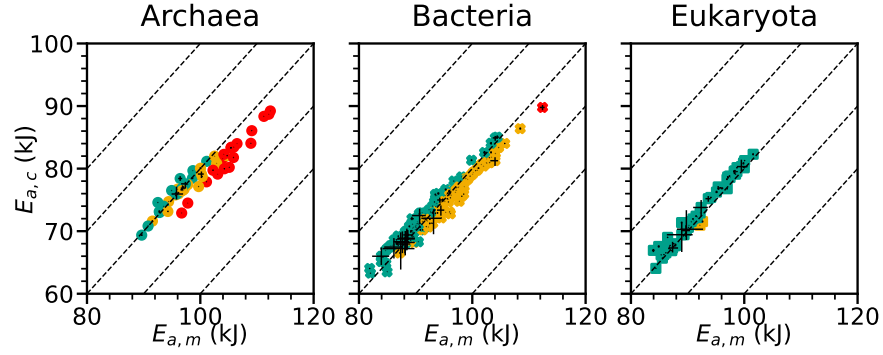
Figure 2.3. | Correlation between $E_{a,c}$ and $E_{a,m}$ in the different superking-doms. Red: hyperthermophiles ($T_{opt} > 80$°C), **Orange**: thermophiles($45 < T_{opt} \leq 80$°C), **Green**: mesophiles ($T_{opt} \leq 45$°C). The dashed lines are lines of slope 1. Error bars correspond to the 95% confidence interval of the posterior distributions obtained with ABC-SMC.

Table 2.2. | Results of regression test for $E_{a,c}$ versus $E_{a,m}$. The slopes and intercepts are given $\pm\sigma$ the standard deviation. P-values are calculated using the two sided Wald test (null hypothesis of the slope being zero) and are all extremely low $< 10^{-4}$.

Superkingdom	Correlation coefficient	Slope $\pm\sigma$	Intercept $\pm\sigma$ (kJ)
Archaea.	0.96	0.76 ± 0.03	2.84 ± 2.88
Bacteria	0.98	0.86 ± 0.01	-6.53 ± 1.20
Eukaryota	0.99	1.02 ± 0.02	-21.08 ± 1.78
All	0.98	0.85 ± 0.01	-5.92 ± 0.98

Archea, $r = 0.98$ for Bacteria and $r = 0.99$ for Eukaryota ($r = 0.94$ for the complete dataset). Interestingly, this correlation is close to being of slope 1 (Archaea: 0.76, Bacteria: 0.86 and Eukaryota: 1.02, see table 2.2).

But this figure represents the value of these parameters in presumably adapted organisms, and thus cannot be interpreted directly as the shape of a tradeoff between the values of $E_{a,c}$ and $E_{a,m}$, and the condition for the existence of an evolutionary singularity at $f'(E_{a,m}^{ESS}) = 1$. Before drawing conclusions on the existence and shape on a trade-off, let us first examine what parameter value change carried the increase in maximum temperature of growth in our model. The value of T_{max} in our model is entirely determined by $\lambda\tau$ and the difference $E_{a,m} - E_{a,c}$ (equation 2.4). But the inference shows that the increase in T_{max} is carried principally by an increase in $E_{a,m} - E_{a,c}$ and that the product $\lambda\tau$ contributes marginally at most (figures 2.4 and 2.5).
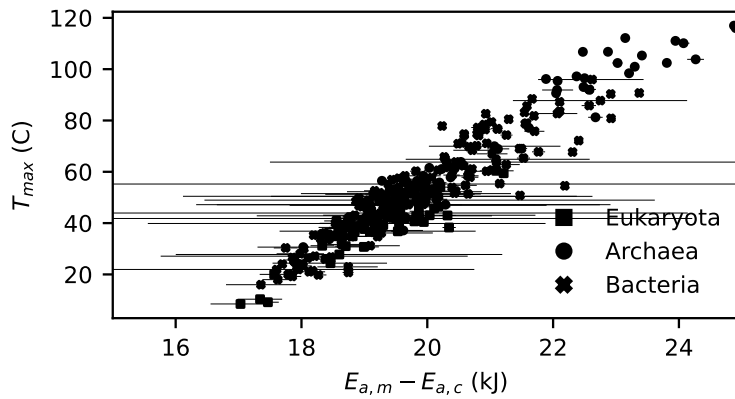
Figure 2.4. | Maximum growth temperature versus activation energies difference. Error bars correspond to the 95% confidence interval of the posterior distributions obtained with ABC-SMC. A linear regression shows a line of slope 13.82 ± 0.28 K kJ^{-1} and intercept 50.82 ± 5.55 kJ with $r = 0.94$ and $p < 0.01$.

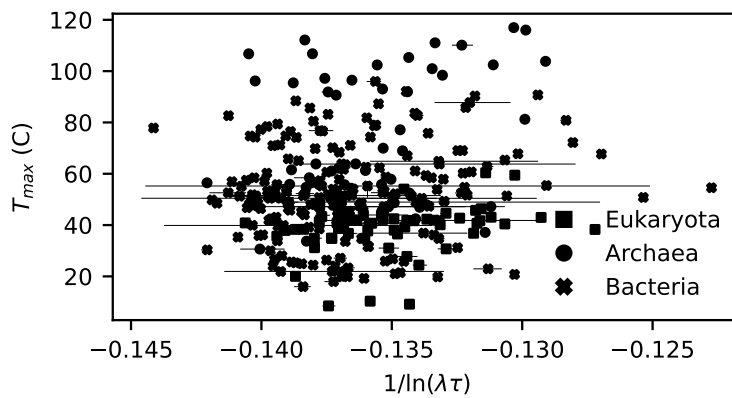**Figure 2.5. | Maximum growth temperature versus logarithm of $\lambda\tau$.** Error bars correspond to the 95% confidence interval of the posterior distributions obtained with ABC-SMC.

A second observation is that there is a slight residual correlation between $E_{a,m}$ and the maximum temperature. Organisms with higher temperature maxima (and equivalently higher values of $E_{a,m} - E_{a,c}$ also have higher values $E_{a,m}$ (figure 2.6). According to the theory, organisms could have adapted to higher temperature just as well through a decrease in the value of $E_{a,c}$, but it appear not to be the case in the data set (see figures 2.3 and 2.6).

2.5. Discussion

It is not easy to extract a clear prediction from the theory to be compared with the dataset of inferred values of parameters $\{E_{a,m}, E_{a,c}\}$. If the relation between $E_{a,c}$ and $E_{a,m}$, is assumed to be be such that there is a unique ESS, then the theory would predict that a species's value of $E_{a,m}$ (and consequently that of $E_{a,m}$) converges to a unique value, or that the observed dispersion of $E_{a,m} - E_{a,c}$ around this value would negatively correlated with environmental temperature, as shown in section 2.2. This does not appear to be the case in the dataset as the values of $E_{a,c}$ and $E_{a,m}$ very widely (figure 2.3) without indication of lower dispersion at higher temperatures (figure 2.4). But of course, the dataset does not show a single species, sharing the same molecule for which the values of $E_{a,c}$ and $E_{a,m}$ are fine-tuned independently from any other adaptive trait, but rather a collection of different species, having different catabolism and probably widely different catabolic enzymes. Each of these enzymes might follow its own relation between $E_{a,c}$ and $E_{a,m}$.

Thus, it could be the case that the relation proposed in section 2.2 would produce the variations of the values of the activation energies shown in figure 2.3. Second, the apparent correlation between the two activation energies cannot be interpreted as the shape of the hypothetical trade-off function, as the dataset consists in values of these parameters in populations that have evolved and thus that might have particular values of $E_{a,m}$ and $E_{a,c}$. The correlation could be contextual, and not representative of any structural link between $E_{a,m}$ and $E_{a,c}$.

When temperature increases, a strain could maintain the same catabolic rate by increasing the catabolic reaction activation energy $E_{a,c}$ following $-E_{a,c}/T_e = C_1$ where C_1 is a (negative) constant and T_e the environmental temperature. In a similar way, the mainte-
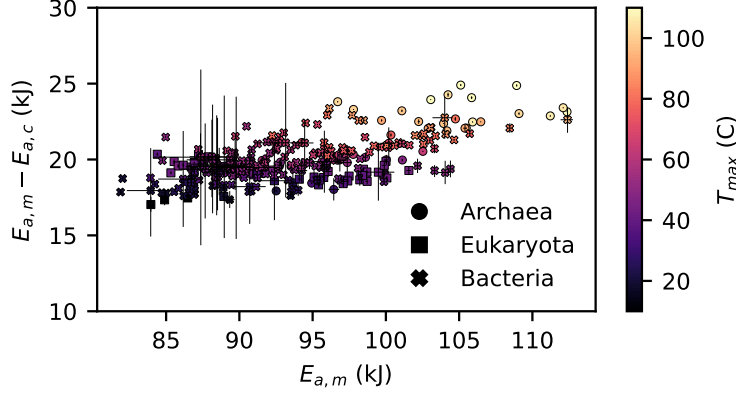
Figure 2.6. | Activation energies difference versus maintenance rate activation energy. Error bars correspond to the 95% confidence interval of the posterior distributions obtained with ABC-SMC. Markers are colored according to the estimated value of T_{max}. Linear regression yields a line of slope 0.15 ± 0.01, intercept 5.9 ± 0.98 kJ, $r = 0.62$ and $p < 0.01$.

nance rate could be kept constant if $-E_{a,m}/T_E = C_2$. If this were the case, that evolution maintains the rate of both catabolism and maintenance constant given an environmental temperature, there would be a linear correlation between $E_{a,c}$ and $E_{a,m}$. This would imply a linear relation between $E_{a,m}$ and $E_{a,c}$ as well as between $E_{a,m}$ and $E_{a,m} - E_{a,c}$.

$$
\begin{cases}
-\frac{E_{a,c}}{RT_e} = C_1 \\
-\frac{E_{a,m}}{RT_e} = C_2
\end{cases}
\iff
\begin{cases}
E_{a,c} = E_{a,m}\frac{C_1}{C_2} \\
E_{a,m} - E_{a,c} = E_{a,m}\left(1 - \frac{C_1}{C_2}\right)
\end{cases}
\tag{2.21}
$$

where $C_1 < C_2 < 0$ (for the growth condition $E_{a,m} > E_{a,c}$ to be satisfied) and thus $1 > C_1/C_2 > 0$. This would imply that the slope of $E_{a,m} - E_{a,c}$ versus $E_{a,m}$ is equal to one minus the slope of $E_{a,c}$ versus $E_{a,m}$.

The dataset suggests that this is probably an important component of the observed correlations, as the inferred slope for $E_{a,m}$ versus $E_{a,m} - E_{a,c}$ is approximately 0.15 and the slope of $E_{a,c}$ versus $E_{a,m}$ is about 0.85, in agreement with the scenario that the effective rates are kept constant across environmental temperatures (table 2.2 and figure 2.6). But there is no evidence that the growth rate (and thus the difference between the catabolic and maintenance rate) is constant with environmental temperature, as figure 2.7 shows an absence of slow-growing thermophiles and hyperthermophiles. Furthermore, figure 2.6 shows that a linear component
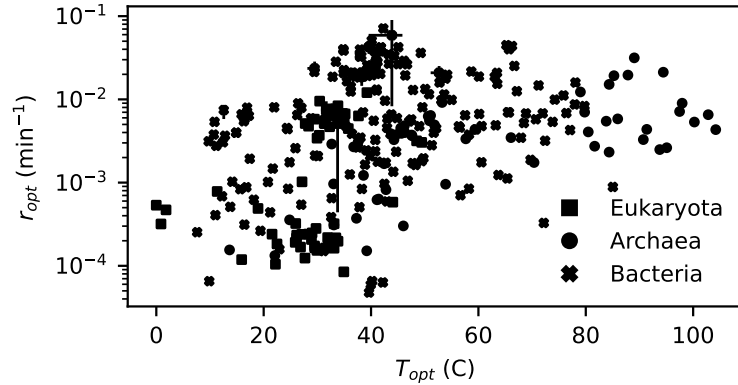
Figure 2.7. | **Growth rate at the optimal temperature.** Error bars correspond to the 95% confidence interval of the posterior distributions obtained with ABC-SMC.

only explains 62% of the variation in $E_{a,m} - E_{a,c}$ versus $E_{a,m}$, as well as a non zero intersect (which would be the case for constant $E_{a,c}/T_e$ and $E_{a,m}/T_e$. This figure 2.6, along with figure 2.4 suggest that there is a residual component of an increase in $E_{a,m} - E_{a,c}$ with environmental temperature that does not simply correspond to $E_{a,c}/T_e$ and $E_{a,m}/T_e$ being constant.

To back up this interpretation, the parameter inference shown here must be accompanied with the additional information of the environmental temperature at which the species or strains present in the dataset are found. So far, we have made the assumption that T_{opt} (and thus indirectly T_{max}, as they are structurally correlated in our model, see equation 2.4) is a good proxy for environmental temperature T_e. This might not be true, as the widely used Eppley curve as a relation between the growth rate of species present in an environment and the environmental temperature predicts that the environmental temperature is lower than the optimal growth temperature of[82]. The difference between the environmental temperature and the optimum temperature might not be constant[94]. The existence of this difference is also suggested by our model as if the relation between $E_{a,m}$ and $E_{a,c}$ is one that allows an ESS to exist, then the ESS maximizes T_{max}, and thus increases T_{opt} regardless of the environmental temperature. Thomas et al. (2012)[94] published a compiled data base of planktonic growth rates as a function of temperature, along with estimates of the environmental temperatures based on the localization at which the species are found. Unfortunately, their dataset only contains planktonic species living

at temperatures lower than 30°C, which is not expected to capture trends in parameters relating to the existence of potential absolute upper temperature limit. Our work highlights that the ideal database to study the adaptation to high temperatures and the possibility of an upper temperature limit to life caused by molecular constrains on adaptation, such as the one encompassed in the trade-off relation between $E_{a,m}$ and $E_{a,c}$ in section 2.2, is one that contains growth data at different temperatures of strains that are closely related, sharing the same catabolic reaction, along with the environmental temperature.

Nonetheless, the inferred correlation between $E_{a,c}$ and $E_{a,m}$ shown here in figure 2.3 holds some potential for discussion. The observation that species surviving to higher temperatures have a larger difference between the activation energy of maintenance and the activation energy of the catabolic reaction accords with the assumption that these parameters set the upper limit T_{max} rather than $\lambda\tau$. It is puzzling that the increase in $E_{a,m} - E_{a,c}$ is skewed towards higher values of $E_{a,m}$ rather than lower values of $E_{a,c}$ (as seen in figures 2.3 and 2.6). Under the assumption that there exists a trade-off relation between $E_{a,c}$ and $E_{a,m}$ that satisfies the conditions for an ESS to exist, this could be explained by a potential trade-off between $E_{a,c}$ and $E_{a,m}$, which allows a maximum value of $E_{a,m} - E_{a,c}$ at a relatively high value of $E_{a,m}$ as an ESS.

Another explanation stems from the model limitations. Indeed, catabolic enzymes are not the only functional molecules under natural selection that could be constrained by the value of $E_{a,m}$. The cell performs multiple functions, most of which could be linked to activation energies of reactions involving proteins, but they have different importance for the cell. Thus it could be that the cell has overall functional molecules with higher activation energies of denaturation, and thus a higher $E_{a,m}$, but have catabolic enzymes with lower specific $E_{a,m}$ and $E_{a,c}$. In other words, it might be that the postulated trade-off between $E_{a,c}$ and $E_{a,m}$ could not hold true at higher values of $E_{a,m}$ as it only captures a coarse grain description of the the thermoresistance of the diversity of molecules in the cell, instead of just that of catabolic enzymes. If this were to be the explanation for the apparent asymmetry with respect to $E_{a,m}$ in figure 2.6, catabolic enzymes of an hyperthermophile should show less signs of molecular adaptation to high temperatures (*e.g* less charged residues, more thermolabiles one, longer sequences[108])

than the rest of the proteome would. This would highlight energy intake rate as a crucial determinant of the effective maximum temperature of growth.

Even if the interpretation of these results in the context of the history of adaptation to temperature of Earth's biosphere remains speculative, the existence of databases such as the one published in Corkrey et al. (2016)[93] and the possibility to fit model parameters on them is highly valuable to the field of astrobiology (as noted by the authors themselves[109]). Here, we were able to constrain the parameter space that we want to use in order to quantitatively assess habitability and biosignatures. If we were to design prior distributions for physiological parameters used in the biological model in order to perform bayesian inference of habitability and biosignatures, an imaginary naive astrobiologist could possibly make the mistake of drawing independently the values of $E_{a,c}$ and $E_{a,m}$ and therefore litter their simulations with cases where unrealistic organisms are assumed. Based on the work presented in this chapter, not only do we propose a class of models suited to assess habitability, but we also have the means to define empirical prior distribution for its parameters, grounded in what life on Earth is able to explore in terms of molecular adaptation to temperature. This will be useful to continue the work presented in part III of this thesis. Part III is focused on building a model of a terrestrial planet that I plan to extend with a Bayesian inference workflow that also accounts for the biological model. Rather than assuming a specific candidate organism (as I do in part II of this thesis), the approach and results of this chapter will allow me to go beyond this restrictive assumption.

Part II.

The hypothesis of life in our solar system: Enceladus

Lime and limpid green, a second scene
A fight between the blue you once knew
Floating down, the sound resounds
Around the icy waters underground
Jupiter and Saturn, Oberon, Miranda and Titania
Neptune, Titan, stars can frighten

–Syd Barrett (Pink Floyd), *Astronomy Domine* in *The Piper at the Gates of Dawn*, 1967

An intriguing icy moon

In this part of the thesis, I present applications of the modeling described in part I to a solar system body of astrobiological interest : Enceladus. Enceladus is a relatively small (ca. 500 km in diameter) satellite of Saturn (6th planet from the Sun). Enceladus sits at a vertiginous distance from the Earth; the Cassini-Huygens mission by NASA, ESA and ASI, which is the only prolonged mission so far that has focused on the Saturnian system, took close to seven years to reach it. Enceladus receives very little light from the Sun, almost a hundred times less than the Earth does, has a very low surface temperature (about 75 K) and negligible surface pressure. From the Earth, Enceladus appears to be so bright that astronomers proposed that its surface was covered with water ice[110], before a closer inspection was permitted by the Voyager probes starting in 1980.

And upon closer inspection by Voyager 1 and 2 in the 1980s, Enceladus's surface appeared so smooth and so bright that it must have been composed of fresh material[111], implying that some internal activity must exist and continuously renew the surface. Furthermore, the observation that Enceladus is located in the most dense region of the water ice composed E-ring (figure 2.1), suggested that it could be composed of material escaping from Enceladus, possibly fresh surface snow ejected by impacts. The mystery of how Enceladus is connected to Saturn's least visible ring seems to have prompted to include fly-bys of Enceladus to the Cassini mission

The curiosity that was the interaction between Enceladus and Saturn's E-ring might have allowed one of the most significant discoveries about our solar system. Even though it had been speculated that Enceladus could have a liquid ocean[112], the main target of the Cassini-Huygens mission launched in 1997 was the investigation of Titan, a larger moon of Saturn with a thick atmosphere. But Cassini performed two fly-bys of Enceladus in 2005, and gathered data suggesting that the E-ring originates from a sustained thin atmosphere filled with ice dust located at the warmer south pole[113].
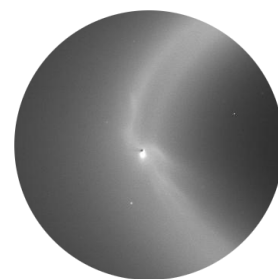
Figure 2.1.: Enceladus's plume feeding into Saturn's diffuse E-ring as seen by the Cassini probe. Credit: NASA/JPL

During the first extension of the mission, it appeared clear that this dust comes from a liquid water ocean erupting from cracks at the south pole[114,115]. And after a few more fly-bys, the plume of Enceladus revealed the presence of carbon dioxide, ammonia, methane, dihydrogen and even some short organic molecules[64,116]. The explanation for a sustained liquid water ocean, which is unexpected from a small body with limited radiogenic heating and that should cool rapidly, comes from tidal heating[89]; tidal interaction with Saturn causes friction in the rocky core and consequently generates heat.

Figure 2.2.: Long exposure shot of Enceladus in visible light during an eclipse Credit: NASA/JPL

Enceladus seems to have it all: a liquid water ocean, continuously generated heat, rock-water interactions, possible hydrothermal chemistry and environments parallel to Earth's deep ocean hydrothermal vents in which microbial life is abundant; and it is even spraying ocean samples in space where probes can collect them without even having to land on the surface. But so many questions remain. How resemblant is Enceladus's hydrothermal environment to those on Earth? How likely is it that it supports Earth-like life? Are the measures by Cassini of volatile chemicals evidence for or against Earth-like hydrothermal life in Enceladus's ocean?

The case of Enceladus is ripe for the application of the model described in chapter 1 together with an inference framework. In the first chapter of this part, chapter 3, I reproduce the contents of an article that I have written in collaboration with François Guyot, Boris Sauterey, Stéphane Mazevet and Régis Ferrière, and that was published in June 2021 in the journal *Nature Astronomy*[117]. In this publication, we are interested in relating the fluxes of volatile chemicals in Enceladus's plume to interior processes: abiotic ones that may determine the habitability of Enceladus's deep ocean, and biotic ones. Using the model of thermophilic chemo-autotrophs developed in part I as well as physical modeling of Enceladus's deep ocean, we were able to provide an estimate to the probability that the geochemical influence of a population of Earth-like microbes matches the observations made by the Cassini probe, and compared it to the probability that a well known abiotic process would. Essentially, this corresponded to testing the hypothesis of Earth-like life against the Cassini data.

We asked, "if there was a methanogenic biosphere in Enceladus's ocean, would Cassini have measured the amount of methane it did,

or would we have expected more methane produced from a biosphere? and if there was a biosphere, would there be the observed abundance of molecular hydrogen in the plume instead of it being entirely consumed by hydrogenotrophs?". We found that the observed quantity of methane in the plume is far greater than what we would expect from abiotic reduction of carbon dioxide, but matches well with biotic production (there is even slightly more methane in the plume than we would typically expect there to be produced by a population of H_2-methanogens). Second, we found that the consumption of dihydrogen by a modeled population is not sufficient to deplete hydrogen from the plume. Thus, the modeling developed in part I enable us to make progress in assessing Enceladus's habitability by turning qualitative discussions (would not hydrogen be absent from the plume should hydrogenotrophs be present?) into quantitative predictions (simulating the distribution of expected values of hydrogen concentration in the plume under the assumption of hydrogenotrophs being present). We showed that the hypothesis of an Earth-like biosphere remained a credible one given currently available data and under the current paradigm for Enceladus's deep ocean processes.

In chapter 4, we further explored the hypothesis of a methanogenic population inhabiting Enceladus's deep ocean. Using the modeling developed in part I, we estimated the size and productivity of such a hypothetical biosphere. We also contributed to untangle how ecological concepts, such as standing biomass (or stock) and primary production, relate to biosignatures in the context of Enceladus. There is little chance that a population of hydrothermal microbes will be observed in its environment in the foreseeable future given that it would require penetrating the 30 km thick ice shell. Yet, we might expect most of the biomass to be concentrated where the hydrothermal flow is located[118], rather than being diluted in the entire ocean or being present in the plume at the same concentrations than in the hydrothermal environment. This raises the question of how the concentrations of cells or biologically-produced organics in the plume relate to those in the hydrothermal environments. So far, estimates of the detectability of a hypothetical Enceladean biosphere rely on using cell concentration values observed around Earth's hydrothermal vents or using models that equate the calculated population size diluted in some volume (a part of the ocean or its totality) with the concentration in the space plume[63,119–121]. Here, we leverage tools from ecological theory to explicitly model a

population that remains in its environment (standing biomass) and how the concentration of cells and organics that may escape this environment scales with this population (production).

Doing so allows us to see more clearly how the hypothesis of a biosphere being present at Enceladus's seafloor connects with evidence of its existence in the plume where sample can be retrieved. Moreover, using quantitative modeling that describes both a population's role in geochemical processes and its size and production of organic matter allows for coupling different type of data together. Indeed, in chapter 3 we show that under certain conditions that seem plausible, a population of methanogens could produce the observed quantity of methane in the plume. But under different conditions, or assumptions, a population of methanogens could also produce less methane than observed. Therefore, assuming that a process or another is at the origin of the observed methane has an impact on how the hypothesis of a biosphere is shaped. Under the assumption that the observed methane is of biological origin, then it is equivalent to make the assumption of a particular population that would produce such quantity of methane. On the other hand, under the assumption that the observed methane is abiotic, then the hypothesized population is a less productive one, possibly counting less individuals making it harder to detect. And if the hypothesis of a population is considered independently from an assumption of the methane's origin, than a larger range of population sizes and productivity is possible.

Chapter 4 explores this range of possible population sizes under the assumption that the methane is of biological origin as well as independently from assuming the methane's origin. We also calculate how these estimated population sizes and productivity translate into potentially detectable cells or organics in the plume. Here, the type of biosignatures that are considered (cells, biomolecules) relate more directly to the existence of a population than the abundance of catabolic molecules (dihydrogen, methane) do. Even though the risk of false positive exists (some mineral structures resemble fossilized cells[122] and amino acids can be synthesized abiotically[123]), the risk of a false negative should not be neglected when designing an expansive and long mission. In other words, we should design a mission with tools of sufficient resolution so that the absence of detection can be interpreted. Chapter 4 looks at detectability under the angle of determining the minimum sampling effort or the

minimal resolution for amino-acid detection that is required to confidently observe signatures of the modeled population if it exists as a way to ensure that a negative result can be interpreted as evidence against its existence. This chapter is also the reproduction of an article, currently being revised for publication in the *Planetary Science Journal*.

Chapter 3.

Bayesian analysis of Enceladus's plume data to assess methanogenesis

Abstract

Observations from NASA's Cassini spacecraft established that Saturn's moon Enceladus has an internal liquid ocean. Analysis of a plume of ocean material ejected into space suggests alkaline hydrothermal vents on Enceladus' seafloor. On Earth, such deep-sea vents harbor microbial ecosystems rich in methanogenic archaea. Here, we use a Bayesian statistical approach to quantify the probability that methanogenesis (biotic methane production) might explain the escape rates of molecular hydrogen and methane in Enceladus' plume, as measured by Cassini instruments. We find that the observed escape rates (i) cannot be explained solely by the abiotic alteration of the rocky core by serpentinization; (ii) are compatible with the hypothesis of habitable conditions for methanogens; (iii) score the highest likelihood under the hypothesis of methanogenesis, assumed the probability of life emerging is high enough. If the probability of life emerging on Enceladus is low, the Cassini measurements are consistent with habitable yet uninhabited hydrothermal vents and point to unknown sources of methane (*e.g.*, primordial methane) awaiting to be discovered by future missions.

Résumé

Les observations collectées par la sonde Cassini (NASA) ont permis d'établir que sous sa surface de glace, la lune de Saturne Encelade dispose d'un océan global d'eau liquide. Cet océan dégaze dans l'espace au travers de crevasses sous la forme d'un panache dont l'analyse chimique suggère l'existence de cheminées hydrothermales alkalines sur le plancher océanique. Sur la Terre, ce type de cheminée abrite de riches communautés microbiennes, dans lesquelles les archées méthanogènes sont abondantes. Nous utilisons une approche bayésienne afin de quantifier la probabilité que la méthanogénèse (production biotique de

méthane) explique les taux d'échappement de dihydrogène et de méthane dans le panache d'Encelade, tels qu'ils ont été estimés à partir des données recueillies lors de la mission Cassini. Ces taux d'échappement (i) ne sont pas expliqués par la seule altération abiotique des minéraux du coeur rocheux par la serpentinization, (ii) sont compatibles avec l'hypothèse de conditions habitables pour des méthanogènes et (iii) sont vraisemblables sous l'hypothèse de la méthanogénèse, dès lors que la probabilité d'émergence de la vie est suffisamment élevée. Si celle-ci s'avérait être faible, les mesures faites par la sonde Cassini seraient cohérentes avec des évents hydrothermaux habitables mais non habités tout en renvoyant à des sources abiotiques de méthanes encore inconnues ou non étudiées (*e.g* méthane primordial) qui devront être découvertes par de futures missions.

3.1. Introduction

The NASA-led Cassini space mission has provided unprecedented insights into the Saturnian system[124]. Observations from multiple fly-bys of the moon Enceladus confirmed the existence of a global ocean[125]. Sampling of the south-pole plume and analysis by Cassini revealed the presence of molecular hydrogen (H_2), methane (CH_4), and other gases. The detection of H_2 by Cassini's Ion and Neutral Mass Spectrometer (INMS) was confirmed and interpreted as a signature of hydrothermal activity[64]. These discoveries pointed to ocean worlds like Enceladus, but also Europa in the Jovian system and recently Ceres in the asteroid belt[28,126], as possibly harboring conditions that resemble Earth's habitable hydrothermal vents[26,27,127] (Fig. 3.1a). If Enceladus' plume sampled by Cassini has its origin in a global ocean harboring hydrothermal vents[128], the composition of the plume provides information on the environment of the deep-sea vents.

Hydrothermal circulation on Enceladus may resemble Earth's alkaline hydrothermal activity, producing H_2 and CH_4, among other gases[89,129]. If H_2 present in the hydrothermal fluid is produced in Enceladus' core[64], serpentinization is a plausible source[89], while other potential sources are likely insufficient to explain the observed H_2 flux[64]. Methane might originate from the (abiotic) conversion of H_2 and carbon dioxide (CO_2) to CH_4 in serpentinization waters according to reaction (3.1) (written for one mol of the electron donor H_2)[62]:

$$H_2 + \frac{1}{4}\,CO_2 \longrightarrow \frac{1}{4}\,CH_4 + \frac{1}{2}\,H_2O \qquad (3.1)$$
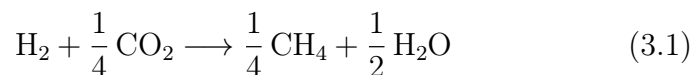
or from other abiotic sources such as a primordial stock of CH_4 [130], or a stock of organic molecules in the core being pyrolysed[131].

Hydrothermal activity might also sustain a biological origin of methane[64]. In Earth deep-sea hydrothermal vents, chemoautotrophic single-celled organisms harness thermodynamical disequilibrium generated by chemical gradients as their energy source, rather than sunlight[132]. Some hydrothermal vents are known to be habitats for abundant thermophilic and hyperthermophilic methanogenic microorganisms that convert H_2 and CO_2 (or its dissolved forms, dissolved inorganic carbon, or DIC) into methane[118,133] according to (3.1) as the net reaction. On Enceladus, hydrothermal vents shaped by internal heating might pro-

71

vide similar energy sources[89,134]. Considering the habitability of Earth's hydrothermal vents to methanogens and the putative role of methanogenic metabolism in early Earth biosphere function and evolution[135], Enceladus' habitability by hydrogenotrophic methanogens has been discussed[85,131,136]. Theoretical work evaluated the viability of methanogenesis based on observed thermodynamical disequilibrium[64], while the successful incubation of Earth methanogens in putative Enceladean environments was achieved experimentally[85].

Our goal is to take this approach a critical step further: to quantify the probability that biological methanogenesis might explain the Cassini observations of the plume that were reported in Waite et al. (2017)[64]. By integrating mathematical models of geophysical, geochemical and biological processes within a Bayesian statistical framework, we aim at quantifying the plausibility of alternate scenarios of habitability and biological activity, rather than assessing their mere possibility, and evaluate in probabilistic terms how distinguishable they are from one another.

3.2. Results

The difficulty in estimating the plausibility of alternate scenarios of habitability and inhabitation arises from dealing with information that is incomplete and comes from non-independent sources. A Bayesian framework is well suited for quantifying inference uncertainty[34,137]. In general, the Bayesian approach aims at quantifying the probability that alternate hypotheses be true given actual observations. By translating the different hypotheses into mathematical models, simulations can be used to find the likelihoods of the data occurring under the alternate scenarios. *A priori* (prior) knowledge of factors that influence the probability of each hypothesis being true, including previous observations, is combined with the likelihoods to give the *a posteriori* (posterior) probability of each hypothesis being true.

Here we apply this framework and contrast a model for a biotic scenario, denoted by B, in which methanogenesis might occur at Enceladus' hydrothermal vents, to a null abiotic model, denoted by A, in which methane production is abiotic. Absence of methanogenesis may be because the hydrothermal environments are not

habitable for organisms with a methanogenic metabolism, or because, even if they were, such metabolisms never evolved – due to life not emerging on Enceladus in the first place, or the evolutionary steps to methanogenesis not having taken place. The probability of the B model given our knowledge of the system follows from Bayes' theorem[34] (Extended Data Fig. C.1):

$$P(B|x^0) = \frac{P(x^0|B)P_{prior}(B)}{P(x^0|A)P_{prior}(A) + P(x^0|B)P_{prior}(B)} \qquad (3.2)$$

where x^0 is the vector of observed values of "observables", carefully chosen quantities that may include a biosignature; $P(B|x^0)$ is the *a posteriori* probability of scenario B given the observations; $P_{prior}(X)$ is the *a priori* probability of scenario X, where $X = A$ or B; and $P(x^0|X)$ is the likelihood of the data under scenario X. The observables that describe the composition of the plume are the inferred H_2 and CH_4 escape rates (Φ_{H_2} and Φ_{CH_4} in mol yr^{-1}) and the ratio ($H_2 : CH_4$) [64]. These escape rates are derived from mass spectrometry abundances relative to water and the estimated water ejection rate in the plume[64]. The escape rates are insightful because they and the production rates are expected to be of the same order of magnitude[64,138] (Methods).

To estimate each term in equation (3.2), we combine a process-based modeling approach with a summary of current knowledge of possible conditions in Enceladus' hydrothermal vents. We begin with constructing a mechanistic model of relevant interior processes. Although considerable uncertainty remains on Enceladus' interior and history[139], significant advances have been made regarding the structure of its core and ocean circulation. Based on these results, we build a 1D model of fluid and heat flow. Assuming a porous core with at least one heat source (tidal friction or radiogenic heating)[134,140,141], we carefully address the upward advection of water from hydrothermal vents to the ice ceiling in oceanic plumes shaped by buoyancy and Coriolis forces[89,142,143]. We then assemble a model of hydrothermal fluid (hereafter abbreviated HF) and oceanic water mixing in a mixing layer (ML) that sets a gradient of conditions around a hydrothermal vent.

Next we design an ecological model of methanogenesis constrained by our model of interior processes. The ecological model describes the biomass dynamics of hydrogenotrophic methanogenic metabolisms

similar to thermophilic and hyperthermophilic archaea that have been found in Earth's hydrothermal vents[144]. We assume the putative ecosystem to be located at the core-ocean interface, in the ML surrounding a hydrothermal vent and in which ocean water and HF from the core are mixed (Methods). The biomass growth rate depends on the amount of energy obtained from catabolism (equation (3.1)). The catabolic rate competes with the rate at which energy is lost through processes of biological decay[62]. Chemical environmental conditions determine the Gibbs free energy obtained for each mol of electron donor; environmental temperature influences both catabolic[84] and maintenance[78] energy rates, setting limits to the viability of the ecosystem (Fig. 3.1b, c). The model thus yields a quantitative criterion for habitability: a set of conditions on physical and chemical input parameters under which biomass production by a hydrogenotrophic methanogenic metabolism can reach a stationary state and persist (Fig. 3.1d). The biotic scenario corresponds to the case of a so-defined habitable environment that is actually inhabited. The model can then predict the composition of the surrounding water mass at biomass production steady-state.
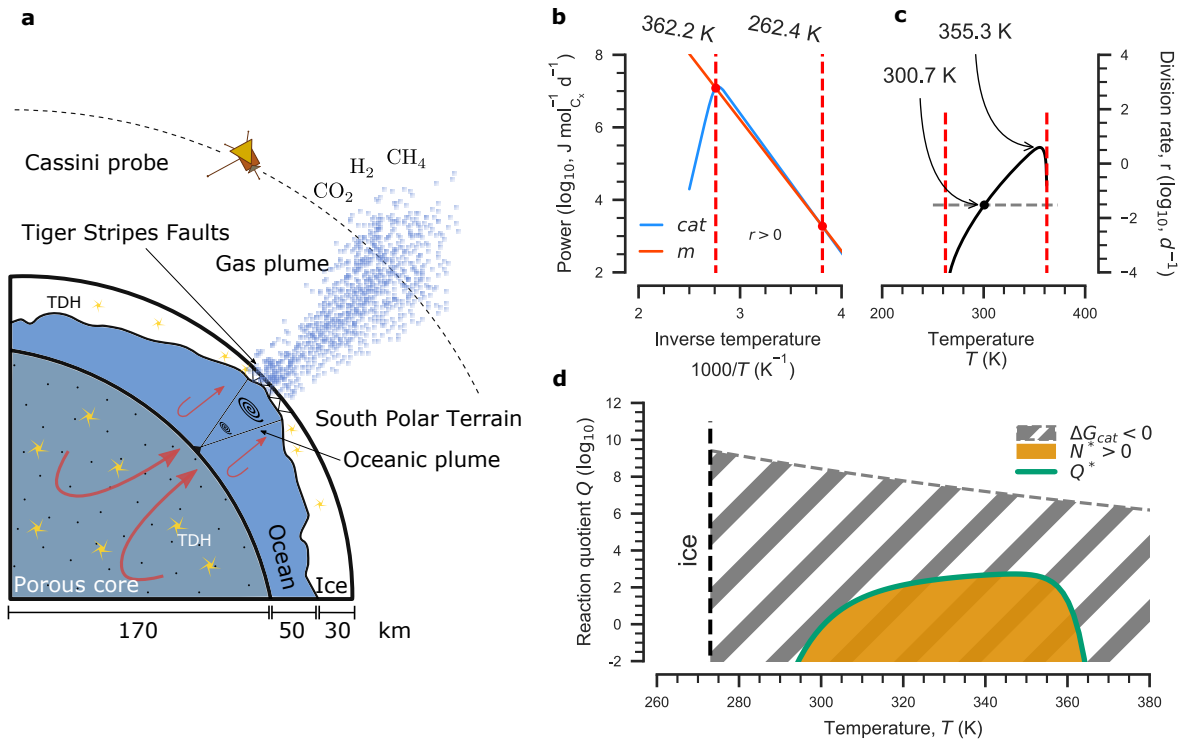
Figure 3.1. | General modeling framework. a Assumed interior structure of Enceladus. Yellow stars indicate Tidal Dissipative Heating (TDH). Red arrows denote water circulation, in the core[89] and in the ocean, where ocean plumes are shaped by buoyancy and Coriolis forces[89,143] (black spirals). The Cassini spacecraft is represented (not to scale) in one of its fly-bys of Enceladus, during which it crossed the gas plume of oceanic material escaping into space (dotted trajectory). **b** Catabolic (blue curve) and maintenance (red curve) energy of the modeled hyperthermophilic hydrogenotrophic methanogen in standard chemical conditions ($\Delta_r G = \Delta_r G_0$) as a function of temperature. Red dashed lines (vertical) delineate the temperature range over which the energy produced by catabolism is greater than maintenance requirements, resulting in positive growth rate, hence a positive division rate, r. **c** Division rate as a function of temperature. Red dashed lines (vertical) delineate the range of temperature over which the cell division rate is positive. The gray dashed line (horizontal) corresponds to a baseline death rate of $0.03 \, \mathrm{d}^{-1}$, which sets a minimum division rate needed for net population growth. At the black dot (300.7 K), the division rate and the death rate balance out. Between the lower thermal limit for $r > 0$ and the black dot, division occurs, but at a slower rate than death, thus leading the population to extinction. The temperature at which the division rate is highest (355.3 K) is indicated. This temperature is called the optimal temperature, T_{opt}. **d** Thermo-chemical (local) conditions conducive to a non-zero population size at steady state (orange). N^* is the number of individuals at population steady-state. The green line is the chemical quotient (Q) imposed by the population at steady-state, denoted by Q^*. The gray hatched region bounded by the gray dashed curve indicates the set of conditions under which methanogenesis is thermodynamically favored, *i.e.* $\Delta_r G_{cat} < 0$. The black dashed line (vertical) indicates the freezing temperature of water. Parameters used in b-d are given in Extended Data Table. C.2. See Methods for detail.

Input parameters of the ecological model are the composition and temperature of the HF and composition of the ocean in species of interest (H_2, DIC, CH_4), gathered from the literature and forming our prior knowledge of the system (Extended Data Table C.1). The distributions of these parameters thus define the prior space, θ. A well-supported estimate for the temperature of Enceladus' ocean is 275 K, close to thermal equilibrium with ice[64,128,129]. The HF temperature is estimated to be in the range of 300-620 K [89]. On Enceladus, the source of CO_2 on a geological timescale is unlikely to be magma outgassing, like it is on Earth. As a consequence, we assume that the ocean is the reservoir of CO_2, possibly as carbonates[129]. Using chemical data from the Cassini mission, the ocean DIC concentration was estimated between 10^{-1} and $4 \cdot 10^{-3}$ mol kg^{-1} [129]. The CH_4 concentration in the HF is also a critical parameter of methanogenesis, because its abundance may negatively influence the thermodynamical drive of reaction (3.1). We first consider methane having its origin in serpentinization, for which an upper bound of CH_4 concentration in the HF can be estimated. There is much debate about the abiotic rate of reaction (3.1) in serpentinization waters[145] but recent experimental studies set a maximum concentration of 10^{-4} mol kg^{-1} at the hydrostatic pressure of shallow hydrothermal vents ($\approx$ 10 MPa)[146], close to what is expected at Enceladus' hydrothermal systems[85]. Next we extend our analysis by raising the upper bound on the concentration of CH_4 in the HF to 0.1 mol kg^{-1}, to account for other possible abiotic sources for which mechanistic modeling remains beyond reach.

From these estimates, we define the prior distributions, capturing the knowledge and uncertainties of possible conditions in Enceladus' interior. From the prior distributions, the model input parameters are drawn to run 50,000 simulations, resulting in a distribution of so-called "pseudo-data" in the space of observables (Fig. 3.2 and Extended Data Fig. C.2). The pseudo-data distribution can be split into the two classes: "habitable" (H), which correspond to the set of parameter values for which there is at least one methanogenic metabolism that can function steadily in the surroundings of the hydrothermal vent; and "uninhabitable" ($\bar{H}$) otherwise. Measuring the volume of the parameters space falling in the "habitable" class gives an *a priori* probability that Enceladus be habitable, $P_{prior}(H) \approx 0.32$. This value is obtained by integrating over the whole prior distributions, including compositions in the putative environment of methanogenic metabolisms that may

be likely as well as unlikely. Thus, a rather large range of individually credible values of interior parameters allow methanogenic metabolisms to persist, according to our model.
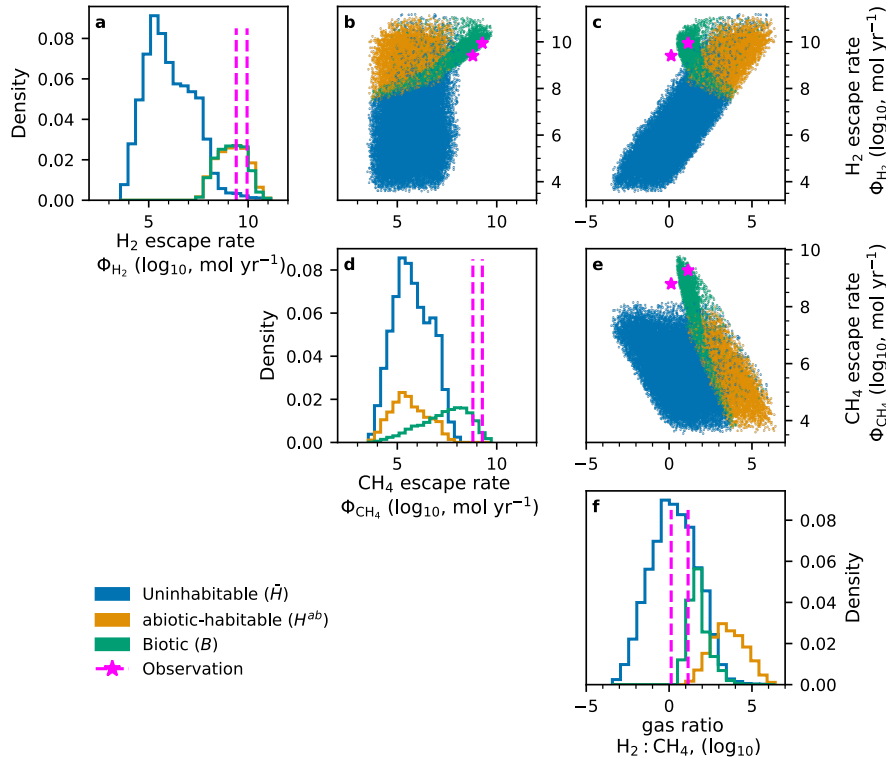
Figure 3.2. | Cassini observations and distributions of model outputs over the space of observables : inferred H_2 and CH_4 fluxes (Φ_{H_2} and Φ_{CH_4}), and gas ratio H_2 : CH_4. a, d, f, Density distributions of observables pseudo-data generated by model simulations. In blue, subset of simulations in which no population of methanogens could grow ('uninhabitable' scenario, $\bar{H}$). In orange, subset of simulations in which a population of methanogens is possible but their activity is not taken into account ('abiotic-habitable' scenario, H^{ab}). In green, subset of simulations in which methanogens can grow, and their activity is taken into account to produce pseudo-data ('biotic' scenario, B). Magenta dashed lines (vertical) indicate the actual Cassini observations[64]. Note the $\log_{10}$ scale on the horizontal axis. **b, c, e,** Joint distributions of observable pseudo-data generated by the model. Magenta stars indicate the Cassini observations. Note the $\log_{10}$ scale on both axes. This figure was generated from a set of 50,000 simulations using random values of internal parameters drawn from the distributions described in Extended Data Table C.1. In about 32% of these simulations, the drawn set of parameters allowed the modeled population of methanogens to grow ('habitable', H), the remaining 68% were found to pertain to the 'uninhabitable' scenario ($\bar{H}$, blue). The 'habitable' subset was evenly split at random into two subsets of $8,008$ simulations. In one subset, we did not simulate methanogenesis ('abiotic-habitable' scenario, H^{ab}, orange), while we simulated methanogenesis coupled with the geochemical model in the second subset ('biotic' scenario, B, green). See Methods and Extended Data Tables C.2 and C.3 for model equations and parameter values.

Simulations accounting for methanogenesis in combination with serpentinization water chemistry consistently explain the observed rates of CH_4 and H_2 emissions and the ratio ($H_2 : CH_4$) (Fig. 3.2, green distributions). In contrast, simulations in which CH_4 only originates from abiotic reactions in serpentinization water, cannot explain all the observations (Fig. 3.2, blue and orange distributions). Only the class of biotic models yields a non-zero likelihood for every observable (Extended Data Fig. C.3a), provided the *a priori* probability of life emergence, $P(B|H)$, is large enough (Extended Data Fig. C.3c). In fact, the concentration of CH_4 in the HF must be at least approximately $10^{-3.5}$ mol kg^{-1} in order to explain the observed flux of $\approx 10^9$ mol yr^{-1} (Extended Data Fig. C.4a), whereas the maximum concentration of CH_4 in the HF allowed by serpentinization alone, 1 mmol kg^{-1} [146] (see Methods) translates into a maximal CH_4 escape rate of $\approx 10^8$ mol yr^{-1} (Extended Data Fig. C.2a). The observed flux of CH_4 thus lies far from what can be expected from the abiotic conversion of H_2 and CO_2 through serpentinization; in contrast, it falls in the range of expected values when there is biological methanogenesis (Fig. 3.2b, d, e). Conversely, if the methane flux were re-measured at values tenfold lower than Cassini's, serpentinization alone could explain the data, yet methanogenesis would still be possible (Extended Data Fig. C.4b).

Besides serpentinization, CH_4 in Enceladus' plume might originate from other abiotic sources such as primordial outgassing [130] or organic pyrolysis [131]. These sources of CH_4 in Enceladus' ocean are too poorly constrained to be modeled mechanistically. Nevertheless, we can test the robustness of our results by considering an alternative scenario in which the maximal concentration of CH_4 in the HF is set to an arbitrary higher value of 0.1 mol kg^{-1}, possibly due in part to pyrolysis [64]. The high methane concentration, abiotic scenario yields a set of abiotic-habitable simulations that encompasses the empirical observations (Extended Data Fig. C.4 and C.5), and a slightly lower *a priori* probability that Enceladus be habitable $P_{prior}(H) \approx 0.27$. In this case, the observations may be explained either by the biotic or abiotic scenario. However, the estimated likelihoods still indicate that the observations are more likely under the B scenario (Extended Data Fig. C.3b) provided that $P(B|H)$ is large enough (Extended Data Fig. C.3d). To compute the posterior probabilities of the uninhabitable, abiotic-habitable, and biotic models, across the whole range $P(B|H) \in [0, 1]$ (or con-

versely, $P_{prior}(B) \in [0, 0.27]$), we use a random forest classification algorithm (ABC-RF, see Methods)[147]. Results are shown in Fig. 3.3, except for the probability of uninhabitability, which remains the lowest of all three models for all values of $P(B|H)$. With the *a priori* belief (in the Bayesian terminology) that all values of $P(B|H)$ between 0 and 1 are equally likely, the preferred scenario is, on average, B with probability $P_{P(B|H) \in [0,1]}(B|x^0) = 0.59$. If $P(B|H)$ is less than 0.2, the preferred model predicts abiotic-habitable conditions, yet $P(B|x^0)$ is still higher than the *a priori* probability $P_{prior}(B)$. For values of $P(B|H)$ in the range $0.2 - 0.4$, the abiotic-habitable and biotic models are equally probable (which is also reflected in the ABC-RF classifier score dipping), and higher values of $P(B|H)$ lead to select methanogenesis as the preferred model.

Our findings shed light on the significance of H_2 and CH_4 as biosignatures. It has been argued that the detection of H_2 might signal environments that are potentially habitable yet uninhabited (inhabitation by hydrogenotrophs supposedly implying consumption and depletion of H_2). Assuming that the H_2 plume ejection rate matches the production rate in the core[64], our model shows that levels of H_2 outgassing in the plume do correlate with the energy source available to putative hydrogenotrophs around hydrothermal vents (Extended Data Fig. C.2a). However, the escape rate of H_2 appears to be poorly informative of whether or not hydrogenotrophic metabolisms might actually be present (Fig. 3.2a). In fact, the observed escape rate of H_2 is compatible with active methanogenesis. This is because the change in H_2 escape rate that would be due to the activity of hydrogenotrophs is negligible in comparison with measurement uncertainty combined with prior uncertainty on H_2 molecular concentration in the HF. Thus, the H_2 escape rate may be a signature of habitability but it may not be used to infer inhabitation.

Another potential biosignature is the production of CH_4 [36,136]. Because increasing the CH_4 concentration reduces the available energy that reaction (3.1) yields to the cell (Methods), abiotic production may compete with biotic processes[145]. It appears that the abiotic conversion of H_2 and CO_2 to CH_4 in serpentinization waters is too weak to significantly affect habitability, as a higher concentration of CH_4 in the hydrothermal fluid ($[CH_4]_f$) does not correlate with a significantly lower fraction of habitable simulations

(Extended Data Fig. C.2a). As a consequence, the observation of CH_4 in the plume is not informative on whether hydrothermal vents might be habitable to methanogens. On the other hand, in line with general considerations of CH_4 as a biosignature[36], quantifying CH_4 escape in the plume is very informative about whether or not models that include biological methanogenesis can explain the data (Extended Data Fig. C.2b).
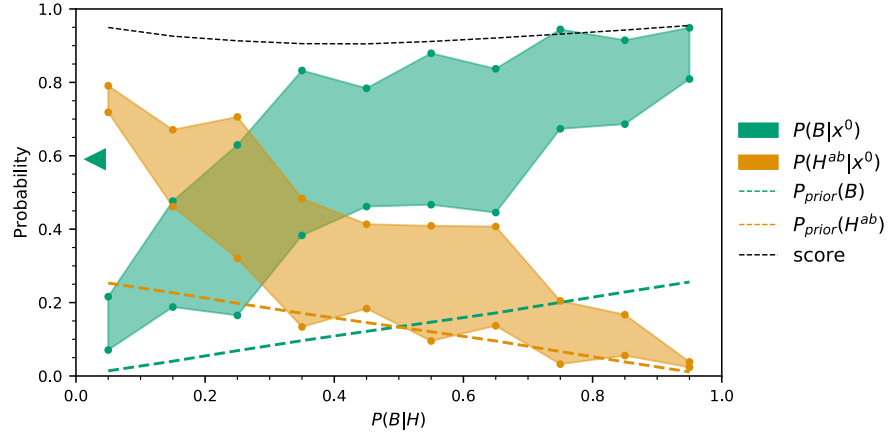
Figure 3.3. | Posterior probabilities of abiotic-habitable and biotic models, and classifier score. $P(B|H)$ is the prior probability of life emergence in habitable environments. Here the model accounts for unknown abiotic sources of methane in the hydrothermal fluid, by allowing for an *a priori* concentration higher than in the case of serpentinization only. This scenario yields $P_{prior}(H) \approx 0.27$. For each $P(B|H)$ value, the circles (green or orange) indicate the posterior probability of the biotic scenario (B, green) and abiotic-habitable scenario (H^{ab}, orange) for the lower and upper bounds of the observation range; the intervals between circles are colored for legibility. The green dashed line is $P_{prior}(B) = P_{prior}(H) \times P(B|H)$, the orange dashed line is $P_{prior}(H^{ab}) = P_{prior}(H) \times (1 - P(B|H))$. The black dotted line is the ABC-RF classifier score (see Methods). The green triangle on the vertical axis shows the mean value of the posterior probability $P(B|x^0)$ across $P(B|H) \sim U(0,1)$. Note that $P(\bar{H}|x^0)$ (not shown) is very low, and always less than $P(B|x^0)$ or $P(H^{ab}|x^0)$. See Methods for model equations, Extended Data Table C.1 for prior internal parameter ranges, and Extended Data Tables C.2, C.3 for parameters values of model simulations and ABC-RF.

3.3. Discussion

In summary, models that combine abiotic processes involving production of H_2 in Enceladus' core and biological methanogenesis near hydrothermal vents can explain the Cassini data (Fig. 3.2). Given the observations, the posterior probability of the biotic scenario is the highest provided the prior probability of life emergence in

habitable environments exceeds a threshold, *ca.* 0.35. Below this threshold, the highest posterior probability is scored by the subset of abiotic models that predict habitability (Fig. 3.3).

Considering the possibility that deep-sea vent conditions might be conducive to life emergence[148], better constraining the age and duration of such conditions of temperature and composition in Enceladus should help define ranges of credible values for the probability of life emergence, $P(B|H)$ (Fig. 3.3). Alternate hypotheses have been proposed for the age and formation of Enceladus, as well as for the evolution of its interior – ranging from a modern origin of the moon 500 Myr ago without an ocean, to a primordial origin at 4,500 Myr with the existence of a modern ocean[139]. Waite et al. (2017)[64] estimate that the observed production of H_2 may have been sustained by serpentinization in Enceladus for several billion years. Such insights suggest that habitable conditions on Enceladus may have existed around deep-sea vents long enough for life to emerge and methanogenesis to evolve. In the alternate scenario where life origin would require a surface environment with ultraviolet light and atmospheric sources of molecules to feed the prebiotic chemistry[149],the prior probability of life emergence in Enceladus' ocean, $P(B|H)$, might be very small. In this case, methane levels inferred from Cassini's observations can be explained in a large fraction of models that predict abiotic habitability, with an abiotic source of methane that remains to be identified.

We emphasize that methane in Enceladus' plume might originate from abiotic sources not included in our model. In our approach, we sampled interior parameters, including $[CH_4]_f$ in log-uniform, independent prior distributions. More accurate modeling of alternate abiotic sources will require to reconsider the structure of these distributions, *e.g.* correlating $[CH_4]_f$ with the H_2 concentration in the hydrothermal fluid ($[H_2]_f$). Our framework has the capacity to accommodate these changes and more generally to account for mechanisms of abiotic methane production other than serpentinization chemistry (outgassing of primordial methane accumulated in the core during formation or pyrolytic production[64]) when new insights into these processes become available for Enceladus.

Isotopic measurements such as the ^{14}N and ^{15}N of NH_3 as well as the ^{13}C to ^{12}C and deuterium-to-hydrogen ratios of CH_4 might shed

new light on the nature of Enceladus' core and the origin (primordial or modern) of methane. There are challenges, however – instrumental (the Ion and Neutral Mass Spectrometer (INMS) onboard Cassini had an insufficient mass resolution to accurately measure these ratios[130]) and analytical (environmental conditions characteristic of hydrothermal vents –pressure and temperature– may alter isotope fractionation of carbon by methanogens, rendering the isotopic markers of life less clear[75]). Groundbreaking data might come from observations of the plumes of the Jovian icy moon Europa (James Webb Space Telescope (JWST)[150], Clipper[151]) and from proposed missions targeting Enceladus itself (ELSAH[152], ELF[153] or E2T[154]). Such data are critically needed to identify abiotic sources of methane that might explain Cassini's observations without calling for methanogenesis. In a broader perspective, our work demonstrates how the integration of interior and ecological models can be achieved, so that a Bayesian inferential approach for the detection of habitability and biosignatures can be implemented – an approach that holds much promise for ocean worlds that future programs will discover and observe[34,137].

3.4. Methods

Mixing of core-ocean interface waters and plume composition

A hydrothermal hot spot dissipates thermal energy with power F (W) by advection of hydrothermal fluid (HF) at temperature T_f into seafloor oceanic waters (OW) at temperature T_o. We follow McCollom, (1999)[27] to model HF and OW mixing in a horizontally structured mixing layer (ML). ML waters buoyantly rise according to their temperature and escape the ML to be replaced by OW and HF. We first define the shape of J_f (kg s^{-1} m^{-2}), the mass flux density of HF into the ML as a function of the distance, u (m), to the hot spot center:

$$J_f(u) = J_{max} e^{-\left(\frac{u}{c}\right)^2} \tag{3.3}$$

where J_{max} (kg s^{-1} m^{-2}) and c (m) are derived by constraining the hot spot to dissipate power F and by forcing the hot spot center (where $J_f = J_{max}$) to be entirely composed of HF:

$$\int_S J_f dS = \int_0^\infty 2\pi r J_f(u) du = \frac{F}{C_p(T_f - T_o)} \tag{3.4}$$

where S (m^2) is the hot spot surface area, hence

$$c^2 = \frac{F}{\pi J_{max} C_p(T_f - T_o)} \tag{3.5}$$

where C_p is the specific heat capacity of water ($4,200$ J K^{-1} kg^{-1}).

The mass flux density J_c (kg s^{-1} m^{-2}) of buoyancy escape of ML waters is expressed as a function of the temperature anomaly $T' = T(r) - T_o$ following Goodman et al. (2004)[142]:

$$J_c = \frac{1}{u_s} \rho_o \sqrt{2\epsilon g \alpha T'} \tag{3.6}$$

where $u_s = 1$ m^2 is a unitary surface (for readability, it is replaced with its value in following equations), ρ_o ($1,000$ kg m^{-3}) is seawater mass density, ϵ (1 m) is the ML thickness, α (3×10^{-4} K^{-1}) is the coefficient of thermal expansion of water and g (0.12 m s^{-2}) is the local gravitational acceleration (see values in Extended Data Table C.2). Assuming a non-divergent fluid, we

can write a system of partial differential equations to express the dimensionless mixing ratio $x = \frac{m_f}{m_f + m_o}$ (subscript f denotes the HF and o denotes the OW) and temperature $T = T_o + x(T_f - T_o)$ as a function of time:

$$
\begin{aligned}
\frac{\partial x}{\partial t} &= \frac{1}{m}(J_f - x J_c) \\
\frac{\partial T}{\partial t} &= \frac{\partial T}{\partial x}\frac{\partial x}{\partial t} = \frac{1}{m}\left(J_f(T_f - T_o) - J_c(T - T_o)\right)
\end{aligned}
\tag{3.7}
$$

where $m = m_f + m_o$ is the ML mass density, which is constant. The steady state can be solved analytically. We can then derive the steady-state composition and temperature of the ML:

$$
\begin{cases}
T^*(u) &= \left[J_f(u)\frac{(T_f - T_o)}{\rho_o\sqrt{g 2\epsilon\alpha}}\right]^{\frac{2}{3}} + T_o \\[2mm]
J_c(T^*(u)) &= (2\rho_o^2 g\epsilon\alpha J_f(u)(T_f - T_o))^{\frac{1}{3}} \\[2mm]
x^*(u) &= \left[\frac{J_f(u)^2}{2\rho_o^2 g\epsilon\alpha(T_f - T_o)}\right]^{\frac{1}{3}}
\end{cases}
\tag{3.8}
$$

where the asterisk symbol superscript denotes the steady-state value.

In the absence of chemical reactions taking place in the ML, we can write the concentration C_i^0 of compound i (mol kg^{-1}) in the steady-state ML as a function of the concentration of i in the HF (C_i^f) and in the ocean (C_i^o):

$$
C_i^0(r) = x^* C_i^f + (1 - x^*)C_i^o
\tag{3.9}
$$

The derived set of concentrations then serves as the initial condition for our biological model. An example of a hot spot compositional structure is shown in Supplementary Fig. C.6a.

The scaling relationships derived in Goodman et al. (2004)[142] and Goodman and Lenferink (2012)[143] for Europa were used in Choblet et al. (2017)[89] to show that the Coriolis effect was important for the most part of Enceladus' oceanic plumes (OPs) ascension, thus suggesting well-defined plumes that experience little dilution with oceanic waters. In Goodman et al. (2004)[142], an OP starts with warm water rising in a turbulent regime, forming a cone, until the Coriolis effect becomes important and the water mass forms a cylinder. When the ocean plume encounters the ice ceiling, it starts growing into a cone shape (Fig. 3.1a); a steady state is reached when the cone radius equals the Rossby radius of deformation. At

this point, the plume begins to shed large eddies that travel horizontally. In our approach, we propose that the composition of the OP is the total mix of all convecting water masses:

$$C_i^{OP} = \frac{\int J_c C_i dS}{\int J_c dS} \tag{3.10}$$

Internal cell dynamics model

Here, we describe how we model the dependence of metabolism on environmental conditions through the thermodynamics of the catabolic reaction, upon which the bio-ecological model is built as a simplified variant of Sauterey et al. (2020)[22]. Catabolism is the set of reactions that a cell uses to harvest the energy needed for the synthesis of complex organic molecules to repair cell components or to grow. Catabolism can be written for 1 mol of electron donor (eD) as:
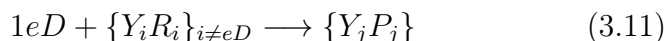
$$1eD + \{Y_i R_i\}_{i \neq eD} \longrightarrow \{Y_j P_j\} \tag{3.11}$$

where $\{R_i\}$ are the reactants, $\{P_j\}$ the products and $\{Y_{i,j}\}$ their stoichiometry (counted negative for reactants and positive for products). The Gibbs free energy of the catabolic reaction (J mol_{eD}^{-1}) is expressed as a function of temperature T (K) and reaction quotient Q_{cat} (dimensionless):

$$\Delta_r G_{cat} = \Delta_r G_{0,cat} + RT \log_e(Q_{cat}) \tag{3.12}$$

where

$$Q_{cat} = \prod_i a_i^{Y_i} \approx \prod_i C_i^{Y_i}. \tag{3.13}$$

Here a_i is the activity of species i, approximated by its concentration C_i. $\Delta_r G_{0,cat}$ is the Gibbs free energy of the reaction when all activities are unity, expressed as a function of temperature and standard values $\Delta_r G_{0,S}$ and $\Delta_r H_{0,S}$ found in chemistry tables:

$$\Delta_r G_{0,cat} = \Delta_r G_{0,S} \frac{T}{T_S} + \Delta_r H_{0,S} \frac{T_S - T}{T_S} \tag{3.14}$$

where $T_S = 298$ K is the standard temperature. Even spontaneous reactions ($\Delta_r G < 0$) may not occur, should their kinetics be infinitely slow; that is, when the activation energy needed to start them is very high. A fundamental property of living organisms is that they synthesize enzymes that significantly lower the activation energy of catabolic reactions so that they may occur at higher rates, making the potential energy they hold available for maintenance and anabolism (*i.e.* biomass production).

Our biological model is designed to track both the catabolic reaction rate and the energy that catabolism yields to the cell. The cell is able to run its catabolism at a certain specific rate, q_{cat} (mol_{eD} s^{-1} $\text{mol}_{C_x}^{-1}$), which depends on temperature. A general model of enzymatic rate q_e (mol_{eD} s^{-1} mol_{enzyme}^{-1}) as a function of temperature was derived in Daniel et al. (2010)[84] and validated experimentally. In their framework, the enzymatic rate is determined by the abundance of activated enzymes E_{act}. Higher temperature accelerates the catalyzed reaction, but also the conversion of activated enzymes to a deactivated state E_{inact}. The overall net enzyme catalysis rate q_e is modeled using an Arrhenius law for the rate of catalysis of the reaction by the activated enzyme (k_{cat}, mol_{eD} s^{-1} $\text{mol}_{E_{act}}^{-1}$) and an equilibrium law for the ratio of inactivated to activated enzyme $K_{eq} = \frac{E_{inact}}{E_{act}}$ (dimensionless):

$$
\begin{aligned}
q_e &= \frac{k_{cat}}{1+K_{eq}} \\
k_{cat} &= \frac{k_b}{h} T e^{-\frac{\Delta G_{acat}}{RT}} \\
K_{eq} &= e^{\frac{\Delta H_{eq}}{R}\left(\frac{1}{T_{eq}}-\frac{1}{T}\right)}
\end{aligned}
\tag{3.15}
$$

where k_b (1.38×10^{-23} J K^{-1}) is the Boltzmann constant, h (6.63×10^{-34} J s) is the Planck constant. The other kinetic parameters are enzyme-dependent. In our approach of modeling a generic hyperthermophile, we use values given in Daniel et al. (2010)[84] for an enzyme of *Thermus sp.* RT41a, an organism growing best at around 75°C, the highest growth temperature in their dataset. These values are (Extended Data Table C.2), $\Delta G_{acat} = 72,000$ J mol^{-1} (activation energy of the catabolic reaction), $\Delta H_{eq} = 305,000$ J mol^{-1} (equilibrium enthalpy of activated to deactivated enzyme) and $T_{eq} = 363.15$ K (equilibrium temperature of activated to deactivated enzyme). In the Supplementary Results and Discussion, we explore the consequence of varying the values of these parameters. We assume random variation, rather than variation driven by evolutionary adaptation to temperature. Taking evolutionary adaptation into account might result in a larger set of conditions interpreted as habitable and a higher productivity of the modeled population. This might eventually cause significant differences in dihydrogen depletion and methane production in the plume. The consequences of evolutionary adaptation will be addressed in future work, using the approach pioneered in Sauterey et al. (2020)[22].

The specific catabolic rate q_{cat} (per mole of biomolecule carbon C_x, hence in unit mol_{eD} $\text{mol}_{C_x}^{-1}$ s^{-1}) is obtained by scaling q_e with the

enzymatic fraction τ (dimensionless, or $\mathrm{mol}_{enzyme}\,\mathrm{mol}_{C_x}^{-1}$) of biomass (that is, the number of catabolic enzymes per biomolecule in the cell) so that $q_{cat} = \tau q_e$. The parameter value $\tau \approx 1.73 \times 10^{-5}$ is estimated by fitting the model to data from Taubner et al. (2018)[85] as described later on.

Some of the energy provided by the catabolism goes to the maintenance of the cell and represents a minimal energy for living processes (*e.g.* repairing denatured proteins and damaged DNA). No growth occurs when only this amount of energy is available to the cell. An empirical and general relationship between the cell maintenance energy rate (e_m, kJ d^{-1} mol$_{C_x}^{-1}$) and temperature was established in Tijhuis et al. (1993)[78]:

$$
\begin{aligned}
e_m &= 84\ e^{\frac{69,400}{R}\left(\frac{1}{T_S} - \frac{1}{T}\right)} \\
q_m &= -\frac{e_m}{\Delta_r G_{cat}}
\end{aligned}
\tag{3.16}
$$

where q_m (d^{-1}) is the rate at which the catabolism must run to meet the maintenance needs. When $q_{cat} < q_m$, the cell decays and eventually dies (Fig. 3.1b). Otherwise, the remaining catabolic energy then goes to fueling the anabolic reaction, which drives the synthesis of cell building blocks. The anabolic reaction is rarely spontaneous and often requires more energy than catabolism alone may provide. In effect, the cell is able to store energy in the form of ATP until enough is available for anabolism. The rate at which the anabolism runs is much lower than the catabolic reaction rate (think of catabolism as a small gear wheeling the larger gear of anabolism).

More recent observations (Lever et al., 2015[155] and references therein) point out that e_m as modeled in Tijhuis et al. (1993)[78] might be overestimated. Although a variety of underlying processes to explain minimal energy requirements have been proposed[155], a detailed mechanistic model that could explain the available observations is still lacking. Given the persistent uncertainties regarding the minimal energy requirements of cellular life, we chose the conservative approach of using Tijhuis et al.'s model[78] – *i.e.*, the parameterization that disfavors habitability the most.

Kleerebezem and Van Loosdrecht (2010)[62] use a generic chemical composition of biomass that is useful to compute the Gibbs free

energy required to synthesize a mol of biomass (ΔG_{ana}). To this energy is added the cost of dissipation that occurs during metabolism. An empirical relationship between characteristics of the metabolism and the amount of dissipated energy (ΔG_{diss}) is[62]:

$$\Delta G_{diss} = 200 + 18(6 - NoC)^{1.8} + exp\left[((-0.2 - \gamma)^{2.16})(3.6 + 0.4NoC)\right]$$
(3.17)

where NoC is the carbon chain length in the carbon source and γ is the oxidation number of carbon in the carbon source. In general $\Delta G_{diss} >> \Delta_r G_{ana}$. The energy cost of anabolism $\Delta G_{diss} + \Delta_r G_{ana}$ can therefore be approximated by ΔG_{diss}. The anabolic rate per mol of biomolecule is therefore given by

$$q_{ana} = -\frac{\Delta_r G_{cat}}{\Delta G_{diss}}(q_{cat} - q_m)$$
(3.18)

For a given metabolism, q_{ana} is strongly dependent on temperature through q_{cat} and q_m, and also depends on the availability of substrates through $\Delta_r G_{cat}$. The cell accumulates biomolecules at the rate q_{ana} times the number of biomolecules in the cell. We do not represent the number of biomolecules in each cell but rather the mean value for the population. The cells are then set to undergo division at a rate, r, proportional to their internal biomolecule content.

Ecosystem dynamics and steady state

Using quasi-steady-state approximation on internal cell dynamics, the ecosystem dynamics are driven by the dynamics of the cell population and the chemical environment (substrates and products):

$$\begin{array}{rcl}
\frac{dN}{dt} & = & N(q_{ana} - d) \\
\frac{\partial C_i}{\partial t} & = & \frac{1}{\epsilon u_s \rho_o}\left(J_f(C_i^f - C_i^o) + J_c(C_i^o - C_i)\right) + NB^* q_{cat} Y_i^{cat}
\end{array}$$
(3.19)

where N is the surface density of the number of individuals in the population per kg of water (thus in kg^{-1} m^{-2}), d (s^{-1}) is a baseline death rate accounting for density-independent mortality, and B^* (mol$_{C_x}$) is the steady-state internal cell biomass, or quantity of biomolecules. To our knowledge, there is no estimation of d for methanogens in their natural habitat; we therefore chose to use the value estimated in Connolly and Coffin (1995)[156] for marine plankton, and we explore the consequence of varying its value in Supplementary Results and Discussion.

Solving equation (3.19) for steady-state, and using equation (3.13) yields an expression for the steady-state reaction quotient Q_{cat}^*:

$$
\begin{aligned}
Q_{cat}^* &= exp\left[-\tfrac{1}{RT}\left(\Delta G_0 + (d + \tfrac{e_m}{\Delta G_{diss}})\tfrac{\Delta G_{diss}}{q_{cat}}\right)\right] \\
\log_e Q_{cat}^* &= \log_e K - \tfrac{1}{RT}\left(d + \tfrac{e_m}{\Delta G_{diss}}\right)\tfrac{\Delta G_{diss}}{q_{cat}}
\end{aligned}
\tag{3.20}
$$

where K (dimensionless) is the equilibrium constant of the reaction. Q_{cat}^* denotes the steady-state value of the reaction quotient, which is the value at which available energy in the cell's environment exactly compensates death (or removal from the environment) and maintenance, and therefore sets a limit value on Q_{cat} for growth, as detailed below.

We assume that if the initial conditions allow for a positive growth rate, the composition will converge toward this non-equilibrium stationary state, as seen in numerical simulations (Supplementary Fig. C.6b, c). Initial conditions are favorable to microbial population persistence if Q_{cat}^* is larger than Q_{cat} evaluated at the initial conditions, $Q_{cat}^0|_T$:

$$
Q_{cat}^*(T) > Q_{cat}^0|_T
\tag{3.21}
$$

which provides a criterion for population viability. In the absence of any other factors, the steady-state concentration of i, C_i^*, is given by

$$
C_i^* = C_i^0 + Y_i^{cat}(C_{e_D}^0 - C_{e_D}^*).
\tag{3.22}
$$

The electron donor concentration at steady state, e_D^*, can be solved by using equation (3.20) and

$$
Q_{cat}^* = \frac{1}{C_{e_D}^*}\prod_{i\neq e_D}\left(C_i^0 + Y_i^{cat}(C_{e_D}^0 - C_{e_D}^*)\right)^{Y_i^{cat}}
\tag{3.23}
$$

In the case of Enceladus, we apply this bio-ecological model to a generic methanogenic hyperthermophile, with enzyme kinetic properties described hitherto, in a horizontally structured hydrothermal hot spot. The chemical reaction of hydrogenotrophic methanogenesis written per mol of electron donor (H_2) is given by equation (3.1) and has $\Delta_r G_{0,S} = -32.6$ kJ mol^{-1}, $\Delta_r H_{0,S} = -63.2$ kJ mol^{-1} for reactants in gaseous state. To express $\Delta_r G_{0,cat}$ in the aqueous phase, $\Delta_r G_{0,cat}^{aq}$, from $\Delta_r G_{0,cat}$ in the gaseous phase, $\Delta_r G_{0,cat}^{gas}$, we add a corrective term using enthalpies of dissolution:

$$
\Delta_r G_{0,cat}^{aq} = \Delta_r G_{0,cat}^{gas} - RT\sum_i Y_i \log_e(H_i)
\tag{3.24}
$$

where $\Delta_r G^{gas}_{0,car}$ is computed using equation (3.14), $H_i = \frac{C_i}{P_i}$ (mol kg^{-1} Pa^{-1}) are Henry's law coefficients, $H_{H_2} = 7.8 \ 10^{-4}$ and $H_{CH_4} = 1.4 \ 10^{-3}$, taken independent from temperature. The solubility constant of CO_2 is taken as a function of temperature fitted from outputs of the Aspen plus software:

$$H_{CO_2} = \exp\left[\frac{9345.17}{T} - 167.8108 + 23.3585 \log_e(T) + \right.$$
$$\left. (0.023517 - 2.3656 \ 10^{-4}T + 4.7036 \ 10^{-7}T^2)35.0 \right] \tag{3.25}$$

Regarding anabolism, we assume that the carbon source is also CO_2, hence $NoC = 1$ and $\gamma = 4$ in equation (3.17) giving ΔG_{diss}.

Estimation of the catabolic enzyme-to-biomass scaling factor

Here, we estimate a credible value for the yet unconstrained enzyme-to-biomass ratio parameter. This ratio is needed in order to derive a specific catabolic rate from enzyme-scale kinetic modeling, as mentioned earlier. To do so, we fit our model to the results of growth experiments in Taubner et al. (2018)[85]. In their study, Taubner et al. (2018)[85] experimented on *M. okinawensis*, *M. marburgensis* and *M. villosus*. We chose to use growth data of *M. villosus*, as *M. villosus* has a higher growth temperature than the other two (*ca.* 80 °C *versus ca.* 65 °C), in accordance with the kinetic parameter values we chose (see the Internal Cell Dynamics section above). Because data in Taubner et al. (2018)[85] measure cell density as optical density, we focus on the initial growth rate, a parameter that appears in the Verhulst logistic model. Our model being analog to a logistic model, we fit parameters n_0, r and K_n (initial population density, growth rate and carrying capacity respectively) of

$$n(t) = \frac{K_n}{1 + (\frac{K_n}{n_0} - 1)e^{-rt}} \tag{3.26}$$

to the experimental growth curve using least mean square method in the "curve fit" function in the Scipy python package[157]. The estimated value of the growth rate, r, is then used to obtain τ from

$$r \approx q_{ana} = \lambda(\tau q_e - q_m) \tag{3.27}$$

hence

$$\tau \approx \frac{\frac{r}{\lambda} + q_m}{q_e} \tag{3.28}$$

where λ, q_e and q_m are obtained from the composition and temperature of the growth medium in the experiment[85]. In Supplementary Fig. C.6b we compare a logistic curve using a growth rate generated by the model at experimental temperature (80 ± 1 °C) and chemical conditions ($[H_2] = 1.5$ mmol kg^{-1}, $[CO_2] = 7.7$ mmol kg^{-1}, and negligible $[CH_4] = 10^{-10}$ mol kg^{-1}), with the τ value inferred from the growth data of *M. villosus* in Taubner et al. (2018)[85]. We find $\tau \approx 1.73 \cdot 10^{-5} \text{mol}_{enzyme} \text{ mol}_{C_x}^{-1}$. We then compared this value to mass-specific resting metabolic rates of unicellular organisms[77]. To do so, we determined the cell mass predicted by our model using Kleerebezem and Van Loosdrecht (2010)[62] which provides an empirical relationship between cell volume V_c (μm^3) and cell structural mass $M_{C_x} = 18 \cdot 10^{-15} \cdot V_c^{0.94}$, in mol$_{C_x}$ (this relationship was also used in Sauterey et al. (2020)[22]). By applying this relation to a typical 1 μm radius cell, we obtain $\log_e(B_0) \approx -6$ (W g$^{-3/4}$) for methanogens in our model at the estimated optimal temperature of ≈ 82 °C in standard chemical conditions (see Fig. 3.1b). This value falls at the lower end of the empirical range described in Gillooly et al. (2001)[77]. While τ might be an important parameter in determining the temperature growth curve of an organism, other kinetic parameters of catabolism and maintenance described earlier on also contribute and are estimated separately. As a consequence, when using the value obtained from *M. villosus* growth data, we do not aim at modeling this organism *per se*; rather, we model a generic, hypothetical hyperthermophile with temperature apparent properties described in Fig. 3.1b-d. We explore the consequences of changing the value of parameter τ, along with others in Supplementary Methods, Results and Discussion, as well as in Supplementary Figs. C.8-C.10.

Bayesian inference

Because the model is complex, the likelihood $P(x^0|X)$, $X = A$ or B, cannot be analytically expressed, a problem known as "intractable likelihood". Instead we use an Approximate Bayesian Computation (ABC) approach[158]. ABC relies on approximating the likelihood by simulating outputs, called pseudo-data, from prior distributions of parameters. The likelihood can then be computed from the distribution of simulation outputs. If θ denotes the pa-

rameter vector, x the vector of a pseudo-data point, and x^0 an observation ("true data"), then $P(\theta)$ is specified by the prior distribution, and $P(x^0|\theta)$ is approximated by sampling simulations of a model π linking parameters to the observable, *i.e.* $\pi(\theta) = x$. Then the probability of a parameter set $\hat{\theta}$ given the observation x^0 follows from Bayes theorem:

$$P(\hat{\theta}|x^0) = \frac{P(x^0|\hat{\theta})P(\hat{\theta})}{\int_\theta P(x^0|\theta)P(\theta)d\theta}. \tag{3.29}$$

Equivalently, instead of parameters, the Bayesian approach can be used to infer so-called classes, corresponding to subsets of the parameter space (Extended Data Fig. C.1). See Sisson et al. (2018)[159] for a detailed guide to ABC methods and Csilléry et al. (2010)[158] for examples of applications.

The most basic form of ABC, called "K nearest neighbors" (KNN) ABC, aims at computing the Euclidean distance in the data space to obtain a subset of pseudo-data resembling the observation and the associated subset of the parameter space, so that a posterior distribution of parameters (maximizing the multivariate likelihood of observation) is obtained. Because future characterisation of the habitability or inhabitation of planetary bodies is expected to be a high-dimensional problem, involving a greater number of observables, following Csilléry et al. (2010)[158] we argue that standard ABC, a method suffering the curse of dimensionality, may not be suited. Instead we used a higher-order ABC method, Random Forest ABC (ABC-RF), based on a machine learning method of classification[147]. RF-ABC handles high-dimensional problems much more efficiently than KNN methods[147,158].

A Random Forest is a population of decision trees, that is, oriented graphs (or "flowcharts") in which each node corresponds to a test on a feature (an observable in our context) of the pseudo-data (an example is given in Supplementary Fig. C.7a). Depending on the truth value of the test, the pseudo-data are then passed to a branch or another to the next test. For example, in Supplementary Fig. C.7a, the first test is $R_1 \leq 2.72$. If this test has a truth value of 1 (resp. 0), the data is passed to the next test : $\Phi_{CH_4} \leq 285,179,380$ mol yr^{-1} (resp. $\Phi_{H_2} \leq 78,416,564$ mol yr^{-1}) and so on. The goal of the decision tree is to split the pseudo-data

set in subsets ("leaves") corresponding as faithfully as possible to the classes uninhabitable ($\bar{H}$), abiotic-habitable (H^{ab}) and biotic (B).

The RF is a population of trees that categorizes data points into classes according to the votes of the trees in the decision forest. The pseudo-data (or the training dataset) correspond to a set of features associated with their class (together, they are the reference table) and are used to fit the RF classifier. In other words, the algorithm consists in selecting the decision forest that best classifies the pseudo-data in the training dataset. In order to obtain a population of decision trees that splits the data set well, we evaluate the Gini Impurity, which measures the probability to misclassify a point in a set or subset if classification is done at random. The general expression of the Gini Impurity is:

$$G = \sum_i p(i)(1 - p(i)) \tag{3.30}$$

where $p(i)$ is the probability of attributing class i to a point when the class of the point is i. The overall Gini Impurity of several subsets is the weighted sum of G in each subset.

A measure of the efficiency of the method is the overall classification error rate (or prior error rate), ζ: the fraction of pseudo-data points that the fitted classifier misclassifies. Conversely, the score $1 - \zeta$ measures the success rate of the classifier. One can also measure this score for a specific class and compute how wrong the classifier is when it misclassifies pseudo-data points, for instance "with what class does the classifier confuses B the most?". The representation of how the RF classifier confuses different classes is the confusion matrix, of which an example is shown in Supplementary Fig. C.7b.

We trained a decision forest on the pseudo-data set of $50,000$ simulations generated from the priors reported in Extended Data Table C.1 using the `RandomForestClassifier` function from the python package *ScikitLearn*[160] with parameters reported in Extended Data Table C.3. In ABC-RF, the posterior probability is approximated by averaging the class probability of each tree. The class probability of i in a tree is the fraction of class i in the leaf corresponding to the prediction. A full description of ABC-RF is found in Pudlo et al. (2015)[147].

Building the priors

Input parameters of the ecological model are the composition and temperature of the HF and composition of the ocean in species of interest (H_2, DIC, CH_4), with their distribution defining the prior space θ. In our approach, the temperature of Enceladus' ocean is fixed and thus not drawn from a prior distribution. A well-supported estimate for the temperature of Enceladus' ocean is 275 K, close to thermal equilibrium with ice[64,129]. High ammonia concentrations could lead to a lower freezing point of water, and thus a colder ocean, the consequences of which are discussed in Supplementary Results and Discussion. In this section, we explain the ranges chosen for the concentrations in HF and OW of H_2, DIC and CH_4, and for the temperature of the HF. A summary is given by Extended Data Table C.1.

Constraining H_2 in the hydrothermal fluid and in the ocean. Following Waite et al. (2017)[64], we assume that the dihydrogen present in the hydrothermal fluid is produced in Enceladus' core. Choblet et al. (2017)[89] have argued that serpentinization was a plausible source of H_2 in Enceladus' core, and considering other potential sources Waite et al. (2017)[64] concluded that they were likely insufficient to explain observed H_2 flux. We therefore assume that serpentinization is the primary source of dihydrogen. A maximum value for the H_2 concentration in the hydrothermal fluid is the concentration at saturation with the vapor phase produced during serpentinization[145]. This value may be close to 10^{-1} mol kg^{-1} at pressures of the order of 10 MPa, the expected hydrostatic pressure at Enceladus' seafloor. We neglect the hydrogen saturation concentration variation with temperature and thus make the assumption that the concentration of H_2 in the fluid is drawn independently from temperature, according to

$$[H_2]_f \sim \log_e \mathbf{U}(10^{-8}, 10^{-1}) \text{ mol kg}^{-1} \qquad (3.31)$$

where $\mathbf{U}$ denotes the uniform distribution. We note that, depending on the rock and water composition, the maximum dissolved H_2 may be lower than the equilibrium with hydrostatic vapour phase[145,161]. As a consequence, we may be overestimating the production of H_2 from serpentinization.

We assume that the concentration of dihydrogen in the ocean is very low since it is produced in the core, as suggested by Waite

et al. (2017)[64] :

$$[H_2]_o \sim \log_e \mathbf{U}(10^{-8}, 10^{-6}) \text{ mol kg}^{-1} \qquad (3.32)$$

Note that assuming low levels of dihydrogen in oceanic waters is equivalent to assuming that most of the dihydrogen escapes or is captured in clathrates instead of recirculating in the core. Choblet et al. (2017)[89] suggest that the whole ocean may be processed in the core at relatively short timescales (25-250 Myr) and that the composition of the ocean may depend on ice melting above hydrothermal hot spots and recrystallisation in other regions.

Constraining CH_4. Methane concentration in the hydrothermal fluid is an important parameter of methanogenesis, as an increased concentration reduces the thermodynamical favorability of the reaction (3.1). In a first set of simulations, we limit the source of CH_4 to serpentinization chemistry, a source that was suggested in previous studies[130]. The rate of reaction (3.1) in serpentinization waters is subject to debate but recent experimental work suggests that this reaction conducted abiotically faces significant energy barriers and would be extremely slow across the temperature range considered here[146]. The same study showed that in low-pressure (10 MPa) hydrothermal systems where a H_2 vapor phase can form, the reaction is significantly accelerated. Because the hydrostatic pressure at the bottom of Enceladus ocean might be of that order[85], we assume that CH_4 concentration in the hydrothermal fluid can be as high as reported by McCollom (2016)[146], *i.e.* 0.1 mmol kg^{-1}, so that:

$$[CH_4]_f \sim \log_e \mathbf{U}(10^{-8}, 10^{-4}) \text{ mol kg}^{-1}. \qquad (3.33)$$

Note that we neglect any conversion of H_2 and CO_2 in the mixing layer, where temperatures are lower. In the alternate scenario, we do not limit $[CH_4]_f$ to serpentinization chemistry, and use an arbitrarily higher upper bound so that

$$[CH_4]'_f \sim \log_e \mathbf{U}(10^{-8}, 10^{-1}) \text{ mol kg}^{-1}. \qquad (3.34)$$

In the ocean, and following what was done for H_2, we take

$$[CH_4]_o \sim \log_e \mathbf{U}(10^{-8}, 10^{-6}) \text{ mol kg}^{-1}. \qquad (3.35)$$

Constraining the dissolved inorganic carbon (DIC). On the geological timescale, Earth's oceans are recharged with CO_2

through volcanic outgassing and carbonate dissolution. Glein et al. (2015)[129] suggest that dissolution of carbonates may be Enceladus' main source of ocean dissolved carbon dioxide, whereas magma outgassing seems unlikely given the small and relatively cold core of Enceladus. Dissolved inorganic carbon is the total of dissociated forms of CO_2 in water ($DIC = [CO_2] + [HCO_3^-] + [CO_3^{2-}]$). DIC concentration in Enceladus' ocean was estimated using plumes chemical data from the Cassini mission[129]. The total dissolved inorganic carbon was constrained between 0.1 and 0.004 mol kg^{-1} :

$$[DIC]_o \sim \log_e \mathbf{U}(4 \cdot 10^{-3}, 10^{-1}) \text{ mol kg}^{-1}. \tag{3.36}$$

Our first order model does not take into account the complex carbonate chemistry in the Enceladus ocean that Glein and Waite (2020)[162] investigate. Instead, we have identified the activity of CO_{2aq} with the total dissolved inorganic carbon. This is a first approximation which should be refined in the future by coupling the current model with that of Glein and Waite (2020)[162]

For our analysis to be conservative, we assume the hydrothermal fluid to be DIC-poor and thus use a much lower range

$$[DIC]_f \sim \log_e \mathbf{U}(4 \cdot 10^{-8}, 10^{-6}) \text{ mol kg}^{-1}. \tag{3.37}$$

Constraining T_f. In Choblet et al. (2017)[89], temperatures in the core were computed from a range of plausible core porosity (K_p) constrained by the observation of nanometre-sized silica particles and water boiling point (limit of their model). We assume that the water boiling point is not exceeded and that the $\log_e$ of porosity is *a priori* uniformly distributed between 10^{-14} and 10^{-12}. Using the approximation $T \propto \log_e K_p$, we conclude that the hydrothermal fluid temperature is drawn from a uniform distribution :

$$T_f \sim \mathbf{U}(300, 620) \text{ K} \tag{3.38}$$

For comparison, Earth's hydrothermal systems have been observed venting fluids at 640 K [163]. The temperature of Enceladus ocean is set at a single value of $T_o = 275$ K, close to thermal equilibrium with ice, in agreement with previous work[64,129].

Selection of observables

Choosing reliable and informative observables is a crucial step of the inference framework. Observables must be model outputs

that are confidently measured. Because our model captures only a subset of Enceladus geochemical processes that potentially influence the plume composition, we must carefully evaluate whether the model outputs may faithfully translate into measurements that are available from the Cassini mission.

The model takes the composition and temperature of the hydrothermal fluid, and the composition of the ocean, as inputs. Then the model represents the mixing of hydrothermal fluid and ocean water. In this mixing layer, biological methanogenesis might occur, or not. If it does, the local composition of the mixing layer is altered according to the biological model. The mixing layer waters are then mixed together to form an homogeneous oceanic plume water mass. At this point, there is uncertainty in the amount of dilution of these waters with oceanic waters during their ascent across the ocean. Our mixing model predicts an upward advection of 10^4 to 10^5 kg s^{-1} at the hot spot. Using scaling relationships for Europa[142] that have been adapted for Enceladus[89], we find water transports at the top of the column that are three orders of magnitude higher ($\approx 10^8$ kg s^{-1}). This discrepancy between predictions from our mixing model and scaling relations in Goodman et al. (2004)[142] indicates that our approach might greatly underestimate the dilution of ML waters during their ascension towards the ice ceiling, and *a fortiori* neglect the dynamics of ascending waters. To circumvent the challenge of modeling the mixing of the oceanic plume while it travels upward, we select observations that carry information on seafloor processes, independently of dilution in the ascending plumes.

In Waite et al. (2017)[64], the authors assume that the source of dihydrogen in Enceladus compensates for the loss to space from the gas jets at the plume's origin. Following the same approach, we assume that the outward flux is equal to the flux of hydrogen into the ocean (coming out of the mixing layer). Because H_2 is assumed to be produced in the core, we integrate the outward flux from the mixing layer at steady state

$$\Phi_{H_2} = \int_S J_c[H_2] \, dS \ (\text{mol yr}^{-1}) \tag{3.39}$$

and thus define an observable that should be consistent with model outputs regardless of dilution in the oceanic plume.

Following Bouquet et al. (2015)[138], we assume that a source of CH_4 in the core compensates clathrate dissociation so that the release rate in the ocean is approximately equal to the measured ejection rate

$$\Phi_{CH_4} = \int_S J_c[CH_4] \, dS \, (mol \, yr^{-1}) \qquad (3.40)$$

We also use

$$R = \frac{[H_2]}{[CH_4]} \qquad (3.41)$$

as an observable. As the other two observables, R should also be independent of dilution. Using R as an observable, however, requires to further assume that this ratio is conserved when the ocean material travels through the ice. This assumption is discussed in Waite et al. (2017)[64], where it was used to estimate concentrations in H_2, CO_2 and CH_4 in the ocean.

Other observables

Other observables have been considered but were not used in our inference framework. First, the observed flux of CO_2 in the plume, as well as the $H_2 : CO_2$ ratio might contain information on whether hydrogenotrophs might be active or not. We did not use these measurements as observables because the CO_2 source is unknown; as we only assume that CO_2 in the mixing layer comes from the ocean, this makes the observed CO_2 flux and $H_2 : CO_2$ ratio sensitive to dilution of the oceanic plume which, as mentioned above, is a process that is poorly constrained in our model. Furthermore, our knowledge of what might be the CO_2 stock in Enceladus' ocean comes from the Cassini measurements that we aim to use for inference. As a consequence, the observation point would be as informative as the prior knowledge, and thus inference would not be improved.

Second, considering the value in Enceladus's ocean of the Gibbs free-energy associated with reaction (3.1), Waite et al. (2017)[64] inferred a negative value, and concluded that methanogenesis was feasible in Enceladus ocean. The Gibbs free energy $\Delta_r G$ is computed from the reaction quotient Q and temperature T (equation (3.12)). The reaction quotient in the oceanic plume might be useful as an observable because its value in the ML is crucial to habitability (equation (3.21)). In Waite et al. (2017)[64], the concentrations of

reactants used to compute Q are inferred by obtaining CO_2 concentration from carbonate equilibrium (using a pH value for Enceladus' ocean of $9 - 11$) and deriving other concentrations using the ratios $CH_4 : CO_2$ and $H_2 : CO_2$ in the plume. The temperature they use is the putative temperature of Enceladus' ocean (275 K). Here, we did not use the reaction quotient as an observable because of the serious difficulty of computing Q in the plume, and because of its sensitivity to the dilution of the oceanic plume, which is poorly constrained in our model (see above).

Chapter 4.

Biomass and productivity of a putative methanogenic biosphere in Enceladus's deep ocean: implications for its detection

Abstract

Saturn's moon Enceladus is a top candidate in the search for extraterrestrial life in our solar system. Ecological thermodynamic modeling of the plume composition data collected by NASA's Cassini mission led to the hypothesis that a hydrogenotrophic methanogenic ecosystem might exist in the putative hydrothermal vents at Enceladus seafloor. Here, we extend this approach to quantify the ecosystem's expected biomass stock and production and evaluate its detectability from the collection of plume material. We find that despite a hypothetical biosphere in Enceladus's ocean could be small ($<$ 10 tons of carbon), measurable amounts of cells and organics might enter the plume. However, it is critical that missions be designed to gain meaningful insights from a negative outcome (no detection). We show that in order to sample a cell from the plume with 95% confidence, $>$ 0.1 mL of material needs to be collected. This would require material from more than 100 fly-bys through the plume or using a lander. Many factors other than sampling bias, such as cell destruction during outgassing could render cell retrieval very uncertain. Thus, we consider amino-acid abundance as an alternative signature. We find that the absolute abundance of amino-acids, glycine for example, could be very informative if a detection threshold of 1×10^{-7} mol/L could be achieved. Altogether, our findings set relatively high bars on amino-acids detection thresholds and sample volume, but these goals seem within the reach of near-future missions.

4.1. Introduction

On Earth, hydrothermal circulation of seawater in the oceanic lithosphere triggers a set of reactions known as serpentinization that produces dihydrogen (H_2). H_2 molecules may then react with the seawater's carbon dioxide (CO_2) to produce methane (CH_4) according to the reaction equation (here written for 1 mol of H_2, the electron donor):

$$H_2 + \frac{1}{4}CO_2 \longrightarrow \frac{1}{4}CH_4 + \frac{1}{2}H_2O \qquad (4.1)$$
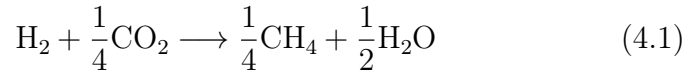
This reaction can occur spontaneously (albeit slowly) in serpentinization fluids[146]. Serpentinization fluids are released at seafloor hydrothermal vents, geological features known to harbor complex ecosystems that rely on chemical gradients instead of sunlight as their primary energy source[132]. In particular, reaction (4.1) can be enzymatically catalyzed by hydrogenotrophic, methanogenic Archaea that use it as their catabolic reaction – the reaction that provides the cell with energy[133]. Biological production of methane through reaction (4.1) is called here methanogenesis.

Enceladus, sixth biggest moon of Saturn, might have similar hydrothermal vents in direct contact with its water ocean laying under a thick ice shell and over a rocky core[125,128,164]. Warm buoyant water released at the seafloor rises upwards forming a rotating ocean plume that reaches the top of the water column[89,120,143]. Through cracks in the ice crust, oceanic material is outgassed and forms a plume of water vapor and ice grains[165]. Some of these particles contain salt and organic compounds, including high-mass molecules (macromolecules), suggesting that they are frozen droplets originating from gas bubbles bursting through an organic-rich film[116]. Bubble walls constitute an interface that attracts organics from the water table it traverses, thus increasing their concentration in the ocean spray[166]. This process, known as bubble scrubbing could occur during the formation of Enceladus's plume[119] as an important process in defining the effective composition of plume material relative to that of the bulk ocean or of the ocean plume.

While hydrothermal circulation in Enceladus's rocky core, unlike Earth's, is likely powered by tidal dissipation[89], serpentinization might occur still[64]. Previous work suggested that reaction (4.1) could be thermodynamically favored in Enceladus's ocean[64]. It was also demonstrated that Earth's hydrogenotrophic methanogens could grow under putative Enceladus's seafloor con-

ditions[85]. Ecological thermodynamic modeling was used to quantitatively evaluate the habitability of Enceladus's hydrothermal vents for methanogens and estimate the likelihood of methanogenesis given H_2 and CH_4 abundances in the plume inferred from the Cassini data. The data appear to be compatible with sufficient H_2 production to allow a population of methanogens to grow and with production of CH_4 by abiotic serpentinization chemistry and a biotic population together ; but as other abiotic sources of methane remain poorly constrained, this does not provide conclusive evidence in favor of living organisms[117]. To further investigate the possibility of a biological population in Enceladus's ocean, the critical challenges are to (i) predict biosignatures that would provide more direct evidence and be accessible to future missions, and (ii) design such a mission so as to maximize scientific return, especially in the case of a negative result.

Previous work has focused on the concentrations of cells[119,167] or organics (*e.g.* amino-acids[120,168]) hypothetically present in the plume material, and discussed how future missions could measure them. Here we build on the model presented in Affholder et al. (2021)[117] to calculate the biomass stock and productivity of a hypothetical population of methanogens in Enceladus's ocean. In doing so, we are able to estimate cell densities and concentrations of biotically produced organics in Enceladus's hydrothermal vent and that could be found in the plume. We argue that the stock biomass that can be supported by Enceladus's hydrothermalism is not necessarily the same quantity as the biomass that can be found in the ocean plume. We therefore model explicitly the relationships between a population living in the hydrothermal vents and cells or organics that escape this environment and travel with buoyant water to the ice shell. Second, our modeling relies on a description of biological energetic processes that ultimately govern the efficiency of hydrogen conversion by a population of methanogens, as well as on a spatial model of the hydrothermal environment and its chemical and temperature gradients. Thus, we believe that our approach yields estimates of cell or biomass density that are more realistic -and more conservative- than those produced by models assuming complete conversion of H_2 into CH_4[120,167] or assuming constant catabolic energy yield for biomass generation (*e.g* ref.[63]). Using this model, we obtain estimates of *a priori* credible amino-acid and cell abundances in the plume under the assumption of methanogenesis, as well as estimates corresponding to a biomass stock and production best matching methane and dihydrogen measurements

in the plume. In doing so, we show how previous data from the Cassini mission, as well as *a priori* information on serpentinization and hydrothermal circulation in Enceladus can be used to provide a quantitative and testable prediction. This could help design the scientific experiments that should be carried out in order to get the best possible scientific return from a future mission to Enceladus.

4.2. Methods

The model presented here builds on the modeling and inference framework in Affholder et al. (2021)[117], but focuses on quantities that were left out of their analysis such as biomass stock and biomass production. Indeed, Affholder et al. (2021)[117] focused on the existence of a population and its effect on the local composition and ultimately on escape rates of volatile species in the plume, but did not evaluate cell densities and ecosystem productivity.

4.2.1. Model of the hydrothermal environment

In Affholder et al. (2021)[117], the hydrothermal environment is given an idealized description as a flat cylinder on the seafloor corresponding to a mixing layer (ML), in which hydrothermal fluid is mixed with sea water. Given a total power dissipated hydrothermally of $F = 5$ GW[89], the hydrothermal fluid (HF) temperature T_f (in K, variable) and the ocean's temperature $T_o = 275$ K [129], steady-state physical quantities defining the hydrothermal environment are derived. $J_f(u)$ and $J_c(u)$ are respectively the surface advection flux in the environment (of hydrothermal fluid) and the upwards buoyancy flux coming out of the ML (both in kg s^{-1} m^{-2}) as a function of u, the distance to the center (meters).

The expression of $J_c(u)$ is function of local temperature $T(u)$ [142]:

$$J_c(u) = \rho\sqrt{2\epsilon g\alpha(T(u) - T_o)} \tag{4.2}$$

where ρ $(1,000$ kg m$^{-3})$ is seawater mass density, α $(3 \times 10^{-4}$ K$^{-1})$ is the coefficient of thermal expansion of water and g $(0.12$ m s$^{-2})$ is the local gravitational acceleration. Strictly for numerical purposes, the thickness of the mixing layer ϵ is assumed to be of the order of a meter (we set it to $\epsilon = 1$ m throughout), as it is intermediate between the height of the tallest spires in Lost City Hydrothermal Field (LCHF ; ≈ 60 m)[169] and the cm local scale of chimneys and ledges where Archaea are present[118]. In practice, the scale-free

properties of the physical model imply that the value of ϵ has no influence on the quantities we calculate (see Appendix D.1).

The shape of function $J_f(u)$ (kg s^{-1} m^{-2}), the mass flux density of HF into the ML as a function of the distance is

$$J_f(u) = J_{max}\mathrm{e}^{-\left(\frac{u}{c}\right)^2} \tag{4.3}$$

and is governed by parameters J_{max} (maximum flux, in kg s^{-1} m^{-2}) and c (horizontal scale, in m). Effectively, c represents the distance from the center at which $J_f(c) = J_{max}/e$, or equivalently $x^*(c) = \mathrm{e}^{-2/3} \approx 0.5$ (the mixing ratio at this distance is 1:1 HF versus seawater). Keeping in mind that this model is an idealized representation of the hydrothermal environment, this scale would be ≈ 8 m for a 5 GW vent releasing 353 K fluid (or about 2 cm for a 40 kW, 353 K vent, the predicted output from the LCHF[170]). They are obtained by ensuring that power F is dissipated by the the advection of HF, and by setting $J_f(0) = J_{max} = J_c|_{T(u)=T_f}$:

$$\int_S J_f dS = \int_0^\infty 2\pi r J_f(u) du = \frac{F}{C_p(T_f - T_o)} \tag{4.4}$$

where S (m^2) is the hot spot surface area, hence

$$c^2 = \frac{F}{\pi C_p \rho \sqrt{\epsilon g \alpha (T_f - T_o)^3}} \tag{4.5}$$

where C_p is the specific heat capacity of water ($4,200$ J K^{-1} kg^{-1}).

Given the chemical composition of the hydrothermal fluid and of the seawater, the steady-state composition in the mixing layer $\{C_i(u)\}$ (concentration of molecule i in mol kg^{-1}) is also obtained. Together, the physical and chemical gradients surrounding the hydrothermal vent define the environment in which a population of methanogens may grow. A population of methanogens changes the steady state composition of the ML as explained in Affholder et al. (2021)[117] and summarized below. The flux of i coming from the hydrothermal environment is then given by:

$$\Phi_i = \int_0^\infty J_c(u) C_i(u) 2\pi u du \tag{4.6}$$

The concentration of i at the base of the ocean plume (OP), assuming that buoyant ML water mixes together is:

$$C_i^{OP} = \frac{\int_0^\infty J_c(u) C(u) 2\pi u du}{\int_0^\infty J_c(u) 2\pi u du} \tag{4.7}$$

It is interesting to note that in Affholder et al. (2021)[117], assumptions that constrain $J_c(u)$ the flux of hydrothermal fluid in the ML lead to a hydrothermal fluid to seawater mixing ratio in the initial ocean plume that is independent of the vent's scale and of the HF's temperature and equals 1/3 (proof is obtained by expressing the stationary state mixing ratio in the initial plume: $x_{OP}^* = \int x J_c / \int J_c$).

4.2.2. Stationary biomass of a methanogenic population

Our biological model assumes that a minimal amount of energy is required to sustain cellular integrity and function, called the maintenance energy, and that the energy yield of the catabolic reaction varies as the population alters the composition of the medium. This second point is relevant to the assumption that a putative Enceladean methanogenic biosphere might be limited by the energy yield of the catabolic reaction more than by electron donor availability. This assumption might be particularly relevant in the context of chemo-litho-autotrophs such as the hydrogenotrophs described here, because the catabolic reaction yields low amounts of energy compared to most other catabolisms[62]. It thus seems important to couple cellular and population dynamics with energy yield changes using the Nernst equation (equation 4.13 ; see also ref.[74]).

Methanogens catalyze reaction (4.1) yielding the specific catabolic rate q_{cat} (s^{-1}) and use the Gibbs free energy associated with it (noted ΔG_{cat}) to fuel their metabolism. In particular, cells need to fulfill their specific maintenance requirements e_m (J mol^{-1} s^{-1}) in order to allocate energy to growth. Affholder et al. (2021)[117] model assumes cell internal steady state (between growth and division), which allows to focus on bulk biomass while ignoring cell density and bypassing the need for a specific relationship between internal biomass and division rate. Such a relationship needs to be modeled in order to derive cell density in addition of biomass concentration. Sauterey et al. (2020)[22] proposed the following expression for the division rate r (s^{-1}) as a function of internal biomass B_c:

$$
\begin{cases}
r(B_c) = \frac{1}{60 \times 60 \times 24} \frac{r_{max}}{1 + ((B_c - 2B_{struct})/B_{struct})^{-\theta}} & \text{if } B_c > 2B_{struct} \\
r(B_c) = 0 & \text{otherwise.}
\end{cases}
$$
(4.8)

where $r_{max} = 50$ d^{-1} (hence the conversion to seconds) is the theoretical maximum initial growth rate (the model hyperthermophilic methanogen *Methanococcus jannaschii* was observed diving up to

55 times a day in optimal conditions[171]), $\theta = 10$ and B_{struct} is a minimal quantity of biomolecules (in carbon moles) the cell needs to divide.

This quantity is derived from the cell's volume V (in μm^3) through[172,173]

$$B_{struct} = 1.8 \times 10^{-14} V^{0.94} \ . \tag{4.9}$$

This empirical law is a power law of cell volume (of the form aV^b) commonly used in ocean ecosystem modeling for diverse biological parameters and rates[172], and was also used in Sauterey et al. (2020)[22] for modeling the Archean Earth's biosphere. The parameters of this power law were found in Menden-Deuer and Lessard (2000)[173]. Here, we assume that cells are spheres of 1 μm radius (which is the typical scale for methanogenic Archaea[174]).

Change in the cell's internal biomass follows

$$\frac{dB_c}{dt} = (q_{ana} - r(B_c))B_c \tag{4.10}$$

where q_{ana} is the specific anabolic rate (s^{-1}), the rate at which biomolecules are produced in the cell. Assuming internal steady-state (B_c^* such that $dB_c/dt = 0$) yields

$$q_{ana} = r(B_c^*) \tag{4.11}$$

allowing the derivation of the following equation for the bulk biomass concentration $B = NB_c^*$ (mol L^{-1}, with N the cell density in L^{-1})

$$\frac{dB}{dt} = (q_{ana} - d)B \tag{4.12}$$

where $d = 0.03$ d^{-1} is a constant, density-independent death rate[117,156]. q_{ana} is computed from the catabolic energy yield $\lambda = -\Delta G_{cat}/\Delta G_{diss}$, where ΔG_{diss} is the energetic cost of building 1 mol of biomass (formally, this term is usually separated into a dissipation term and the negligible biosynthesis Gibbs free energy ΔG_{ana}[117] and

$$\Delta G_{cat} = \Delta G_{cat}^0 + RT \ln Q \tag{4.13}$$

with ΔG_{cat}^0 the standard Gibbs free energy of the catabolic reaction, $R = 8.314$ J K:per mol^{-1} the perfect gas constant, T the temperature (K) and Q the reaction quotient. For reaction (4.1), by approximating activities of chemical species with their aqueous concentrations (denoted by the square brackets), we obtain

$$Q = \frac{[CH_4]^{0.25}}{[H_2][CO_2]^{0.25}} \ . \tag{4.14}$$

q_{ana} also depends on temperature-sensitive kinetic parameters described in Affholder et al. (2021)[117] and recalled here:

$$q_{ana} = \lambda q_{cat} - q_m \qquad (4.15)$$

with q_{cat} the enzymatically-accelerated rate of the catabolic reaction (s^{-1}) and q_m the maintenance rate, $q_m = e_m/\Delta G_{diss}$ (*cf ultra*). Note that we introduce a slight change in notation compared to Affholder et al. (2021)[117] as they defined $q_m = -e_m/\Delta G_{cat}$, which is the threshold catabolic rate (the catabolic rate required to compensate maintenance loss) and not the maintenance rate *per se*. The catabolic rate couples biomass dynamics with the medium's composition:

$$\frac{dC_i}{dt} = \frac{1}{\epsilon\rho}(J_f(C_f^i - C_o^i) + J_c(C_o^i - C_i)) + Y_i q_{cat} B \qquad (4.16)$$

where C_i^o and C_i^f are the concentrations of i in the ocean and the hydrothermal fluid respectively (equation 19 in Affholder et al., 2021[117]) and Y_i the stoichiometric coefficient of molecule i in the catabolic reaction (*e.g.* $Y_{H_2} = -1$).

The biological modeling and temperature alone (equation 4.12) set the value of the steady-state value of the catabolic reaction free energy

$$\Delta G_{cat}^*(T) = -\frac{\Delta G_{diss}}{q_{cat}(T)}(d + q_m) \qquad (4.17)$$

which has its higher value (lower energy limitation) at the optimal growth temperature $T_{opt} \approx 77$ °C, $\Delta G_{cat}^*(T_{opt}) \approx -23$ kJ mol^{-1}. In other words, growth can occur only if $\Delta G_{cat}(T) \leq \Delta G_{cat}^*(T) \leq -23$ kJ mol^{-1} and at the steady-state of the microbial population, $\Delta G_{cat}(T) = \Delta G_{cat}^*(T)$. This limit value of $\Delta G_{cat}^*(T_{opt})$ is slightly lower (and thus more conservative) than estimates of the minimally required catabolic energy yield summarized in Hoehler (2004)[175], that typically stand in the -10 to -20 kJ mol^{-1} range.

Using equations (4.13,4.17) to express the value of the steady-state reaction quotient Q^* and using the procedure described in Affholder et al. (2021)[117] (equations 22 and 23), the steady-state values of bulk biomass concentration B^* and steady-state concentrations of molecules involved in the catabolic reaction C_i^* are obtained. Hence, the addition of equation (4.8), combined with equations (4.11) and (4.15) allows the derivation of the steady-state cell density $N^* = B^*/B_c^*$.

where B_c^* is obtained by solving equation (4.8) at the steady-state of the population (equation 4.12 equal to zero):

$$B_c^* = B_{struct} \left(\left(\frac{r_{max}}{d} - 1 \right)^{-\frac{1}{\theta}} + 2 \right) \qquad (4.18)$$

One might notice that with $\theta = 10$, B_c^* (and thus N^*) is weakly dependent on r_{max} (10% change when r_{max} is changed from 1 to 100). Hence, B_c^* in the first order depends of the empirically derived B_{struct}.

4.2.3. Productivity of a population of methanogens

The productivity of the system is defined as the production of biomass when the system is at steady state. By definition, the productivity at steady-state is equal to the total mortality. It is the quantity of biomass that leaves the stock of living cells per unit of time. It includes 'waste' molecules corresponding to the maintenance loss term, but also the biomass in cells that die. Here, the biomass mortality is equal to the constant death rate plus the maintenance term e_m defined in equation (4.15). Thus, combining equations (4.12) and (4.15), the specific productivity P_B (mol_C s^{-1} mol_C^{-1}) is given by

$$P_B = \left(\frac{e_m}{\Delta G_{diss}} + d \right) \ . \qquad (4.19)$$

Consequently, the productivity of the population at steady state is $P_B B^*$ integrated over the mixing layer.

4.2.4. Dead cells and waste biomass densities in the initial plume

At steady state, the population does not stop dividing, but replaces cells lost to mortality and waste (biomolecules that lost their function) through maintenance. Here, we track two quantities: the number of dead cells produced by the stationary-state population and the productivity of the system. The former is simply the number of cells (dead cells, N_d, kg^{-1}) that may leave the localized environment (hydrothermal vent surroundings). This is equivalent to assuming that these organisms live fixed in the mixing layer (without assuming a specific fixation mechanism, which could be a

biofilm, *eg* ref.[176]). Thus, the derivative of the dead cells concentration at a given location around the hydrothermal vent is

$$\frac{dN_d}{dt} = Nd - \frac{J_c}{\rho\epsilon}N_d \qquad (4.20)$$

with steady-state

$$N_d^* = \frac{\rho\epsilon}{J_c}N^*d \qquad (4.21)$$

where $\rho = 1000$ kg m^{-3} is the seawater density and $\epsilon = 1$ m is the ML thickness. In Appendix D.2, we show that the calculation of the steady-state concentration of cells that leave the mixing layer is independent from the entrainment rate at which dead cells are detached from the biofilm (as long as it is not zero). Second, the productivity defined in equation (4.19) can serve to estimate the total concentration of free-floating biomass in the ML (B_d, mol kg^{-1}) that is carried upward with buoyant water:

$$\frac{dB_d}{dt} = B^*P_B - \frac{J_c}{\rho\epsilon}B_d \qquad (4.22)$$

with steady-state

$$B_d^* = \frac{\rho\epsilon}{J_c}P_B B^* \ . \qquad (4.23)$$

Ultimately, concentrations in the initial ocean plume, are obtained by combining equations (4.7) and (4.23,4.21). Then, the ocean plume may or may not undergo further dilution, and the plume composition might differ from the ocean plume's due to outgassing and possibly bubble scrubbing or other unknown processes.

4.2.5. Prior and posterior densities

Monte-Carlo sampling of numerical simulations

Prior densities are estimated by running 20,000 simulations with parameters randomly drawn in prior densities defined in Affholder et al. (2021)[117]. As the present study focuses on the detectability of a hypothetical biosphere, only 8,763 simulations that produced habitable conditions were retained and the distribution of their outputs (cell density, total biomass, glycine concentration) is referred here to as the prior density. Therefore, this distribution corresponds to the portion of the parameter space bounded by maximum concentrations of H_2 and CH_4 obtained in serpentinization experiments[177], and maximum fluid temperature estimated in

Choblet et al. (2017)[89] that allows a population to exist, regardless of its stock biomass and productivity. The posterior density is estimated from retaining the 500 simulations that produced observables closest to Cassini observations, a standard method known as the k nearest neighbors (see details in ref[117]). The most determining factor for the goodness of fit of the biotic model to the plume composition was the abundance of methane. As a consequence, the posterior distribution corresponds to the subset of the parameter space having methanogens that produce the largest amounts of methane. Thus, the posterior distribution is also referred to as the methane-informed distribution.

We first consider the distributions of simulated cell densities in the ocean plume, corresponding to dead cells escaping the system (Section 4.2.4). Second, simulations (prior and posterior relative to H_2, CH_4) are used as prior densities with respect to the abundance of glycine. Prior and posterior samples are then used to perform a gaussian kernel density estimate implemented in Python's scipy package[105]. We limit visualizations in the observable space (cell density or glycine concentration) corresponding to the 95 % confidence interval of the model (abiotic *or* abiotic+biotic). A hypothetical measure falling outside of the interval should be interpreted as falsifying the biotic *and* abiotic models. Posterior probabilities relative to the measure of glycine concentration in the plume (using a prior informed or not by the measure of volatile abundances by Cassini) are determined using the Bayes' theorem

$$P(m|x^0) = \frac{P(x^0|m) \times P(m)}{P(x^0|m) \times P(m) + P(x^0|\bar{m}) \times P(\bar{m})} \tag{4.24}$$

where m denotes a model or hypothesis (abiotic or abiotic+biotic, respectively noted A and B) and x^0 the observation. $P(x^0|m)$ is the *likelihood* of the model and $P(m)$ is the *prior* probability of m. $\bar{m}$ denotes the complementary of m (*i.e*, theoretically *all other models*, here abiotic or biotic+abiotic accordingly).

Determination of the credible interval

In this section, we determine the interval of the glycine concentration $[Gly]$ values that are predicted by the models A (abiotic) or B (biotic) with reasonable confidence, as to exclude values that are predicted with low probability by either model from our analysis. Here, we determine the interval space of glycine concentration that

lies above a so that

$$\int_0^a P([Gly] = x|B)P(H)P(B|H)+$$

$$P([Gly] = x|A)(1 - P(H)P(B|H))dx \qquad (4.25)$$

$$- 0.025 = 0$$

and below b so that

$$\int_0^b P([Gly] = x|B)P(H)P(B|H)+$$

$$P([Gly] = x|A)(1 - P(H)P(B|H))dx \qquad (4.26)$$

$$- 0.975 = 0$$

with H denoting habitability. In practice, we estimated densities for $\log_{10}[Gly]$ so that the lower numerical integration bound is $\log_{10}[Gly] = -10$ as probabilities of $[Gly]$ being less than 10^{-10} mol kg^{-1} are essentially equal to zero in our model. Equations (4.25, 4.26) are solved numerically using the Scipy optimize package's brentq method[105].

4.2.6. Cell detection false negative rate in a sampling mission

Here, we estimate the probability that a mission sampling plume material fails to capture any cell even though a biosphere is present in Enceladus's deep ocean. We transpose modeling of the probability to observe a cell in a sample in Bedrossian et al. (2017)[167] to the probability that a sampling mission samples any cell at all. We argue that this sampling bottleneck is more relevant to estimating the limits to detecting a putative biosphere than estimating the chance that a cell is in the microscope's field of view, as samples can be concentrated[119,167]. The probability that no cell is present in the sample (negative result, denoted by $\bar{N}$) is given by

$$P(\bar{N}|\rho_b) = \left(1 - \frac{V}{V_{tot}}\right)^{\rho_b V_{tot}} \approx e^{-V\rho_b} \qquad (4.27)$$

where ρ_b is the cell density in the plume, V is the sampled volume, and V_{tot} is the total volume of the plume when the probe is sampling, thus $V_{tot} >> V$. Previous studies have estimated that a fly-by

through Enceladus's plume could realistically collect a 1×10^{-4} mL sample, we thus set $V = 1 \times 10^{-7}$ L as the unit sample volume[119]. Bedrossian et al. (2017)[167] and Porco et al. (2017)[119] propose that several samples can be retrieved (across multiple fly-bys, or by passively collecting falling plume particle on the ice surface). Increasing the sampling effort thus lowers the probability of a false negative result

$$P(\bar{N}|\rho_b, x) \approx e^{-xV\rho_b} \qquad (4.28)$$

Using the estimated probability density of dead cell density escaping the hydrothermal environment given by our biological and circulation model as ρ_b, we can estimate the overall false negative risk, given only the sampling effort

$$P(\bar{N}|x) = \int_{-\infty}^{\infty} P(N|\rho_b = z, x) \times P(\rho_b = z)dz \qquad (4.29)$$

Here, ρ_b is substituted with $N_d \times f_d$ with f_d the dilution factor between water directly above the hydrothermal vent and densities in the plume. This integral is numerically approximated using gaussian kernel approximation on simulated samples of the probability density of ρ_b.

4.3. Results and discussion

4.3.1. Estimates of the total biomass supported by hydrothermalism in Enceladus's ocean

Cell numbers estimate

We simulate biomass concentrations under various conditions in the hydrothermal environment using distributions of hydrothermal fluid composition and temperature described in Affholder et al. (2021)[117]. We also simulate biomass concentrations under the hypothesis that the methanogenic population produces the methane levels measured by the Cassini probe in the plume[64]. In other words, we estimate (i) the standing biomass in Enceladus's hydrothermal environment that is possible given a range of assumptions for the hydrothermal fluid's composition (referred to as the 'prior' estimate) and (ii) the standing biomass that yields the best fit to the plume's composition (posterior). We find that our estimate of the total number of methanogenic cells supported by Enceladus's hydrothermalism (prior: $10^{16.26\pm3.01}$; posterior: $10^{18.38\pm0.07}$)

is orders of magnitude lower than previously estimated (Figure 4.1a). Previous estimates assume either complete conversion of electron donor H_2[120,167] or that the catabolic yield is constant (that is, that the Gibbs free energy change associated with the catabolic reaction is constant) so that the number of cells at steady-state is equal to the chemical energy flux (electron donor flux times catabolic Gibbs free energy) divided by the individual maintenance energy rate[63]. We show that approaches describing the dynamic coupling between catabolic energy yield and cellular growth such as the one presented here and in Higgins and Cockell (2020)[74] lead to more conservative estimates than electron-donor limited approaches (*e.g* ref.[63]) which yield higher estimates (Figure 4.1a).
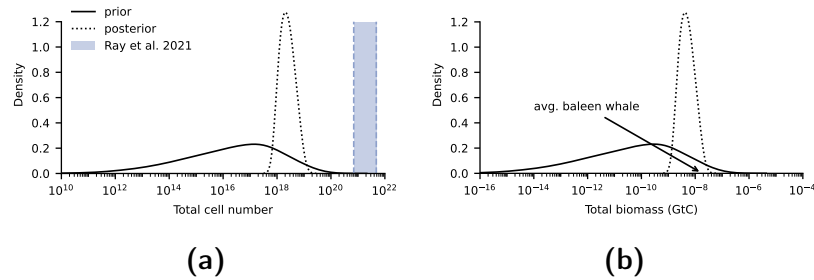

Figure 4.1. | **(a)** Standing cell and **(b)** biomass population estimates. Dark curves are probability density estimates from this study. The continuous line represents the prior estimate, ignoring information from plume abundances of CH_4 and H_2, while this information is used to refine the estimate for the dotted curve (posterior). The blue region in panel (a) represents the estimates in Ray et al. (2021)[63]. In panel (b), the biomass of a single average baleen whale is given as an illustration and is taken from Pershing et al. (2010)[178].

Standing biomass estimate

To better compare Enceladus's putative biosphere to Earth's, we estimate the standing biomass, measured in gigatons of carbon (GtC). We find that the simulated population of methanogens has a very low biomass (Figure 4.1b). In the prior case, the 95 % confidence interval (CI) is $10^{-10.43\pm3.07}$ GtC, or from negligible (less than 1 g C) to about 40 t C. In the methane-informed, or posterior case, the CI is $10^{-8.31\pm0.07}$ GtC or about 4-6 t C, about half the mass of carbon contained in one single typical baleen whale[178]. As a consequence, the methanogenic population that could be supported by a single 5 GW hydrothermal vent in Enceladus's ocean is very small in comparison to the size of Earth's ecosystems. In Appendix D.1, we show that modeling a single 5 GW vent or breaking it up in

smaller vents feeding the same ocean plume is equivalent regarding all the quantities calculated by our model.

On Earth, most methanogenic archea dwelling in hydrothermal vents are fixed *e.g* in microbial mats and free floating cells are due to entrainment by circulating fluid[176]. Conservatively, we should assume that Enceladus's putative biosphere is also fixed and that the plume in space is not directly a sample of the habitable environment. As a consequence, if one is to estimate biomass or cell concentrations in the plume, other quantities than standing biomass have to be derived and integrated to a circulation model.

4.3.2. Total productivity of a putative methanogenic biosphere

Primary production measures the amount of biomass that an ecosystem or population synthesizes per time unit (usually in petagram or gigaton of carbon per year). At steady-state, this quantity is by definition equal to the rate at which biomass escapes the considered system. In our model, the total productivity is orders of magnitude lower (2-4) than that of Earth's hydrothermal vents (mainly because of the size difference ; Figure 4.2a). Scaling with hydrothermal fluid production, the simulated specific productivity of hydrothermal fluid (the carbon mass of biomolecules that can be synthesized per kg of fluid) is close to the inference for Earth's vents (Figure 4.2 [179]). Therefore, the posterior distribution corresponds to a Earth-like hypothesis, at least for the productivity. Affholder et al. (2021)[117] only go as far as showing that there exists a subset of hydrothermal fluid composition within their prior that translates into biotic methane production matching with the observations. But, here, we go into detailing what this subset of parameters corresponds to in terms of ecosystem productivity, and show that it matches the one of Earth's hydrothermal vents ecosystems.

As detailed in the methods section, productivity is the relevant quantity to consider when estimating biomass and cells that leave the hydrothermal environment and that can be later found in the plume. Because of that, we now turn to the concentrations of (dead) cells and organics that would be found in the ocean plume if a population of Earth-like methanogens were to inhabit Enceladus putative hydrothermal vent.
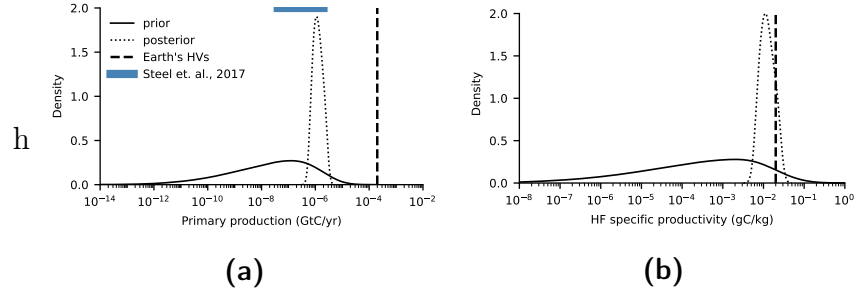
Figure 4.2. | (a) Total hydrothermal vent productivity and **(b)** hydrothermal fluid specific productivity. Dark curves are probability density estimates from this study, relying on Affholder et al. (2021)[117]. The dark continuous and dotted line have the same meaning as in the previous figure. The vertical dotted line indicates an estimate obtained from computations in McCollom (2000)[179].

4.3.3. Densities of cells in the plume predicted by the model

Others have estimated possible methanogenic cell concentrations in different parts of Enceladus's ocean using various models. For example, Steel et al. (2017)[120] and Ray et al. (2021)[63] estimate the flux of available Gibbs free energy in the hydrothermal fluid and divide it by the energy required to form or sustain 1 mol of biomass assuming total conversion of H_2. The authors then calculate the concentrations of cells in various volumes ranging from the plume to the whole ocean. Here, we rather focus on the the fraction of ecosystem productivity corresponding to (dead or entrained) cells removed from the mixing layer as the potential source for cells in the plume (Section 4.2.4). While the productivity estimated in Steel et al. (2017)[120] is in line with our estimates (Figure 4.2a), we estimate a much lower cell density in the plume (Figure 4.3), because we consider that the ocean plume is fed by fossil organic matter.

A second explanation could be that our approach to productivity is very different from the one in Steel et al. (2017)[120] as we focus on steady-state rates. Interestingly, our calculations of cell densities in the plume are not too different (our posterior estimates are even two orders of magnitude greater) from the calculations in Porco et al. (2017)[119] (Figure 4.3). Porco et al. (2017)[119] base their calculations on an estimated 1:1 scaling of surface geothermal fluxes between Enceladus and Earth and the observation of cell densities in the fluid surrounding the vent by Brazelton et al. (2006)[176] (that include but are not limited to methanogens). Because of that, we find that their approach, which is most grounded in the observa-

tion of Earth's hydrothermal ecosystems, is the most conservative point estimate yet. A key explanation for our model's prediction of greater cell densities could be that the death rate value used in our model (Section 4.2.2), which serves as a basis to derive the dead cell densities in the plume, is poorly constrained for methanogens. We used a value that fits marine plankton[156] and that may or may not be greater than the actual basal component of the death rate of methanogens that could relate to cell entrainment. Nevertheless, we hold our simulations of cell densities as plausible as they span from much below the relatively conservative calculation of Porco et al. (2017)[119] to slightly less than the optimistic value in Steel et al. (2017)[120].

While estimates of cell concentrations in Steel et al. (2017)[120] and Porco et al. (2017)[119] fall above the detection threshold value for digital holographic microscopy -an optical microorganism detection method proposed by Bedrossian et al. (2017)[167]-, we find that a non negligible portion of our prior distribution falls below this threshold (Figure 4.3). Modeling the uncertainty of Enceladus's putative hydrothermal fluid composition as prior distributions allows us to calculate not a single point estimate but a distribution of what could be possible. Doing so allows us to bound the risk of false negative: when no cells are detected despite a biosphere existing in the ocean. We thus constrain the sampling effort required to capture cells with sufficiently high confidence.

4.3.4. Sampling effort required for the capture of cells in plume material

Computing the false negative risk (the probability that an experiment gives a negative result even though the tested condition is true) is helpful as it allows us to inform instrument design as to facilitate the interpretation of negative results. Indeed, obtaining a negative result when efforts have been made to bring the false negative risk to low values can be more easily used as an argument to discard the hypothesis, here that methanogens are present in Enceladus's deep ocean. There are various sources of false negative or false positive error about the detection of a cell in a sample. For example, Archean paleontologists are confronted with the existence of abiotic organic biomorphs exhibiting microfossil-like signatures[122]. Second, cells potentially present in the plume will have undergone radical temperature, physical and chemical stress as they travel through the ice shell, experience outgassing and are
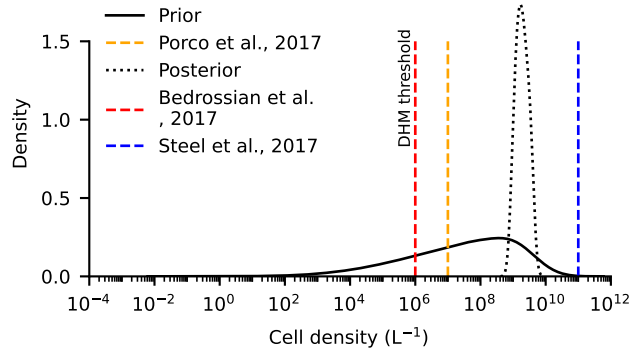
Figure 4.3. | Cell densities in the plume. The continuous and dotted black curves are respectively the prior and posterior probability density estimates of dead cells concentration in water escaping the hydrothermal environment. It is important to note that this estimate ignores possible dilution occurring during the ocean plume's ascension and bubble scrubbing at the ocean-ice interface. The orange dashed line corresponds to the estimate of plausible cell density in the plume from Porco et al. (2017)[119]. The blue dashed line represents the calculation in Steel et al. (2017)[120] ($\approx 10^{11}$ cells kg^{-1}). The red dashed line highlights the lower density threshold for detecting cells using digital holographic microscopy (DHM)[167].

exposed to the vacuum of space and ionizing radiation. The detection method proposed in Bedrossian et al. (2017)[167] relies partly on the motility of cells to effectively observe a larger volume than the one comprised in the field of view of the instrument, which may be overly optimistic considering the stresses mentioned above. The effective impact of these stresses on hypothetical cells in the plume are poorly constrained.

But even assuming that there exists a method that enables us to detect even a single cell in a sample of plume material -whether *in situ* or by the means of a sample return mission[180]-, even if it has experienced intense stress, what are the chances that a single cell or more are sampled ? Small sample sizes can result in sampling bias, altering the effective cell density in the sample relative to that in the plume. In some cases even, this sampling bias can result in no cell at all being sampled from the plume, even in the case that plume material contains cells. We are interested here in constraining the minimal sample size required to obtain at least one cell with 95% confidence or more. In other words, to bring the risk of sampling zero of the cells present in the plume under 5%.

Using equation 4.28, we compute the false negative risk as a function of sampling volume (Figure 4.4). Because processes altering the composition of the plume relative to that of the ocean plume at

the bottom of the ice shell are poorly constrained, we account for dilution up to a factor 1:1000 and for concentration enhancement by bubble scrubbing up to a factor 1000 (Figure 4.4). First, we look at two fly-by collected sample sizes studied in Porco et al. (2017)[119] (fly-by A, 0.04 m² plate at 50 km resulting in a $\approx 10^{-4}$ mL sample) and Guzman et al. (2019)[168] (fly-by B, 1 m² plate at 25 km resulting in a $\approx 10^{-3}$ mL sample). Both sample sizes result in cell detection false negative risks greater than 5% in the uninformed case (prior) unless we assume some amount of bubble scrubbing: at least a 20-fold concentration increase for sample B and by a few hundreds for sample A. To reach acceptable probabilities of sampling a cell without relying on bubble scrubbing and in the uninformed case, the volume that has to be sampled should be at least 0.1 mL, or about a hundred low fly-bys with the larger plate.

While this number may appear considerable, a comparable order of magnitude is envisioned for the Enceladus Orbilander mission concept[121]. But if a large number of fly-bys at 25 km altitude using a relatively large collector plate proves problematic to achieve in practice, other sampling methods should be considered such as passive collection of plume material falling back to the surface, as suggested in Porco et al. (2017)[119]. On the other hand, both these sample sizes would confidently sample at least one cell if we believe that most of the methane found in the plume comes from a population of methanogens (methane-informed case, or posterior). As a result, it could be considerably easier to reject this hypothesis using cell detection oriented instruments than it would be to reject the possibility of the existence of methanogens independently from methane escape rates in the plume. In sum, we find that strategies focusing on cell detection in plume samples have many obstacles that make the scientific return we can expect from them uncertain *a priori*, and that other signatures have to be considered.

4.3.5. Bayesian hypothesis selection for amino-acid detection

Here, we consider another potential biosignature that can be looked for in a sample of plume material: amino-acids abundances (also examined in Steel et al., 2017[120]; Guzman et al., 2019[168]). Amino-acids could be used as an important element for building a case for or against extraterrestrial life[181]. In ocean worlds such as Enceladus, amino-acids could come from a primordial stock depending on the core's origin material, but they are expected to be
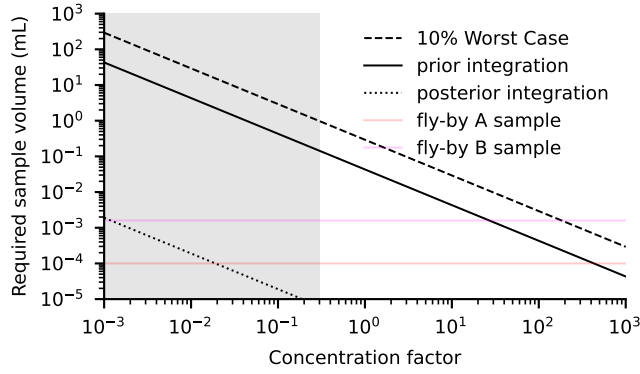
Figure 4.4. | Required sample volume to capture at least one cell with 95 % confidence. The dashed line corresponds to the required sample volume to get at least 1 cell with 95 % probability assuming a cell density equal to the mean of the 10 % simulations with the lower cell density. The continuous (resp. dotted) line represents this minimal sample volume assuming the prior (resp. posterior) integrated probability density for the dead cell density in the plume. Hydrothermal fluid to seawater ratios lower than 1:10 are greyed as they are deemed unlikely in Porco et al. (2017)[119] and Steel et al. (2017)[120]. The horizontal red line denotes sample volume collected from a 50 km fly-by through the plume on a 0.04 m^2 collector plate as estimated in Porco et al. (2017)[119]. The magenta line represents the sample size corresponding to a 25 km fly by with a 1.0 m^2 collector plate as proposed in Guzman et al. (2019)[168].

decomposed on relatively short timescales[182]. On the other hand, the decomposition kinetics are sufficiently slow so that the concentration of amino-acid is kept constant during the ocean plume's ascent that operates on a timescale of dozens of days[120,182]. Together, these arguments make the case that probing the plume for amino-acids could be of astrobiological significance. But amino-acids can also be synthesized abiotically at significant concentrations, especially in hydrothermal settings[123], and as a consequence they cannot serve as an inambiguous biosignature. However, biotic and abiotic production rates are different, and so could be the stoichiometric ratios between different amino-acids depending on their origin[120,183,184]. Therefore, a bayesian approach is suited to explore cases in which the ambiguity can be lifted, and cases in which it cannot.

We center our analysis on one of the most abundant amino-acid: glycine (Gly). Glycine serves also as a reference from which estimates of concentrations of other amino-acids can be proposed using ratios in Steel et al. (2017)[120] and Amend et al. (2013)[183]. According to Steel et al. (2017)[120], abiotic production of amino-acids in the hydrothermal vent could be $F_{aa} = 1.6-87$ g s^{-1}, of which 12% is glycine (f_{Gly}). This production rate is converted to a concentration

in the hydrothermal fluid:

$$[Gly]_{ab}^f = \frac{f_{Gly}F_{aa}}{M_{Gly} \int J_f} \qquad (4.30)$$

where $\int J_f$ is the total advection flux of hydrothermal fluid[117].

In a first approximation, we assume that the putative methanogenic micro-organisms contain the same relative abundances of amino-acids as in *Escherichia coli*. In *E. coli*, around 64 % of cell mass is made of amino-acids, 7 % of which being glycine[120,183,184]. Mass fraction is then converted into concentration using molecular mass of Gly $M_{Gly} = 75.062$ g mol^{-1} and multiplying by the simulated waste biomass B_d^* (equation 4.23). Concentrations in the plume for both abiotic and biotic+abiotic cases are then estimated using equation (4.7) and multiplying by a dilution or concentration factor if applicable. Biotic glycine is expected to be present in protein polymers that could themselves serve as biosignatures. We assume that sample treatment or retrieval methods allow (or impose) the separation of these hypothetical proteins into free amino-acids, and thus focus on the concentration in free amino-acids.

Here, we compare two scenarios, (i) abiotic synthesis of amino-acid (as parameterized in Steel et al., 2017[120]), and (ii) abiotic synthesis plus biotic production using our model (Section 4.2.3). In Figure 4.5, we report the relative confidence that glycine is biotically produced given (i) a measured concentration in the plume (assuming no dilution or bubble scrubbing) and (ii) the prior probability of the biotic production hypothesis. We find that in the uninformed case (4.5a), rejection of biotic production based only on the glycine concentration can be difficult to perform if the prior probability of biotic production is high enough. In other words, if for example, a probe were to measure a concentration [Gly] = 10^{-6} mol L^{-1}, it would preferentially indicate abiotic production unless biotic production is assumed to be likelier than $P(B) \approx 0.15$ *a priori* (or that $P(B|H) \approx 0.38$). But there are cases for which the biotic hypothesis would be rejected regardless of the prior probability : if the glycine concentration is lower than $\approx 2 \times 10^{-7}$ mol L^{-1}, then the biotic model as well as the abiotic model are rejected (the likelihood of one or the other is less than 5%). In such a case, one would conclude that if a non zero concentration is measured, the origin of glycine is likely not abiotic production in the hydrothermal setting as described in Amend et al. (2013)[183] but another unknown pathway or possibly remains of a primordial stock if Enceladus's

core is of carbonaceous chondrite or cometary origin. Nevertheless, this case would be interpreted as the biotic model being unlikely. In the so-called "methane-informed" case, when assuming that most of the plume-found methane is of biotic origin, we find that the abiotic production is favored when $[Gly] < 10^{-5}$ mol L^{-1} (see also Table 4.1), regardless of the prior probability of methanogenesis. This second hypothesis (methane in the plume is biotic) is stronger than the "prior" case (methane in the plume could or could not be of biotic origin), and thus it is expected that it is easier to reject, given that it yields narrower predictions. Because the conditions of rejection differ largely between the two cases (Table 4.1), investigation of methane sources potentially able to explain plume levels could help us in interpreting a hypothetical abundance of glycine. If a methane source concurrent to methanogenesis is identified, then our prior knowledge on a hypothetical biosphere is reduced. The interest of drawing such confidence maps (and the associated interpretation, see Table 4.1) is to help set the detection thresholds that should be aimed for in future *in situ* measurements, should a mission focus on amino-acid detection and quantification.

The confidence maps in Figure 4.5 are calculated assuming that the concentration in the plume is the same as in the ocean plume. In order to accurately determine the interpretation of a future result based on this analysis, one should correct the thresholds we propose in Table 4.1 by the estimated concentration or dilution factor between the bottom of the ice shell and the sampled plume. Three main sources of dilution or concentration could be evoked: (i) plume dilution in the ocean, (ii) organics concentration enhancement in the plume through bubble scrubbing and (iii) organics depletion in the plume due to ionizing radiation from nearby Saturn.

Our model neglects any dilution during the plume ascent and structurally assumes a 1:3 ratio of hydrothermal fluid to seawater (Section 4.2.1). This assumption is well supported by scaling laws derived for Europa's putative ocean plumes in Goodman et al. (2004)[142], later replicated for Enceladus by Choblet et al. (2017)[89], who show that the ocean plume is rotationally controlled until it reaches the ice shell. Steel et al. (2017)[120] also reported a hydrothermal fluid to seawater ratio of 1:10 in the ocean plume using 2D circulation numerical simulations.

The process of bubble scrubbing, or scavenging, is reviewed in Walls et al. (2014)[166], and the possibility of this process for Enceladus's ocean outgassing is thoroughly described in Porco et al. (2017)[119]. Moreover, Postberg et al. (2018)[116] have reported con-

centrated organic macromolecules being present in Enceladus's plume's ice grains, suggesting that bubble scrubbing occurs at the outgassing of oceanic matter to form the plume. Lastly, organics destruction by ionizing radiation in the plume is a poorly constrained phenomenon that could lower the concentration of complex organics in the plume by breaking them down in smaller molecules. Using the model of plume particles initial velocities and trajectories in Degruyter and Manga (2011)[185] (and assuming a 65° initial escape angle), we find that 1 μm radius particles reach 50 km altitude in around 4 min and bigger particles of around 10 μm radius that do not reach the 50 km line fall down to the surface in little over 30 min after having reached the 25 km altitude at around 6 min. These transport times could help defining a strategy to sample unaltered material, for example using low fly-bys or adequate timing of sampling (*e.g.*, when the plume is in the shadow).

Therefore, it is possible that the dilution assumed in Figure 4.5 and Table 4.1 is fairly conservative. Thus, we argue that a glycine-detection mission should aim for a minimal detection capability of $\approx 1 \times 10^{-7}$ mol L^{-1}. Mitić et al. (2009)[186] report on a kinetic spectrophotometry method with a theoretical detection limit just below this threshold (6.5 ng $mL^{-1} \approx 8.7 \times 10^{-8}$ mol L^{-1}). Whether this type of instrument can be used *in situ* or if a sample return is necessary is beyond the scope of this study. To conclude, while it might be hard to interpret a measure of $[Gly] > 2 \times 10^{-7}$ unless organics enhancement can be confidently constrained, reaching sufficiently high detection capability (less than 2×10^{-7}) to enable low false negative probability is possible. Hence, we argue that an amino-acid detection strategy could potentially yield significant scientific value, even if only glycine is studied. The addition of other amino-acids in the framework could dramatically increase its separation power between abiotic and biotic sources as they are characterized by different relative abundances between biotic and abiotic[120,183].

4.4. Conclusions and implications for future missions

By using a detailed model of a possible population of methanogens in Enceladus's ocean, we found that the size of this hypothetical biosphere could be very small compared to previous estimates and to the size of Earth's hydrothermal vent biosphere. Nonetheless, we found that the cell density in the plume could reach relatively

Table 4.1. | Interpretation table of Figure 4.5 in terms of hypothesis selection and rejection. Note that these results assume that concentrations in the plume are representative of concentrations in the ocean plume as they are calculated in our model. If bubble scrubbing were to increase the concentration of organics in the plume by a factor 1000, all thresholds in this table should be multiplied by this much.

Gly concentration range	biotic production (uninformed)	biotic production (methane-informed)
$> 2 \times 10^{-5}$ mol L^{-1}	favored	favored
$2 \times 10^{-7} - 2 \times 10^{-5}$ mol L^{-1}	not favored but not rejected	rejected
$< 2 \times 10^{-7}$ mol L^{-1}	rejected (with abiotic)	rejected (with abiotic)

high values (up to 10^7 cells mL^{-1}) if the biosphere is concentrated at the hydrothermal vent as we assume, instead of homogeneously distributed in the global ocean. Even if our predictions of cell density in the plume are more often than not at or above detectable levels, the case against focusing on cell detection is strong.

First, it is speculative that if cells were present in Enceladus's ocean they could retain their structure during the outgassing process or when colliding with a collector plate at high velocity. Second, cell-like abiotic structures (abiotic biomorphs) that may form in hydrothermal environments could constitute a high false positive risk. Lastly, even if we ignored the previous caveats, we found that the sample volume required to constrain the false negative risk to acceptable values could be high enough so that a very ambitious mission would have to be considered, involving either or both a lander and a long-term orbiter performing a large number of sampling fly-bys (*eg.* the Enceladus Orbilander[121]). On the other hand, we show that aiming for the quantification of hypothetical amino-acids could contribute a great deal to mount evidence for or against the hypothesis of an Earth-like methanogenic biosphere living in Enceladus's deep ocean using potentially smaller sample sizes.

Although positive evidence is hard to achieve so long as there is uncertainty in abiotic processes, glycine abundance consistent with biotic production could then be combined with analysis of its abundance relative to other amino-acids. But considering the possibility of negative evidence should not be neglected. We found that a sufficiently capable instrument (with a lower detection threshold $\approx 10^{-7}$ mol L^{-1}) could help in challenging the hypothesis of Earth-like biotic processes taking place in Enceladus's ocean. As a result of the detection of sufficiently little or no glycine, this hypothe-
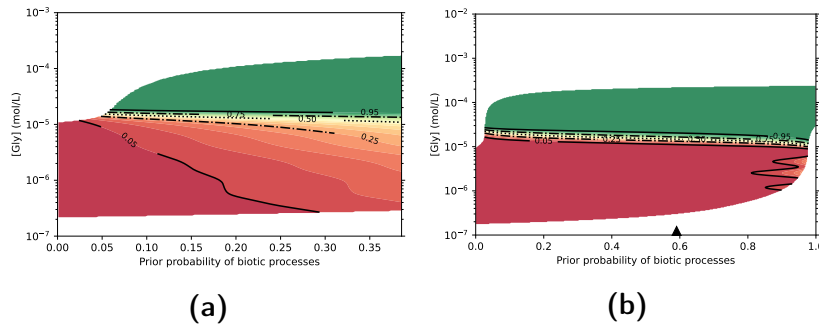
(a)   (b)

Figure 4.5. | **(a)** Map of the posterior confidence in biotic glycine production as a function of the observed glycine concentration and the prior confidence in the existence of methanogens. The map is drawn only for glycine concentration values that fall in the 95 % confidence interval of the total model (abiotic or abiotic+biotic). The prior probability of biotic processes is here bounded by the prior probability of habitability measured by the model, hence the plot stopping at ≈ 0.4. **(b)** Map of the posterior (methane-informed) confidence in biotic glycine production as a function as the observed glycine concentration and the prior confidence in the existence of methanogens using information from methane concentration in the plume. The black triangle denotes the average posterior probability of biotic methane production in Affholder et al. (2021)[117]. The prior probability of biotic amino-acid production here takes its value in the posterior space described in Affholder et al. (2021)[117], it is in the [0, 1] interval.

sis would have to change into a more complex one and be tested against a different observable.

No current evidence points towards Enceladus's ocean being uninhabitable, or even uninhabited by Earth-like life. But a mission designed to be capable of challenging this hypothesis could yield valuable science in the event of positive *or* negative results. Mission concepts currently being studied suggest that such a mission is not beyond reach in the near future.

Concluding remarks

In chapter 3, we have examined the hypotheses that Enceladus's ocean might be a suitable environment for methanogens and that a population of these might effectively present. In doing so, we demonstrated that the biological modeling developed in chapter 1 could indeed be a useful tool to assess habitability beyond the characterization of a body of liquid water; but also that being able to produce quantitative predictions under the hypothesis that a population exists is an essential step in determining the gray areas that remain in our understanding of Enceladus geochemistry and that need clarification in order to consider the presence of a methanogenic population as credible. In particular, we have shown that elucidating the abiotic mechanism that could be at the origin of the methane found in the plume should be a priority in order to challenge the possibility that a methanogenic biosphere inhabits Enceladus's hydrothermal environment.

Chapter 4 has shown that predictions under the hypothesis of a methanogenic biosphere can constitute a diverse ensemble of observables, from the abundance of volatile chemical compounds in the plumes to the presence of organic molecules or possibly cells. Even if only "indirect" markers in the plume are considered, such as abundance of organic molecules that could be produced by abiotic processes and the abundance of methane and dihydrogen, our methodology suggests that it may be fruitful to consider the existence of a biosphere as a hypothesis that may not be proven by any single "signature" but rather as a set of predictions tested individually that can together make a case for or against the hypothesis.

We have demonstrated here how quantitative ecological modeling can help in turning the hypothesis of an extant biosphere in an "operational" one, in the sense that it helps prioritizing the measure of observable quantities and constrain the observational effort to meet low risks of inconclusive evidence. We believe that this is a major challenge that astrobiology faces currently, and that progress in quantitative biology makes us uniquely positioned to address it.

This challenge goes beyond the sole case of Enceladus, as the soon operational James Webb Space Telescope (JWST) and the upcoming generation of telescopes could provide us with unprecedented insights of the atmospheric composition of terrestrial exoplanets. But the characterization of such atmospheres comes at a cost both in time and financially, which constrains the number of such atmospheres that could be characterized. It seems therefore judicious that a framework such as the one developed and used in chapters 3 and 4 is used in order to (i) prospectively analyze how can the selection of exoplanet candidates to characterize and the depth of this characterization can be optimized for scientific return and (ii) how can the habitability and biosignatures be considered in the atmospheric composition of terrestrial exoplanets in relation with their so-called planetary context, consisting in the astronomical situation of the planet (*e.g* orbital distance).

In chapters 5 and 6, we design a coupled model of atmospheric photochemistry, climate and both abiotic and biotic ocean chemistry, using the early Earth as a template. In doing so, we are able to simulate trends in the expected atmospheric composition of terrestrial exoplanets in the habitable zone, in relation with their context relative to their host star, their convection regime (whether they have plate tectonics like Earth does or not) and the presence of a methanogenic biosphere in their ocean. This allows us to lay the foundation for a proposed methodology of prospective hypothesis testing that helps define the sample size required to test these predicted trends in population of terrestrial exoplanets.

Part III.

Exoplanet population level assessment of astrobiological hypotheses

Many years ago the great British explorer George Mallory, who was to die on Mount Everest, was asked why did he want to climb it. He said, "Because it is there." Well, space is there, and we're going to climb it, and the Moon and the planets are there, and new hopes for knowledge and peace are there.

–John F. Kennedy, *Why go to the moon? The Moon speech at Rice University Stadium*, 1962
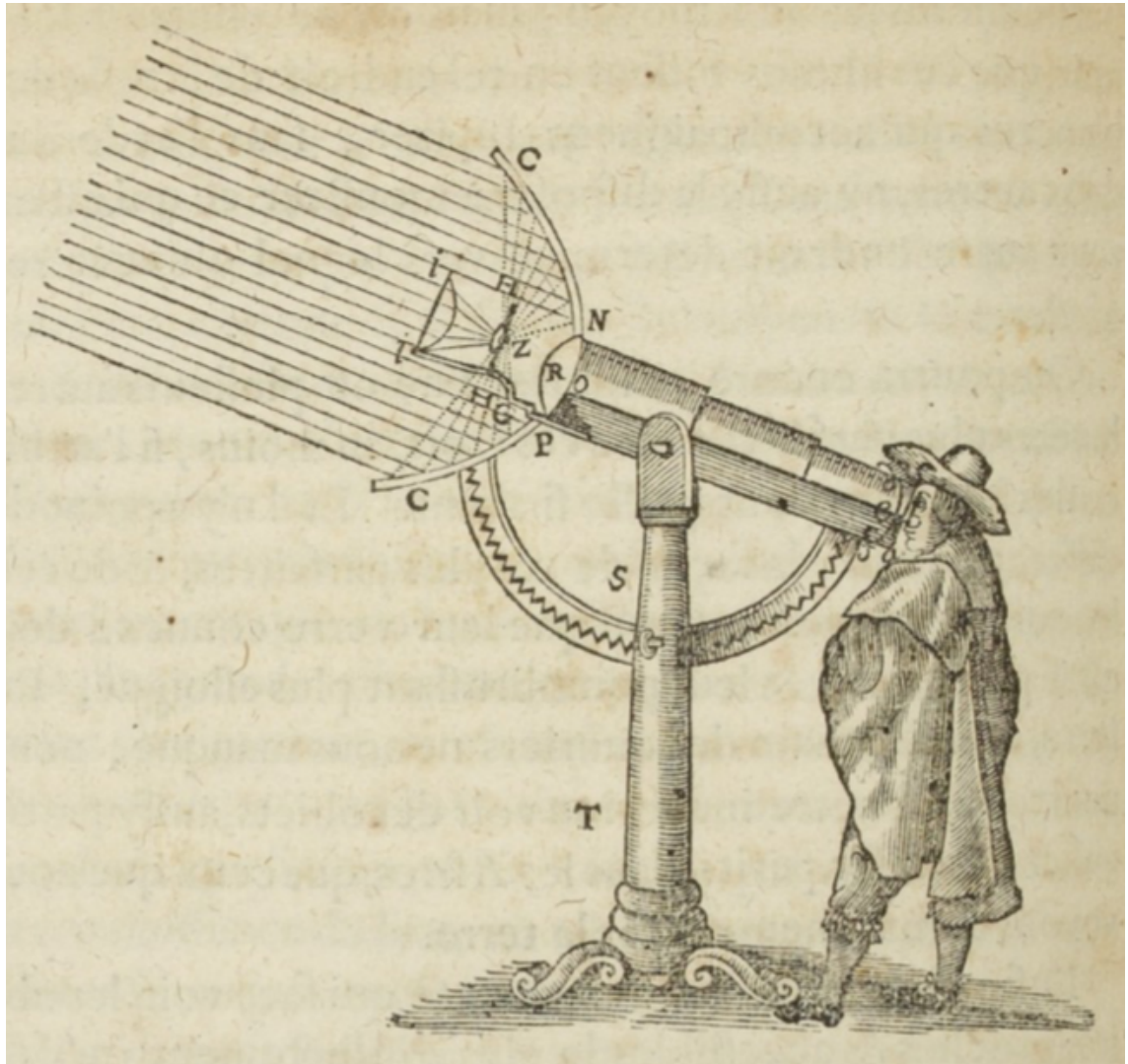
La Dioptrique, René Descartes (1637). (Source `gallica.bnf.fr` / BnF)

Introduction

I**N** part II, we have learned how the biological modeling developed in part I could be used for the inference of biosignatures and habitability, as well as for helping to constrain the design requirements of life detection missions. This was done in the context of Enceladus, a planetary object widely different from the Earth, by its size, its position relative to the Sun, its composition and its interior processes. Yet, Enceladus is only one in a vertiginous abundance of astronomical objects. More than 5000 extrasolar planets have been confirmed to date and were discovered in the past three decades. Among these planets, only around 200 have a mass and radius similar to those of the Earth [a]. Given that, one can only wonder how many of these exoplanets have surface conditions similar to Earth's and possibly a biosphere.

As the Earth is currently the only object known to harbor life, the question of the existence of extraterrestrial life resembling that of the Earth, is deeply connected to the question of the genericity or unicity of Earth in the Universe. Are the properties that have made the Earth able to sustain a biosphere for billions of years widely shared with exoplanets? If the existence of life on Earth was tied to the exact position of the Earth relative to the Sun, the history of the solar system formation, the make-up of the atmosphere and the requirement to have one moon of a certain size, then there would be no reason to believe *a priori* that there might be life anywhere near us in the Universe.

In all probability, the Earth is the only one there is, but how different from the Earth can a planet be regarding its planetary context (orbit, host star, size, etc) before it stops resembling the Earth in its propensity to have habitable conditions on its surface? In other words, how much is habitability tied to the Earth's planetary context? Additionally, would an exact replica of the early Earth follow the exact trajectory that Earth did as a sequence of different atmospheric compositions and climates, biosphere composition and prevalence? Conversely, how much the characteristics

---

a. `https://exoplanets.nasa.gov`

of the Earth and its extant and past biosphere are due to contingency? Reasonably, we see in exoplanet science and observation the potential to help provide at least some answers to these questions.

To tackle these deep questions, we need some clues of the surface conditions of the exoplanets that surround us in the Universe, and not just their respective planetary contexts. But these extrasolar worlds are separated from the Earth by unfathomable distances. Proxima-b, the exoplanet closest to us appears to have an orbit allowing liquid water on its surface[187,188] and is approximately 4 light years away. Voyager 1 travels at about 3.6 au yr^{-1} [b]. At this rate, it would take more than 70,000 years to travel to Proxima-b and take a look at its surface. It is therefore unreasonable to expect that we could measure anything more than what telescopes located on or around the Earth can observe before a long time if ever.

Currently available observation means can at best constrain the mass, radius and orbit of exoplanets as well as the characteristics of their host stars. In the case of gas giants, current telescopes are also able to constrain the composition of their atmospheres, for example by measuring how the atmosphere absorbs the light emitted by the star during transit. Unfortunately, planets with an Earth-like planetary context are much harder to characterize. In fact, we are yet to discover a single planet that orbits a Sun like star, at a distance around 1 au and that has a radius and mass comparable to the Earth's[c]. The NASA James Webb Space Telescope (JWST), currently in the final phase of its deployment at the Lagrange point L2, might be able to characterize the atmospheric composition of a few exoplanets by retrieving their absorption of the host star's light during transit. One example among others of an obstacle to the detection of an Earth like planet orbiting around a Sun-like star is that the Earth has an orbital period of about 365 days, which would make the observation of its transit between the sun and a distant observer a rare event. In addition, only a fraction of planetary systems are in the correct orientation for us to observe transits, thus reducing the number of candidates available for a transit survey. In the short term, the ideal planetary candidate for detection and atmospheric analyses is a relatively large planet orbiting very close to

---

b. as of April 2020, `https://tinyurl.com/voyager-facts`

c. Kepler 22b is probably the currently known planet that best matches all these criteria but it is more than twice as big and twice as dense as the Earth[189]

a dim host star, implying a higher transit probability. An example of such planets is represented by the Trappist system (the exoplanet Trappist-1b has an orbital period of 1.5 days), composed of 7 terrestrial planets potentially sitting in the habitable zone of a brown dwarf host star (of 0.1 solar mass) that have masses and densities close to those of the Earth[190]. The JWST might be able to characterize the atmospheric composition of a few exoplanets resembling those in the Trappist system, but most probably not of Earth-mass planets at an Earth-like orbit around Sun-like stars. It is still unknown whether these planets sitting in a very different context than the Earth have an atmosphere, or can be compared to the Earth in any relevant way (*e.g* they might be in tidally locked orbits). Only concept missions that are not projected to launch before the 2030s or 2040s like the IR/O/UV space observatory recommended by the American National Academy of Sciences[191] would have the technical capacities required to characterize the atmosphere of a few Earth-like planets[d].

The early-Earth as a template

Data that can be obtained from exoplanets are at best indirect evidence of the conditions sustained at their surface, and also potentially contain signatures of the activity of a biosphere participating in its geochemical cycles. In part I, we have argued that assessing the habitability of an environment requires the modeling of the physical and chemical processes that shape an initially lifeless hypothetical environment in which the ability for a candidate organism to grow is determined (see in particular definition 0.1 and the following remark). Furthermore, signatures of an extant biosphere ("biosignatures") are not expected to be unambiguous and the definition of such signatures is the subject of intense effort[36,45,192,193]. The presence of O_2 in the atmosphere of a planet does not seem to necessarily indicate that biotic processes are at work[194], and the existence of a biosphere is not necessarily associated with oxygenic photosynthesis as exemplified by the case of the early Earth[16,60]. The presence of methane taken alone might also not be a reliable biosignature as the history of its abundance on Earth is poorly constrained. It is now widely accepted that biosignatures need to be interpreted given the planetary context[34,45,191], and the theoretical

---

d. this mission would carry out direct observation of exoplanets and would thus not be limited by the transit probability.

work developed in this manuscript also highlights the importance of doing so as the habitability cannot be seen as a directly observable property, but one that is inferred from the context. Using the Earth and its history as a template is also seen as a necessary strategy to guide our understanding of habitability and biosignatures as the Earth is currently the only planet known to be habitable and to harbor life, as well as being the planet with the climate and geological processes best known to us[191,195].

The biological model developed in part I is designed specifically for the representation of chemo-autotrophs resembling those living currently in Earth's hydrothermal vents and those that dominated the early Earth's (3.5 billion years ago) biosphere and biogeochemical system[16,17,24] By many aspects, this early Earth was a very different planet than the one we are living on today. During the Archean, the Sun was 20 to 25% less bright than it is today[196]. Under this dimmer Sun, simple climate models predict that the Earth with the present day atmospheric composition would be entirely frozen. This problem is known as the faint young sun paradox as these calculations are in contradiction with geological evidence for liquid water during the Archean, as well as with that life has emerged (abiogenesis occurred) during this period[16] and has colonized a vast diversity of environments. Later, modeling using 3-D general circulation models (GCMs) as well as a better understanding of the composition of the early Earth's atmosphere, reconciled climate calculations on the early Earth with temperate surface conditions[197]. At the time of the Archean, the Earth's atmosphere had 300 times more carbon dioxide than it has today, and was anoxic[198]. Under this atmosphere, before the advent of oxygenic photosynthesis, despite their low biomass productivity, early microbial ecosystems might have had a significant impact on climate as they produced methane, a potent greenhouse gas[22,23]. The complexification of the early biosphere might have had destabilizing effects on the climate[22], and the advent of the oxygenic photosynthesis could have dramatically perturbed Earth's climate[24,199].

Another critical component of the long term climate is the carbonate-silicate weathering cycle which provides a negative feedback loop on the surface temperature[200]. The weathering of carbonate rich sedimentary rock or of silicated continental crust by rainwater removes carbon dioxide from the atmosphere and carries it to the ocean where the dissolved carbon dioxide can precipitate. The pre-

cipitation of carbonate in the ocean is most of the time followed by its redissolution when the sediment reaches a certain depth called the carbonate compensation depth (CCD), but a fraction of the precipitated carbonates sink in shallow areas and can undergo diagenesis (formation of sedimentary rock). Later on, metamorphism associated with subduction allows carbon dioxide to be outgassed back to the atmosphere. The weathering process is sensitive to temperature, and is thought to increase in rate when the temperature increases as it is expected to result in more abundant precipitations of rainwater, as well as to increase the rate of the weathering chemical reactions. Conversely, when temperatures are lower, the removal of atmospheric CO_2 by weathering diminishes and might stop entirely when continents are covered with ice, letting CO_2 accumulate from volcanic outgassing. Because of that, the carbonate-silicate weathering process is assumed to act as a thermostat: it removes infrared-absorbing carbon dioxide from the atmosphere when the temperature increases, thus stabilizing the climate[32,201]. The efficiency of this long-term carbon cycle seems to be tied to the existence of plate tectonics as the resupply of CO_2 to the atmosphere is ensured by subduction. This may or may not be a generic feature of terrestrial planets; Mars and Venus were probably in another convection regime called *stagnant lid* for the most part of their history[202,203]. The stagnant lid convection regime is characterized by the absence of plate motion. The existence of the weathering cycle anchors the habitability of a planet to its interior processes and its geophysical history over its long term evolution. In the next section, I review the current treatment of the concept of the habitable zone to show that it corresponds to a constraint on the conditions that can exist on a planet's surface given its context, but that it lacks the power to question what states are preferred as attractive points by the dynamical climate system.

The Habitable Zone concept

The Habitable Zone (HZ) concept refers to the range of stellar fluxes compatible with surface conditions allowing liquid water or temperate conditions to exist[33]. The rationale behind the habitable zone is that the stellar flux is set by the star mass and the orbit radius of the considered terrestrial planet. The closer to the star, or the more massive the star is, the more light-energy is received in the atmosphere and the warmer the planet is expected to be until

all liquid water evaporates. Furthermore, the evaporation of an initially liquid water stock is expected to be irreversible as water vapor fills the upper atmosphere where it is photodissociated in dioxygen and dihydrogen; the latter can then escape the planet's gravity at a significant rate. The evaporation of water also allows the surface temperature to rise dramatically as water vapor is itself an infrared absorbing gas. This event is referred to as the runaway greenhouse and may have occurred on Venus[204] [e].

The value of the stellar irradiation flux at which this runaway event is triggered, called the inner edge of the HZ or IHZ, is estimated by using an inverse radiative-convective (usually 1-D) climate model. An atmospheric composition is assumed and the numerical atmospheric model calculates the net outgoing infrared flux F_{IR}, as well as the net incident stellar flux F_S. The ratio F_{IR}/F_S denotes the radiative equilibrium or disequilibrium state of the atmosphere. If $F_{IR}/F_S > 1$, the atmosphere emits more energy than it receives and is thus cooled. Conversely, if $F_{IR}/F_S < 1$, the atmosphere accumulates energy and is thus heated. At $F_{IR}/F_S = 1$, the atmosphere is at radiative equilibrium. In a forward setting, a climate model consists in finding a vertical profile of composition and temperature in the atmosphere so that radiative equilibrium is reached. This procedure is computationally intensive, and the inner edge of the habitable zone is usually determined by using the much faster inverse procedure.

The incident stellar flux is set to the value of the incident solar flux on Earth, and the ratio F_{IR}/F_S is computed for a wide range of temperature and humidity profiles in the atmosphere. When computing the IHZ, it is assumed that the surface partial pressure of water vapor is equal to saturation, the value of which is set by temperature[204,206], and that the stratospheric water vapor pressure is equal to the top of the troposphere value[207]. Because F_S is set as the value of the incident solar flux, the estimated value of F_{IR}/F_S is equal to the value required for the normalized solar flux to sustain the assumed temperature profile, called the effective solar flux $S_{eff} = S/S_\oplus$ (where $S_\oplus = 1360$ W m^{-2} is the solar constant, the value of the present-day solar flux, and S the absolute value of the required solar flux). It is observed from simulations that when the surface temperature reaches a critical value around 340 K, the humidity of the upper atmosphere reaches a level at which the time of

---

e. It is now suggested that Venus may never have had liquid water at its surface, see Turbet et al. (2021)[205]

photodissociation and hydrogen escape approaches the age of the Earth. This limit occurs at $S_{eff} \approx 1.015$, and is called the "moist greenhouse" limit to the IHZ[208]. It is usually proposed that this limit is the relevant boundary for habitability, but at this limit, it still takes billion of years for a water inventory the size of Earth's ocean to be lost, and if one is interested in evaluating the habitability at a given time, especially on a young planet, this limit should not be considered as a hard one to habitability.

A second boundary to the IHZ corresponds to the so-called "runaway greenhouse" mentioned above. At a critical solar influx value (estimated to be $S_{eff} = 1.06$[208]), the atmosphere heats up without increasing the outgoing IR radiation until the ocean is entirely evaporated and the surface temperature reaches extremes (above the critical point of water at 647 K). This dynamical process is irreversible and sets a hard limit on habitability as it evaporates all the water, brings the surface temperature well above the maximum tolerated by organisms and is expected to occur on a much shorter time span than water loss by photodissociation and hydrogen escape. This boundary is computed following the inverse method described above, but whether dynamical surface processes, such as a ecosystem metabolism have the potential to trigger such a runaway (*e.g* by increasing the atmospheric abundance of CO_2) is unknown.

Lastly, the outer edge of the habitable zone is sensitive to the CO_2 pressures that can be reached. Currently the OHZ boundary is estimated based on the assumption that the negative feedback loop provided by the silicate-carbonate cycle allows CO_2 to accumulate until condensation. But whether the carbonate-silicate cycle allows this accumulation, or if the outgassing regime does, is poorly constrained[209,210]. Therefore, this theoretical OHZ boundary may never be reached, and the effective OHZ could be closer to the Sun. Furthermore, these estimates only take the greenhouse effect of CO_2 into account, but other gases such as H_2 and CH_4 can warm the atmosphere.

Building a coupled model

A modeling framework to represent and integrate astrobiological hypotheses, such as the stabilizing effect of the carbonate weathering negative feedback loop underpinning the concept of the habitable zone, or the existence of an Earth-like biosphere, is needed.

This modeling framework must incorporate the planetary context, for example, the climate and photochemistry in a planet's atmosphere is probably strongly influenced by the luminosity, itself determined by the orbit radius and star spectral type. A second planetary property that influences how surface processes shape the habitability of a planet is the planet's interior composition, expected to be strongly related to its mass and density and to set outgassing rates or the fraction of subaerial crust exposed to weathering [210–212].

Lehmer et al. (2020) [209] proposed a framework to couple modeling of the carbonate-silicate weathering cycle to atmospheric observables, and within which the concept of the habitable zone could be tested. But their model relies on a highly parameterized modeling of the climate, ignoring photochemistry and geochemical modeling that is not amenable to coupling with a chemostat-like biological model. Such a coupling between climate, photochemistry and an explicit ecological model was pioneered by Kharecha et al. (2005) [23], and expanded by Sauterey et al. (2020) [22] in order to study the habitability and the climate of the early Earth in the context of a methane-cycling biosphere. This publication, to which I contributed by participating in designing the model, is appended as Appendix E. In this publication, we have shown that there exist clear biosignatures of methanogenic biospheres for early-Earth like planets around Sun-like stars, such as the $CO : CH_4$ ratio (Figure 4.d in Appendix E). We have also shown that the sequence of emergence of new metabolisms could have a dramatic impact on the early-Earth climate, for example that the emergence of methanotrophy could have triggered a snowball Earth event (Figure 5 in Appendix E), suggesting that evolution can disrupt habitability. But this framework and associated results are tied to a parameterization of the early-Earth climate and a semi-coupled carbonate silicate weathering model. In this chapter, I develop a framework that fully couples ocean chemistry, including biological population following the modeling shown in part I of this thesis, as well as atmospheric photochemistry and climate for a variety of solar influx, in the case of a one Earth mass planet orbiting a Sun-like star. Doing so allows us to relate the habitable zone concept to the dynamical evolution of the surface conditions of a terrestrial planet.

In chapter 5, I build upon the model designed for the early Earth in Sauterey et al. (2020) [22] and expand its scope. Doing so is challenging, but leads to identify the critical components that need to

be improved, the parameters that have the most impact on the model outputs and that point out to important assumptions that need discussion or further grounding. Chapter 6 shows an example of a large number of simulations under the assumption of either the plate tectonics or the stagnant lid convection regimes. In particular, we see how Earth-like planets with an ocean, in one or the other of these regimes and with various initial conditions and surface of land exposed to the atmosphere and weathering converge to different steady-state composition of the atmosphere and surface temperatures. This allows to constrain how much of the HZ can actually contain Earth-like planets with temperate surface conditions.

Chapter 5.

A coupled model of exoplanet habitability: generalizing the early Earth

In this chapter, we define the specifications of a modeling framework targeted at assessing the habitability of Earth-like exoplanets and the biosignatures of the biospheres they might harbor. We then describe briefly how the modeling of the co-evolution of the early-Earth's climate with a methanogenic biosphere in Sauterey et al. (2020)[22] can serve as a starting point to this more general framework. We then propose ways to expand this model to turn it in a more general framework in which the climate and habitability (in the sense developed in part I) of Earth-like planets in a broader context can be simulated. This proposition is then implemented and compared to the reference point of the early Earth as a validation.

The starting point that must guide how such a framework is designed is the list of requirements set by the definition of habitability as the viability of a defined population in an environment. In part I, I show that in order to evaluate the habitability criterion H_i, there must be a description of the candidate environment in its dynamical interconnection with its neighboring compartments. The ocean is the natural choice as the potentially habitable environment since life on Earth was probably exclusively present in the ocean until at least 2,700 million years ago[16]. The ocean is in contact with the overlaying atmosphere, and any disequilibrium between gases in the atmosphere and their dissolved counterparts in the ocean translates into a net flux of molecules between the two compartments. To the exception of Kharecha et al. (2005)[23], models of exoplanets do not usually explicitly separate the atmosphere and the ocean as two compartments that are not in equilibrium[208,209,213]. Here, the focal

environment for habitability will be the upper ocean, exchanging molecules with the atmosphere, but that also has its own creative and destructive processes (carbonate ions flux from the continent, subaquatic volcanic outgassing, basalt dissolution, ocean mixing, etc). Kharecha et al. (2005)[23] provide a practical way of modeling the ocean/atmosphere interface in order to couple both compartments in the stagnant boundary layer model that we used in Sauterey et al. (2020)[22].

The second specification that should guide the framework structure, is that the variables we need to keep track of are the partial pressure of different relevant chemical species in the atmosphere. In Sauterey et al. (2020)[22], the model consisted in a set of ordinary differential equations (ODEs) describing the concentrations in the ocean and in the atmosphere. Models of atmospheric photochemistry and climate are computation intensive, it is therefore necessary to resort to parameterized descriptions when one is to couple the atmosphere with other compartments[22–24,214].

# 5.1. Parameterized models of the early Earth's climate and photochemistry

For the early Earth, previous authors (Kharecha et al., 2005[23] in particular) have contributed to constrain the different fluxes and thus the atmospheric composition. To do so, hypotheses can and have been made in order to reduce the complexity of the system and account only for the effect only of the abundances of H_2, CH_4 and CO_2 on the photochemistry, and of CH_4, CO_2 on the surface temperature (at a fixed solar constant representing that of the early Earth, $S/S_\oplus = 0.77$).

5.1.1. Photochemical reactions

In Kharecha et al. (2005)[23] and Sauterey et al. (2020)[22], the photochemistry is assumed to be dominated by the two net reactions

$$CO_2 + H_2 \longrightarrow CO + H_2O \tag{5.1}$$

and

$$CH_4 + CO_2 \longrightarrow 2CO + 2H_2 \tag{5.2}$$
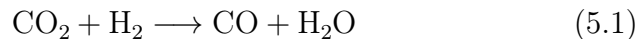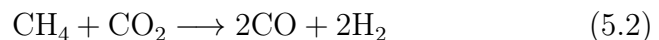
The rates of these reactions are parameterized as function of the abundances of H_2, CO_2 and CH_4 (see in Sauterey et al. (2020)[22]).
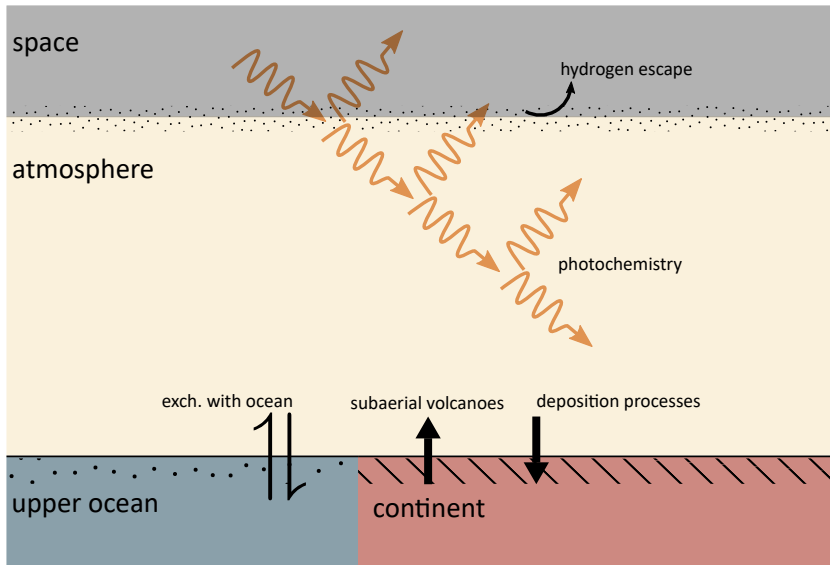
Figure 5.1. | Schematic overview of fluxes and processes governing the evolution of the atmospheric composition.

Although it involves destruction of CO_2 by photochemistry, this carbon sink in the atmosphere is often neglected (*e.g* in Krissansen-Totton and Catling, 2017[213]). Second, this parameterization is limited to a domain where these reactions effectively dominate the photochemistry in the atmosphere. The boundaries of this validity domain are not known. It could be incorrect to assume that these reactions dominate photochemistry at widely different effective solar flux. Thus, the explicit use of a 1-D model without making such assumption is warranted.

5.1.2. Hydrogen escape

Second, the H_2 escape rate to space is also parameterized in these models and assumes that the process is limited by the diffusion of hydrogen-bearing molecules to the upper atmosphere and that the upper atmosphere is dry[22,23]:

$$\Phi_{esc}(H_2) \propto f(H_2) + 2f(CH_4) \qquad (5.3)$$

where $f(X)$ is the mixing ratio of X in the lower atmosphere. The assumption that the stratosphere is dry is an important one. It allows the modeler to simplify the system and discard the calculations of the vertical profile of water vapor. This assumption might work well for a relatively cold planet such as the Earth, but might not be

consistent for planets closer to the IHZ, where a wet stratosphere is assumed[32,208]. In the case of these warmer planets, the hydrogen escape to space corresponds to an irreversible loss of the water budget over time, which is a regime that needs to be considered when generalizing the model to the whole span of the habitable zone.

In this chapter, in order to generalize this model, we adopt a different strategy than the one using parameterized fits of atmospheric photochemistry and climate computations. Using a numerical 1-D model (time and vertical axis) of atmospheric photochemistry and climate called *Atmos* and developed by the group of J. Kasting[32,208] [a], we compute the rates of change of the abundance of H_2, CO_2, CH_4 and CO in an atmosphere where the partial pressure of these gases at the base of the atmosphere is assumed constant. In doing so, we calculate the part related to photochemistry of the derivative of the partial pressures in the atmosphere:

$$\frac{d}{dt} \{pH_2, pCO_2, pCH_4, pCO\} = F(pH_2, pCO_2, pCH_4, pCO) \quad (5.4)$$

To use such calculations in modeling atmospheric evolution, a range of values for each of these partial pressures must be simulated. And because we are interested in modeling atmospheric evolution for different values of the solar flux (*ie.* at different orbits, or at different ages of the star, or for stars with slightly different masses than the Sun), we must also perform simulations for various values of insolation flux. For these reasons, a high dimensional space of variables is explored, which might contain very different regimes. For example, the rate of reaction 5.1 might not change monotically with the abundance of CO_2 in the same way for any value of the solar luminosity. Therefore, we perform a large number (thousands) of simulations using *Atmos*, covering a large range of atmospheric composition and stellar fluxes. The outputs of these simulations are then interpolated to build a numerical object amenable to the computation of the derivative represented by F in equation 5.4. The procedure and its limitations are described in greater detail in section 5.2.

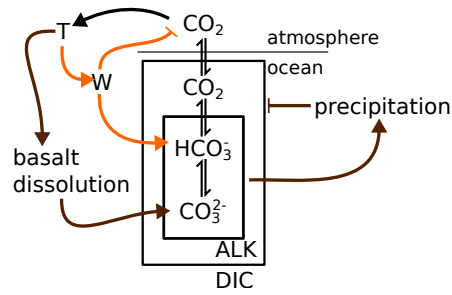a. The source code can be found at `https://github.com/VirtualPlanetaryLaboratory/atmos`

Figure 5.2. | Schematic overview of the carbonate-silicate and basalt dissolution feedback loops. Triangle-headed arrows denote positive interaction, or "promotion/removal of", and flat headed arrows denote negative interaction, or "inhibition/removal of". The orange arrows correspond to the carbonate-silicate feedback loop (exclusively) while brown arrows correspond to the basalt dissolution feedback loop. W : carbonate/silicate weathering. T : temperature. ALK : carbonate alkalinity. DIC : Dissolved Inorganic Carbon.

5.1.3. Carbon cycle

Continental weathering is a process whereby atmospheric carbon is transferred to the ocean as continental crust minerals are weathered. This weathering process requires continental crust to exist, and provides a negative feedback loop on the planet's mean surface temperature. A temperature increase provokes an increase in the weathering rate and thus an increase in the rate of removal of CO_2 from the atmosphere. Carbonate weathering removes 1 mol CO_2 from the atmosphere, for 2 mol HCO_3^- transferred in the ocean

$$CO_2 + H_2O + CaCO_3 \longrightarrow Ca^{2+} + 2HCO_3^- \qquad (5.5)$$
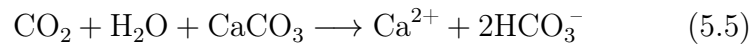
Silicate weathering removes 2 mol CO_2 from the atmosphere for every 2 mol HCO_3^- in the ocean

$$2CO_2 + H_2O + CaSiO_3 \longrightarrow Ca^{2+} + 2HCO_3^- + SiO_2 \qquad (5.6)$$
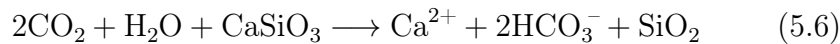
Riverine flux transports these dissolved carbonates to the ocean, where they precipitate at a pH-dependent rate P_o (mol yr^{-1}) following

$$Ca^{2+} + 2HCO_3^- \longrightarrow CO_2 + H_2O + CaCO_3 \qquad (5.7)$$
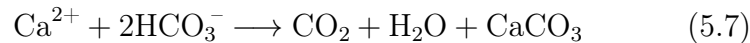
effectively removing one mole of available carbon from the ocean per reaction mole, transferring it to the crust reservoir.

There exists an additional weathering process that indirectly relates to the chemistry of carbonates in the ocean, which might also contribute to a climate stabilizing feedback loop controlling atmospheric CO_2. This process called seafloor weathering consists in the
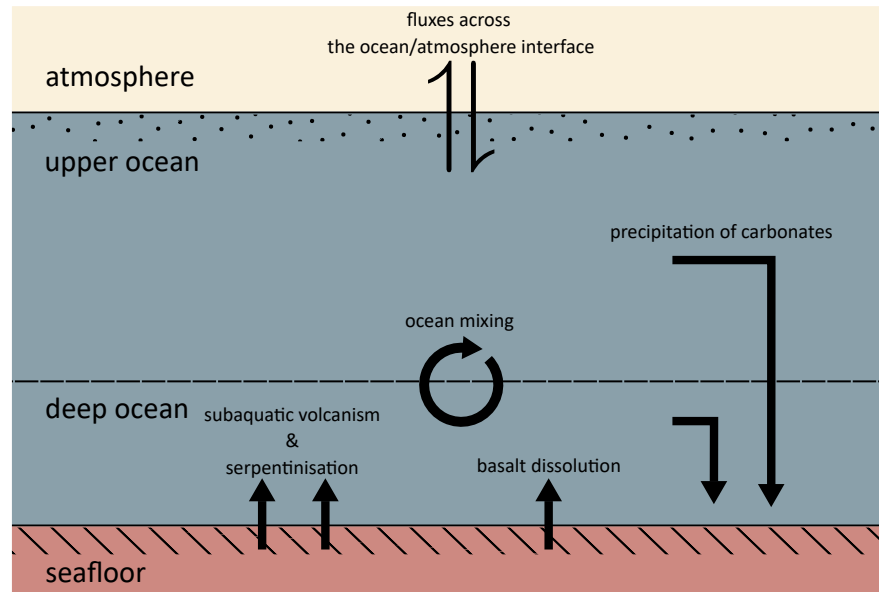
Figure 5.3. | Schematic overview of oceanic chemistry

dissolution of basalt in the deep ocean, that releases cations that are compensated by an increase of the carbonate alkalinity, which in turn promotes carbonate precipitation[213,215,216]. A schematic overview of how the weathering of continental crust and of oceanic basalt contribute to the chemistry of the carbonates in the ocean and its interplay with the surface temperature is shown in figure 5.2

Kharecha et al. (2005)[23] do not consider CO_2 explicitly in their model, stating that the weathering cycle relies on parameters that are poorly constrained for the early Earth such as the surface of sub-aerial continental crust. In Krissansen-Totton and Catling (2017)[213], the authors adopt a backwards in time approach, parameterizing the kinetics and magnitude of weathering processes so as to match their estimates for the modern Earth. They implement their model in a statistical framework that enables them to select the values of the parameters that produce simulations that best match the geological record. Their modeling of the geological carbon cycle relies on a set of differential equations describing the stock of carbon in the atmosphere-ocean reservoir and the carbonate alkalinity of the ocean, assuming that the dissolved species in the ocean are at equilibrium with their counterparts in the gaseous phase.

In Sauterey et al. (2020)[22], the same model is used to account for the negative feedback loop effect that weathering of the continental surface, as well as seafloor weathering, have on the surface temperature. The model by Krissansen-Totton and Catling (2017)[213] uses parameters that explicitly relate to geological or planetary characteristics, making it useful for coupling. The surface of subaearial continental crust, for example, might be related to the water inventory of the planet, its interior composition and convection regime. In particular, the stagnant lid regime might not allow continental crust to be produced and thus stagnant lid regime planets may not have a carbonate-silicate weathering feedback loop like the Earth does. Because the model in Krissansen-Totton and Catling (2017)[213] is a function of those parameters that have values that are poorly constrained for the early-Earth, it is particularly suited for modeling exoplanets that might differ from the Earth in their geological processes, granted that we are able to (i) relate planetary hypotheses, that might be qualitative (such as the stagnant lid convection regime) to values of these parameters in a consistent and meaningful manner or (ii) build a self consistent exhaustive framework that explicitly bridges models of planetary interior with point estimates of the values of these parameters. In chapter 6, we propose a way to explore the hypothesis of the stagnant lid regime from a surface process perspective by modifying the carbon cycle model accordingly.

Regardless of the values of the parameters in the carbon cycle model, its structure should also be modified to account for explicitly separated ocean and atmosphere reservoirs, as required by the biological model. Reaction 5.5 is usually summarized as the addition of two positive charges in the ocean, and thus an increase of two moles of carbonate alkalinity in the ocean, and the addition of one mole of carbon in the atmosphere-ocean reservoir. And following the same logic, during carbonate precipitation (reaction 5.7), one mole of carbon effectively leaves the ocean atmosphere reservoir. Later in this chapter, we describe our proposed modeling of the carbon cycle, based on Krissansen-Totton and Catling (2017)[213] where the ocean and atmosphere are two explicit compartments, so that reaction 5.5 corresponds to one mole of carbon removed from the atmosphere, and two added to the ocean. In doing so, we allow the ocean and the atmosphere to be in disequilibrium, so that the fluxes to or from the atmosphere due to biological activity can be modeled. A schematic representation of the fluxes and

compartments in the model is shown in figure 5.3.

5.1.4. Coupled ecosystem modeling

The addition of biological modeling to a model of atmospheric evolution is no small task. As we have shown in this section, doing so requires to explicitly model the ocean and the atmosphere as different compartments that are not necessarily at equilibrium and thus exchange molecules. Kharecha et al. (2005)[23] estimated the biological fluxes given estimates of other fluxes such as the H_2 flux and assuming a global steady state (the sum of all hydrogen fluxes should be zero). In their model, the net primary production of H_2-based ecosystems is constrained based on bioenergetics consideration similar to those that are described in part I. They also estimate the stationary-state concentration of H_2 in the ocean as forced by a population of hydrogenotrophic methanogens using an analytical method that partially corresponds to the one described in parts I and II, as they assume that only H_2 is not buffered by exchanges with the atmosphere and sets the steady-state for the population.

Here, we have developed a methodology that allows us to not make any prior assumption on what substrate will ultimately limit the yield of the catabolic reaction and on the buffering capacity of the atmosphere in the short term. In Sauterey et al. (2020)[22] (Appendix E), the biological model is fully explicit and enters a large system of ordinary differential equations that is solved numerically. This procedure is expansive in computation time, even if the atmospheric chemistry is parameterized. In the case where more cumbersome numerical objects are used to describe atmospheric processes, analytical work to predict the biological model's steady-state (shown in part I) are useful in that they allow to obtain the ocean steady-state in very short computation time.

Unfortunately, the derivation of the steady-state shown in chapter 1 is valid for a single species ecosystem, and it might not be possible to obtain a multi-species steady-state analytically unless additional assumptions are made. Nonetheless, in a first application of the model, it is useful that a rapid tool to evaluate habitability and biological steady-state is available as the system of dynamic variables can be reduced to the composition of the atmosphere so that a large number of simulations can be produced. The fact that
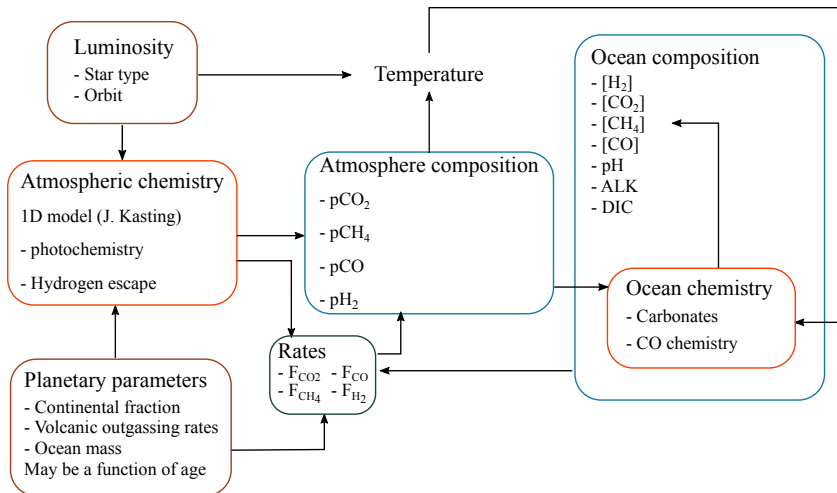
Figure 5.4. | Schematic description of the modeling framework.

the steady-state of the ocean composition is used, instead of dynamical variable that will enter the system of ODEs, implies that a separation of timescales is assumed. In practice, this amounts to assuming that the atmospheric composition is updated, then the ocean composition is updated accordingly and changes the value of the derivative of atmospheric composition.

Overall, models currently available are not readily compatible with biological modeling, as the latter requires that the model has a specific structure which is more complex. Second, these models are not easily generalized, even to the relatively limited case of Earth-like planets orbiting a Sun-like star. In the next section, we describe the procedure that we have adopted in order to provide a first step to generalized frameworks suited for biological modeling of biosignatures and habitability.

5.2. Proposed generalization

In this section, our goal is to build a system of differential equations that would encapsulate the effect of geophysical, photochemical and potentially biological processes on the habitability of an Earth-like planet, as well as on the potentially observable quantities that relate to habitability and biosignatures. We build this framework not from the ground up, but from existing models of the early-Earth's climate and habitability that need to be modified and

coupled together in order to gain both in generality and applicability to the biological modeling of habitability and biosignatures introduced in part I. In practice, we will model the atmospheric evolution of an Earth like planet with a reduced atmosphere for various relative luminosity values as well as geological features (such as the abundance of continental crust, or the rate of volcanic outgassing). In the following subsections, we will build block by block and compartment by compartment, the processes that will together form the system of differential equations describing the evolution of the atmospheric composition. In other words, we build the function F in the equation 5.4.

5.2.1. Atmospheric photochemistry and climate

We use *Atmos*, a 1-D coupled photochemistry and climate model. We run this model for various imposed boundary conditions in order to calculate the surface temperature and rates of photochemical processes as a function of the compositional state of the lower atmosphere. In doing so, the climate is calculated consistently with the vertical profile of the atmospheric composition determined by the photochemical model and vice versa. In this set-up, we compute the climate and the rate of creation and destruction of different chemical compounds in the atmosphere by fixing the relative luminosity $F_{rel} = S/S_{\oplus}$, as well as the mixing ratios of H_2, CH_4 and CO_2 in the lower atmosphere for each simulations.

In order to reduce dimensionality, we have left out CO from these calculations. The vertical profile of the mixing ratio of CO is determined by a boundary condition determined as a deposition flux $v_{dep} = 1.2 \times 10^{-4}$ cm s^{-1}, as in Kharecha et al. (2005)[23]. The adoption of a fixed flux as a boundary condition means that we assume that the geochemical processes affecting the abundance of CO in the atmosphere have a negligible effect on the rates of photochemical reactions, as in Sauterey et al. (2020)[22].

The chosen value for this deposition velocity corresponds to estimates based on the consumption of CO by organisms in the ocean, and is 4 orders of magnitude higher than abiotic estimates[23]. Because this higher value was the one used in Sauterey et al. (2020)[22] we kept it unchanged here for consistency. But Sauterey et al. (2020)[22] model an ecosystem where CO consuming microbes can exist. Here, in the first applications of the framework shown in the next chapter 6, no such organisms are simulated. In order to build
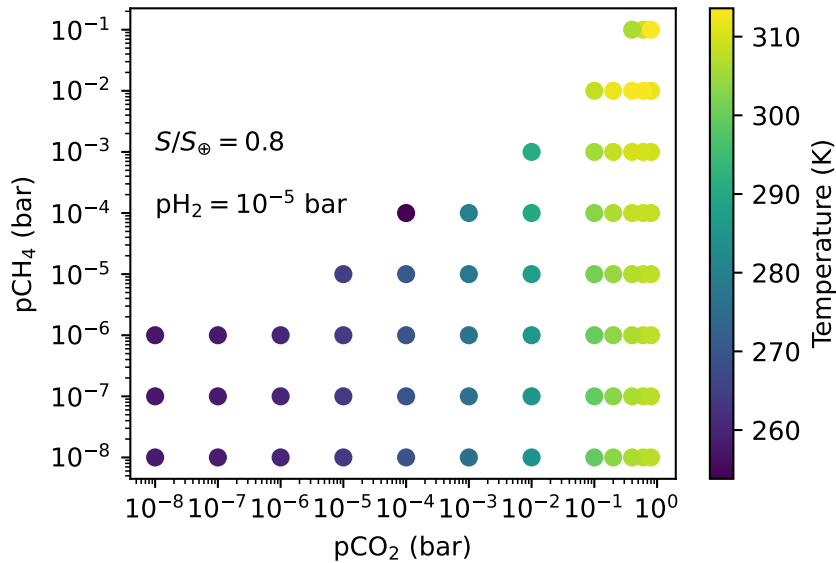
Figure 5.5. | Climate calculations in the pCO_2/pCH_4 space for $S/S_\oplus = 0.8$ and $pH_2 = 10^{-5}$ bar. The dots represent simulations made with the photochemistry/climate coupled model, and their color reflects the calculated surface temperature at radiative equilibrium/

a consistent coupled framework, the deposition flux of CO used in the coupled model has to be reconciled with the modeling of the ocean chemistry, that includes abiotic hydratation of CO but also potentially its consumption by organisms. Fortunately, the scope of the value of this deposition flux is very limited. Indeed this parameter only sets the vertical profile of CO in the photochemical calculations, and the abundance of CO in the atmosphere is expected to have a negligible effect on the rates of the photochemical reactions (as well as on the climate), as suggested by the parameterization in Sauterey et al. (2020)[22]. Later on, we will describe how the (abiotic) chemistry of CO in the ocean is modeled and serves effectively as the deposition velocity so that the evolution of the abundance of CO in the atmosphere can be simulated.

We ran 6312 simulations of the photochemistry-climate coupled model for boundary conditions in the lower atmosphere varying from 10^{-8} to 10^{-1} bars of H_2, CH_4 and from 10^{-8} to 0.8 bars for CO_2 and with a relative luminosity $S/S_\oplus$ varying from 0.4 to 1.4, corresponding to orbital distances from the Sun comprised between 0.85 and 1.58. The 4-D space (3 lower atmosphere partial pressures and relative luminosity) constituted by this grid is slightly modi-

fied in order to avoid simulating atmospheres inconsistent with the model's assumptions. The model assumes a total pressure of 1 bar in the atmosphere, completed with N_2. To avoid the $pN_2 = 0$ bar cases, we remove simulations where $pH_2 + pCH_4 + pCO_2 \geq 1$ bar.

Additionally, it is expected that organic hazes start forming when the $CH_4 : CO_2$ ratio exceeds unity[217]. These hazes might have a anti-greenhouse climatic effect that we do not simulate in our version of *Atmos* in order to save computation time. Because of that, we do not simulate atmospheres where $pCH_4 \geq pCO_2$. Furthermore, some simulations do not converge to a radiative equilibrium. The reasons for which this happens is not always obvious, but in the case of relatively high relative luminosity values and/or high partial pressures of greenhouse gases such as CO_2 or CH_4, the atmosphere could be in a runaway scenario, or simply in a state where the assumption of the radiative equilibrium in the separation of time scales hypothesis is no longer valid. A slice of this grid is visible in figure 5.5.

These simulations that have not converged (as measured by $F_{IR}/F_{SOL} \neq 1$ after 5,000 iterations, or the photochemical model reaching the maximum of 50,000 iterations) are removed from the dataset used for interpolation and simulation of atmospheric evolution. Ultimately, 4806 "successful" simulations are retained and used in the general coupled model. As shown later, some simulations of the dynamical evolution of the atmospheric composition may reach the border of the 4-D volume in which the atmosphere is modeled, in this case the simulation needs to be halted.

It is important to note here that for the whole range of our atmospheric photochemistry and climate simulations, we have assumed the same type of vertical profile of water vapor. We used the one described in the documentation of *Atmos* as "Manabe/Wetherald with constant stratospheric water" (Manabe and Wetherald, 1967[206]). It is described as flexible, but is not the most adapted for hot atmospheres (where a saturated troposhere is preferred). Because of that, we do not reproduce the same IHZ boundary as in Kopparapu et al. (2013)[208], as ours extends for higher values of relative luminosity (figure 5.6). Specifically, low pCO_2 atmospheres are able to remain temperate in our model, which implies an habitable zone that extends much closer to the Sun. And even atmospheres with a higher pCO_2 converged to radiative equilibrium at relatively low temperatures (nowhere near the temperatures predicted by a greenhouse runaway scenario), in disagreement with the current

paradigm of the runaway greenhouse IHZ[208].

On the other hand, our assumption of a 1 bar atmosphere prevents the possibility for us to model dense, CO_2 rich atmosphere that could remain temperate at relative luminosity values as low as $S/S_\oplus = 0.34$ [[208]].

Our goal here is not to reproduce the HZ results from other authors but to enable the assessment of habitability as defined in part I and inferred in part II. In doing so, our model is by definition only valid within the boundaries of the habitable zone, characterized by surface liquid water as well as the atmosphere being temperate and at radiative equilibrium. The greenhouse runaway regime corresponds to a very different regime and range of temperatures, and another modeling framework would be required to describe its dynamics. Grounding our modeling of an Earth-like planet in the regime of the habitable zone justifies that we use the water profile with constant stratospheric abundance described above rather than the saturated troposhere that has been used to determine the IHZ. This constant stratospheric water profile is empirically grounded in observation of the modern Earth's atmosphere. How valid this profile is beyond the particular case of the modern Earth is not known, and while the saturated troposphere profile is assumed to be likelier in general, this has yet to be tested by observations. Therefore, and consistently with taking the particular case of the Earth as a starting point to our generalization, we adopt this water profile in our simulations.

Within the radiative equilibrium regime, we observe that the temperatures calculated in our climate simulations are in relatively good agreement with previously published results (figure 5.7). But there seems to exist a noticeable difference between 3D and 1D models in that 1D models seem to overestimate the warming effect of low partial pressures of CO_2, and underestimate it at higher abundances. General circulation 3D models of climate are expected to constitute a reference, and the differences mentioned above are to be kept in mind when interpreting the results of our simulations relying on the *Atmos* climate model.

Both the photochemical rates and the temperature calculations are linearly interpolated using a routine available in Python's Scipy package[105]. Obtaining a suitable interpolation scheme is particularly challenging. The high-dimension nature of the posed problem, and the fact that the parameter space in which we have converged
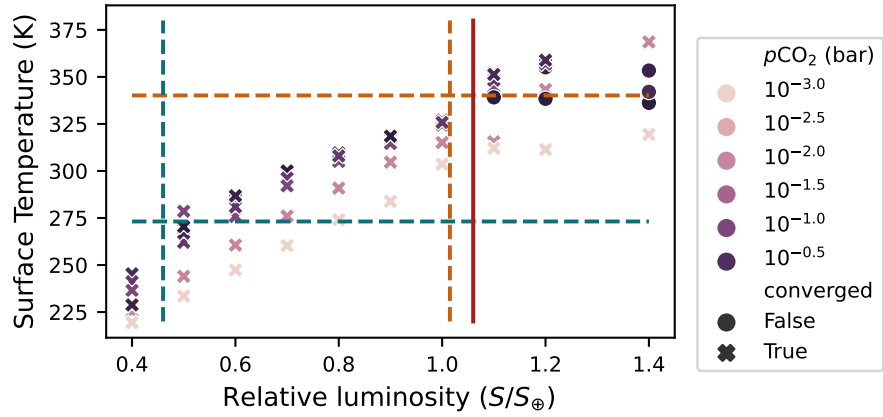
Figure 5.6. | **Comparison of habitable zone results**. The simulations are represented as crosses when they have converged and circles when they have not. In the non converged cases, the temperature retained and plotted is the one in the last recorded iteration of the climate simulation, but does not correspond to an atmosphere in radiative equilibrium. The color code of the simulations is shown in the legend and corresponds to the partial pressure of CO_2 forced constant at the bottom of the atmosphere. The blue dashed lines correspond the outer edge of the HZ. The horizontal one is set at $T = 0$°C, and the vertical one is set at the OHZ $S/S_\oplus = 0.46$ value calculated in [208] for pCO_2 =1 bar. The orange dashed lines represent the IHZ. The horizontal one is set at $T = 340$ K, as the rate of hydrogen escape at this temperature is expected to deplete the water reservoir in the timescale of billion of years, when a saturated troposphere is assumed [32,208]. The vertical one is set at the IHZ moist runaway limit $S/S_\oplus = 1.015$ estimated in Kopparapu et al. (2013) [208]. The solid red vertical one corresponds to the greenhouse runaway limit $S/S_\oplus = 1.06$ estimated in Kopparapu et al. (2013) [208]
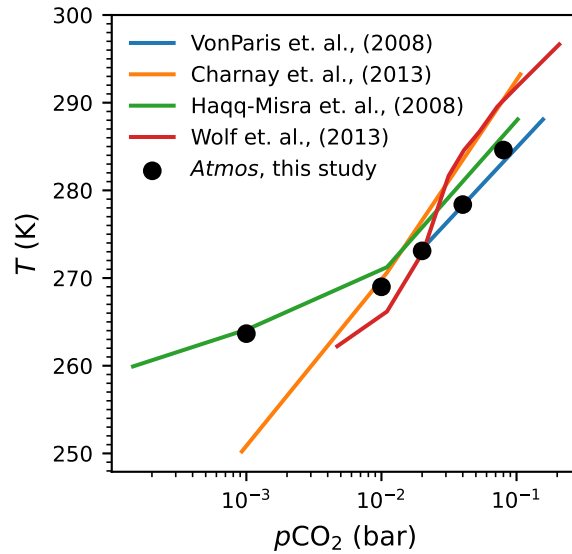
Figure 5.7. | Comparison between climate simulations from the *Atmos* model used here (black circles) and previously published simulations for an early Earth at $S/S_\oplus = 0.8$ (approximately 2.8 billion years ago)[197,218–220].

simulations is not a regular 4-D parallelogram, imposes extremely limiting constrains on interpolation. As the results of these simulations are used in a numerical solving scheme of ODEs, it is important that the interpolated photochemical rates retain some physical grounding. Some interpolation algorithm suited for ND interpolation can lead to unrealistic variations in the photochemical rates or in the surface temperature. For example, a convenient interpolation class of methods in N dimensions is called the radial basis function interpolator. This method relies on the summation of as many functions as there are data points available, each function reaching a maximum at one datapoint (for example one could sum gaussian functions centered on the data points). But this leads to the interpolated function having multiple local extrema that are purely due to the numerical method and not an actual behavior underlying the position of the data points. Because this might lead to unexpected pollution of the dynamical properties of the model, we resort to using the much simpler linear interpolator on the logarithm of the atmospheric partial pressures and the relative luminosity. One interpolation function is used to obtain the surface temperature T_s in Kelvins (as well as the planetary albedo A_p)

$$\{T_s, A_p\} = F_1(\log_{10} p\mathrm{H}_2, \log_{10} p\mathrm{CO}_2, \log_{10} p\mathrm{CH}_4, S/S_\oplus) \qquad (5.8)$$

and another one is used to obtain the photochemical fluxes (Φ_i, molecules cm^{-2} s^{-1})

$$\{\Phi_{H_2}, \Phi_{CO_2}, \Phi_{CH_4}, \Phi_{CO}\} = F_2(\log_{10} pH_2, \log_{10} pCO_2, \log_{10} pCH_4, S/S_\oplus)$$
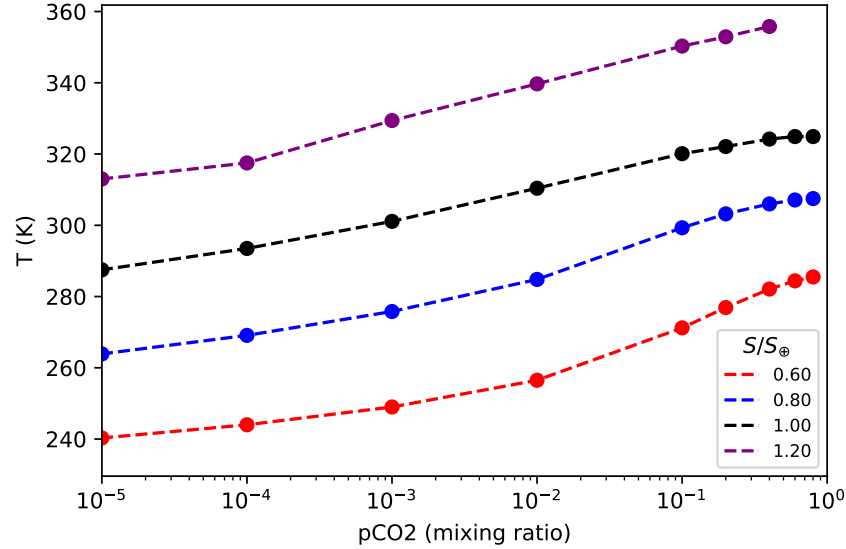(5.9)

Figure 5.8. | Outputs and interpolation of the 1-D climate model for various values of relative luminosity and as a function of CO_2 molecular mixing ratio. For these simulations, $pCH_4 = 10^{-8}$ and $pH_2 = 10^{-4}$. Circles are simulated points, and the dotted line is the ND interpolation evaluation.

Figure 5.8 shows the simulated climates for various values of pCO_2 and $S/S_\oplus$, as well as the linear interpolation. It seems that the climate does change linearly with pCO_2 for a wide range of values and that the greater density of grid points at higher pCO_2 suffices to capture the behavior of the simulations using the linear interpolation.

In the case of photochemistry, however, the linear interpolation shows some limits in its ability to nicely reproduce the behavior expected from the simulations, as seen in figure 5.9. In figure 5.9, the molecular photochemical fluxes are shown on the logarithmic scale, hence the linear interpolation seen as a convex curve between the simulated points. It may have been preferable to interpolate the log of the fluxes instead, but these fluxes can be either positive or negative. Therefore, to interpolate the $\log F_i$ instead of F_i, one must first detect where the sign change occurs. The visualization of the variation of these fluxes in only one dimension in figure 5.9
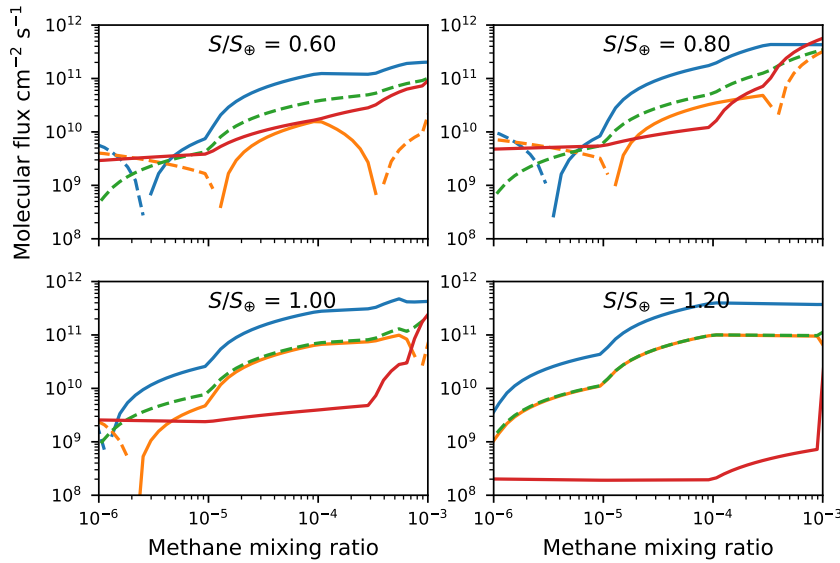
Figure 5.9. | Interpolation of molecular fluxes in the 1 bar atmosphere as calculated by the 1D photochemical model *photochem* as a function of methane mixing ratio for various solar constant values. Solid lines indicate positive flux values (production) and dashed lines indicate negative flux values (destruction or loss). The blue line corresponds to dihydrogen flux Φ_{H_2}, the orange line corresponds to the carbon dioxide flux Φ_{CO_2}, the green line corresponds to the methane flux Φ_{CH_4} and the red line corresponds to the carbon monoxide flux Φ_{CO}. Fluxes are given in molecules $cm^{-2} s^{-1}$, methane abundance is given in mixing ratio (or bar for the 1 bar atmosphere). For these computations, constant mixing ratios $pCO_2 = 10^{-3}$ and $pH_2 = 10^{-3}$ are set.

is misleading in that it suggests that doing so could be relatively straightforward, but the reader should keep in mind that the interpolation is made on a 4-dimensional space, in which detecting zeroes is not easy. Second, the variation of the photochemical fluxes is not always exponential. For instance, the parameterized rate of reaction 5.1 in Sauterey et al. (2020)[22] shows linear sensitivity to pCO_2.

This discrepancy between the interpolated function and the simulations should not excessively perturb the dynamics of the system as the general behavior (extrema and zeroes) of Φ_i should be respected by the linear interpolation. So far, we have identified one potential drawback of using a linear interpolation of the photochemical rates in the ODE system numerical integration. Linear interpolation makes the rates Φ_i non differentiable at the simulated points (as there is an angle). Therefore, the numerical calculation of the jacobian matrix of the system is expected to be difficult around these points. This particular problem would only apply for

certain numerical integration algorithms, but not for the simpler ones (such as the explicit Euler forward integrator, that does not require computing the jacobian matrix).

In figure 5.10, we compare the outputs of the photochemistry simulations (interpolated) with the parameterization of photochemical rates in the early Earth used in Sauterey et al. (2020)[22]. While the two models are in good agreement for the photochemical fluxes of H_2 and CH_4, some important differences can be observed. First, the rate of production of CO that we have simulated can be as much as five times lower than predicted by the parameterized model. This might help prevent a CO runaway when a lower deposition velocity is assumed (see the ocean chemistry of CO described below). Second, in high and low methane abundance regimes, the two models predict comparable rates of CO_2 destruction, the numerical simulations indicate a positive flux of CO_2 at intermediate values of CH_4. The photochemical production or destruction of CO_2 is ignored altogether in Sauterey et al. (2020)[22], and is not considered in the carbon cycle described in Krissansen-Totton et al. (2016)[37]. Yet, this production of carbon dioxide (most likely from the photo oxidation of methane) might play an important role in compensating the effects of a methane producing biosphere on the carbon cycle and the climate.

5.2.2. Ocean-Atmosphere coupling

For the ocean, we also write a dynamical system to describe the rate of evolution of the gas concentrations, as well as the rate at which carbonates precipitate and potentially the rates of consumption and production of solutes by a biological population.

The first rate that we describe is the rate of exchange with the atmosphere. To do so, we use of the Stagnant Boundary Layer model (SBL)[23]. This approaches assumes that the uppermost layer of the ocean is at equilibrium with the atmosphere, $[X_i] = \alpha_{X_i} pX_i$ where α_{X_i} is the Henry's law coefficient for X_i and pX_i its partial pressure in the lower atmosphere. This boundary layer is in contact with the rest of the ocean, where the concentration of X_i might be different because other processes either produce it or remove it. Because of that, there is a diffusive flux that obeys:

$$F_{oc}(X_i) = v_{X_i}(\alpha_{X_i} pX_i - [X_i]) \times C \qquad (5.10)$$
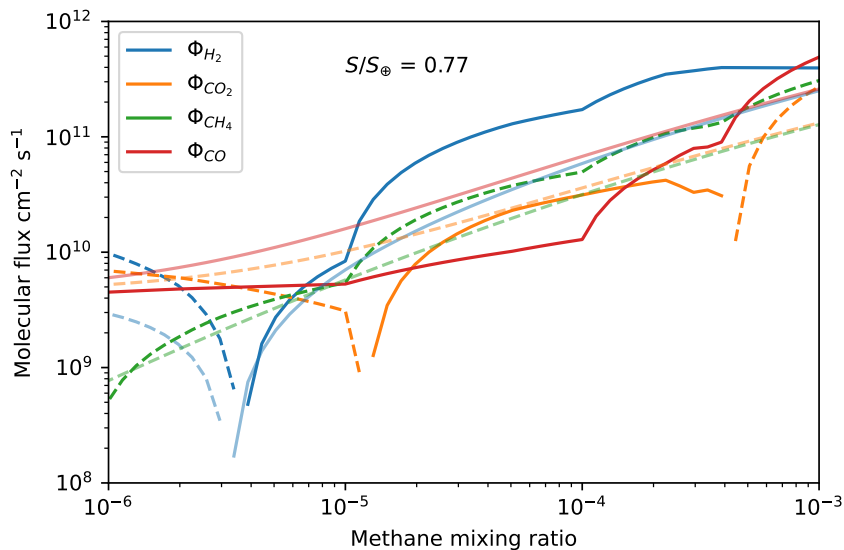
Figure 5.10. | Comparison between the photochemical fluxes in the atmosphere of the early Earth (3.8 billion years ago, $S/S_\oplus = 0.77$) as calculated by the *Atmos* model (solid colored lines) and as parameterized in Sauterey et al. (2020)[22] (soft-colored lines). **Blue**: dihydrogen flux Φ_{H_2}. **Orange**: carbon dioxide flux Φ_{CO_2}. **Green**: methane flux Φ_{CH_4}. **Red**: carbon monoxide flux Φ_{CO}. **Solid lines**: positive fluxes. **Dashed lines**: negative fluxes. Fluxes are given in molecules cm^{-2} s^{-1}, methane abundance is given in mixing ratio (or bar for the 1 bar atmosphere). For these computations, constant mixing ratios $pCO_2 = 10^{-3}$ and $pH_2 = 10^{-3}$ are set.

where F_{oc} (molecules cm^{-2} s^{-1}) is the flux of molecule X_i across the atmosphere-ocean interface (counted positive for positive flux to the ocean) for the chemical species X_i, v_{X_i} is a piston velocity across the stagnant boundary layer (cm s^{-1}, for a 40 μm thick SBL) for species X_i, α_{X_i} is the Henry coefficient for species X_i (mol L^{-1} bar^{-1}), pX_i is the gas partial pressure of species X_i (bar), $[X_i]$ is the concentration of X_i in the ocean (mol L^{-1}) and $C = \mathcal{A}/10^3$ molecules $mol^{-1}/(cm^3$ $L^{-1})$ with $\mathcal{A} = 6.02 \times 10^{23}$ the Avogadro number. The formulation above is useful to integrate the ocean positive or negative flux to the processes that have an impact on the atmospheric composition but is impractical to model dynamic processes in the ocean.

In this case, it is useful to derive a diffusion constant:

$$D_{X_i} = \frac{v_{X_i}}{z_{oc}} \ s^{-1} \qquad (5.11)$$

where z_{oc} is the depth of the ocean (in cm). The volume of the ocean is set constant in our simulations (3×10^{21} kg), but the surface is not, as it depends on the fraction of the planet that is covered with

continents. Thus, the depth of the ocean is a calculated parameter

$$z_{oc} = \frac{V_{oc}}{S_p(1 - f_{land})} \tag{5.12}$$

where $S_p = 5.1 \times 10^{18}$ cm^{-2} is the total surface of the planet, and f_{land} is the emerged land fraction (so that the ocean surface $S_{oc} = (1 - f_{land})S$.

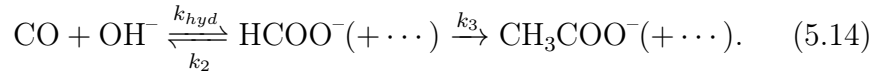In the absence of any other factor, the derivative of the concentration of X_i in the ocean would follow

$$\frac{d[X_i]}{dt} = \frac{D_{X_i}}{M_o}(\alpha_{X_i} pX_i - [X_i]) \tag{5.13}$$

where M_o is the ocean mass (so that $[X_i]$ in in mol kg^{-1}).

5.2.3. Ocean chemistry

Carbon monoxide ocean chemistry

Here we explicitly model the carbon monoxide chemistry in the ocean, following Kharecha et al. (2005)[23]. The hydration of CO into formate in the ocean's surface is the only identified abiotic process that can sink carbon monoxide that otherwise accumulates in the atmosphere where it is produced by photochemical reactions (see figure 5.9). Here, we assume a 1-layer ocean, in which CO can be hydrated into formate (HCOO$^-$) which is then converted into acetate (CH$_3$COO$^-$) by surface photochemistry and reconverted back to CH$_4$ and CO$_2$ spontaneously. The (non equilibrated) reaction gives:

$$\text{CO} + \text{OH}^- \underset{k_2}{\overset{k_{hyd}}{\rightleftharpoons}} \text{HCOO}^-(+\cdots) \xrightarrow{k_3} \text{CH}_3\text{COO}^-(+\cdots). \tag{5.14}$$

As in Kharecha et al. (2005)[23], we assume that the acetate conversion into CH$_4$ and CO$_2$ is not kinetically limiting and thus considered instantaneous. Solving this dynamic, including the atmosphere-ocean exchange of CO, for steady-state yields:

$$\begin{aligned}
[\text{CO}] &= \frac{\alpha_{\text{CO}} p\text{CO} D_{\text{CO}}(k_2+k_3)}{k_3 k_{hyd}[\text{OH}^-]+(k_2+k_3)D_{\text{CO}}} \\
[\text{HCOO}^-] &= \frac{\alpha_{\text{CO}} p\text{CO} D_{\text{CO}} k_{hyd}[\text{OH}^-]}{k_3 k_{hyd}[\text{OH}^-]+(k2+k3)D_{\text{CO}}}
\end{aligned} \tag{5.15}$$

where D_{CO} is the diffusion constant relating to the flux of CO across the atmosphere/ocean interface described in the previous subsection. [OH$^-$] is obtained from the pH value (which is a dynamic

variable described together with the carbonate chemistry below) :

$$pH + pOH = pK_e$$

with $pK_e = 14$ the ionic product of water in standard conditions. Effectively, the chemistry of CO leads to the accumulation of CH_3COO^- (acetate) in the ocean as a sink of atmospheric CO.

Carbon cycle in a coupled ocean-atmosphere model

Here, we build upon the modeling of carbonate chemistry and the carbonate-silicate weathering cycle developed by Krissansen-Totton and Catling [213]. This consists in reworking the equations presented in Krissansen-Totton and Catling [213] with small adjustments. This model, initially developed for a backwards in time going model assuming ocean-atmosphere equilibrium, was then semi-coupled in the forward, more exhaustive, model of atmosphere photochemistry, climate and ocean chemistry in Sauterey et al. (2020) [22]. In Sauterey et al. (2020) [22], carbonate chemistry in the ocean is computed off-line from the rest of the model, by also assuming ocean-atmosphere equilibrium while the rest of their model explicitly couples the atmosphere and the ocean as potentially out-of-equilibrium. This introduces some inconsistency in the model, especially when biological populations consuming CO_2 are present as their effect on the saturation state in the ocean is not directly taken into account. Explicitly modeling carbonate chemistry in the ocean allows for resolving this inconsistency.

The carbon cycle involves all the compartments described in the model: the atmosphere, surface ocean and a deep ocean. It is interesting to note at this point that the increase in model complexity introduced by the carbon cycle model is greater than the one required to include biological modeling. But doing so is necessary as the carbon cycle is expected to constitute an essential component of the climate system, and interacts with biological populations as they consume CO_2 for example. The ocean interacts with the atmosphere through dissolution of volatile gases in the stagnant boundary layer, and the surface and deep ocean are mixed at a constant rate $J = 6.8 \times 10^{16}$ kg yr^{-1}.

The chemical basis of carbonate and silicate weathering and its effect on the atmospheric greenhouse gas budget is described in

reactions 5.5 and 5.6. The overall dynamics of the carbonate system in the ocean (subscript o) and deep ocean (subscript d) follows

$$
\frac{dC_o}{dt} = \overbrace{D_{\mathrm{CO_2}}(\alpha_{\mathrm{CO_2}}p\mathrm{CO_2} - [\mathrm{CO_2}])}^{\text{atmosphere exchange}} - \overbrace{\frac{J}{M_o}(C_o - C_d)}^{\text{ocean mixing}}
$$

$$
+ \frac{S}{M_o}\big(\overbrace{f_{land}F_{cont}}^{\text{weathering}} + \overbrace{(1 - f_{land}) \times (F_{out} - P_o)}^{\text{oc. outgassing and precipitation}}\big)
$$

$$
\frac{d\mathrm{ALK}_o}{dt} = \frac{Sf_{land}}{M_o}(F_{cont} - 2P_o) - \frac{J}{M_o}(\mathrm{ALK_o} - \mathrm{ALK_d})
$$

$$
\frac{dC_d}{dt} = \frac{J}{M_d}(C_o - C_d) + (1 - f_{land})\frac{S}{M_d}(F_{out} - P_d)
$$

$$
\frac{d\mathrm{ALK}_d}{dt} = \frac{J}{M_d}(\mathrm{ALK_o} - \mathrm{ALK_d}) + 2(1 - f_{land})\frac{S}{M_d}(F_{diss} - P_d)
$$

$$
\frac{dC_d}{dt} = \frac{J}{M_d}(C_o - C_d) - (1 - f_{land})\frac{S}{M_d}P_d
$$

(5.16)

where C_o and C_d are the DIC concentrations in the upper and deep ocean respectively and likewise ALK_d and ALK_o describe the carbonate alkalinity (see below), $D_{\mathrm{CO_2}} \approx 0.25$ yr^{-1} is the diffusion constant of $\mathrm{CO_2}$ in the SBL model (computed using a piston velocity $v_{\mathrm{CO_2}} = 4.8 \times 10^{-3}$ cm s^{-1}). M_o expresses the mass of the upper ocean (see table 5.1) and $M_d = 0.01 \times M_o$ the mass of the deep ocean. $F_{cont} = 2F_{carb} + 2F_{sil}$ is the continental weathering flux (mol yr^{-1} cm^{-2}) and S the planetary surface (cm^2).

What concerns us now is to derive the rates of weathering F_{carb} and F_{sil}, as well as the rates of carbonate precipitation P_o and P_d, and the rate of alkalinity increasing basalt dissolution F_{diss}. These rates have been given parameterized equations in Krissansen-Totton and Catling (2017)[213], that use their modern values as references; we reproduce them here but express them in mol yr^{-1} cm^{-2}.

$$
F_{carb} \times S_p = \tilde{f}_{land}F_{carb}^{ME}\left(\frac{p\mathrm{CO_2}}{p\mathrm{CO_2}^{ME}}\right)^{\chi} e^{\frac{T_s - T_{ME}}{T_e}}
\tag{5.17}
$$

where $\tilde{f}_{land}$ denotes the continental fraction relative to that of the modern Earth, F_{carb}^{ME} is the value of the modern Earth carbonate weathering flux, $p\mathrm{CO_2}^{ME}$ is the modern Earth value of $p\mathrm{CO_2}$, T_{ME} the modern Earth's surface temperature, χ is the coefficient setting the dependency of weathering rate on $p\mathrm{CO_2}$, and T_e is the e-folding temperature of the weathering reaction. Following the same formalism,

$$
F_{sil} \times S_p = \tilde{f}_{land}F_{sil}^{ME}\left(\frac{p\mathrm{CO_2}}{p\mathrm{CO_2}^{ME}}\right)^{\alpha_s} e^{\frac{T_s - T_{ME}}{T_e}}
\tag{5.18}
$$

The value of these parameters are given in table 5.1.

Most of the precipitation of carbonates that corresponds to an effective removal of carbon from the system occurs above on continental shelf, above the carbonate compensation depth (CCD). In the open ocean, carbonates can sink to depth greater than the CCD, at which they are dissolved again. Krissansen-Totton and Catling (2017)[213] also propose a functional form of the pelagic precipitation rate, in which the area of the ocean that is above the CCD is parameterized. The expression of the effective precipitation rate is

$$P_o \times S_p = k_{shelf}(\Omega_o - 1)^{1.7} + k_{pelagic}\Omega_o^{2.84} \qquad (5.19)$$

where $k_{shelf} = 1.03 \times 10^{13}$ mol yr^{-1} corresponds to the reference value of above-shelf precipitation and $k_{pelagic} = 1.40 \times 10^{12}$ mol yr^{-1} is the one for pelagic precipitation[213]. The coefficients $n_1 = 1.7$ and $n_2 = 2.84$ set the sensitivity of precipitation rates to the saturation state Ω, which is detailed below.

The deep ocean also has a precipitation term:

$$P_d \times S_p = k_p(\Omega_d - 1)^{1.7} \qquad (5.20)$$

where $k_p = 5.12 \times 10^{11}$ mol yr^{-1}.

The saturation state Ω is given in compartment c (upper or deep ocean) by

$$\Omega_c = \frac{[\text{Ca}^{2+}]_c[\text{CO}_3^{2-}]_c}{K_{sol}} \qquad (5.21)$$

where K_{sol} (mol^2 kg^{-2}) is the solubility product of carbonates (Appendix F). The concentration $[\text{CO}_3^{2-}]$ is obtained from resolving the pH-dependent carbonate equilibrium. Resolving carbonate equilibrium is not trivial. We assume that carbonate equilibrium is instantaneous and we follow Krissansen-Totton and Catling (2017)[213] and Krissansen-Totton et al. (2018)[201] in tracking carbonate alkalinity (ALK) and total dissolved inorganic carbon (DIC) as dynamical quantities in order to solve the pH and consequently the carbonate

Table 5.1. | Physical and chemical constants. Parameters with parameterized expressions are detailed in Appendix F.

Parameter	Value	Description	Unit	Reference
v_{H_2}	1.3×10^{-2}	SBL piston velocity of H_2	cm s^{-1}	ref. [22]
v_{CO_2}	4.8×10^{-3}	SBL piston velocity of CO_2	cm s^{-1}	ref. [22]
v_{CH_4}	4.5×10^{-3}	SBL piston velocity of CH_4	cm s^{-1}	ref. [22]
v_{CO}	4.8×10^{-3}	SBL piston velocity of CO	cm s^{-1}	ref. [22]
α_{H_2}	7.8×10^{-4}	Henry coefficient for H_2	mol L^{-1} bar^{-1}	ref. [22]
α_{CO_2}	Appendix F	Henry coefficient for CO_2	mol L^{-1} bar^{-1}	ref. [22]
α_{CH_4}	1.4×10^{-3}	Henry coefficient for CH_4	mol L^{-1} bar^{-1}	ref. [22]
α_{CO}	1×10^{-3}	Henry coefficient for CO	mol L^{-1} bar^{-1}	ref. [22]
C	6.02×10^{20}	Unit conversion constant	L mol^{-1} cm^{-3}	
P_{tot}	1	Total atmospheric pressure	bar	assumed
S_p	5.1×10^{18}	Planetary surface	cm^{-2}	
M_{air}	28.16×10^{-3}	Air molar mass	kg mol^{-1}	ref. [22]
n_{tot}	$P_{tot}S_p \times 10^{-5}/(gM_{air})$	Total air mol	mol	
g	9.80	Earth's gravitational acceleration	m s^{-2}	
pK_w	14	Water ionic constant		
M_o	3×10^{21}	Ocean mass	kg	
M_d	$0.01 \times M_o$	Ocean mass	kg	
J	$J = 6.8 \times 10^{16}$	Ocean mixing rate	kg yr^{-1}	ref. [213]
k_{hyd}	$\exp{-\frac{10,570}{T+25.6}}$	CO hydratation rate coefficient	mol^{-1} s^{-1}	ref. [23]
k_2	6.4×10^{-5}	Rate coefficient for photodissociation of $HCOO^-$ to CO	s^{-1}	ref. [23]
k_3	2.7×10^{-6}	Rate coefficient for CH_3COO^- formation from $HCOO^-$	s^{-1}	ref. [23]
χ	0.3	CO_2 parameter for F_{carb}		ref. [213]
α_s	0.3	CO_2 parameter for F_{sil}		ref. [213]
T_e	25	weathering e-folding temperature	K	ref. [213]
T_{ME}	15	surface temperature of the modern Earth	°C	ref. [213]
F_{carb}^{ME}	10.5×10^{12}	carbonate weathering flux on modern Earth	mol yr^{-1}	ref. [213]
F_{sil}^{ME}	10.5×10^{12}	silicate weathering flux on modern Earth	mol yr^{-1}	ref. [213]
K_{sol}	Appendix F	Solubility product of carbonates	mol^2 kg^{-2}	ref. [213]
k_{ref}	Appendix F	Solubility product of carbonates	mol^2 kg^{-2}	ref. [213]
k_{shelf}	1.03×10^{13}	above shelf reference precipitation rate	mol yr^{-1}	ref. [213]
$k_{pelagic}$	1.40×10^{12}	pelagic reference precipitation rate	mol yr^{-1}	ref. [213]
k_p	5.12×10^{11}	deep ocean reference precipitation rate	mol yr^{-1}	ref. [213]
k_{diss}	3.17×10^{29}	Reference basalt dissolution rate	mol yr^{-1}	ref. [213]
pH^{ME}	8.2	Modern pH of Earth's ocean		ref. [213]
E_{bas}	92	Activation energy of basalt dissolution	kJ mol^{-1}	ref. [213]
F_{out}^{ME}	8.0×10^{12}	Present day volcanic outgassing of CO_2	mol yr^{-1}	ref. [213]
β	1	Basalt dissolution sensitivity to basalt supply		ref. [213]
γ	0.5	Basalt dissolution sensitivity to pH		ref. [213]
$Serp^{ME}$	10^{11}	Modern methane production by serpentinization	mol yr^{-1}	ref. [22]
$Volc^{ME}$	5.35×10^{12}	Modern voclanic outgassing of H_2	mol yr^{-1}	ref. [22]

equilibrium :

$$\text{DIC} = [\text{CO}_2]_{\text{aq}} + [\text{HCO}_3^-] + [\text{CO}_3^{2-}] \tag{5.22}$$

$$\text{ALK} = [\text{HCO}_3^-] + 2[\text{CO}_3^{2-}] \tag{5.23}$$

$$[\text{HCO}_3^-] = \frac{[\text{CO}_2]_{\text{aq}}\text{K}_1}{[H^+]} \tag{5.24}$$

$$[\text{CO}_3^{2-}] = \frac{[\text{HCO}_3^-]\text{K}_2}{[H^+]} \tag{5.25}$$

where K_1 is the equilibrium constant for $[\text{CO}_2]_{aq} \rightleftharpoons [\text{HCO}_3^-]$ and K_2 is the equilibrium constant for $[\text{HCO}_3^-] \rightleftharpoons [\text{CO}_3^{2-}]$. These equilibrium constants are given as functions of temperature in Appendix F.

By combining these equations, we obtain :

$$\begin{cases} \text{DIC} & = & [\text{CO}_3^{2-}]\left(\frac{[\text{H}^+]^2}{K_1 K_2} + \frac{[\text{H}^+]}{K_2} + 1\right) \\ \text{ALK} & = & [\text{CO}_3^{2-}]\left(\frac{[\text{H}^+]}{K_2} + 2\right) \end{cases} \tag{5.26}$$

ultimately yielding a quadratic equation that can be solved for $[\text{H}^+]$:

$$[\text{H}^+]^2 \frac{\text{ALK}}{K_1 K_2} + [\text{H}^+]\frac{\text{ALK} - \text{DIC}}{K_2} + \text{ALK} - 2\text{DIC} = 0 \tag{5.27}$$

As a result, $[\text{CO}_2]_{aq}$, $[\text{HCO}_3^-]$ and $[\text{CO}_3^{2-}]$ are obtained and the precipitation rate of carbonate is computed. Carbonate and silicate weathering correspond to an alkalinity flux (carbonate ions) into the ocean. This flux increases the saturation state of the ocean and promotes carbonate precipitation. This process allows carbon to enter a geological cycle ; if plate tectonics allows this carbonate deposited on the seafloor to be resurfaced as continental material, fresh weatherable material is kept available and the feedback loop continues to function.

But another process promoting carbonate precipitation exists and constitutes an additional negative feedback loop on the climate. Temperature-dependent basalt dissolution (occurring at rate F_{diss}, mol yr^{-1} cm^{-2}) in the seafloor releases calcium ions that increase carbonate alkalinity as a result of ionic balance and ultimately promotes carbonate precipitation[213,215,216]. We use the expression from Krissansen-Totton and Catling[213]:

$$F_{diss}S_p = k_{diss}\left(\frac{F_{out}}{F_{out}^{ME}}\right)^{\beta}\left(\exp{-\frac{E_{bas}}{RT_p}}\right)\left(\frac{[\text{H}^+]_p}{[\text{H}^+]_p^{ME}}\right)^{\gamma} \tag{5.28}$$

where $k_{diss} = 3.17 \times 10^{29}$ (mol yr^{-1}) is set so that the expression given here equals F_{diss}^{ME} when given modern Earth parameter values, F_{out} is the outgassing rate of CO_2 (which is a parameter of the simulations, see below) and $F_{out}^{ME} = 8.0 \times 10^{12}$ mol yr^{-1} is the present value of volcanic outgassing of CO_2.ratio between the outgassing rate of CO_2. The rate of volcanic outgassing is assumed to scale with the production of fresh basalt, which is a limiting factor the basalt dissolution rate. $E_{bas} = 92$ kJ mol^{-1} is the activation energy of basalt dissolution, T_p the temperature of pore-space water (K), $\beta = 1$ and $\gamma = 0.5$ set the sensitivity of the basalt dissolution rate to basalt supply and pH respectively. $[H^+]_p^{ME}$ is the modern value of pH in Earth's ocean $-\log_{10}[H^+]_p^{ME} = 8.2$. These parameters are recalled in table 5.1.

5.3. Volcanic outgassing

The last set of abiotic processes that interplays with the composition of the ocean and of the atmosphere are the volcanic outgassing rates, both subaerial and subaquatic, of CO_2, H_2 and CH_4. Currently our modeling does not offer a self consistent framework that includes a full explicit view of interior processes. In future efforts one should implement modeling tying together the parameters g (gravity constant), M_o (ocean mass), f_{land} (continental fraction) and F_{out}, $Volc$, $Serp$ (volcanic outgassing rates of CO_2, H_2 and serpentinization flux of CH_4 respectively). This is no small task and much is unknown about how these parameters relate to one another. But it is also the purpose of exoplanet observation to help constrain these links between the planetary geological context (expected composition of the interior, mass etc) and the geological processes that interact with surface conditions. Therefore, it would be helpful to at least structure the framework so that these rates are not "hard-coded" separately, but are handled as correlated.

Here, we remain in the case of a 1 Earth mass planet, assuming the same interior composition and processes, although we want to enable some variation on the mode of these processes. In particular, chapter 6 explores the habitability of a stagnant-lid regime Earth. These different regimes imply different volcanic activities[202]. Here, we propose a parameterization where the volcanic activity is expected to scale with the rate of volcanic outgassing of CO_2 and the other outgassing rates in the same manner. Thus, we allow the rate

of CO_2 volcanic outgassing to be set as a parameter and force the other outgassing rates to obey

$$Serp = Serp^{ME} \frac{F_{out}}{F_{out}^{ME}} \tag{5.29}$$

and

$$Volc = Volc^{ME} \frac{F_{out}}{F_{out}^{ME}} \tag{5.30}$$

where $Serp^{ME}$ and $Volc^{ME}$ are their values for the modern Earth (see table 5.1).

Additionally, the outgassing rate is expected to depend strongly on the planet age[213]. We could thus include an outgassing dependency on planet age that would follow proposed trends, *eg* Krissansen-Totton and Catling (2017)[213] for the Earth throughout its history and Dorn et al. (2018)[211] for a 1 Earth mass stagnant lid planet.

5.3.1. Solving the ocean steady-state

In the upper ocean the generic form of the differential equation governing the rate of change of concentration C_i follows

$$\begin{array}{rcl} \frac{dC_i}{dt} & = & D_i(\alpha_i P_i - C_i) + \frac{1}{M_o}\left[F_{i,geol} - J(C_i - C_{i,d})\right] \\ \frac{dC_{i,d}}{dt} & = & \frac{1}{M_d}\left[J(C_i - C_{i,d}) + F'_{i,geol}\right] \end{array} \tag{5.31}$$

where D_i is the diffusion mixing constant obtained from the stagnant boundary layer model, α_i is the Henry's law coefficient for i, P_i its partial pressure in the lower atmosphere, J the ocean mixing constant, $C_{i,d}$ the concentration of i in the deep ocean and F_{geol} in mol yr^{-1} (resp. $F'_{i,geol}$) summarizes the geological fluxes of i in the upper ocean (resp. deep ocean). For example, in the case of CO_2, $F_{i,geol}$ includes subaquatic volcanic outgassing. Together, these differential equations can be solved for steady-state assuming a constant partial pressure of i in the atmosphere (which in effect corresponds to a separation of time scales in the model) so that the abiotic steady-state of the concentration of i in the upper ocean C_i^* can be expressed as:

$$C_i^* = \alpha_i P_i + \frac{F_{i,geol} + F'_{i,geol}}{D_i M_o} \tag{5.32}$$

The set of abiotic steady-state concentrations serves to apply the habitability metric defined in part I of this thesis. And following the

procedure described in chapter 1, the steady-state concentrations forced by a biological population can be obtained. Note that this analytical procedure, which help make the simulations significantly less computation expansive, is only developed for a single species ecosystem, and that the complexification of the biosphere probably requires to simulate numerically the concentrations in the ocean.

5.3.2. Forward-in-time modeling of atmosphere evolution

As a result, for a given state of the system determined by

$$Y = \{p\mathrm{H}_2, p\mathrm{CO}_2, p\mathrm{CH}_4, p\mathrm{CO}, \mathrm{DIC}_o, \mathrm{DIC}_d, \mathrm{ALK}_o, \mathrm{ALK}_d\} \quad (5.33)$$

the fluxes across the ocean atmosphere interface can be calculated by solving the ocean steady-state as described above. The value of the ocean steady-state flux across the interface (equation 5.10) then contributes to the derivative of the atmosphere system, and equation 5.16 describes the rates of change of the carbon budget and alkalinity of the ocean and deep ocean. The generic form of the derivative of $p\mathrm{X}_i$ in the atmosphere gives

$$\frac{dp\mathrm{X_i}}{dt} = -\frac{F_{oc}(p\mathrm{X_i}, [\mathrm{X_i}]) \times (1 - f_{land})S_p}{n_{tot}} \times P_{tot} + F_{i,geol} + \Phi_{X_i} \quad (5.34)$$

where n_{tot} and P_{tot} are the total number of air moles in the atmosphere and the total atmospheric pressure, given in table 5.1. $F_{i,geol}$ represents the sum of geological subaerial fluxes such as volcanic outgassing or weathering, and Φ_{X_i} the photochemical flux given by the interpolated *Atmos* model. The surface temperature is measured as a state of the system, depending on the atmospheric composition and therefore does not appear as a dynamic variable. Therefore, Y encapsulates the system self consistently, and in effect we have assembled all the blocks to build the differential equation $\dot{Y} = F(Y)$, that we can numerically integrate over time. This is done using an implicit solver called LSODA, a Fortran solver from ODEPACK[221] wrapped in Python's Scipy package[105], based on the backwards differentiation formula with automatic stiffness detection[222]. Using this integration method was found useful as the system appears to be stiff in some occasions (some variables change at rates much greater than others).

Now that we have the means of simulating the atmospheric evolution, two strategies can be followed. One consists in simulating the
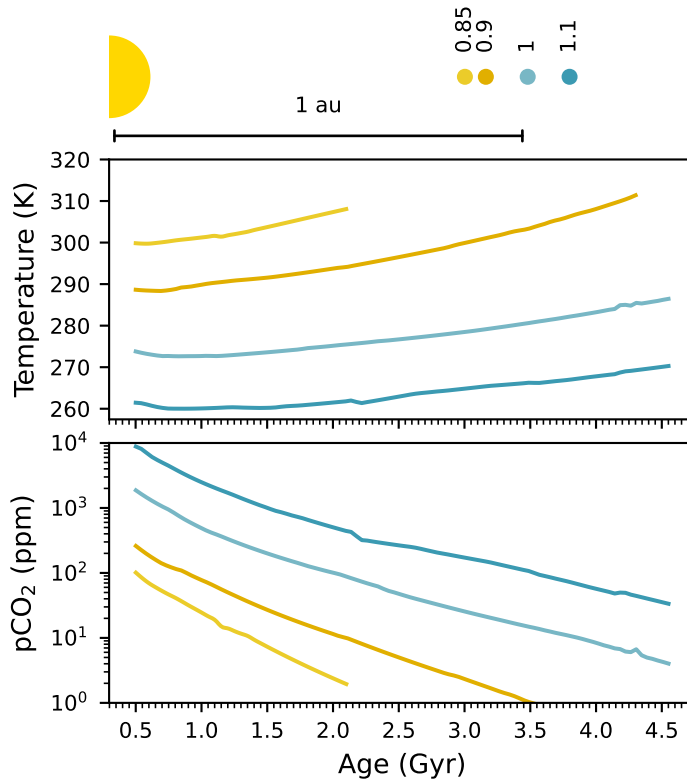
Figure 5.11. | **Long term climate simulation** of an Earth-like planet with constant $f_{land} = 0.25$, volcanic outgassing of CO_2 following the median scenario in Krissansen-Totton and Catling (2017)[213], evolution of solar luminosity is taken from Ribas (2009)[223]. The initial atmospheric composition is the same for all four simulations, $pCO_2 = 0.1$ bar, $pH_2 = 10^{-3}$ bar, $pCH_4 = 10^{-6}$ bar and $pCO = 10^{-6}$, the initial pH is set as pH $= 7$. The simulations at $d = 0.9$ and $d = 0.85$ au were halted before the end of the integration time of 4.5 Gyrs (at 2 Gyrs and 4 Gyrs respectively) because the integration algorithm required the calculation of the system's derivative outside of the interpolation domain of the atmospheric photochemistry and climate.

evolution of the atmosphere over geological times, as if we would simulate the trajectory of a planet over its geological history. If we chose to do so, then the evolution in time of geological processes (that correspond to external forcing on the system) has to be modeled. For example, this would consist in setting the geological fluxes as function of the time, $F_{i,geol}(t)$ as the outgassing rate of CO_2 changed over the course of Earth's history. Similarly, the luminosity of the Sun has increased over the past 3.8 billion years, and thus we could imagine that the photochemical and climate functions are also functions of time $\Phi_{X_i}(Y, F_{rel}(t))$.

Alternatively, one could simply set the geological fluxes and the relative luminosity for a simulation and then integrate the system of ODEs until a steady-state is reached. In numerical simulations this steady-state is reached typically after a few million years (Myr), but we simulate until 50 Myr in order to ensure that cases that are slower to converge are effectively at steady-state. This procedure can be repeated for different initial conditions and different parameter values such as the relative luminosity F_{rel}, the rate of volcanic outgassing F_{out} and fraction of emerged surface f_{land}. This enables some flexibility in the assumptions on the correlations between different parameters, such as the age of the planet and the rate of volcanic outgassing. Doing so does still allows us to perform simulations on the scale of a billion years, assuming a particular function of time for the geological forcing. This can be done by running the model using equilibrium continuation, where the steady-state of a simulation is used as the initial state of the next one; for which the geological parameters have been suitably modified. Additionally, doing so allows to better understand the effect that the different parameters have on the system compared to a simulation spanning billions of years where F_{rel} and F_{out} change together. Lastly, this allows us also to explore more diverse cases, such as older lifeless planets with weaker volcanic outgassing but still with a reduced atmosphere.

Such simulations are performed under various scenarios in the next chapter, where we also apply our criterion of habitability for a methanogenic population in the range of planetary contexts within the habitable zone.

Chapter 6.

Habitability of stagnant lid and plate tectonics Earth-sized planets

6.1. Introduction

In chapter 5, we have built a modeling framework, coupling what we believe are important geochemical processes that contribute to determine the habitability of a planet set in a certain geophysical and astronomical context. This framework is also designed so that a biological model suited to assess habitability and predict biosignatures can be used. Such a tool enables us to simulate the climate and atmospheric composition of Earth-like planets under various scenarios regarding surface processes including the presence of a hypothetical biosphere.

Among the many applications this tool could have, we choose here to focus on a limited number that are presented in this chapter. The concept of the habitable zone assumes that within its boundaries, the carbonate-silicate weathering cycle acts as a thermostat. A planet closer to its host star is expected to have less CO_2 in its atmosphere than a planet further away, as the carbon cycle is assumed to remove carbon dioxide from the atmosphere at a temperature dependent rate (see chapter 5)[32,208]. So far, this hypothesis seems to explain well Earth's geological history, as the Sun increased in luminosity during this time[213]. In a broader context, it is unknown whether the carbonate silicate cycle is effectively able to maintain temperate conditions on the complete span of the habitable zone. The observation of the atmospheric composition of terrestrial exoplanets situated in various places of the habitable zone might help test the hypothesis that the carbonate-silicate cycle

acting as a thermostat is a common occurrence.

In particular, one should first examine what observational effort would be required to test the apparently simple prediction that pCO_2 is negatively correlated with $S/S_\oplus$ (or equivalently positively correlated with the orbital distance). Lehmer et al. (2020)[209] have used a simple version of the carbonate-silicate weathering cycle model[37] to constrain the order of magnitude of the number of Earth-like planets that would need to be characterized in order to test this hypothesis. Their analysis results in the estimation that future telescopes that could be able to detect CO_2 in the atmosphere of Earth-like planets such as the Large UV/Optical/IR Surveyor (LUVOIR) concept[195], or the Habitable Exoplanet Observatory (HabEx)[224] would have to characterize more than 80 candidates in order to assess this predicted trend with sufficient confidence.

Their calculations are based on the sampling of parameters of the carbonate-silicate cycle model (such as the land fraction f_{land}, or volcanic outgassing rate F_{out}) in uniform law that represent the uncertainties on their values inferred in Krissansen-Totton et al. (2018)[201]. Their model leaves out processes that might be of importance, such as photochemistry, but also ignores age as an explicit variable. The planetary age variable is present in their analysis in that it serves to justify the basis for the the range of the uniform distribution in which the parameters are sampled. As time passed on Earth, the outgassing rate has gradually decreased which interplayed with the continental weathering cycle to explain the reduction in atmospheric CO_2 between 3.8 Gyr ago and today, as the solar luminosity increased. While their assumption of sampling parameters in uniform distribution might be conservative in that it does not assume any particular scenario of outgassing rate evolution and weathering regime, it might be interesting to constrain how information on the age of exoplanets could reduce the number of required candidates to test for the existence of a trend in pCO_2.

Lastly, in the pioneering work in Lehmer et al. (2020)[209], the calculation of the required number of candidates to test for the existence of a trend is based on the null hypothesis that pCO_2 is log-uniformly distributed. More precisely, they calculate the minimum number of candidates sampled in their assumed distribution in the plane $\{pCO_2, S/S_\oplus\}$ so that the probability that the obtained samples match a log-uniform distribution falls below a conservative

threshold. In fact, what they do is even more complex as they assume that the null hypothesis of a log-uniform distribution of $p\mathrm{CO_2}$ is restricted to the fraction of this distribution that yields temperature in the liquid water range of 248-355 K in their model. Because of the correlation between temperature and both $p\mathrm{CO_2}$ and $S/S_\oplus$, this constrain results in a forced trend in $p\mathrm{CO_2}$ versus $S/S_\oplus$ in the null hypothesis.

We argue here that this methodology can be taken a step further. Indeed, Lehmer et al. (2020) [209] do not test the concept of the habitable zone as a range of $S/S_\oplus$ in which the carbonate-silicate weathering cycle ensures temperate conditions. Rather they test the hypothesis that it does *instead* of some other unconstrained process that would also ensure temperate conditions. This is an important clarification as their methodology assumes that there must be a $p\mathrm{CO_2}$ thermostat which is not the carbonate silicate cycle. It would be more useful that the null hypothesis be defined mechanistically so that the hypothesis that the carbon cycle enables planets to be temperate within the HZ could be tested.

A good starting point would be to simply simulate what would be the distribution of exoplanets in the $p\mathrm{CO_2}$, $S/S_\oplus$ space if there was no carbonate-silicate cycle at all. Conveniently, there exists another good reason to simulate such cases. The other terrestrial planets in the solar system do not seem to have been in a plate tectonics convection regime for most of their existence [202,225]. Given that, it seems unlikely that a planet in the concurrent regime, called the stagnant lid convection regime, would have carbonate-silicate weathering as this process relies on the constant supply of continental crust, which is not expected to be produced unless plate subduction occurs. It is therefore legitimate to raise the question of whether most terrestrial planets have a carbonate-silicate weathering feedback loop on surface temperature.

One should, however bear in mind that there is a known process other than carbonate-silicate weathering that regulates $p\mathrm{CO_2}$ and surface temperature, which is the dissolution of basalt at the seafloor, as mentioned in chapter 5. This process is expected to exist on stagnant-lid planets, and it has been shown that it could regulate surface temperature on stagnant-lid planets in a way that maintains liquid water on their surface within the bounds of the habitable zone [210].

Therefore, it seems more fruitful to contrast the scenarios of the stagnant-lid regime and the of plate tectonics regime. In doing so, we compare the hypothesis of the existence of both seafloor dissolution and the carbonate-silicate weathering cycle as thermostats to the one where only seafloor dissolution acts as a weaker thermostat. How do these scenario compare regarding the existence of temperate conditions in the habitable zone, and how these conditions can subsist over the geological timescale? Do these two scenarios predict distinguishable trends of $p\mathrm{CO}_2$ versus $S/S_\oplus$, and how can the hypothesis of terrestrial planets being in general in the plate tectonics (resp. stagnant lid) regime can be assessed?

In this chapter, we use the modeling framework developed in chapter 5 in order to perform simulations of exoplanets in the habitable zone under the two convection regimes. In a first step, we do not assume any model of outgassing rate as a function of planet age, and thus the comparison between the two scenarios corresponds to the comparison of planets on which the carbonate-silicate weathering cycle exists together with seafloor weathering with planets where only seafloor weathering exists. In a second step, we introduce the age variable as a parameter of the model, and explicitly assume scenarios of the evolution of F_{out} through time under both convective regimes. In doing so, we examine whether information on the age of exoplanets could be used in combination with $p\mathrm{CO}_2$, $S/S_\oplus$ data to test for the existence of trends in this now 3D space ($p\mathrm{CO}_2$, $S/S_\oplus$ and τ).

This chapter is emphasizes the simulation of geophysical processes even though the framework is built to allow the simulation of a hypothetical biosphere and is motivated by the assessment of biosignatures. Doing so requires some additional developments, such as the choice of parameters describing the biological rates, potentially from the empirical distribution produced in chapter 2. For the most part, this remains to be done, yet in this chapter, we present a set of "proof of concept" simulations, for which *ad-hoc* values of parameters were used in order to demonstrate the framework capability.
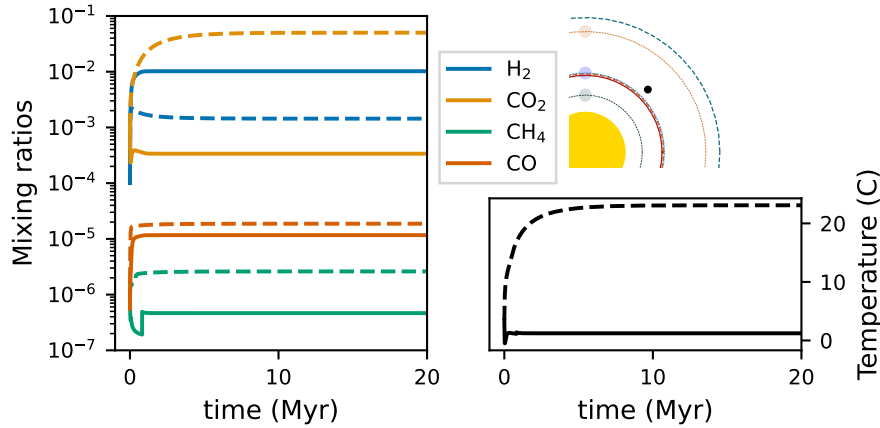
Figure 6.1. | Short-term trajectory of atmospheric composition. Simulation of the numerical model for a planet in the HZ, at $S/S_\oplus = 0.8$, with $f_{land} = 0.25$ and $F_{out} = 8.0 \times 10^{12}$ mol yr^{-1}, the value on the modern Earth. The solid lines (resp. dashed lines) in the left and bottom right panels represent the trajectory for a planet with continental weathering (resp. without continental weathering). **Left** panel shows the evolution over time of the atmospheric composition, measured in mixing ratios in the 1 bar atmosphere. **Bottom-right** panel shows the evolution over time of the surface temperature (in Celsius). **Top-right** panel situates the simulated planet (black dot) within the habitable zone and in the context of the solar system. The red dashed and solid lines delineate the IHZ (moist runaway and greenhouse runaway respectively). The blue dashed line represents the OHZ. The orbits of Venus, Earth and Mars are represented.

6.2. Simulations of exoplanets in the habitable zone

Here, we simulate the evolution of the atmospheric composition of terrestrial exoplanets in the habitable zone under various conditions of insolation, subaerial land fraction and outgassing rates. For each simulation, we integrate the system of ODEs defined in chapter 5 until a steady-state is reached. Examination of simulations, such as those shown in figure 6.1 show that at 20 Myr, simulations should have reached approximate steady-state. Conservatively, we run simulations over 50 Myr.

6.2.1. Initialization

For a simulation, the initial state and the parameter values are sampled in distributions given in table 6.1. Later in this chapter, we also perform simulations where we assume a relation between the age and the rate of volcanic outgassing. In this case, the age variable (τ) is used to internally calculate the outgassing rate as described in

Table 6.1. | Planetary parameters and initial values of time-dependent variables and their distributions

parameter	meaning	distribution	range	unit
pH_2^0	initial pH_2	Log-Uniform	$10^{-5} - 10^{-2}$	bar
pCO_2^0	initial pCO_2	Log-Uniform	$10^{-4} - 0.5$	bar
pCH_4^0	initial pCH_4	Log-Uniform	$10^{-6} - 10^{-4}$	bar
pCO^0	initial pCO	Log-Uniform	$10^{-6} - 10^{-4}$	bar
pH^0	initial pH	Uniform	6.5-7.5	
f_{land}	continental fraction	Uniform	0.0-0.35	
F_{out}	CO_2 outgassing rate	Log-uniform	$0.01 - 100$	F_{out}^{ME}
τ	planet age	uniform	0.5-4.5	Gyr
$S/S_\oplus$	Relative luminosity	uniform	0.4-1.2	$S_\oplus$

section 6.2.3. In a first experiment, outgassing is left unconstrained, and the values are sampled in the distribution described in table 6.1 (therefore, the value of τ in these simulations has no importance, as it serves only for the outgassing model in this current version of the framework). A simulation is thus initialized with fixed values of these planetary parameters, that will remain fixed for the 50 Myr of the integration period.

Rather than initializing the simulation with values of ALK and DIC, that are time-dependent variable in the ODE described in section 5.3.2, we use initial pH and pCO_2 to calculate the initial values of ALK and DIC in the ocean using equations 5.22-5.25, assuming that $[CO_2]$ is at equilibrium with the atmosphere:

$$[CO_2]_0 = \alpha_{CO_2} \times pCO_2^0 \tag{6.1}$$

The ALK and DIC in the deep ocean is then calculated at steady-state with the upper ocean, only taking into account ocean mixing, which results in equal values in the deep and upper ocean.

Together, the initial atmospheric composition sampled from table 6.1 and the calculated initial alkalinities and dissolved carbon form the initial values of the time dependent variables in the simulation, and numerical integration can be started from there.

6.2.2. Physical basis for non convergent simulations

The system of ODEs is then integrated forward in time as described in section 5.3.2. But the model is only valid within some

boundaries in the atmospheric composition. As detailed in chapter 5, the model assumes a fixed 1 bar atmosphere, the photochemistry and climate are not calculated in the case where organic hazes might be present (when $p\mathrm{CH}_4 > p\mathrm{CO}_2$, see figure 5.5). But there is no inherent mechanism in the model that prevents the system to reach these bounds. Therefore, a number of simulations are halted as they require calculations that are outside of the model's validity range of values for the time-dependent variables.

It is interesting to try to understand why some simulations were halted and to what climatic or planetological scenario it corresponds. It is particularly important in order to discuss potential biases in the distribution of simulations that have converged, as well as the validity of the model within the habitable zone altogether.

In order to prevent the model to be evaluated outside its validity domain, the convex hull of the simulated 1-D atmospheric model is calculated[226], and SciPy's geometry suite[105] is then used to assess whether a particular set of values of $\{S/S_\oplus, p\mathrm{H}_2, p\mathrm{CO}_2, p\mathrm{CH}_4\}$ is inside of this hull, before evaluation is attempted. That allows us to characterize that a simulation has failed because of model validity problems instead of numerical integration problems (such as the impossibility for the integration method to meet the required accuracy).

We then go on and roughly classify the simulations that have failed by examining the last calculated state of the system. We do so largely arbitrarily as only the step before evaluation of the system in a forbidden state is retained. If this last step is the initial step, we assume that the calculation of the first step has failed as the initial state is too far from the system steady-state, simulations in this case are labeled as "initial step out of grid". We then assess how close $p\mathrm{CO}_2$ and $p\mathrm{CH}_4$ are from one another. If the simulation is failed and the difference between carbon dioxide and methane abundances is less than one order of magnitude, we assume that the simulation enters the organic haze regime. The climate simulations in section 5.2.1 inform us that at relatively high values of $S/S_\oplus$ and $p\mathrm{CO}_2$, no atmospheric state respecting radiative equilibrium is found. We have interpolated this limit as a function $f_{rad} : p\mathrm{CO}_{2lim} \mapsto S/S_\oplus$. If none of the previously defined conditions is true, and that $p\mathrm{CO}_{2fin} > f_{rad}(S/S_\oplus) - \epsilon$ where ϵ is defined arbitrarily as one tenth order of magnitude, then the simulation is labeled as "no radiative equilibrium". In practice, this limit is not very meaningful as it only occurs outside the OHZ, where the

model is not valid anyway. Lastly, if the failed simulation displays $pH_2 + pCH_4 + pCO_2 > 0.3$ bar, we assume that the cause of failure is "atmospheric build up", *ie* that the accumulation of gases (usually CO_2) increases the total atmospheric pressure over 1 bar.

This is not easily done in practice, since the validity boundaries correspond to a geometric object in the 4-D space and some of them may not be identifiable to a scenario of atmospheric evolution (does $pCH_4 > pCO_2$ automatically mean organic hazes?). Second, a higher order integration algorithm is used to simulate the system, and thus the calculation of a step requires the calculation of the derivative at hypothetical system states, that might fall outside of the model validity domain [a]. Additionally, the integration method used here is defined as "implicit", meaning that an equation is solved numerically at each time-step, which can also cause the algorithm to try to evaluate the derivative on forbidden states of the system.

6.2.3. Outgassing rate over geological time scales

In a first experiment, we assume no particular relation between time (age) and the rate of volcanic outgassing F_{out}. The decrease in volcanic outgassing over time is expected to have contributed to the lower pCO_2 in modern Earth's atmosphere, but it is not often seen how this effect contributed compared to the response of the carbonate-silicate weathering cycle to the increase of the solar flux over time. Second, the stagnant lid planets are expected to have a different history of CO_2 outgassing than planets in the plate tectonics regime have, as the heat dissipation mechanism is different, and there is limited resupply of carbon to the mantle (in the plate tectonics regime, subduction of sediment bearing oceanic crust ensures that the some carbon is returned to the mantle)[210,211].

Therefore, in a second *in silico* experiment, we assume that the rate of volcanic outgassing is under control of both age and the convection regime. To some extent, how volcanic outgassing changes over the geological history of a terrestrial planet can be constrained by models of heat dissipation assuming either convection regime.

---

a. A good way to visualize that is to look at the equations of the Runge-Kutta method of order 4 (`https://en.wikipedia.org/wiki/Runge-Kutta_methods`), where the derivative of the system is calculated around the solution at half an integration step.
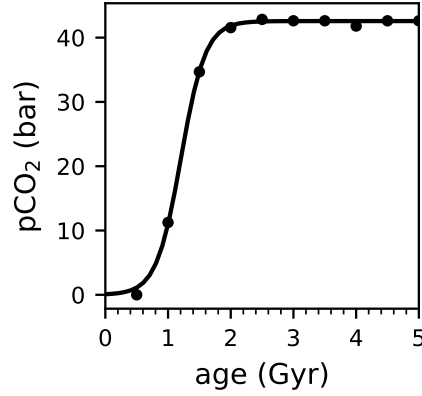
Figure 6.2. | Fit of CO_2 accumulation in the atmosphere for a 1 Earth mass stagnant lid planet. The black dots are the data from Dorn et al. (2018)[211], and the continuous line is the function described by equation 6.4

Krissansen-Totton and Catling (2017)[213] have used a parameterized model of outgassing rate as a function of time, that we will use here as a reference for plate tectonics regime planets. For the stagnant-lid regime planets, we use the calculations in Dorn et al. (2018)[211] as a reference model of outgassing rate as a function of time.

In Krissansen-Totton et al. (2018)[201] and Lehmer et al. (2020)[209], the planetary heat as a function of planetary age follows

$$Q = (1 - \frac{4.5 - \tau}{4.5})^{-n_{out}} \tag{6.2}$$

where n_{out} is the age power law exponent that we here fix as $n_{out} = 0.7$. The outgassing rate of CO_2 is then calculated using

$$F_{out} = F_{out}^{ME} \times Q^m \tag{6.3}$$

where m is the internal heat power law exponent, here fixed $m = 1.1$. $F_{out}^{ME} \times S_p = 8.0 \times 10^{12}$ mol yr^{-1} (table 5.1).

For stagnant lid planets, we retrieved data in Dorn et al. (2018)[211] that consists in the value of pCO_2 over time, assuming that it accumulates in the atmosphere.

As we observed that pCO_2 reached a constant value after some time in their model, we fitted a sigmoid-type function:

$$pCO_2(\tau) = \frac{42.57}{1 + 481.28e^{-5.12\tau}} \tag{6.4}$$

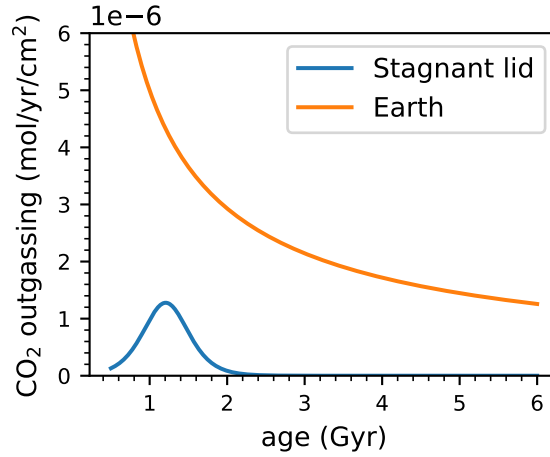**Figure 6.3.** | Parameterized models for the outgassing rate of CO_2 as a function of age for the Earth[201] (orange line) and for a 1-Earth mass stagnant lid planet[211] (blue line).

In order to obtain the value of the volcanic outgassing rate, we took the time derivative

$$F_{out}(\tau) = p\dot{C}O_2(\tau) = \frac{104,899.02e^{-5.12\tau}}{(1 + 481.28e^{-5.12\tau})^2} \tag{6.5}$$

As a result, we obtain the outgassing rate functions of the planet age represented in figure 6.3.

Dorn et al. (2018)[211] model the outgassing rate on stagnant-lid planets of various masses. Their results show that planetary mass has an important effect on the relation of outgassing to planetary age. In particular, more massive planets have an outgassing rate that is more spread out in time (reaching a lower maximum value but with sustained outgassing for longer). Here, we have used their results for a one Earth-mass planet, but their modeling could in principle be used in order to relate outgassing scenarios to planetary mass.

6.3. Trends in the atmospheric CO_2 of Earth-like planets in the habitable zone

Here, we are particularly interested in the distribution of pCO_2 in the atmosphere of habitable zone terrestrial planets, in relation
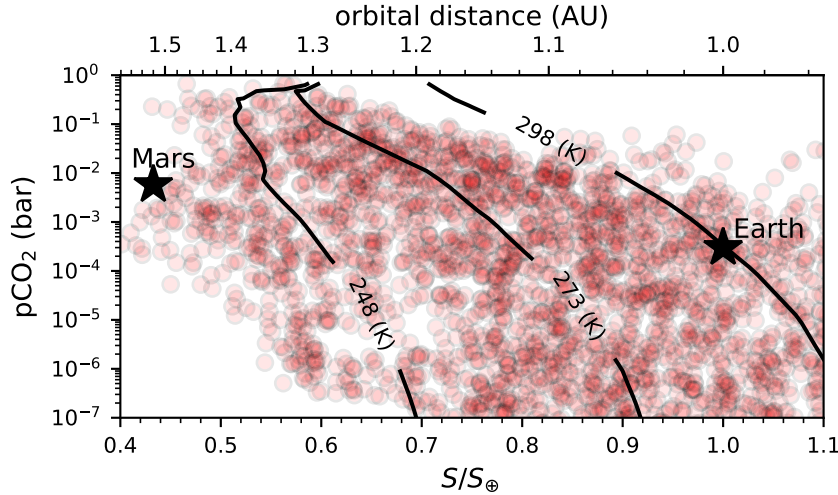
Figure 6.4. | Results of simulated steady state atmospheres in the pCO_2 versus $S/S_\oplus$ space under the assumption of continental weathering. The Earth and Mars are denoted as black stars. The climate model is used with fixed abundances of CH_4 and H_2 using average values in the dataset. Linear regression of pCO_2 versus $S/S_\oplus$ infers a slope of -5.81 ± 0.16 (standard deviation), in units of $\log_{10}(\text{bar})\ S_\oplus^{-1}$, with correlation coefficient value $r^2 = 0.29$.

with the incident flux $S/S_\oplus$. We performed simulations using initial states and parameters in table 6.1. These simulations were performed in parallel on a computation cluster and their computing time was observed to vary from a few minutes to more than 8 hours. Simulations that exceeded that time limit of 8 hours were stopped and labeled as having failed to converge.

6.3.1. Planets with continental weathering

We attempted the simulation of 5,000 "plate tectonics" planets, with both continental and seafloor weathering, with parameters and initial states sampled following table 6.1. Among these attempted simulations, 3043 have converged and 1366 have not due to validity limit problems (and 591 because of numerical failure to converge).

Figure 6.4 shows the converged simulations of pCO_2 at atmospheric steady-state for the sampled values of incident flux. We observe that for intermediates incident flux (0.7-1 $S_\oplus$), the vast majority of simulated planets have a surface temperature allowing a liquid water ocean to be in contact with the atmosphere. Using a 3D general circulation model, Charnay et al. (2013)[197] estimate that an equatorial ice free band subsists at mean global surface temperatures above 248 K. Nevertheless, it is to be noted that we
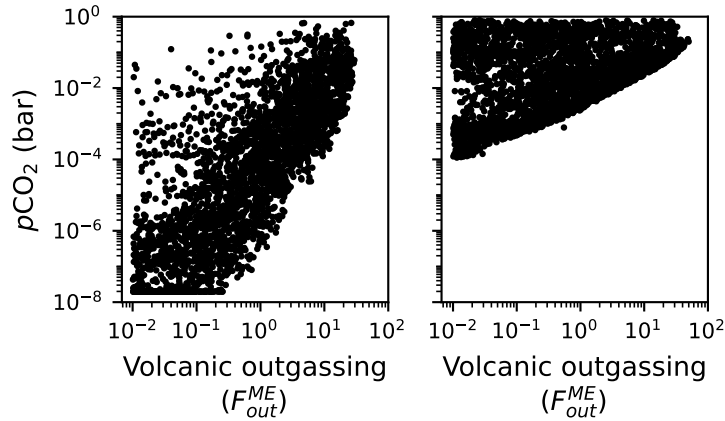
Figure 6.5. | Simulated pCO_2 as a function of the value of the outgassing flux relative to that of the modern Earth. **Left** for planets with a continental weathering cycle and **right** for planets with only seafloor weathering. In the case where there is continental weathering a linear regression infers a slope of 0.23 ± 0.01 (standard deviation) $\log_{10}$ (bars) $(\log_{10}(F_{out}/F_{out}^{ME}))^{-1}$, with r^2-value$= 0.38$. In the case where there is only seafloor weathering, a linear regression infers a slope of 0.04 ± 0.002 (standard deviation) $\log_{10}$ (bars) $(\log_{10}(F_{out}/F_{out}^{ME}))^{-1}$, with r^2-value$= 0.11$.

find that a large proportion (56% of the simulated planets have relatively cold climates, with surface temperatures less than 273 K. Our modeling may not accurately represent the situation of planets with cold climates. First, there is no implemented cutoff of atmospheric exchanges and weathering. Second, the surface albedo used for the climate calculations is fixed throughout the range of temperatures explored. The increase in surface albedo when the ice cover grows could precipitate the planet in a runaway glaciation (also called runaway ice-albedo feedback).

Figure 6.4 shows that there is a negative trend in $\log pCO_2$ versus $S/S_\oplus$, that explains about a third of the variance (r^2-value: 0.29). Our simulations show that the rate of volcanic outgassing is an important determinant of the atmospheric CO_2 at steady state, as it captures close to 38% of the variance (figure 6.5, left panel). In this set of simulations, where the volcanic outgassing is left unconstrained, there is an important variability in the pCO_2 at steady-state of the atmosphere.

It seems that planets with an active surface weathering cycle tend to be efficiently cooled at relatively high incident fluxes, as the cases where the steady-state temperature is greater than 298 K are rare
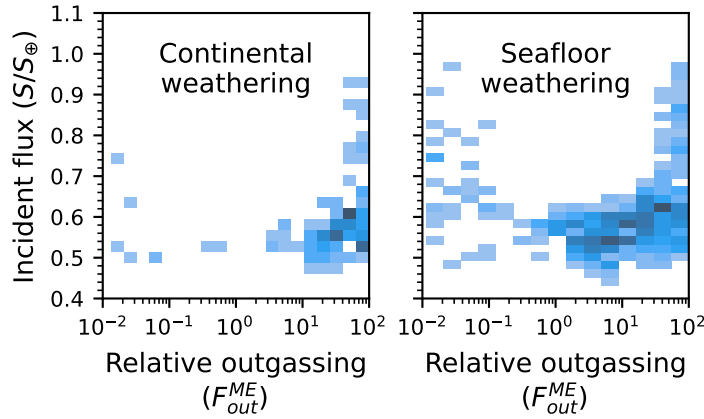
Figure 6.6. | Distribution of non convergent runs identified as atmospheric pressure increasing over 1-bar in the incident flux versus outgassing rate parameter space. Darker color indicate higher point density. **Left**: simulations with continental and seafloor weathering. **Right**: simulations with only seafloor weathering.

in our simulations (figure 6.4). On the other hand, the prevalence of "cold" planets further out in the habitable zone indicate that planets with continental weathering are expected *a priori* to infrequently have temperate conditions when $S/S_\oplus$ is low (around 20% of simulated planets with $S/S_\oplus < 0.8$ have mean surface temperatures above 273 K, and 10% for $S/S_\oplus < 0.7$).

There is however some bias in the sample presented in figure 6.4, as simulations using lower values of $S/S_\oplus$ are less likely to have converged (figure 6.6). For low values of incident flux, simulations were more likely to leave the model validity domain as CO_2 could accumulate and results in total atmospheric exceeding 1 bar (see section 6.2.2). As a result, there could be a larger fraction of terrestrial planets with warmer climates at lower incident flux values.

6.3.2. Planets without continental weathering

We also calculated the steady-state atmospheric composition of 3,692 (out of 5,094 attempts, 1400 did not converge because of model validity conditions) planets where only seafloor weathering participates in the geological carbon cycle, representing "stagnant-lid" planets. In this set of simulations (figure 6.7), we observe that the steady-state value of pCO_2 is on average higher than in the case where continental weathering exists (the average of $\log_{10} pCO_2$
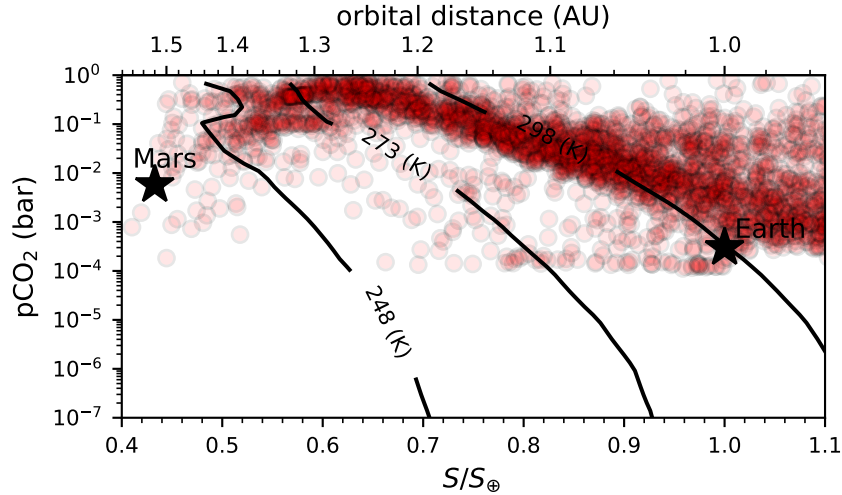
Figure 6.7. | Results of simulated steady state atmospheres in the $p\text{CO}_2$ versus $S/S_\oplus$ space under the assumption of only seafloor weathering. The Earth and Mars are denoted as black stars. The climate model is used with fixed abundances of CH_4 and H_2 using average values in the dataset. Linear regression predicts a slope of -3.36 ± 0.06 (standard deviation), in units of $\log_{10}(\text{bar}) \, S_\oplus^{-1}$, with correlation coefficient value $r^2 = 0.44$.

is 2×10^{-2} bar, whereas it is 4.5×10^{-5} bar in the continental weathering case).

It appears that the presence or absence of continental weathering has an important impact on the expected climate of terrestrial exoplanets in the habitable zone. The simulations without this geological process in figure 6.7 are more likely to be warmer than those that have continental weathering. A low incident flux, this means that stagnant lid regime planets could be less likely to be frozen than their plate tectonics regime counterparts. The model predicts a negative trend of $p\text{CO}_2$ versus incident flux. This highlights the role of seafloor weathering as a negative feedback loop on climate. However, this negative trend is less pronounced than in the continental weathering case (a linear fit yields a slope of -3.36 versus $-5.81 \, \log_{10}(\text{bar}) \, S_\oplus^{-1}$ when continental weathering exists). As a consequence of the comparatively weaker feedback loop provided by seafloor weathering, planets without continental weathering are expected to be comparatively warmer at higher incident flux values. Although our model is not capable of assessing whether these planets could enter a greenhouse runaway because of their weaker control on climate, these simulations suggest that planets in the stagnant lid regime can be habitable in a narrower range of condi-

tions relative to planets in the plate tectonics convection regime.

The correlation between $p\mathrm{CO_2}$ and $S/S_\oplus$ shows a higher value of correlation coefficient in the seafloor weathering case (figure 6.7, $r^2 = 0.44$), than it does for the continental weathering case (figure 6.4, $r^2 = 0.29$). Figure 6.7 shows that this trend may not be linear on the complete range of incident flux values (and may even have a positive slope at lower $S/S_\oplus$, although one should keep in mind the bias introduced by the limit of the 1 bar atmosphere). It may appear counter intuitive that the incident flux is a better predictor of $p\mathrm{CO_2}$ in the case of planets that have only the comparatively weaker seafloor weathering as a control mechanism of atmospheric $\mathrm{CO_2}$. Our interpretation is that in this set of simulations, the outgassing rate is left uncorrelated to the convection regime, and that the weathering rates are in part determined by the value of the outgassing rate as a proxy of the supply rate of weathearable material (equations 5.17, 5.18 and 5.28). Given that, simulations for which a low outgassing rate is assumed can reach lower values of $p\mathrm{CO_2}$ for planets with continental weathering compared to those with only seafloor weathering (figure 6.5. Therefore, volcanic outgassing acts as a hidden variable that increases *a priori* the variability of $p\mathrm{CO_2}$, especially in the case of planets where there is continental weathering. As shown in section 6.2.3, the outgassing rate of planets in either convective regime could be better constrained, and thus so would be the distributions of the $p\mathrm{CO_2}$ in the atmosphere of exoplanets.

6.3.3. Age-constrained outgassing rate

The age of exoplanets assumed to follow relatively closely the age of the host star (as suggested by planet accretion models[227]), can be constrained to around ±2 Gyrs with current techniques[190], and it is plausible that future instruments can estimate host star ages with precision <1 Gyrs (see Bixel and Apai, 2020[46] and references therein). Therefore, planetary age could constitute an additional observable context to the interpretation of measures of the atmospheric composition. This could be particularly helpful in assessing trends of $\mathrm{CO_2}$ atmospheric abundances as outgassing rates are expected to decrease over geological timescales and could be very different for stagnant lid regime and plate tectonics regime terrestrial planets (section 6.2.3) and determine the steady-state $p\mathrm{CO_2}$, especially in the case of plate tectonics planets (figure 6.5).
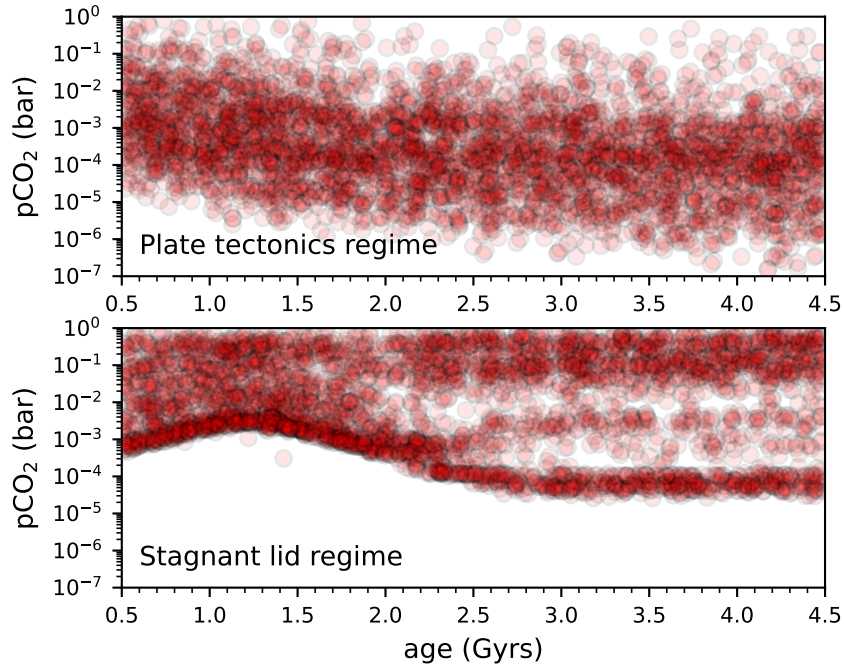
Figure 6.8. | Simulated steady-state pCO$_2$ versus planetary age. **Top**: for plate tectonics regime planets, with comparatively larger and sustained outgassing rate through time. **Bottom**: for stagnant lid regime planets with lower and short-lived volcanic outgassing.

Therefore, we also generated sets of simulated atmospheric compositions for which the CO$_2$ outgassing rate is taken as a function of age following equations 6.3 and 6.5 rather than in the uniform distribution described in table 6.1. In this set of simulations, the outgassing rate scenario estimated to have been the Earth's is assumed to be representative of plate tectonics regime planets and is associated with the existence of continental weathering. The stagnant lid regime outgassing scenario is associated with the absence of continental weathering. As such, the two sets of simulations assume different ranges of volcanic outgassing rates.

These simulations are reported in figures 6.8 and 6.9. For plate tectonics regime planets, the outgassing model (equation 6.3) corresponds to values that are above than the average assumed in the set of simulations where it is left unconstrained. Because of that, the steady-state value of the atmospheric CO$_2$ partial pressure is comparatively greater than in the unconstrained case. This has some consequences on the expected occurrence rate of planets with temperate conditions in the habitable zone. Even though the
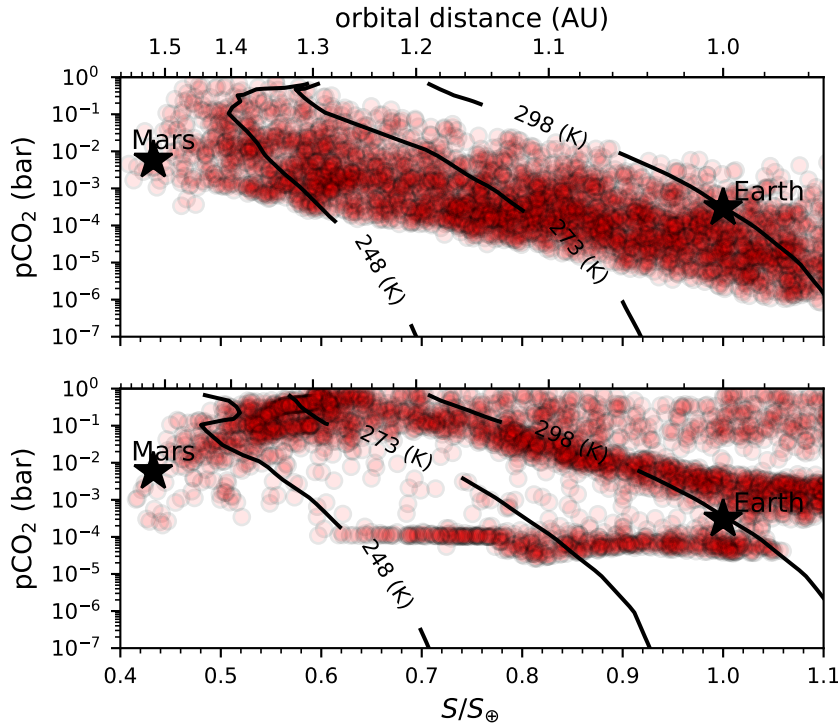
Figure 6.9. | Simulated steady-state $p\mathrm{CO_2}$ versus planetary incident flux when outgassing rate is age and regime related. **Top**: for plate tectonics regime planets. **Bottom**: for stagnant lid regime planets.

abundance of simulations with very low ($< 10^{-4}$ bar) atmospheric CO_2 is lower, most plate tectonics regime planets (ca. 90%) with $S/S_\oplus < 0.8$ are expected to have global mean surface temperatures lower than 273 K.

In the plate tectonics regime, the assumption of an outgassing scenario reduces considerably the variability in $p\mathrm{CO_2}$ versus $S/S_\oplus$ (a linear fit explains $r^2 = 63\%$ of the variance, compared to 29% in the case where outgassing is unconstrained). In the case of the stagnant-lid regime, however, it becomes apparent that the relation between $\log(p\mathrm{CO_2})$ is not linear. The addition of a scenario on volcanic outgassing does not considerably change qualitatively the distribution of simulations in the $\{p\mathrm{CO_2}, S/S_\oplus\}$ plane. This is expected from the observation that outgassing rate does not determine the steady state atmospheric CO_2 as much when continental weathering is absent (figure 6.5).

There are however some notable features that emerge when the outgassing rate is constrained. The existence of a cluster of sim-

ulations with $pCO_2 \approx 10^{-4}$ bar in figure 6.9 could correspond to simulations of "older" (age>2.5 Gyrs) planets that have a very low outgassing rate (figure 6.8). This highlights the possibility that older stagnant lid planets may be less likely to have temperate climates.

Another interesting cluster of simulations in the stagnant lid case, is the one composed of relatively old planets ($\tau > 2.5$ Gyrs) and high CO_2 partial pressure ($pCO_2 > 10^{-2}$ bar) in figure 6.8. It appears surprising that such cases would arise when the outgassing rate is very low (see figure 6.3). This scenario of a CO_2-rich atmosphere of an older stagnant lid planet could be due in our simulations to an initial state with a relatively high pCO_2, which is not removed from the atmosphere as seafloor weathering is limited by the supply of fresh basalt. This highlights the possibility of bistability, and even hysteresis in the atmospheric CO_2 abundance in stagnant lid planets. For instance, it could be possible that a large outgassing event releases large amounts of CO_2 in the atmosphere without supplying weatherable material, and thus that the atmosphere remains CO_2-rich. It is not clear whether the weathering of subaerial basalt could have the same effect as seafloor weathering. Therefore, it could be that subaerial volcanoes participate in increasing atmospheric CO_2 but not the supply of weatherable minerals in the same way that subaquatic volcanic activity does.

6.4. A perspective on simulated biosignatures

Here, we are interested in applying the model developed in part I and used to assess the habitability of Enceladus in part II in the context of terrestrial exoplanets in the habitable zone. We use the same approach as in chapter 3, which we briefly recall here. We also use a slightly different set of parameters than in chapters 3 and 4 in order to simulate an example organism that is not hyperthermophilic. The growth rate is expressed as

$$q_{growth} = -\frac{\Delta_r G_{cat}}{\Delta G_{diss}}(q_{cat} - q_m) - d \qquad (6.6)$$

where $\Delta_r G_{cat}$ (kJ mol^{-1}) is the Gibbs free energy of the catabolic reaction, calculated using the Nernst equation assuming ideal solu-

tion (activities equal to the concentrations)

$$\Delta_r G_{cat} = \Delta_r G_{cat}^0 + RT \sum_i \ln C_i \tag{6.7}$$

with C_i denotes the concentrations of the solutes involved in the catabolic reaction. Here, we assume a monospecific ecosystem with chemoautotrophic methanogens that have catabolic reaction

$$H_2 + \frac{1}{4} CO_2 \longrightarrow \frac{1}{4} CH_4 + \frac{1}{2} H_2O \tag{6.8}$$
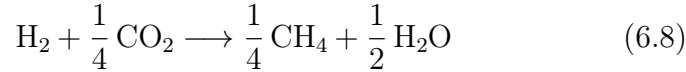
The energy ΔG_{diss} corresponds to the Gibbs free energy dissipation required for the synthesis of one mole of biomass. For hydrogenotrophic methanogens, $\Delta G_{diss} \approx 1000$ kJ mol^{-1} [62,117]. The catabolic rate q_{cat} (d^{-1}) is taken as a function of temperature following[84,117]:

$$q_{cat} = \tau_c \frac{\frac{k_b}{h} T e^{-\frac{\Delta G_{acat}}{RT}}}{1 + \exp\left\{\frac{\Delta H_{eq}}{R}\left(\frac{1}{T_{eq}} - \frac{1}{T}\right)\right\}} \tag{6.9}$$

where $k_b = 1.38 \times 10^{-23}$ J K^{-1} and $h = 6.63 \times 10^{-34}$ J s are the Botlzmann and the Planck constant respectively. We fix the values $\Delta G_{acat} = 68$ kJ mol^{-1}, $\Delta H_{eq} = 121$ kJ mol^{-1} and $T_{eq} = 70$°C to match those of the AKP enzyme of mesophilic *E. coli*[84]. We take the maintenance rate (in units of d^{-1}) as a function of temperature from Tijhuis et al. (1993)[78]:

$$q_m = \frac{1000}{\Delta G_{diss}} 24 \times 3.5 e^{\frac{69400}{R}\left(\frac{1}{298} - \frac{1}{T}\right)} \tag{6.10}$$

The scaling factor is taken as $\tau_c = 2 \times 10^{-5}$[117] and the constant death rate is set to $d = 0.01$ d^{-1}. This parameterization of the model results in a temperature growth curve of a relatively slow growing thermophilic microbe, that does not grow below $T \approx -7$°C and above $T \approx 80$°C (figure 6.10).

We use the steady-state of the system and parameters in the simulations of plate-tectonics planets (*e.g* figure 6.9, top panel) as the initial state and parameters for the habitability and potential biosignatures of a methanogenic population. In these simulations, we artificially limit the fraction of the ocean that can be "inhabited" by the population to 10% of the upper ocean volume. This
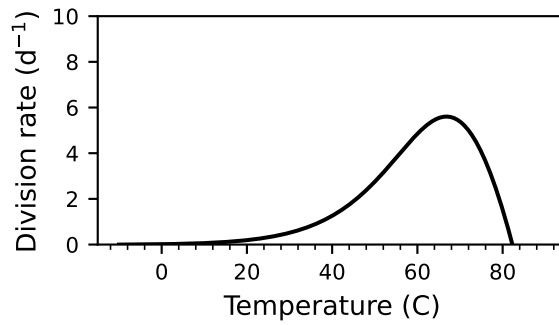
Figure 6.10. | Temperature growth curve of the simulated hydrogenotrophic methanogen used for the simulations of biosignatures.
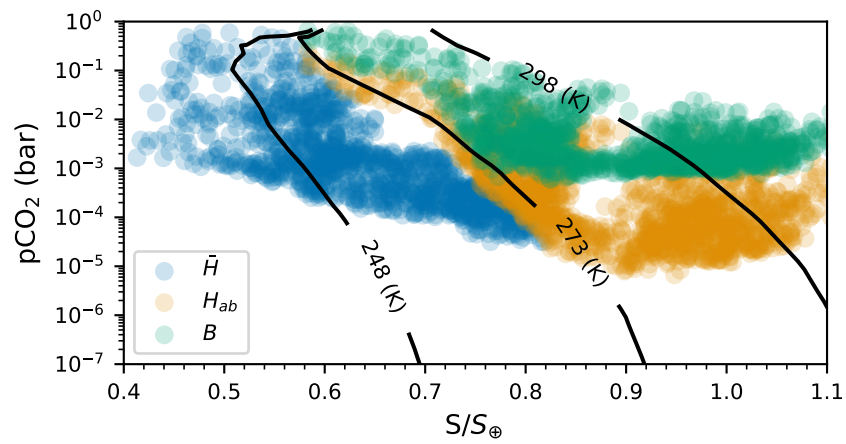

Figure 6.11. | **Atmospheric CO$_2$ trend versus incident flux** $S/S_\oplus$ **when a population of hydrogenotrophic methanogens is simulated.** The blue dots denote simulations where the ocean was not found to be a viable environment for the population, orange dots denote a viable ocean and green dots are simulation with a methanogenic population.

helps with the convergence of the simulations as the disruption introduced by the biological population can be very large and result in numerical instability.

Like in chapter 3, this results in simulations where some cases correspond to conditions in the ocean where this population is viable ("habitable") and other cases where it is not ("uninhabitable"). Therefore, there are three types of simulations, the uninhabitable ones denoted by $\bar{H}$ where only abiotic process exist, the habitable ones where only abiotic processes exist denoted by H_{ab} and the biotic ones, that are habitable and where the population is simulated (denoted by B).

The distribution of these simulations in the $\{pCO_2, S/S_\oplus\}$ is shown in figure 6.11. We observe that only simulations that have a surface temperature greater than -7°C result in an ocean where the population is viable, as expected from the temperature growth curve of the modeled organism (figure 6.10). Simulations in which the population affects the ocean composition result in higher atmospheric abundance of CO_2, and thus higher temperatures. Interestingly, this also results in a trend in the pCO_2 versus $S/S_\oplus$ distribution that is slightly different in the biotic case. This increase in pCO_2 seems to be in contradiction with methanogens consuming CO_2 but could be due to the effects photochemistry, photochemical production of CO_2 scales with the atmospheric abundance of CH_4 (figure 5.9).

The biotic production of methane generally translates into an increase of pCH_4, although at lower incident flux, biological methane production is paradoxically associated with a lower pCH_4 (figure 6.12). This effect is not easily explained, but photochemistry could also be the cause of it, as the photochemical coupling between CH_4 and CO_2 changes regime at lower incident flux (figure 5.9).

The examination of the predicted atmospheric composition in the case of biotic production of methane (figures 6.13 and 6.14) shows that the biosignature patterns expected for a methanogenic biosphere on the primitive Earth[22] could remain relevant across a wider range of incident flux values.

It is to be noted that the figures 6.11-6.14 only show simulations that have converged. We found that in this set of simulations, the possible formation of organic haze is the dominant cause of non convergence (23% of the simulations have not converged, 97% of the
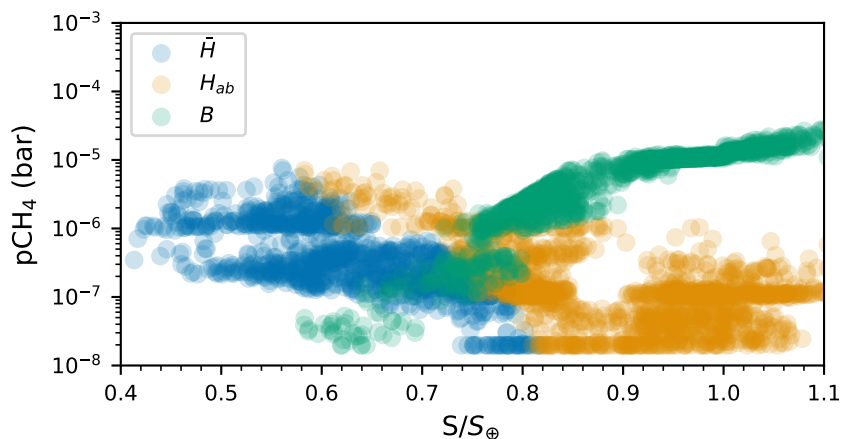
Figure 6.12. | Distribution of simulated atmospheric CH₄ for plate tectonics planets with and without biotic production of methane. Blue dots denote simulations where the ocean is not viable to the population of methanogens, orange dots simulations where the ocean is a viable environment and green dots simulations with biotic production of methane.
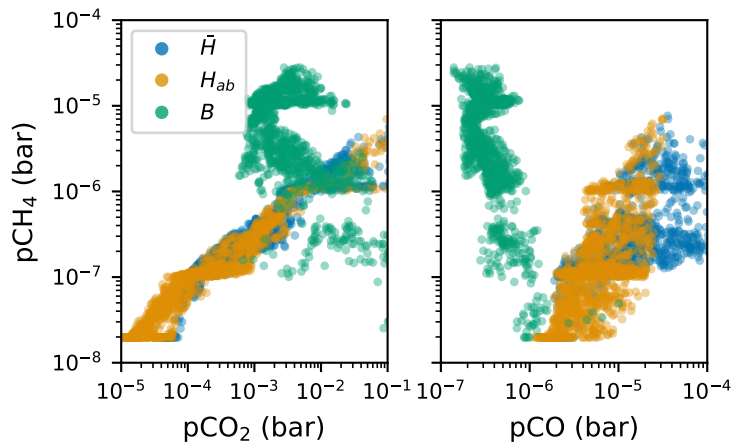

Figure 6.13. | Biotic and abiotic simulations in the atmospheric composition phase space. Left: $p\mathrm{CH_4}$ versus $p\mathrm{CO_2}$ and **right**: $p\mathrm{CH_4}$ versus $p\mathrm{CO}$. The blue dots denote simulations in which the ocean is not viable to the modeled methanogens, orange dots denote a viable ocean, but only abiotic processes are simulated and the green dots denote simulations with biotic methane production.
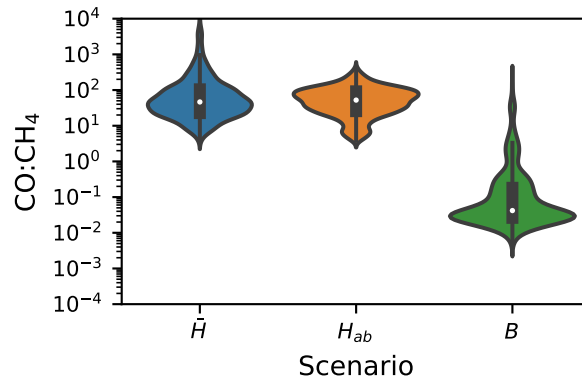
Figure 6.14. | Distribution of the CO : CH$_4$ ratio in abtiotic and biotic simulations. The blue distribution corresponds to the abiotic "uninhabitable" case, the orange one to the abiotic "habitable" one and the green distribution to the biotic scenario.

non-convergent simulations were labeled as possible formation of organic haze following methodology in section 6.2.2). Moreover, the formation of organic haze was found to be more likely in simulations with biotic production of methane (29% of the simulations under the biotic scenario), and was found to occur only at $S/S_\oplus > 0.95$.

Nevertheless, the application of the biological modeling of a very simple biosphere in the simulation of Earth-like exoplanets in the habitable zone paves the way towards defining biosignatures as patterns both in the relative abundances of different atmospheric gases (figures 6.13 and 6.14) and in the relation of these abundances with the planetary context (figures 6.11 and 6.12). Importantly, these results highlight that it may be difficult to identify a biosignature that would be unambiguous regardless of the context. The CO : CH$_4$ proposed signature shown in figure 6.14 has been assessed as a signature robust to early-Earth ecosystem composition [22]. But figure 6.14 shows that while the CO : CH$_4$ ratio is expected to be different in the biotic and abiotic cases *on average*, it is not infrequent that both cases yield similar values.

For these reasons, we believe that biosignatures should be understood as a set of consistent patterns and trends in the space of atmospheric "observables" and planetary context parameters. Consequently, the inference of exoplanet biosignatures should rely on the analysis of a population of exoplanets taken together rather than analysis at the scale of a single exoplanet's atmosphere and context. This raises the question of the strategy that should be fol-
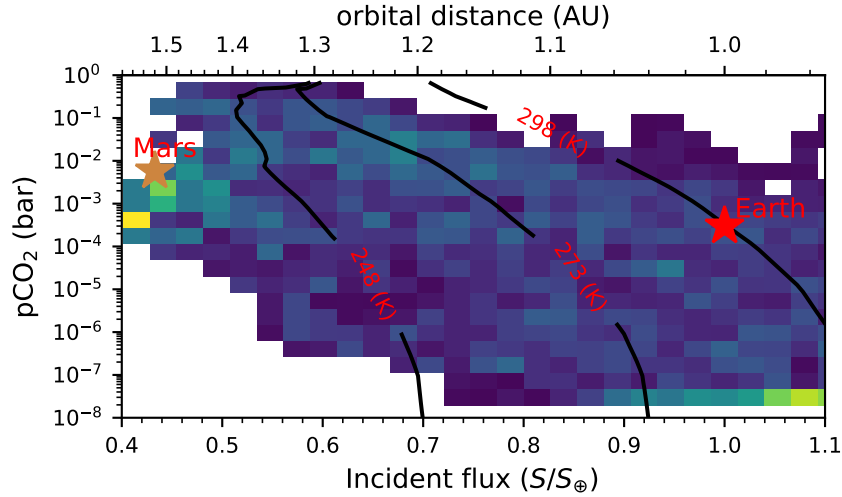
Figure 6.15. | Distribution of simulated exoplanets with a carbonate-silicate weathering cycle in the habitable zone. The colored tiles correspond to a 2D histogram normalized so that the sum on the vertical axis is equal to one. Yellow color indicates higher density of simulated atmospheres. The contour lines correspond to the surface temperature calculations assuming that pH_2 and pCH_4 are fixed to the average values in the dataset.

lowed in order to design the optimal sample of terrestrial exoplanets to screen for biosignatures.

6.5. Hypothesis testing

We are now interested in constraining the number of planets that must be characterized in order to test astrobiological hypotheses with sufficient confidence. As a starting point to develop this methodology, we examine the opposition between the predicted trends in pCO_2 versus $S/S_\oplus$ for exoplanets with and without continental weathering (such as those simulated in figures 6.4 and 6.4). We frame this problem as two concurring hypotheses about terrestrial planets in the habitable zone:

Hypothesis 6.1. $\mathcal{H}_{cw}$: All planets in the HZ have continental weathering and seafloor weathering.

and

Hypothesis 6.2. $\mathcal{H}_{sw}$: All planets in the HZ have only seafloor weathering.

These hypotheses are chosen in order to demonstrate how this framework can serve to constrain the number and depth at which
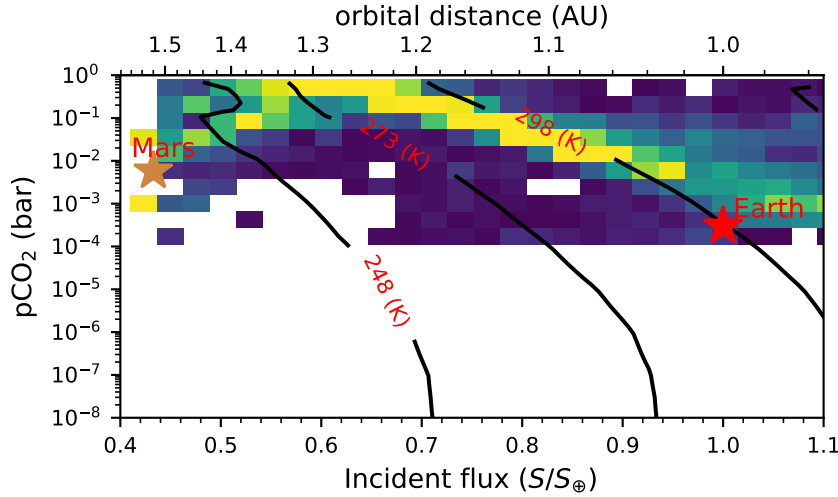
196

Figure 6.16. | Simulations of exoplanets without a carbonate-silicate weathering cycle in the habitable zone. The colored tiles correspond to a 2D histogram normalized so that the sum on the vertical axis is one. Yellow color indicates higher point density. The contour lines correspond to the surface temperature calculations assuming that pH_2 and pCH_4 are fixed to the average values in the dataset.

exoplanets should be characterized. To test the hypotheses relative to the presence or absence of continental weathering, without additional assumptions on outgassing regimes, the problem boils down to one "observable", pCO_2, and one "context" variable, $S/S_\oplus$. This makes for a relatively simple case in term of hypothesis testing; the addition of other dimensions to the observable and context variables makes it more difficult to visualize.

6.5.1. An observation model

In order to evaluate these hypotheses, we assume that we have at hand an instrument capable of detecting the presence of CO_2 in the atmosphere of a terrestrial exoplanet if $pCO_2 > \zeta$, where ζ is a certain threshold reflecting of the observation sensitivity (it may scale with the number or transits for a transit survey, or the aperture for a direct imaging survey). In other words we assume that the CO_2 content of a terrestrial exoplanet atmosphere can be assessed by a binary operator

$$\Gamma = \begin{cases} 1 & \text{if} \quad pCO_2 > \zeta \\ 0 & \text{if} \quad pCO_2 \leq \zeta \end{cases} \tag{6.11}$$
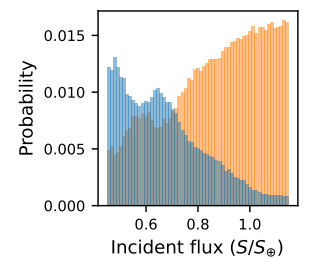

Figure 6.17.: Simulated distributions of detected (**blue**) and undetected (**orange**) CO_2, assuming a detection threshold $\zeta = 10^{-3}$ bar and continental weathering $\mathcal{H}_{cw}$.

197

A sample in that sense corresponds to a set $X = \{(S/S_\oplus)_i, \Gamma_i\}_{i \in [0,n]}$ where n is the sample size. We can simulate such samples using the simulated distributions in figures 6.15 and 6.16 in order to approximate $P(pCO_2 > \zeta|(S/S_\oplus), \mathcal{H})$, *e.g* figure 6.17. In practice, this is done here by calculating the frequency of simulations that have $pCO_2 > \zeta$ for a given $S/S_\oplus \pm 0.05$.

6.5.2. Prospective hypothesis testing

Our goal here is to plan for a successful mission, in that it would provide us with compelling evidence in favor of either one of these hypotheses, assuming that one of them is true. Here, we use a prospective analysis method based on the calculation of the Bayes factor, as such methods are suited to cases where two alternate hypotheses are studied in a context where they can be given prior probabilities[228,229].

The Bayes factor measures the evidence brought by the observation of a sample. The general form of the Bayes theorem writes as

$$P(\mathcal{H}|x^0) = \frac{P(x^0|\mathcal{H})P(\mathcal{H})}{P(x^0)} \qquad (6.12)$$

where x^0 denotes data or an observation and $\mathcal{H}$ denotes a hypothesis (or a model), in our case $\mathcal{H}_{cw}$ or $\mathcal{H}_{sw}$. The term $P(\mathcal{H}|x^0)$ is called the posterior probability (or plausibility) of π and $P(x^0|\mathcal{H})$ (sometimes noted $\mathcal{L}_\mathcal{H}(x^0)$) is called the *likelihood*. The probabilities $P(\mathcal{H})$ and $P(x^0)$ are the prior probabilities. The Bayes factor emerges when the relative plausibility of two competing hypotheses $\mathcal{H}_1$ and $\mathcal{H}_2$ is expressed:

$$\frac{P(\mathcal{H}_1|x^0)}{P(\mathcal{H}_2|x^0)} = \frac{P(\mathcal{H}_1)}{P(\mathcal{H}_2)} \times \overbrace{\frac{P(x^0|\mathcal{H}_1)}{P(x^0|\mathcal{H}_2)}}^{\text{Bayes factor}} \qquad (6.13)$$

The Bayes factor is commonly noted[229,230]

$$\mathrm{BF}_{12} = \frac{P(x^0|\mathcal{H}_1)}{P(x^0|\mathcal{H}_2)} \qquad (6.14)$$

It is usually defined that $\mathrm{BF}_{12} > 100$ consists in "extreme evidence" in favor of $\mathcal{H}_1$ over $\mathcal{H}_2$ [229], as it corresponds to the likelihood of the sample under $\mathcal{H}_1$ being a hundred times that of under $\mathcal{H}_2$ (see table 6.2 for evidence classification).

We are interested in designing an observational campaign so that the risk of obtaining inconclusive or misleading evidence is minimized.

BF$_{12}$	Evidence
>100	Extreme
30 - 100	Very strong
10 - 30	Strong
3-10	Moderate
1-3	Anecdotal
1	No evidence

Table 6.2.: Classification of evidence for Bayes factors, adjusted from Stefan et al. (2019)[229] .

We thus simulate samples $X_{\mathcal{H}_{cw}}$ $X_{\mathcal{H}_{sw}}$ under $\mathcal{H}_{cw}$ and $\mathcal{H}_{sw}$ respectively, and measure the Bayes factor for the competing (untrue) hypothesis

$$\mathrm{BF}_{sw,cw}(X_{\mathcal{H}_{cw}}) = \frac{P(X_{\mathcal{H}_{cw}}|\mathcal{H}_{sw})}{P(X_{\mathcal{H}_{cw}}|\mathcal{H}_{cw})} \qquad (6.15)$$

and

$$\mathrm{BF}_{cw,sw}(X_{\mathcal{H}_{sw}}) = \frac{P(X_{\mathcal{H}_{sw}}|\mathcal{H}_{cw})}{P(X_{\mathcal{H}_{sw}}|\mathcal{H}_{sw})} \qquad (6.16)$$

This measures the evidence in favor of the incorrect hypothesis. For sufficient statistical power to be achieved, not only the risk of false positive must be minimized, but so must be the risk of insufficient confidence in the rejection of the incorrect hypothesis. These risks emerge from a sample yielding evidence for the incorrect hypothesis by chance. In order to constrain the probability of this event, we perform Monte-Carlo sampling of 200,000 values of $\mathrm{BF}_{sw,cw}(X_{\mathcal{H}_{cw}})$ and $\mathrm{BF}_{cw,sw}(X_{\mathcal{H}_{sw}})$, for various values of the detection threshold ζ and the sample size. The distributions of $\mathrm{BF}_{sw,cw}(X_{\mathcal{H}_{cw}})$ for sample sizes of 5 and 10 and a detection threshold $\zeta = 10^{-3}$ bar are given as an example in figure 6.18. We show the values of the probabilities $P(\mathrm{BF}_{sw,cw}(X_{cw}) > 10^{-2})$, $P(\mathrm{BF}_{sw,cw}(X_{cw}) > 1)$, $P(\mathrm{BF}_{cw,sw}(X_{sw}) > 10^{-2})$ and $P(\mathrm{BF}_{cw,sw}(X_{sw}) > 1)$ in figure 6.19. For every value of the sample size, the maximum value between of the risk under $\mathcal{H}_{sw}$ and $\mathcal{H}_{cw}$ must be considered if no *a priori* probability is given to either one of these hypotheses. This maximum required sample size as a function of the risk level is given in figure 6.20.

The results of this prospective analysis show that the sample size required to bound the risk of achieving less than extreme evidence in favor of either hypothesis under 5% is 22 if the threshold for detected CO_2 signal in the atmosphere is 0.1 bar, but falls to 13 if 0.01 bar of CO_2 can be detected (see table 6.3). Those sample sizes are well within the expected yields of a space observatory like LUVOIR[195]. Lowering the Bayes factor cutoff for insufficient negatives from 10^{-2} (extreme evidence) to 30 (very strong evidence) brings down the required sample size to 9 at a pCO_2 detection threshold of 10^{-3} bar and a 5% risk, within the expected yield of HabEx[224].

These constraints on the required sample size to assess hypotheses must be considered in the light of the expected number of so-called "exo-Earths" candidates, Earth like planets in the habitable
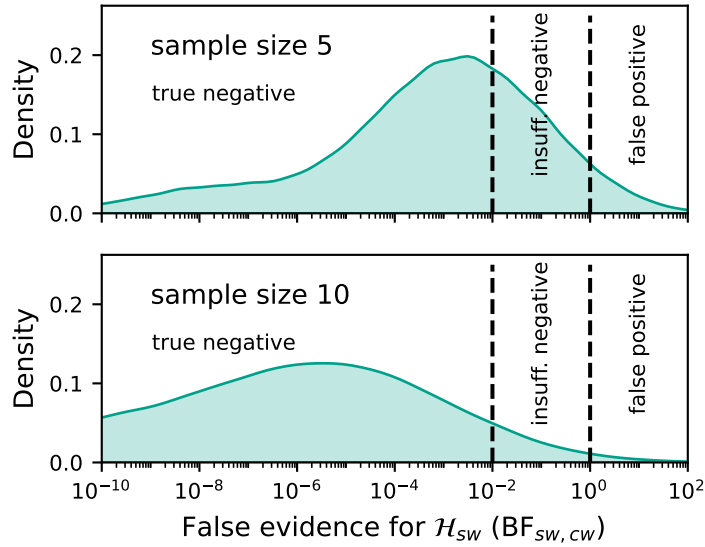
Figure 6.18. | Distributions of the Bayes factor evidence for $\mathcal{H}_{sw}$ when samples are simulated under $\mathcal{H}_{cw}$. **Top:** assuming a sample size of 5 and **bottom** for a sample size of 10. The CO_2 detection threshold assumed here is $\zeta = 10^{-3}$ bar. The case where $BF_{sw,cw} < 10^{-2}$ corresponds to the correct rejection with extreme evidence of the competing hypothesis. The case where the Bayes factor is comprised between 10^{-1} and 1 corresponds to the correct rejection of the competing hypothesis with lower evidence, that we call here insufficient. Lastly, in the case where the Bayes factor is greater than one, evidence points in favor of the incorrect hypothesis, thus resulting in a false positive.
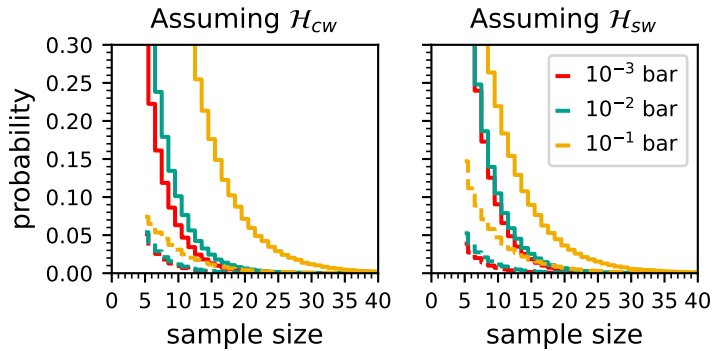
Figure 6.19. | **Probabilities of false positive (dashed lines) and insufficient negative (continuous lines) for different values of the CO_2 detection threshold and assuming one or the other hypothesis.**
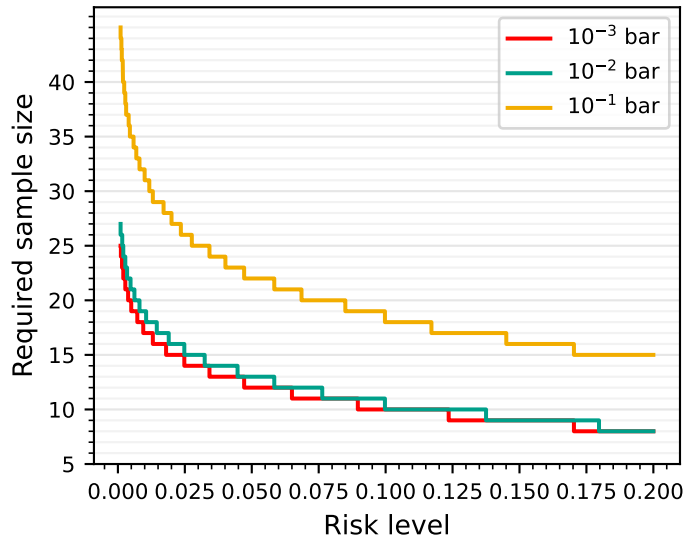
Figure 6.20. | Required sample size as a function of the risk of insufficient evidence for different values of CO_2 detection threshold.

Table 6.3. | Required sample size for selected combinations of CO_2 detection thresholds and accepted risk of Bayes factor evidence being less than 100.

Detection threshold	Risk level	Sample size
10^{-3} bar	5%	12
10^{-3} bar	1%	17
10^{-2} bar	5%	13
10^{-2} bar	1%	19
10^{-1} bar	5%	22
10^{-1} bar	1%	32

zone around a Sun-like star. No planet of this type has been yet discovered, and in fact current instruments would be unable to do so. Because of that, estimates of their occurrence rate often derive from statistical models of observed trends in the population of exoplanets that have been observed[231,232]. A promising approach is the simulation of planet accretion in the protoplanetary disk, as well as the early dynamics of the newly formed planets orbits[233]. It has been recently proposed that these approaches could be combined together in order to propose better estimates in the near future[234].

The occurrence rate of planets of interest, here Earth-like planets provides an upper estimate of the number of these candidates that can effectively be characterized given an instrument with set specifications. Bixel and Apai (2021)[235] have recently proposed a framework that incorporates instrumental constrains together with exoplanet occurrence rate estimates in order to provide estimates of the sample size that can effectively be achieved by a given observatory. The prospective hypothesis testing methodology developed here could inform such approaches in order to help astronomers maximize the scientific return of observation missions.

6.6. Discussion

In this chapter, we have demonstrated how the framework developed in chapter 5 holds the potential for multiple applications. In particular these simulations enable the exploration of how different geological and geochemical processes that individually pertain to habitability interact with each other in shaping the surface conditions of a terrestrial planet set in a range of stellar contexts. Our results suggest that the long term habitability of stagnant-lid planets may be vulnerable to catastrophic outgassing events as bistability is observed in their atmospheric CO_2. Speculatively, such catastrophic events could correspond to a late large impact, or catastrophic resurfacing. The evolution of the rate of volcanic outgassing rate of CO_2 through time for stagnant lid planets remains poorly constrained, and all models are not in agreement with each other[210,211]. Nevertheless, competing predictions regarding the outgassing rates on such planets could in principle be implemented in our modeling framework. Therefore, the results presented in section 6.3.3 could be reproduced with different outgassing rate functions of planetary age in order to reflect uncertainty on the stagnant-lid regime.

The example of prospective hypothesis testing given in section 6.5 could be refined to include other contextual information such as planetary age and assess the resulting increase in separation power between different scenarios. As shown in figure 6.8, the age variable is not expected to be as predictive of atmospheric CO_2 as incident stellar flux is under the plate tectonics regime. But interior models that assess the sensitivity of volcanic outgassing rates to planetary mass (such as Dorn et al., 2018[211]) could be integrated to this framework in order to increase the dimensionality in which trends are predicted, and thus the separation between predictions under different scenarios. It could be useful to increase the degrees of freedom in the model so as to identify possible non-identifiabilities between observations and scenarios (different scenarios yielding the same observation). This however comes with the risk of combining effects that are not all understood with the same level of confidence and thus confuse quantitative predictions.

The assessment of a hypothetical observation experiment in section 6.5 focuses on competing hypotheses that are homogeneous, in that we compare a scenario where all planets have continental weathering to another where none of them do. Such binarity could be an extreme assumption, and it may be more sound to consider the case where terrestrial planets are in either regime with a given probability. Heterogeneity in convection regimes could in principle increase dramatically the number of exoplanets that need to be characterized in order to distinguish predicted trends. This problem could be addressed by changing the framework in section 6.5 in order to include the prior probability that a planet is in either regime. This is made readily possible by the Bayesian formalism adopted here, where the evidence-related terms are extracted from the Bayes' theorem to obtain the Bayes factor (equation 6.13). Lastly, this prior probability could be informed by interior models that constrain how the stagnant lid and plate tectonics regime originate in relation with planetary mass and composition.

Lastly, the framework presented here paves the way to the quantitative assessment of biosignatures in the space of varying planetary contexts. In order to do so, the set of parameters or traits defining a candidate biosphere needs to be carefully constrained in order to predict neither particular nor "impossible" biosignatures. Impossible biosignatures correspond to that of organisms with combinations of traits that ignore certain physical and chemical constraints

that are thus able to grow in environments which are actually inhospitable. It could be possible to circumvent this problem by assessing the combinations of the biological model parameters that are found in Earth's biosphere and leverage its diversity in order to model organisms as generically as possible while making it certain that such organisms can exist. Chapter 2 provides the basis to do so, and future work should be concerned with using these results as prior information on the biological model parameters.

Concluding remarks

General perspectives

In this thesis, I have explored many different facets of the concepts of habitability and biosignatures. We have first seen, in part I, how one could build a measure of habitability from the ground up. In an era where liquid water has been found beyond Earth and is expected to be characterized at the surface of extrasolar planets in the coming years, such a metric that goes beyond establishing this criterion for habitability is needed. By accepting to let go of the idea of a universal and unambiguous signature of life as well as of holistic approaches, we can humbly start with what we know and follow the steps until they lead us somewhere, be it positive or negative detection. While some authors have identified the need for this type of approaches[23,34,109], the work presented in this manuscript is to my knowledge the first attempt at such an integration between ecological and geochemical modeling in the context of habitability.

We have developed a model, in chapter 1, designed to focus on one particular limitation to growth (and thus the ability of microorganisms to survive): the energy yield of the catabolic reaction. In that, it provides us with a unitary measure of habitability, that can be integrated over different environments and over organisms with different catabolic reaction or enzyme kinetics. It seems sound that energy availability acts as an essential step in determining whether an organism can grow in a given environment, but it should be kept in mind that the energy-centered approach adopted here applies to organisms that have low energy yield catabolic reactions. Therefore, this model is by no means intended to be a universal one, but it does provide us with a useful framework to build up from, especially if one considers these low-energy ecosystems as a necessary first step in the evolution and complexification of the biosphere.

The growth of such organisms being more likely to be limited by energy availability rather than anabolic nutrients remains an assumption. Even though it has been a decade since Kleerebezem and Van Loosdrecht (2010)[62] have proposed a framework to carry out thermodynamic state analysis of environmental systems, there have not been to my knowledge much research on what limits the

growth and production of extremophiles in their natural settings. In oceanic ecosystems, a nutrient is deemed limiting if its addition results in a "bloom" (this was famously done with iron in the austral ocean[67]). If anaerobic microbes are indeed limited by the energy yield of the catabolic reaction in their natural settings, the addition of an anabolic nutrient should not result in a bloom.

In chapter 2, we have demonstrated how the parameters of the model developed in chapter 1 can be interpreted in relation to functional traits. To me, it is crucial that an "operational" conceptualization of extraterrestrial life can be related to the organisms that we know on Earth. This stems from a methodological argument; the hypothesis of life being able to survive in an environment completely alien to those where we know life can exist, such as the clouds of Venus[236] or the atmosphere of brown dwarf stars[237] is an interesting prospective exercise, but exposes us to an unconstrained risk of false positives. Chapter 2 attempts to propose the basis for extrapolating from the set of thermokinetic parameters that have been estimated to integrate the viability criterion in chapter 1 over different physiological parameters.

It is a modest contribution as there are so many environmental variables that could be relevant to habitability such as pH, salinity or ionizing radiation. The model developed in chapter 1 could in principle be adapted to take those variables into account: pH can affect the yield of the catabolic reaction, salinity and ionizing radiation (pH as well) could also be interpreted as factors increasing the maintenance rate. These are surely directions to explore but work is needed in order to translate these limitation into a quantified energetic cost for the cell. Furthermore, this model helps us identify the empirical knowledge that is lacking to better refine the field of possibilities that a criterion for habitability should be able to explore. Chapter 2 calls for putting together a growth temperature data set, concerning a relatively narrow group of organisms that share the same metabolism and live at high temperatures.

This, I hope, can serve as a basis to design experiments that could help us better understand the presumed existence of an absolute temperature limit to life. Last, chapter 2 uses growth rate data to estimate the range of values that kinetic parameters of the model can take in naturally occurring organisms, but has not be tested for ecosystem-level predictions. It is still unknown whether this model is accurate in estimating population size and production in natural environments, or their participation to geochemical fluxes

(*e.g* methane production). Yet, this is a necessary step to take
in order to assess the validity of this type of model when applied
to predicting quantitative biosignatures. This calls for a different
experimental setting than those that could be used to assess growth
rates as a function of temperature. Here, experiments must be
carried out in bioreactors, analogs to the chemostat model described
in the introduction to part I. This might be particularly challenging
to do in practice, as methanogens need strictly anaerobic conditions
and require dihydrogen which is impractical to experiment with,
due to its hazardous properties.

With those limitations well in mind, I have shown in chapter
3 that there is nonetheless much that can be learned by apply-
ing this model. How surprising, after all, that the production of
methane by a population of methanogens matches with the obser-
vations made by the Cassini mission. It is perhaps even more puz-
zling that so much dihydrogen is expected to be left in the plume
when a population of methanogens is present. Both these observa-
tions could probably not have been made based on purely verbal
arguments. Models can remind us that there is no such thing as
common sense in science, and that it is always worthwhile to lever-
age rigorous mathematical conceptualization to put hypothesis into
numbers that can be compared to observations. That the methane
abundance in the plume matches with the simulated biotic produc-
tion has little to do with claiming that life does exist in Enceladus,
but rather helps shaping the hypothesis that it does.

In chapter 4, we related the hypothesis of a bioshere to abundance
of organic molecules in the plume. Ideally, we should look for an
unambiguous sign of life, but such a thing may be extremely difficult
to obtain (*e.g* sampling in Enceladus's hydrothermal vent would
require drilling through tens of kilometers of ice), and unambiguous
indirect biosignatures may not exist (amino acids can be produced
abiotically or biotically). Therefore, it is the collection of consistent
predictions that hold up to different observations that could make
for the most convincing evidence of life. In chapter 4, we have
taken a step in that direction by showing that an amino acid such
as glycine can still serve as an interesting biosignature, if it is found
in quantities not predicted by abiotic synthesis and consistent with
methane abundance in the plume. Moreover, if several amino acids
are detected, their abundance relative to one another could also be
examined as a potential indication of their origin.

Lastly, our model of a hypothetical biosphere considers only

autotrophic methanogens. The addition of heterotrophs or graz-
ers that consume the primary production by hydrogenotrophic
methanogens should be considered as it could have an impact on
the expected concentrations of biomolecules that can be found in
the plume. Alternate scenario could also be considered, such as
heterotrophic primary production from fermentation of primordial
organic matter (*e.g* glycine). This catabolic reaction could pro-
vide an alternate scenario to explain the presence of dihydrogen in
the plume. This work is currently being studied, partly under my
supervision, by a Master student in our group.

Terrestrial exoplanets cannot be characterized to the same extent
that Enceladus was by the Cassini mission, but the advent of new
space and ground based observatories permits some hope as to the
possibility to characterize their atmosphere. Confident in the fact
that our framework could be useful and relevant also in the case
of exoplanets, I undertook the daunting task of adapting it to a
climate and geochemical modeling in chapter 5. As an entry point
to navigate the complexity such models can entail, I took as a
starting point the technical requirements to apply the biological
model, combined with an apparently simple question: do terrestrial
exoplanets even have the stabilizing carbonate-silicate weathering
cycle that Earth does? How could this question be answered by
characterizing the atmospheres of these exoplanets? In doing so,
I hope that the level of complexity of the model in chapter 6 is
adequate while remaining sufficiently flexible to ask big "what if"
questions. What if the Earth did not have plate tectonics? What if
it was slightly closer to or farther from the Sun? What would the
Earth look like had oxygenic photosynthesis never appeared and
the biosphere remained anaerobic? The model in chapter 5 takes
a step in helping us explore how perturbation of the parameters or
features (such as plate tectonics) that we think have made Earth an
habitable planet affect habitability. Therefore, it allows us to better
understand how the Earth is situated in the context of habitable
terrestrial planets. Does Earth-like habitability (liquid water ocean,
temperate conditions) apply only to a narrow range of contexts
around that of the Earth? Or is it a property that is shared more
widely by planets in different contexts with different features?
Chapter 6 considers our ability to test predictions and sugges-
tions stemming from simulations against the observation of terres-
trial exoplanets atmospheres. We have shown that there is a trade-
off between the depth at which atmospheres are characterized (the

threshold for CO_2 detection) and the number of exoplanets that need to be characterized in order to achieve statistical power. Because the number of candidate Earth-like planets may be very limited, we also suggest how the addition of context variables such as planetary age and or mass could help achieving a higher resolving power between predicted trends in exoplanet populations.

There remains work to be done to better simulate exoplanet biosignatures, *e.g* using the results of chapter 2 to sample the parameters for the biological model, or modeling the coexistence of different metabolisms as in Sauterey et al. (2020)[22]. But the proposition in chapter 6 that biosignatures can be interpreted as trends in the atmospheric compositions of a population of exoplanets rather than at the scale of any single one is a somewhat bold statement. Could it be that the first indications that life exists beyond our solar system will be in the form of an estimated frequency that does not point to any particular exoplanet? Following the methodology used to estimate whether planets have or do not have a continental weathering cycle, the hypothesis that is considered is expressed at the population level. Precisely, in section 6.5 we compare the hypotheses "all terrestrial planets have a continental weathering cycle" and "no terrestrial planet has a continental weathering cycle". These hypotheses could be re-framed in order to account for heterogeneous cases where frequencies are attached to either scenario but the principle remains that we do not infer the existence or nonexistence of the continental weathering cycle at the scale of one exoplanet. Even though "population-level biosignatures" may be our best chance in the short term given the limitations of the instruments in the coming decades, there remains possible that planet-level biosignatures, such as the $CH_4 : CO$ ratio can be defined. I hope that exploring the parameter and metabolic space with our model will help assess whether such markers remain relevant biosignatures in diverse planetary contexts and interior scenarios.

Personal comments

All things considered, the solar system is scarcely explored, but there have not been *any* observation of "Earth-like" exoplanets. No Cassini mission to return jaw-dropping pictures not even more blurry ones from Voyager, no Perseverance rover with its flying companion. Nothing. And there will virtually never be any such observations for exoplanets. Because so little is known about terrestrial exoplanets, the subject of their habitability and biosignatures is of vertiginous complexity. It has been both incredibly exciting and immensely frustrating to navigate the many degrees of freedom that our relative ignorance allows.

It has been even more challenging that these degrees of freedom do not pertain to any one well-defined scientific field, but to various areas of scientific knowledge. On top of the bridging between thermodynamics and ecological modeling in chapter 1, the physical circulation modeling in chapters 3 and 4, I had to try myself at understanding how the climate and photochemistry are modeled, what limits exoplanet detection and the characterization of their atmosphere and how planetary systems form. The dialog with experts of the different fields that compose the assemblage proposed in this manuscript has also turned out to be an interesting experiment in itself. Researchers in their fields have different vocabularies, and sometimes the same words do not have the same meaning to every one depending on their area of expertise. I observed that to be particularly true for the vocabulary related to Bayesian statistics. Every field has its own usual point of entry to statistics, people with a background in biology tend to have a strong frequentist culture, where null hypotheses (noise) are often made simple at the cost of great effort in experimental design; whereas I found people with a background in physics to tend to be focused on a physical description of the noise model (*e.g* by finely modeling the physical basis of an instrument's measure). Therefore two languages coexist to describe more or less the same mathematical objects, between hypothesis-based statistics and "signal-to-noise" oriented measure. Having to place myself at the intersection of these worlds has been

extremely enriching.

Multiplying the perspectives on Bayesian statistics, or any other object or method makes them all the more accessible to me and to others. Second, my interest for science and research as well as my motivation for pursuing a doctorate has always been rooted in a curiosity for all fields of science. I chose my undergraduate studies in biology as it was for me the way to study all natural sciences together. I then took a year during my masters to study ocean and atmosphere sciences. This also allowed me to witness how seemingly closely related natural sciences such as ecology and geosciences can be built upon different scientific cultures and paradigms. I always wanted to cultivate knowledge in diverse areas of science, and in that I am convinced that the projects exposed in this manuscript were the best exercise of research I could hope for.

Lastly, I want to acknowledge the context in which this manuscript was written and the research work presented here has been carried out. There has been a ongoing global pandemic for the better part of the three years that this doctoral project took. We have had to learn to work from our homes, for me it was in a relatively small shared parisian apartment. This has not been easy, and it was frustrating to be locked inside while working on such an interdisciplinary subject, that calls for meeting with people from different backgrounds and areas of expertise. But people have lost their lives to this epidemic, a great number of them in fact. Others have lost their livelihood, or were locked inside their house with a violent spouse. Besides the pandemic, a war has started on the European continent. People in Ukraine have lost their homes to bombs, and their relatives to war crimes. There have been many people seeking asylum, from this war and others, here in France and in other European countries. Often, these people have fled war but continue facing violence in their host countries. All these crises unfold with climate change as a background. Each year that passes, people throughout the world and in underprivileged countries the most, are more likely to face food insecurity, more frequent hazardous weather conditions and risk having to leave their homes due to climate change in the coming years and decades.

Yet, I have spent all my energy and time to work on the possible detection of indirect evidence or absence of evidence of life on distant worlds. Why not instead work closer to environment related

214

policy-making, or on climate change science? Why not participate to find technical ways to mitigate the effects of climate change, or to feed the planet? Why engage in such an apparently pointless exercise of projection to worlds so distant to ours that they cannot affect us in the slightest? I believe there is purpose in pursuing fundamental knowledge. The body of knowledge that is shared by all of mankind, the awe-inspiring discoveries and questions that we get to ask constitute together a common goal that makes peace all the more worth seeking. They also grant us the freedom to choose the sense we find in the universe and the purpose we give to life, which makes our lives more precious and deserving of shared love. It is therefore an honor and a privilege to be entrusted by the public with its money and infrastructure to participate in this common quest for knowledge, aimed to better understand ourselves and each other in peace and cooperation.

Bibliography

[1] Museo Galileo -Institute and Museum of the History of Science . Feather and guinea experiment.

[2] Thomas Kuhn. *The structure of scientific revolutions.* University of Chicago press, 1962.

[3] Imre Lakatos. Falsification and the methodology of scientific research programmes. In *Can theories be refuted?*, pages 205–259. Springer, 1976.

[4] Paul Feyerabend. *Against method.* New Left Books, 1975.

[5] Leeuwenhoek Antoni Van. Observations, communicated to the publisher by Mr. Antony van Leewenhoeck, in a dutch letter of the 9th Octob. 1676. here English'd: concerning little animals by him observed in rain-well-sea- and snow water; as also in water wherein pepper had lain infused. *Phil. Trans. R. Soc.*, 12(133):821–831, 1677.

[6] Carl R Woese and George E Fox. Phylogenetic structure of the prokaryotic domain: the primary kingdoms. *Proceedings of the National Academy of Sciences*, 74(11):5088–5090, 1977.

[7] Louis Pasteur. *Études sur le vin, Ses maladies causes qui les provoquent. Procédés nouveaux pour le conserver et pour le vieillir.* Imprimerie Impériale, 1866.

[8] Charles Darwin. *On the origin of species by means of natural selection.* John Murray, 1859.

[9] Deborah S Kelley, Jeffrey A Karson, Donna K Blackman, Gretchen L FruÈh-Green, David A Butterfield, Marvin D Lilley, Eric J Olson, Matthew O Schrenk, Kevin K Roe, Geoff T Lebon, et al. An off-axis hydrothermal vent field near the Mid-Atlantic ridge at 30 N. *Nature*, 412(6843):145–149, 2001.

[10] Robert Hooke. *Micrographia or Some physiological descriptions of minutes bodies made by magnifying glasses : with observations and inquiries thereupon.* Jo. Martyn and Ja. Allestry (London), 1665.

[11] Charles S Cockell. Are microorganisms everywhere they can be? *Environmental Microbiology*, 23(11):6355–6363, 2021.

[12] Stanley L Miller. A production of amino acids under possible primitive earth conditions. *Science*, 117(3046):528–529, 1953.

[13] Guilhem Doulcier. *Evolution of Collective-level Darwinian Properties.* Theses, Université Paris sciences et lettres, December 2019. URL `https://pastel.archives-ouvertes.fr/tel-02917058`.

[14] Philippe Nghe, Wim Hordijk, Stuart A Kauffman, Sara I Walker, Francis J Schmidt, Harry Kemble, Jessica AM Yeates, and Niles Lehman. Prebiotic network evolution: six key parameters. *Molecular BioSystems*, 11(12):3206–3217, 2015.

[15] Thomas Heams. *Infravies-Le vivant sans frontières*. Média Diffusion, 2019.

[16] Fabia U Battistuzzi, Andreia Feijao, and S Blair Hedges. A genomic timescale of prokaryote evolution: insights into the origin of methanogenesis, phototrophy, and the colonization of land. *BMC evolutionary biology*, 4(1):1–14, 2004.

[17] Madeline C Weiss, Filipa L Sousa, Natalia Mrnjavac, Sinje Neukirchen, Mayo Roettger, Shijulal Nelson-Sathi, and William F Martin. The physiology and habitat of the last universal common ancestor. *Nature microbiology*, 1(9):1–8, 2016.

[18] Horace A. Barker. *Bacterial Fermentations*. Wiley, 1956.

[19] Lynn Sagan. On the origin of mitosing cells. *Journal of theoretical biology*, 14(3):225–IN6, 1967.

[20] Ron Sender, Shai Fuchs, and Ron Milo. Revised estimates for the number of human and bacteria cells in the body. *PLoS biology*, 14(8):e1002533, 2016.

[21] Yinon M Bar-On, Rob Phillips, and Ron Milo. The biomass distribution on Earth. *Proceedings of the National Academy of Sciences*, 115(25):6506–6511, 2018.

[22] Boris Sauterey, Benjamin Charnay, Antonin Affholder, Stéphane Mazevet, and Régis Ferrière. Co-evolution of primitive methane-cycling ecosystems and early Earth's atmosphere and climate. *Nature Communications*, 11(1):1–12, 2020.

[23] P Kharecha, James Kasting, and J Siefert. A coupled atmosphere–ecosystem model of the early Archean Earth. *Geobiology*, 3(2):53–76, 2005.

[24] Kazumi Ozaki, Eiichi Tajika, Peng K Hong, Yusuke Nakagawa, and Christopher T Reinhard. Effects of primitive photosynthesis on Earth's early climate system. *Nature Geoscience*, 11(1):55–59, 2018.

[25] Engineering National Academies of Sciences and Medicine. *Origins, Worlds, and Life: A Decadal Strategy for Planetary Science and Astrobiology 2023-2032*. The National Academies Press, Washington, DC, 2022.

[26] Ray T Reynolds, Steven W Squyres, David S Colburn, and Christopher P McKay. On the habitability of Europa. *Icarus*, 56(2):246–254, 1983.

[27] Thomas M McCollom. Methanogenesis as a potential source of chemical energy for primary biomass production by autotrophic organisms in hydrothermal systems on Europa. *Journal of Geophysical Research: Planets*, 104(E12): 30729–30742, 1999.

[28] Andreas Nathues, Nico Schmedemann, G Thangjam, JH Pasckert, K Mengel, J Castillo-Rogez, EA Cloutis, H Hiesinger, M Hoffmann, L Le Corre, et al. Recent cryovolcanic activity at Occator crater on Ceres. *Nature Astronomy*, 4(8):794–801, 2020.

[29] Michel Mayor and Didier Queloz. A Jupiter-mass companion to a solar-type star.

Nature, 378(6555):355–359, 1995.

[30] Muriel Gargaud, Ricardo Amils, and Henderson James Cleaves. *Encyclopedia of astrobiology*, volume 1. Springer Science & Business Media, 2011.

[31] Nicola McLoughlin. Biogenicity. In Muriel Gargaud, Ricardo Amils, José Cernicharo Quintanilla, Henderson James (Jim) Cleaves, William M. Irvine, Daniele L. Pinti, and Michel Viso, editors, *Encyclopedia of Astrobiology*, pages 171–172. Springer Berlin Heidelberg, Berlin, Heidelberg, 2011. ISBN 978-3-642-11274-4. doi: 10.1007/978-3-642-11274-4_171. URL https://doi.org/10.1007/978-3-642-11274-4_171.

[32] James F Kasting, Daniel P Whitmire, and Ray T Reynolds. Habitable zones around main sequence stars. *Icarus*, 101(1):108–128, 1993.

[33] Su-Shu Huang. Occurrence of life in the universe. *American scientist*, 47(3):397–402, 1959.

[34] David C Catling, Joshua Krissansen-Totton, Nancy Y Kiang, David Crisp, Tyler D Robinson, Shiladitya DasSarma, Andrew J Rushby, Anthony Del Genio, William Bains, and Shawn Domagal-Goldman. Exoplanet biosignatures: a framework for their assessment. *Astrobiology*, 18(6):709–738, 2018.

[35] Jacques Monod. *Le Hasard et la Nécessité : Essai sur la philosophie naturelle de la biologie moderne*. Seuil, 1970.

[36] Joshua Krissansen-Totton, Stephanie Olson, and David C Catling. Disequilibrium biosignatures over Earth history and implications for detecting exoplanet life. *Science advances*, 4 (1):eaao5747, 2018.

[37] Joshua Krissansen-Totton, David S Bergsman, and David C Catling. On detecting biospheres from chemical thermodynamic disequilibrium in planetary atmospheres. *Astrobiology*, 16(1):39–67, 2016.

[38] Stuart Bartlett and Michael L Wong. Defining lyfe in the universe: From three privileged functions to four pillars. *Life*, 10 (4):42, 2020.

[39] Stuart Bartlett, Jiazheng Li, Lixiang Gu, Lana Sinapayen, Siteng Fan, Vijay Natraj, Jonathan H Jiang, David Crisp, and Yuk L Yung. Assessing planetary complexity and potential agnostic biosignatures using epsilon machines. *Nature Astronomy*, 6(3):387–392, 2022.

[40] Alfred C Redfield. The biological control of chemical factors in the environment. *American scientist*, 46(3):230A–221, 1958.

[41] Christopher P Kempes, Michael J Follows, Hillary Smith, Heather Graham, Christopher H House, and Simon A Levin. Generalized stoichiometry and biogeochemistry for astrobiological applications. *Bulletin of Mathematical Biology*, 83(7):1–22, 2021.

[42] EE Sel'Kov. Self-oscillations in glycolysis 1. a simple kinetic model. *European Journal of Biochemistry*, 4(1):79–86, 1968.

[43] Jacques Laskar and Philippe Robutel. The chaotic obliquity of the planets. *Nature*, 361 (6413):608–612, 1993.

[44] Jacques Laskar, Frédéric Joutel, and Philippe Robutel. Stabilization of the Earth's obliquity by the Moon. *Nature*, 361(6413): 615–617, 1993.

[45] Joshua Krissansen-Totton, Maggie Thompson, Max L Galloway, and Jonathan J Fortney. Understanding planetary context to enable life detection on exoplanets and test the Copernican principle. *Nature Astronomy*, 6(2):189–198, 2022.

[46] Alex Bixel and Dániel Apai. Testing earthlike atmospheric evolution on exo-earths through oxygen absorption: required sample sizes and the advantage of age-based target selection. *The Astrophysical Journal*, 896 (2):131, 2020.

[47] Charles S Cockell, T Bush, C Bryce, S Direito, M Fox-Powell, JP Harrison, H Lammer, H Landenmark, Javier Martin-Torres, N Nicholson, et al. Habitability: a review. *Astrobiology*, 16(1):89–117, 2016.

[48] Charles S Cockell, Adam H Stevens, and Rebecca Prescott. Habitability is a binary property. *Nature Astronomy*, 3(11): 956–957, 2019.

[49] Joseph Grinnell. The niche-relationships of the California Thrasher. *The Auk*, 34(4):427–433, 1917.

[50] Robert A Armstrong, Helge Drange, John S Parslow, Thomas M Powell, Arnold H Taylor, and Ian J Totterdell. Trophic resolution. In *Towards a Model of Ocean Biogeochemical Processes*, pages 71–92. Springer, 1993.

[51] Hal L Smith and Paul Waltman. *The theory of the chemostat: dynamics of microbial competition*, volume 13. Cambridge university press, 1995.

[52] Eric J Chapman and Carrie J Byron. The flexible application of carrying capacity in ecology. *Global ecology and conservation*, 13:e00365, 2018.

[53] Odo Diekmann et al. A beginner's guide to adaptive dynamics. *Banach Center Publications*, 63:47–86, 2004.

[54] Stephen J Martin, Roy R Funch, Paul R Hanson, and Eun-Hye Yoo. A vast 4,000-year-old spatial pattern of termite mounds. *Current Biology*, 28(22):R1292–R1293, 2018.

[55] Charles Darwin. *The formation of vegetable mould, through the action of worms: with observations on their habits*. J. Murray, 1881.

[56] Filip JR Meysman, Jack J Middelburg, and Carlo HR Heip. Bioturbation: a fresh look at Darwin's last idea. *Trends in Ecology & Evolution*, 21(12): 688–695, 2006.

[57] Nancy Merino, Heidi S Aronson, Diana P Bojanova, Jayme Feyhl-Buska, Michael L Wong, Shu Zhang, and Donato Giovannelli. Living at the extremes: extremophiles and the limits of life in a planetary context. *Frontiers in microbiology*, 10:780, 2019.

220

[58] Jesse P Harrison, Nicolas Gheer-aert, Dmitry Tsigelnitskiy, and Charles S Cockell. The limits for life under multiple extremes. *Trends in microbiology*, 21(4): 204–212, 2013.

[59] Eriita G Jones and Charles H Lineweaver. To what extent does terrestrial life "follow the water"? *Astrobiology*, 10(3): 349–361, 2010.

[60] EG Nisbet and NH Sleep. The habitat and nature of early life. *Nature*, 409(6823):1083–1091, 2001.

[61] William F Martin and Filipa L Sousa. Early microbial evolution: the age of anaerobes. *Cold Spring Harbor Perspectives in Biology*, 8(2):a018127, 2016.

[62] Robbert Kleerebezem and Mark CM Van Loosdrecht. A generalized method for thermodynamic state analysis of environmental systems. *Critical Reviews in Environmental Science and Technology*, 40(1): 1–54, 2010.

[63] Christine Ray, Christopher R Glein, J Hunter Waite, Ben Teolis, Tori Hoehler, Julie A Huber, Jonathan Lunine, and Frank Postberg. Oxidation processes diversify the metabolic menu on Enceladus. *Icarus*, 364:114248, 2021.

[64] J Hunter Waite, Christopher R Glein, Rebecca S Perryman, Ben D Teolis, Brian A Magee, Greg Miller, Jacob Grimes, Mark E Perry, Kelly E Miller, Alexis Bouquet, et al. Cassini finds molecular hydrogen in the Enceladus plume: evidence for hydrothermal processes. *Science*, 356(6334):155–159, 2017.

[65] Steven F Sholes, Joshua Krissansen-Totton, and David C Catling. A maximum subsurface biomass on Mars from untapped free energy: Co and h2 as potential antibiosignatures. *Astrobiology*, 19(5): 655–668, 2019.

[66] Ramses M Ramirez, Ravi Kopparapu, Michael E Zugger, Tyler D Robinson, Richard Freedman, and James F Kasting. Warming early Mars with CO2 and H2. *Nature Geoscience*, 7(1):59–63, 2013.

[67] William G Sunda and Susan A Huntsman. Iron uptake and growth limitation in oceanic and coastal phytoplankton. *Marine chemistry*, 50(1-4):189–206, 1995.

[68] Alfred Clarence Redfield. *On the proportions of organic derivatives in sea water and their relation to the composition of plankton*, volume 1. university press of liverpool Liverpool, 1934.

[69] Eva E Stüeken, Roger Buick, Bradley M Guy, and Matthew C Koehler. Isotopic evidence for biological nitrogen fixation by molybdenum-nitrogenase from 3.2 Gyr. *Nature*, 520(7549):666–669, 2015.

[70] Charles S Cockell. Trajectories of martian habitability. *Astrobiology*, 2014.

[71] Morgan L Cable, Carolyn Porco, Christopher R Glein, Christopher R German, Shannon M MacKenzie, Marc Neveu, Tori M Hoehler, Amy E Hofmann, Amanda R Hendrix, Jennifer Eigenbrode, et al. The science case for a return

to Enceladus. *The planetary science journal*, 2(4):132, 2021.

[72] Tori M Hoehler. An energy balance concept for habitability. *Astrobiology*, 7(6):824–838, 2007.

[73] Tori M Hoehler, Jan P Amend, and Everett L Shock. A "follow the energy" approach for astrobiology. *Astrobiology*, 7(6):819–823, 2007.

[74] PM Higgins and CS Cockell. A bioenergetic model to predict habitability, biomass and biosignatures in astrobiology and extreme conditions. *Journal of the Royal Society Interface*, 17 (171):20200588, 2020.

[75] Ken Takai, Kentaro Nakamura, Tomohiro Toki, Urumu Tsunogai, Masayuki Miyazaki, Junichi Miyazaki, Hisako Hirayama, Satoshi Nakagawa, Takuro Nunoura, and Koki Horikoshi. Cell proliferation at 122 C and isotopically heavy CH4 production by a hyperthermophilic methanogen under high-pressure cultivation. *Proceedings of the National Academy of Sciences*, 105(31): 10949–10954, 2008.

[76] Cyril Norman Hinshelwood. The chemical kinetics of the bacterial cell. Technical report, 1946.

[77] James F Gillooly, James H Brown, Geoffrey B West, Van M Savage, and Eric L Charnov. Effects of size and temperature on metabolic rate. *science*, 293 (5538):2248–2251, 2001.

[78] L Tijhuis, Mark CM Van Loosdrecht, and JJ Heijnen. A thermodynamically based correlation for maintenance Gibbs energy requirements in aerobic and anaerobic chemotrophic growth. *Biotechnology and bioengineering*, 42(4):509–519, 1993.

[79] Joseph J Heijnen and Robbert Kleerebezem. Bioenergetics of microbial growth. *Encyclopedia of Industrial Biotechnology: Bioprocess, Bioseparation, and Cell Technology*, 1:267–291, 1999.

[80] Tori M Hoehler, Marc J Alperin, Daniel B Albert, and Christopher S Martens. Apparent minimum free energy requirements for methanogenic Archaea and sulfate-reducing bacteria in an anoxic marine sediment. *FEMS Microbiology Ecology*, 38(1):33–41, 2001.

[81] John Rumble. *CRC handbook of chemistry and physics*. CRC press, 2017.

[82] Richard W Eppley. Temperature and phytoplankton growth in the sea. *Fish. bull*, 70(4): 1063–1085, 1972.

[83] Philipp Noll, Lars Lilge, Rudolf Hausmann, and Marius Henkel. Modeling and exploiting microbial temperature response. *Processes*, 8(1):121, 2020.

[84] Roy M Daniel, Michelle E Peterson, Michael J Danson, Nicholas C Price, Sharon M Kelly, Colin R Monk, Cristina S Weinberg, Matthew L Oudshoorn, and Charles K Lee. The molecular basis of the effect of temperature on enzyme activity. *Biochemical journal*, 425(2): 353–360, 2010.

[85] Ruth-Sophie Taubner, Patricia Pappenreiter, Jennifer Zwicker, Daniel Smrzka, Christian Pruckner, Philipp Kolar, Sébastien Bernacchi, Arne H Seifert, Alexander Krajete, Wolfgang Bach, et al. Biological methane production under putative Enceladus-like conditions. *Nature Communications*, 9(1):748, 2018.

[86] L Rosso, JR Lobry, and Jean-Pierre Flandrois. An unexpected correlation between cardinal temperatures of microbial growth highlighted by a new model. *Journal of Theoretical Biology*, 162(4):447–463, 1993.

[87] G Schubert, C Covey, A Del Genio, LS Elson, G Keating, A Seiff, RE Young, J Apt, CC Counselman III, AJ Kliore, et al. Structure and circulation of the Venus atmosphere. *Journal of Geophysical Research: Space Physics*, 85(A13):8007–8025, 1980.

[88] M Ya Marov, VS Avduevsky, NF Borodin, AP Ekonomov, VV Kerzhanovich, VP Lysov, B Ye Moshkin, MK Rozhdestvensky, and OL Ryabov. Preliminary results on the venus atmosphere from the Venera 8 descent module. *Icarus*, 20(4):407–421, 1973.

[89] Gaël Choblet, Gabriel Tobie, Christophe Sotin, Marie Běhounková, Ondřej Čadek, Frank Postberg, and Ondřej Souček. Powering prolonged hydrothermal activity inside Enceladus. *Nature Astronomy*, 1(12):841, 2017.

[90] Joseph R Michalski, Tullis C Onstott, Stephen J Mojzsis, John Mustard, Queenie HS Chan, Paul B Niles, and Sarah Stewart Johnson. The martian subsurface as a potential window into the origin of life. *Nature Geoscience*, 11(1): 21–26, 2018.

[91] Igor N Berezovsky and Eugene I Shakhnovich. Physics and evolution of thermophilic adaptation. *Proceedings of the National Academy of Sciences*, 102(36): 12742–12747, 2005.

[92] Konstantin B Zeldovich, Igor N Berezovsky, and Eugene I Shakhnovich. Protein and DNA sequence determinants of thermophilic adaptation. *PLoS computational biology*, 3(1):e5, 2007.

[93] Ross Corkrey, Tom A McMeekin, John P Bowman, David A Ratkowsky, June Olley, and Tom Ross. The biokinetic spectrum for temperature. *PLoS One*, 11(4): e0153343, 2016.

[94] Mridul K Thomas, Colin T Kremer, Christopher A Klausmeier, and Elena Litchman. A global pattern of thermal adaptation in marine phytoplankton. *Science*, 338(6110):1085–1088, 2012.

[95] JPPM Smelt and S Brul. Thermal inactivation of microorganisms. *Critical reviews in food science and nutrition*, 54(10): 1371–1385, 2014.

[96] Ghjuvan Micaelu Grimaud, Francis Mairet, Antoine Sciandra, and Olivier Bernard. Modeling the temperature effect on the specific growth rate of phytoplankton: a review. *Reviews in Environmental Science and Bio/Technology*, 16 (4):625–645, 2017.

[97] David A Ratkowsky, June Olley, TA McMeekin, and A Ball. Relationship between temperature and growth rate of bacterial cultures. *Journal of bacteriology*, 149(1):1–5, 1982.

[98] Frank H Johnson and Isaac Lewin. The growth rate of E. coli in relation to temperature, quinine and coenzyme. *Journal of Cellular and Comparative Physiology*, 28(1):47–75, 1946.

[99] Ross Corkrey, Cameron Macdonald, and Tom McMeekin. The biokinetic spectrum for temperature and optimal darwinian fitness. *Journal of theoretical biology*, 462:171–183, 2019.

[100] Stefan AH Geritz, Eva Kisdi, Johan AJ Metz, et al. Evolutionarily singular strategies and the adaptive growth and branching of the evolutionary tree. *Evolutionary ecology*, 12 (1):35–57, 1998.

[101] Johan AJ Metz, Roger M Nisbet, and Stefan AH Geritz. How should we define 'fitness' for general ecological scenarios? *Trends in ecology & evolution*, 7 (6):198–202, 1992.

[102] Peter A Abrams. Modelling the adaptive dynamics of traits involved in inter-and intraspecific interactions: an assessment of three methods. *Ecology Letters*, 4(2):166–175, 2001.

[103] Roy M Daniel. The upper limits of enzyme thermal stability. *Enzyme and Microbial Technology*, 19(1):74–79, 1996.

[104] Olivier Bernard and Barbara Rémond. Validation of a simple model accounting for light and temperature effect on microalgal growth. *Bioresource technology*, 123:520–527, 2012.

[105] Pauli Virtanen, Ralf Gommers, Travis E Oliphant, Matt Haberland, Tyler Reddy, David Cournapeau, Evgeni Burovski, Pearu Peterson, Warren Weckesser, Jonathan Bright, et al. SciPy 1.0: fundamental algorithms for scientific computing in Python. *Nature methods*, 17(3):261–272, 2020.

[106] Emmanuel Klinger, Dennis Rickert, and Jan Hasenauer. pyABC: distributed, likelihood-free inference. *Bioinformatics*, 34(20):3591–3593, 2018.

[107] Irene Maffucci, Damien Laage, Fabio Sterpone, and Guillaume Stirnemann. Thermal adaptation of enzymes: impacts of conformational shifts on catalytic activation energy and optimum temperature. *Chemistry–A European Journal*, 26(44):10045–10056, 2020.

[108] Donal A Hickey and Gregory AC Singer. Genomic and proteomic adaptations to growth at high temperature. *Genome biology*, 5(10):1–7, 2004.

[109] R Corkrey, TA McMeekin, JP Bowman, DA Ratkowsky, J Olley, and T Ross. The biokinetic spectrum for temperature: astrobiological significance. In *2016 Australasian Astrobiology Meeting*, pages 26–27, 2016.

[110] DP Cruikshank, Carl B Pilcher, and D Morrison. Identification of a new class of satellites in the outer solar system. *The Astrophysical Journal*, 217:1006–1010, 1977.

[111] B Buratti and J Veverka. Voyager photometry of rhea, dione, tethys, enceladus and mimas. *Icarus*, 58(2):254–264, 1984.

[112] Ray T Reynolds, Christopher P McKay, and James F Kasting. Europa, tidally heated oceans, and habitable zones around giant planets. *Advances in Space Research*, 7(5):125–132, 1987.

[113] Frank Spahn, Jürgen Schmidt, Nicole Albers, Marcel Hörning, Martin Makuch, Martin Seiß, Sascha Kempf, Ralf Srama, Valeri Dikarev, Stefan Helfert, et al. Cassini dust measurements at Enceladus and implications for the origin of the E ring. *Science*, 2006.

[114] Frank Postberg, Sascha Kempf, Jürgen Schmidt, N Brilliantov, Alexander Beinsen, Bernd Abel, Udo Buck, and Ralf Srama. Sodium salts in E-ring ice grains from an ocean below the surface of Enceladus. *Nature*, 459 (7250):1098, 2009.

[115] J Hunter Waite, WS Lewis, BA Magee, JI Lunine, WB McKinnon, CR Glein, O Mousis, DT Young, T Brockwell, J Westlake, et al. Liquid water on Enceladus from observations of ammonia and 40 Ar in the plume. *Nature*, 460 (7254):487, 2009.

[116] Frank Postberg, Nozair Khawaja, Bernd Abel, Gael Choblet, Christopher R Glein, Murthy S Gudipati, Bryana L Henderson, Hsiang-Wen Hsu, Sascha Kempf, Fabian Klenner, et al. Macromolecular organic compounds from the depths of Enceladus. *Nature*, 558(7711): 564–568, 2018.

[117] Antonin Affholder, François Guyot, Boris Sauterey, Régis Ferrière, and Stéphane Mazevet. Bayesian analysis of Enceladus's plume data to assess methanogenesis. *Nature Astronomy*, pages 1–10, 2021.

[118] Matthew O Schrenk, Deborah S Kelley, Sheryl A Bolton, and John A Baross. Low archaeal diversity linked to subseafloor geochemical processes at the Lost City hydrothermal field, mid-atlantic ridge. *Environmental Microbiology*, 6(10):1086–1095, 2004.

[119] Carolyn C Porco, Luke Dones, and Colin Mitchell. Could it be snowing microbes on Enceladus? assessing conditions in its plume and implications for future missions. *Astrobiology*, 17 (9):876–901, 2017.

[120] Elliot L Steel, Alfonso Davila, and Christopher P McKay. Abiotic and biotic formation of amino acids in the Enceladus ocean. *Astrobiology*, 17(9):862–875, 2017.

[121] Shannon M MacKenzie, Marc Neveu, Alfonso F Davila, Jonathan I Lunine, Kathleen L Craft, Morgan L Cable, Charity M Phillips-Lander, Jason D Hofgartner, Jennifer L Eigenbrode, J Hunter Waite, et al. The Enceladus orbilander mission concept: balancing return and resources in the search for life. *The Planetary Science Journal*, 2(2):77, 2021.

[122] Isis Criouet, J-C Viennet, Pierre Jacquemot, Maguy Jaber, and Sylvain Bernard. Abiotic formation of organic biomorphs under

diagenetic conditions. *Geochemical Perspectives Letters*, 16:40–46, 2021.

[123] Everett L Shock and Mitchell D Schulte. Organic synthesis during fluid mixing in hydrothermal systems. *Journal of Geophysical Research: Planets*, 103(E12):28513–28527, 1998.

[124] Linda Spilker. Cassini-Huygens' exploration of the Saturn system: 13 years of discovery. *Science*, 364(6445):1046–1051, 2019.

[125] PC Thomas, R Tajeddine, MS Tiscareno, JA Burns, J Joseph, TJ Loredo, P Helfenstein, and C Porco. Enceladus's measured physical libration requires a global subsurface ocean. *Icarus*, 264:37–47, 2016.

[126] BE Schmidt, HG Sizemore, KHG Hughson, KD Duarte, VN Romero, JEC Scully, PM Schenk, DL Buczkowski, DA Williams, Andreas Nathues, et al. Post-impact cryo-hydrologic formation of small mounds and hills in Ceres's Occator crater. *Nature Geoscience*, 13(9):605–610, 2020.

[127] Andrew Martin and Andrew McMinn. Sea ice, extremophiles and life on extra-terrestrial ocean worlds. *International Journal of Astrobiology*, 17(1):1–16, 2018.

[128] Hsiang-Wen Hsu, Frank Postberg, Yasuhito Sekine, Takazo Shibuya, Sascha Kempf, Mihály Horányi, Antal Juhász, Nicolas Altobelli, Katsuhiko Suzuki, Yuka Masaki, et al. Ongoing hydrothermal activities within Enceladus. *Nature*, 519(7542):207, 2015.

[129] Christopher R Glein, John A Baross, and J Hunter Waite Jr. The pH of Enceladus' ocean. *Geochimica et Cosmochimica Acta*, 162:202–219, 2015.

[130] O Mousis, JI Lunine, JH Waite, B Magee, WS Lewis, KE Mandt, Didier Marquer, and D Cordier. Formation conditions of Enceladus and origin of its methane reservoir. *The Astrophysical Journal Letters*, 701(1):L39, 2009.

[131] CP McKay, Bishun N Khare, Ranjamin Amin, Martin Klasson, and Timothy A Kral. Possible sources for methane and C2–C5 organics in the plume of Enceladus. *Planetary and Space Science*, 71(1):73–79, 2012.

[132] Holger W Jannasch and Michael J Mottl. Geomicrobiology of deep-sea hydrothermal vents. *Science*, 229(4715):717–725, 1985.

[133] Reiner Hedderich and William B Whitman. Physiology and biochemistry of the methane-producing Archaea. *The Prokaryotes: Prokaryotic Physiology and Biochemistry*, pages 635–662, 2013.

[134] BJ Travis and G Schubert. Keeping Enceladus warm. *Icarus*, 250:32–42, 2015.

[135] William Martin, John Baross, Deborah Kelley, and Michael J Russell. Hydrothermal vents and the origin of life. *Nature Reviews Microbiology*, 6(11):805, 2008.

[136] Christopher P McKay, Carolyn C Porco, Travis Altheide, Wanda L Davis, and Timothy A Kral. The possible origin and persistence of life on Enceladus

and detection of biomarkers in the plume. *Astrobiology*, 8(5): 909–919, 2008.

[137] Ralph D Lorenz. A Bayesian approach to biosignature detection on ocean worlds. *Nature Astronomy*, 3(6):466–467, 2019.

[138] Alexis Bouquet, Olivier Mousis, J Hunter Waite, and Sylvain Picaud. Possible evidence for a methane source in Enceladus' ocean. *Geophysical Research Letters*, 42(5):1334–1339, 2015.

[139] Marc Neveu and Alyssa R Rhoden. Evolution of Saturn's mid-sized moons. *Nature astronomy*, 3(6):543–552, 2019.

[140] Dina Prialnik and Rainer Merk. Growth and evolution of small porous icy bodies with an adaptive-grid thermal evolution code: I. application to Kuiper belt objects and Enceladus. *Icarus*, 197(1):211–220, 2008.

[141] James H Roberts. The fluffy core of Enceladus. *Icarus*, 258: 54–66, 2015.

[142] Jason C Goodman, Geoffrey C Collins, John Marshall, and Raymond T Pierrehumbert. Hydrothermal plume dynamics on Europa: Implications for chaos formation. *Journal of Geophysical Research: Planets*, 109(E3), 2004.

[143] Jason C Goodman and Erik Lenferink. Numerical simulations of marine hydrothermal plumes for Europa and other icy worlds. *Icarus*, 221(2):970–983, 2012.

[144] Begüm D Topçuoğlu, Lucy C Stewart, Hilary G Morrison, David A Butterfield, Julie A

Huber, and James F Holden. Hydrogen limitation and syntrophic growth among natural assemblages of thermophilic methanogens at deep-sea hydrothermal vents. *Frontiers in microbiology*, 7:1240, 2016.

[145] NH Sleep, A Meibom, Th Fridriksson, RG Coleman, and DK Bird. H2-rich fluids from serpentinization: geochemical and biotic implications. *Proceedings of the National Academy of Sciences*, 101(35):12818–12823, 2004.

[146] Thomas M McCollom. Abiotic methane formation during experimental serpentinization of olivine. *Proceedings of the National Academy of Sciences*, 113 (49):13965–13970, 2016.

[147] Pierre Pudlo, Jean-Michel Marin, Arnaud Estoup, Jean-Marie Cornuet, Mathieu Gautier, and Christian P Robert. Reliable ABC model choice via random forests. *Bioinformatics*, 32(6):859–866, 2015.

[148] Michael J Russell, Laura M Barge, Rohit Bhartia, Dylan Bocanegra, Paul J Bracher, Elbert Branscomb, Richard Kidd, Shawn McGlynn, David H Meier, Wolfgang Nitschke, et al. The drive to life on wet and icy worlds. *Astrobiology*, 14(4): 308–343, 2014.

[149] Dimitar D Sasselov, John P Grotzinger, and John D Sutherland. The origin of life as a planetary phenomenon. *Science Advances*, 6(6):eaax3419, 2020.

[150] Jason Kalirai. Scientific discovery with the James Webb Space Telescope. *Contemporary Physics*, 59(3):251–290, 2018.

[151] Cynthia B Phillips and Robert T Pappalardo. Europa Clipper mission concept: Exploring Jupiter's ocean moon. *Eos, Transactions American Geophysical Union*, 95(20):165–167, 2014.

[152] Jennifer Eigenbrode, Robert E Gold, Christopher P McKay, Terry Hurford, and Alfonso Davila. Searching for life in an ocean world: The Enceladus Life Signatures and Habitability (ELSAH) mission concept. *cosp*, 42:F3–6, 2018.

[153] Morgan L Cable, Karla Clark, Jonathan I Lunine, Frank Postberg, Kim Reh, Linda Spilker, and J Hunter Waite. Enceladus Life Finder: The search for life in a habitable moon. 2016.

[154] Giuseppe Mitri, Frank Postberg, Jason M Soderblom, Peter Wurz, Paolo Tortora, Bernd Abel, Jason W Barnes, Marco Berga, Nathalie Carrasco, Athena Coustenis, et al. Explorer of Enceladus and Titan (E2T): Investigating ocean worlds' evolution and habitability in the solar system. *Planetary and space science*, 155:73–90, 2018.

[155] Mark A Lever, Karyn L Rogers, Karen G Lloyd, Jörg Overmann, Bernhard Schink, Rudolf K Thauer, Tori M Hoehler, and Bo Barker Jørgensen. Life under extreme energy limitation: a synthesis of laboratory- and field-based investigations. *FEMS microbiology reviews*, 39 (5):688–728, 2015.

[156] John P Connolly and Richard B Coffin. Model of carbon cycling in planktonic food webs. *Journal of Environmental Engineering*, 121(10):682–690, 1995.

[157] Pauli Virtanen, Ralf Gommers, Travis E. Oliphant, Matt Haberland, Tyler Reddy, David Cournapeau, Evgeni Burovski, Pearu Peterson, Warren Weckesser, Jonathan Bright, Stéfan J. van der Walt, Matthew Brett, Joshua Wilson, K. Jarrod Millman, Nikolay Mayorov, Andrew R. J. Nelson, Eric Jones, Robert Kern, Eric Larson, CJ Carey, İlhan Polat, Yu Feng, Eric W. Moore, Jake Vand erPlas, Denis Laxalde, Josef Perktold, Robert Cimrman, Ian Henriksen, E. A. Quintero, Charles R Harris, Anne M. Archibald, Antônio H. Ribeiro, Fabian Pedregosa, Paul van Mulbregt, and SciPy 1. 0 Contributors. SciPy 1.0–Fundamental Algorithms for Scientific Computing in Python. *arXiv e-prints*, page arXiv:1907.10121, Jul 2019.

[158] Katalin Csilléry, Michael GB Blum, Oscar E Gaggiotti, and Olivier François. Approximate Bayesian computation (ABC) in practice. *Trends in ecology & evolution*, 25(7):410–418, 2010.

[159] Scott A Sisson, Yanan Fan, and Mark Beaumont. *Handbook of approximate Bayesian computation*. Chapman and Hall/CRC, 2018.

[160] F. Pedregosa, G. Varoquaux, A. Gramfort, V. Michel, B. Thirion, O. Grisel, M. Blondel, P. Prettenhofer, R. Weiss, V. Dubourg, J. Vanderplas, A. Passos, D. Cournapeau, M. Brucher, M. Perrot, and E. Duchesnay. Scikit-learn: Machine learning in Python.

Journal of Machine Learning Research, 12:2825–2830, 2011.

[161] Benjamin M Tutolo, William E Seyfried, and Nicholas J Tosca. A seawater throttle on H2 production in Precambrian serpentinizing systems. *Proceedings of the National Academy of Sciences*, 117(26):14756–14763, 2020.

[162] Christopher R Glein and J Hunter Waite. The carbonate geochemistry of Enceladus' ocean. *Geophysical Research Letters*, 47(3):e2019GL085885, 2020.

[163] JL Charlou, JP Donval, Y Fouquet, P Jean-Baptiste, and N Holm. Geochemistry of high H2 and CH4 vent fluids issuing from ultramafic rocks at the Rainbow hydrothermal field (36 14' N, MAR). *Chemical geology*, 191(4):345–359, 2002.

[164] Luciano Iess, DJ Stevenson, M Parisi, D Hemingway, RA Jacobson, JI Lunine, F Nimmo, JW Armstrong, SW Asmar, M Ducci, et al. The gravity field and interior structure of Enceladus. *Science*, 344(6179):78–80, 2014.

[165] JR Spencer, CJA Howett, A Verbiscer, TA Hurford, M Segura, and DC Spencer. Enceladus heat flow from high spatial resolution thermal emission observations. *EPSC Abstracts*, 8, 2013.

[166] Peter LL Walls, James C Bird, and Lydia Bourouiba. Moving with bubbles: a review of the interactions between bubbles and the microorganisms that surround them. *American Zoologist*, 54(6):1014–1025, 2014.

[167] Manuel Bedrossian, Chris Lindensmith, and Jay L Nadeau. Digital holographic microscopy, a method for detection of microorganisms in plume samples from Enceladus and other icy worlds. *Astrobiology*, 17(9):913–925, 2017.

[168] Melissa Guzman, Ralph Lorenz, Dana Hurley, William Farrell, John Spencer, Candice Hansen, Terry Hurford, Jassmine Ibea, Patrick Carlson, and Christopher P McKay. Collecting amino acids in the Enceladus plume. *International Journal of Astrobiology*, 18(1):47–59, 2019.

[169] Deborah S Kelley, Jeffrey A Karson, Gretchen L Fruh-Green, Dana R Yoerger, Timothy M Shank, David A Butterfield, John M Hayes, Matthew O Schrenk, Eric J Olson, Giora Proskurowski, et al. A serpentinite-hosted ecosystem: the lost city hydrothermal field. *Science*, 307 (5714):1428–1434, 2005.

[170] Robert P Lowell. A fault-driven circulation model for the lost city hydrothermal field. *Geophysical Research Letters*, 44(6): 2703–2709, 2017.

[171] WJ Jones, JA Leigh, F Mayer, CR Woese, and RS Wolfe. Methanococcus jannaschii sp. nov., an extremely thermophilic methanogen from a submarine hydrothermal vent. *Archives of Microbiology*, 136(4):254–261, 1983.

[172] Ben A Ward, Stephanie Dutkiewicz, Oliver Jahn, and Mick J Follows. A size-structured food-web model for the global ocean. *Limnology and*

Oceanography, 57(6):1877–1891, 2012.

[173] Susanne Menden-Deuer and Evelyn J Lessard. Carbon to volume relationships for dinoflagellates, diatoms, and other protist plankton. *Limnology and oceanography*, 45(3):569–579, 2000.

[174] Aharon Oren. The family Methanococcaceae. In *The Prokaryotes–Other Major Lineages of Bacteria and the Archaea*, pages 215–224. Springer, 2014.

[175] TM Hoehler. Biological energy requirements as quantitative boundary conditions for life in the subsurface. *Geobiology*, 2(4):205–215, 2004.

[176] William J Brazelton, Matthew O Schrenk, Deborah S Kelley, and John A Baross. Methane-and sulfur-metabolizing microbial communities dominate the Lost City hydrothermal field ecosystem. *Applied and environmental microbiology*, 72(9):6257–6270, 2006.

[177] Thomas M McCollom and Christopher Donaldson. Generation of hydrogen and methane during experimental low-temperature reaction of ultramafic rocks with water. *Astrobiology*, 16(6):389–406, 2016.

[178] Andrew J Pershing, Line B Christensen, Nicholas R Record, Graham D Sherwood, and Peter B Stetson. The impact of whaling on the ocean carbon cycle: why bigger was better. *PloS one*, 5(8):e12444, 2010.

[179] Thomas M McCollom. Geochemical constraints on primary productivity in submarine hydrothermal vent plumes. *Deep Sea Research Part I: Oceanographic Research Papers*, 47(1):85–101, 2000.

[180] Marc Neveu, Ariel D Anbar, Alfonso F Davila, Daniel P Glavin, Shannon M MacKenzie, Charity M Phillips-Lander, Brent Sherwood, Yoshinori Takano, Peter Williams, and Hajime Yano. Returning samples from Enceladus for life detection. *Frontiers in Astronomy and Space Sciences*, 7:26, 2020.

[181] Marc Neveu, Lindsay E Hays, Mary A Voytek, Michael H New, and Mitchell D Schulte. The ladder of life detection. *Astrobiology*, 18(11):1375–1402, 2018.

[182] Ngoc Truong, Adam A Monroe, Christopher R Glein, Ariel D Anbar, and Jonathan I Lunine. Decomposition of amino acids in water with application to in-situ measurements of Enceladus, Europa and other hydrothermally active icy ocean worlds. *Icarus*, 329:140–147, 2019.

[183] Jan P Amend, Douglas E LaRowe, Thomas M McCollom, and Everett L Shock. The energetics of organic synthesis inside and outside the cell. *Philosophical Transactions of the Royal Society B: Biological Sciences*, 368(1622):20120255, 2013.

[184] Alexandra Moura, Michael A Savageau, and Rui Alves. Relative amino acid composition signatures of organisms and environments. *PloS one*, 8(10):e77319, 2013.

[185] Wim Degruyter and M Manga. Cryoclastic origin of particles on the surface of Enceladus. *Geophysical research letters*, 38(16), 2011.

[186] Snežana S Mitić, Aleksandra N Pavlović, Snežana B Tošić, Biljana B Arsić, and Slavica M Sunarić. Quantitative determination of glycine in commercial dosage forms by kinetic spectrophotometry. *Journal of Analytical Chemistry*, 64(7):683–689, 2009.

[187] Guillem Anglada-Escudé, Pedro J Amado, John Barnes, Zaira M Berdiñas, R Paul Butler, Gavin AL Coleman, Ignacio de La Cueva, Stefan Dreizler, Michael Endl, Benjamin Giesers, et al. A terrestrial planet candidate in a temperate orbit around Proxima Centauri. *Nature*, 536(7617):437–440, 2016.

[188] Martin Turbet, Jérémy Leconte, Franck Selsis, Emeline Bolmont, François Forget, Ignasi Ribas, Sean N Raymond, and Guillem Anglada-Escudé. The habitability of Proxima Centauri b-II. possible climates and observability. *Astronomy & Astrophysics*, 596:A112, 2016.

[189] William J Borucki, David G Koch, Natalie Batalha, Stephen T Bryson, Jason Rowe, Francois Fressin, Guillermo Torres, Douglas A Caldwell, Jørgen Christensen-Dalsgaard, William D Cochran, et al. Kepler-22b: A 2.4 Earth-radius planet in the habitable zone of a Sun-like star. *The Astrophysical Journal*, 745(2):120, 2012.

[190] Michaël Gillon, Amaury HMJ Triaud, Brice-Olivier Demory, Emmanuël Jehin, Eric Agol, Katherine M Deck, Susan M Lederer, Julien De Wit, Artem Burdanov, James G Ingalls, et al. Seven temperate terrestrial planets around the nearby ultracool dwarf star TRAPPIST-1. *Nature*, 542 (7642):456–460, 2017.

[191] National Academies of Sciences, Engineering and Medicine. *Pathways to Discovery in Astronomy and Astrophysics for the 2020s*. The National Academies Press, Washington, DC, 2021.

[192] Edward W Schwieterman, Nancy Y Kiang, Mary N Parenteau, Chester E Harman, Shiladitya DasSarma, Theresa M Fisher, Giada N Arney, Hilairy E Hartnett, Christopher T Reinhard, Stephanie L Olson, et al. Exoplanet biosignatures: a review of remotely detectable signs of life. *Astrobiology*, 18(6): 663–708, 2018.

[193] C CatlingDavid, Y KiangNancy, D RobinsonTyler, J RushbyAndrew, Del GenioAnthony, et al. Exoplanet biosignatures: a framework for their assessment. *Astrobiology*, 2018.

[194] Victoria S Meadows, Christopher T Reinhard, Giada N Arney, Mary N Parenteau, Edward W Schwieterman, Shawn D Domagal-Goldman, Andrew P Lincowski, Karl R Stapelfeldt, Heike Rauer, Shiladitya DasSarma, et al. Exoplanet biosignatures: understanding oxygen as a biosignature in the context of its environment. *Astrobiology*, 18(6):630–662, 2018.

[195] LUVOIR Team et al. The LUVOIR mission concept study final report. *arXiv preprint arXiv:1912.06219*, 2019.

[196] DO Gough. Solar interior structure and luminosity variations. In *Physics of solar variations*, pages 21–34. Springer, 1981.

[197] Benjamin Charnay, François Forget, Robin Wordsworth, Jérémy Leconte, Ehouarn Millour, Francis Codron, and Aymeric Spiga. Exploring the faint young sun problem and the possible climates of the Archean Earth with a 3-D GCM. *Journal of Geophysical Research: Atmospheres*, 118 (18):10–414, 2013.

[198] David C Catling and James F Kasting. *Atmospheric evolution on inhabited and lifeless worlds*. Cambridge University Press, 2017.

[199] Joseph L Kirschvink, Eric J Gaidos, L Elizabeth Bertani, Nicholas J Beukes, Jens Gutzmer, Linda N Maepa, and Rachel E Steinberger. Paleoproterozoic snowball Earth: Extreme climatic and geochemical global change and its biological consequences. *Proceedings of the National Academy of Sciences*, 97(4): 1400–1405, 2000.

[200] James CG Walker, PB Hays, and James F Kasting. A negative feedback mechanism for the long-term stabilization of Earth's surface temperature. *Journal of Geophysical Research: Oceans*, 86(C10):9776–9782, 1981.

[201] Joshua Krissansen-Totton, Giada N Arney, and David C Catling. Constraining the climate and ocean pH of the early Earth with a geological carbon cycle model. *Proceedings of the National Academy of Sciences*, 115(16):4105–4110, 2018.

[202] VS Solomatov and L-N Moresi. Stagnant lid convection on Venus. *Journal of Geophysical Research: Planets*, 101(E2): 4737–4753, 1996.

[203] CC Reese, VS Solomatov, and L-N Moresi. Heat transport efficiency for stagnant lid convection with dislocation viscosity: Application to Mars and Venus. *Journal of Geophysical Research: Planets*, 103(E6): 13643–13657, 1998.

[204] Andrew P Ingersoll. The runaway greenhouse: A history of water on Venus. *Journal of Atmospheric Sciences*, 26(6):1191–1198, 1969.

[205] Martin Turbet, Emeline Bolmont, Guillaume Chaverot, David Ehrenreich, Jeremy Leconte, and Emmanuel Marcq. Day–night cloud asymmetry prevents early oceans on Venus but not on Earth. *Nature*, 598 (7880):276–280, 2021.

[206] Syukuro Manabe and Richard T Wetherald. *Thermal equilibrium of the atmosphere with a given distribution of relative humidity.* John Wiley & Sons Ltd Hoboken, NJ, USA, 1967.

[207] James F Kasting. Runaway and moist greenhouse atmospheres and the evolution of Earth and Venus. *Icarus*, 74(3):472–494, 1988.

[208] Ravi Kumar Kopparapu, Ramses Ramirez, James F Kasting, Vincent Eymet, Tyler D

Robinson, Suvrath Mahadevan, Ryan C Terrien, Shawn Domagal-Goldman, Victoria Meadows, and Rohit Deshpande. Habitable zones around main-sequence stars: new estimates. *The Astrophysical Journal*, 765(2):131, 2013.

[209] Owen R Lehmer, David C Catling, and Joshua Krissansen-Totton. Carbonate-silicate cycle predictions of Earth-like planetary climates and testing the habitable zone concept. *Nature communications*, 11(1):1–10, 2020.

[210] Bradford J Foley and Andrew J Smye. Carbon cycling and habitability of Earth-sized stagnant lid planets. *Astrobiology*, 18(7): 873–896, 2018.

[211] Caroline Dorn, Lena Noack, and AB Rozel. Outgassing on stagnant-lid super-Earths. *Astronomy & Astrophysics*, 614: A18, 2018.

[212] Ravi Kumar Kopparapu, Ramses M Ramirez, James SchottelKotte, James F Kasting, Shawn Domagal-Goldman, and Vincent Eymet. Habitable zones around main-sequence stars: dependence on planetary mass. *The Astrophysical Journal Letters*, 787(2):L29, 2014.

[213] Joshua Krissansen-Totton and David C Catling. Constraining climate sensitivity and continental versus seafloor weathering using an inverse geological carbon cycle model. *Nature communications*, 8(1):1–15, 2017.

[214] Kazumi Ozaki and Christopher T Reinhard. The future lifespan of Earth's oxygenated atmosphere. *Nature Geoscience*, 14(3):138–142, 2021.

[215] KM Gillis and LA Coogan. Secular variation in carbon uptake into the ocean crust. *Earth and Planetary Science Letters*, 302 (3-4):385–392, 2011.

[216] Jeffrey C Alt and Damon AH Teagle. The uptake of carbon during alteration of ocean crust. *Geochimica et Cosmochimica Acta*, 63(10):1527–1535, 1999.

[217] Kevin J Zahnle. Photochemistry of methane and the formation of hydrocyanic acid (HCN) in the Earth's early atmosphere. *Journal of Geophysical Research: Atmospheres*, 91(D2): 2819–2834, 1986.

[218] ET Wolf and OB Toon. Hospitable Archean climates simulated by a general circulation model. *Astrobiology*, 13(7):656–673, 2013.

[219] Jacob D Haqq-Misra, Shawn D Domagal-Goldman, Patrick J Kasting, and James F Kasting. A revised, hazy methane greenhouse for the Archean Earth. *Astrobiology*, 8(6):1127–1137, 2008.

[220] Philip von Paris, Heike Rauer, J Lee Grenfell, Beate Patzer, Pascal Hedelt, Barbara Stracke, Thomas Trautmann, and Franz Schreier. Warming the early Earth—CO2 reconsidered. *Planetary and Space Science*, 56(9):1244–1259, 2008.

[221] Alan C Hindmarsh. ODEPACK, a systematized collection of ODE solvers. *Scientific computing*, pages 55–64, 1983.

[222] Linda Petzold. Automatic selection of methods for solving stiff and nonstiff systems of ordinary differential equations. *SIAM journal on scientific and statistical computing*, 4(1):136–148, 1983.

[223] Ignasi Ribas. The sun and stars as the primary energy input in planetary atmospheres. *Proceedings of the International Astronomical Union*, 5(S264):3–18, 2009.

[224] B Scott Gaudi, Sara Seager, Bertrand Mennesson, Alina Kiessling, Keith Warfield, Kerri Cahoy, John T Clarke, Shawn Domagal-Goldman, Lee Feinberg, Olivier Guyon, et al. The habitable exoplanet observatory (habex) mission concept study final report. *arXiv preprint arXiv:2001.06683*, 2020.

[225] JM Dohm. Summarized evolution of mars. In *48th Annual Lunar and Planetary Science Conference*, number 1964, page 1962, 2017.

[226] C Bradford Barber, David P Dobkin, and Hannu Huhdanpaa. The quickhull algorithm for convex hulls. *ACM Transactions on Mathematical Software (TOMS)*, 22(4):469–483, 1996.

[227] Alessandro Morbidelli, Jonathan I Lunine, David P O'Brien, Sean N Raymond, and Kevin J Walsh. Building terrestrial planets. *Annual Review of Earth and Planetary Sciences*, 40:251–275, 2012.

[228] Felix D Schönbrodt and Eric-Jan Wagenmakers. Bayes factor design analysis: Planning for compelling evidence. *Psychonomic bulletin & review*, 25(1):128–142, 2018.

[229] Angelika M Stefan, Quentin F Gronau, Felix D Schönbrodt, and Eric-Jan Wagenmakers. A tutorial on bayes factor design analysis using an informed prior. *Behavior research methods*, 51 (3):1042–1058, 2019.

[230] Robert Weiss. Bayesian sample size calculations for hypothesis testing. *Journal of the Royal Statistical Society: Series D (The Statistician)*, 46(2):185–191, 1997.

[231] Gijs D Mulders, Ilaria Pascucci, and Dániel Apai. An increase in the mass of planetary systems around lower-mass stars. *The Astrophysical Journal*, 814 (2):130, 2015.

[232] Gijs D Mulders, Ilaria Pascucci, and Dániel Apai. A stellar-mass-dependent drop in planet occurrence rates. *The Astrophysical Journal*, 798(2):112, 2015.

[233] Christoph Mordasini, Yann Alibert, and Willy Benz. Extrasolar planet population synthesis-i. method, formation tracks, and mass-distance distribution. *Astronomy & Astrophysics*, 501(3): 1139–1160, 2009.

[234] Gijs D Mulders, Christoph Mordasini, Ilaria Pascucci, Fred J Ciesla, Alexandre Emsenhuber, and Dániel Apai. The exoplanet population observation simulator. ii. population synthesis in the era of kepler. *The Astrophysical Journal*, 887(2):157, 2019.

[235] A Bixel and D Apai. Bioverse: a simulation framework to assess the statistical power of future biosignature surveys. *Bulletin of the American Astronomical Society*, 53(3):0303, 2021.

[236] Jane S Greaves, Anita MS Richards, William Bains, Paul B Rimmer, Hideo Sagawa, David L Clements, Sara Seager, Janusz J Petkowski, Clara Sousa-Silva, Sukrit Ranjan, et al. Phosphine gas in the cloud decks of venus. *Nature Astronomy*, 5(7):655–664, 2021.

[237] Manasvi Lingam and Abraham Loeb. Brown dwarf atmospheres as the potentially most detectable and abundant sites for life. *The Astrophysical Journal*, 883(2):143, 2019.

Acronyms

ABC Approximate Bayesian Computation. 51–55, 57, 58, 79, 80, 91–93

ASI Agenzia Spaziale Italiana. 63

ATP Adenosine Triphosphate. 87

CCD Carbonate Compensation Depth. 137, 165

CTMI Cardinal Temperature Model with Inflexion. 50–53

DIC Dissolved Inorganic Carbon. 71, 76, 94, 96, 147, 164, 165

eD electron Donor. 85

ES Evolutionary Singularity. 46

ESA European Space Agency. 63

ESS Evolutionarily Stable Strategy. 48, 49, 56, 59

HF Hydrothermal Fluid. 73, 74, 76, 78, 79, 83, 84, 94, 104–106

HZ Habitable Zone. 10, 137, 138, 141, 155, 156, 175, 177

IHZ Inner Edge of the Habitable Zone. 138, 139, 146, 154–156, 177

INMS Ion and Neutral Mass Spectrometer. 71, 82

JWST James Webb Space Telescope. 82, 128, 134, 135

KNN K-Nearest Neighbors. 92

LCHF Lost City Hydrothermal Field. 104, 105

LUVOIR Large UV/Optical/IR Surveyor. 174, 199

MCMC Monte-Carlo Markov Chain. 51

ML Mixing Layer. 73, 74, 83, 84, 97, 98, 104–106, 110

MRM Master-Reaction Model. 41

NASA National Aeronautics and Space Administration. 9, 63, 69, 71

ODE Ordinary Differential Equation. 144, 151, 157, 159, 172, 177, 178

OHZ Outer Edge of the Habitable Zone. 139, 156, 177, 179

OP Ocean Plume. 105

OW Oceanic Water. 83, 84, 94

RF Random Forest. 79, 80, 92, 93

SBL Stagnant Boundary Layer. 160, 161, 164, 166

SMC Sequential Monte-Carlo. 51–55, 57, 58

TDH Tidal Dissipative Heating. 75

Appendices

Appendix A.

Résumé long en français

La découverte d'un grand nombre de planètes autour d'étoiles autres que le Soleil (environ 5 000 à ce jour), ainsi que l'exploration du système solaire des deux dernières décennies ouvre la voie à ce qui constitue peut-être une nouvelle ère de l'exploration spatiale. Pendant de nombreux siècles, la question de l'existence de vie en dehors de la Terre, ou de l'existence d'autres planètes autour d'autres étoiles ont été des questions d'ordre philosophique (ou même méthodologique) plus que d'ordre scientifique à proprement parler. Les récents développements en astronomie comme en biologie dite quantitative, mais aussi en climatologie et en sciences des planètes en général, nous positionnent aujourd'hui de telle sorte qu'il semble judicieux de mettre à jour et même d'élaborer un cadre théorique apte à traiter la question de l'*habitabilité*, ou propension d'une planète ou d'un environnement à abriter un écosystème, et celle des *biosignatures*, ou la détection d'une biosphère extraterrestre au travers de son empreinte dans l'environnement global ou *a minima* dans une grandeur *observable* d'une planète ou de tout autre corps astronomique susceptible d'abriter la vie. Parce qu'il s'agit bien d'*inférence*, un tel cadre ne peut être purement théorique, mais doit pouvoir se référer à la fois à une donnée empirique comme définissant une connaissance *a priori* et à une donnée existante ou potentielle permettant d'aboutir à une connaissance *a posteriori*.

Dans cette thèse, il est question de participer à l'élaboration de ce cadre théorique en prenant comme point de départ la théorie des écosystèmes pour formellement définir une mesure de la *viabilité* d'une population dans un environnement qui s'étend ensuite à la notion plus globale d'habitabilité. Cela est l'objet de la partie I, dans laquelle sont d'abord détaillées les grandes lignes d'un modèle apte à discuter de la viabilité d'une population dans un environnement mais aussi de faire le lien entre une potentielle population dans cet environnement et les échanges de matière à plus grande échelle

qui contribuent à définir de potentielles biosignatures, mais également à définir les conditions climatiques et géochimiques globales. Ce formalisme de l'habitabilité met en exergue un point important qui peut sembler contre-intuitif. Il apparaît en effet que l'habitabilité ou la viabilité d'un environnement devrait se mesurer sur une représentation *a priori* de celui-ci, définie par le contexte dans lequel il se situe, les flux de matière entrant et sortant, mais non sur l'environnement tel qu'il nous apparaît. En effet, celui-ci peut apparaître inhospitalier précisément car une population d'organismes y consomme les ressources.

Dans le chapitre 1, nous développons un modèle plus particulier qui s'inscrit dans ce cadre mais qui considère le bilan énergétique de la cellule et précisément le *rendement* énergétique de la réaction catabolique [a]. Ce modèle centré sur des considérations énergétiques semble adapté à la compréhension des contraintes de croissance portant sur les organismes qualifiés de lithoautotrophes, c'est à dire qui tirent l'énergie et les matériaux nécessaires à leur croissance dans des réactions chimiques concernant des espèces chimiques minérales et non organiques. Leurs réactions cataboliques produisent souvent beaucoup moins d'énergie que ne le fait la respiration, réaction catabolique des organohétérotrophes que nous sommes. La biosphère de la Terre primitive était vraisemblablement dominée par ce type d'organisme dont la diversité et l'ubiquité jusque dans les environnements les plus extrêmes sont longtemps restées méconnues. Ce modèle utilise les équations empiriques de la thermodynamique et de la thermocinétique, qui dépendent de paramètres eux aussi empiriques, dans le sens où ils sont mesurables, qui peuvent être interprétés dans une certaine mesure comme se référent à des traits fonctionnels de l'organisme. En particulier, ces paramètres déterminent la vitesse à laquelle la réaction catabolique peut se produire, correspondant alors aux propriétés des enzymes du catabolisme, ainsi que la vitesse à laquelle les molécules fonctionnelles de la cellule sont détruites, correspondant à la vulnérabilité à la température de celles-ci.

Dans le chapitre 2, nous examinons comment ces paramètres, interprétés comme des traits fonctionnels, pourraient être contraints les uns par rapport aux autres, et comment la sélection naturelle opérant sur ces traits pourrait définir les limites de l'adaptation des

---

a. les réactions cataboliques, ou catabolisme, correspondent aux réactions chimiques par lesquelles l'organisme acquiert de l'énergie qui sert ensuite à réaliser les réactions chimiques constructives coûteuses en énergie qui composent l'*anabolisme*.

organismes à la température. Ensuite, nous estimons la valeur de ces paramètres pour divers organismes vivant dans des environnements à des températures différentes et dont les données de croissance en fonction de la température sont publiées. Ce faisant, nous identifions les corrélations entre ces paramètres et les discutons à la lumière de l'analyse théorique du modèle et de l'adaptation des organismes à la température. Enfin, cet espace inféré dans lequel les paramètres du modèle prennent leurs valeurs pour reproduire les données de croissance de populations réelles est proposé comme socle *a priori* afin d'utiliser le modèle dans le contexte de la mesure de l'habitabilité et la prédiction de biosignatures.

Dans la seconde partie de cette thèse (partie II), nous appliquons le modèle défini au chapitre 1 pour estimer l'habitabilité et la potentielle existence d'une population de méthanogènes dans l'océan de la lune de Saturne dénommée Encelade. Cette lune a certainement un océan d'eau liquide sous sa surface gelée, au fond duquel il existerait une circulation hydrothermale qui pourrait être similaire à celle existant dans les océans de la Terre et qui abritent de riches communautés microbiennes. De plus, des particules et des gaz provenant de cet océan se retrouvent projetés dans l'espace au travers de crevasses dans la surface de glace d'Encelade. Encelade se trouve donc être un candidat unique pour la recherche de vie extraterrestre. Il dispose d'un océan d'eau liquide, de cheminées hydrothermales pour lesquelles nous pouvons définir un type d'organisme "candidat" à partir de ceux présents dans les cheminées hydrothermales des océans de la Terre, mais aussi d'un moyen d'échantillonage, son panache, qui nous épargne de devoir pénétrer l'épaisse couche de glace de surface pour atteindre l'océan.

Le chapitre 3 s'attache à mesurer l'habitabilité de l'environnement hydrothermal d'Encelade en définissant la variété des compositions chimiques *a priori* plausible dans le fluide hydrothermal et l'océan environnant. Ensuite, nous relions par le moyen d'un modèle de circulation autour du système hydrothermal les processus définissant la composition de l'environnement hydrothermal, y compris la présence hypothétique de micro-organismes méthanogènes, au quantités observables dans le panache extérieur. La composition chimique de ce panache ayant été en partie caractérisée par la mission Cassini, nous examinons à la lumière de ces données la plausibilité que l'environnement hydrothermal d'Encelade soit en effet habitable pour des micro-organismes tels que ceux que l'on trouve dans les environnement hydrothermaux sur Terre, ainsi qu'une popula-

tion composée de tels organismes puisse expliquer la composition chimique observée du panache. Nous trouvons que la composition du panache est compatible avec l'hypothèse d'un environnement hydrothermal habitable, et que l'abondance de méthane observée est vraisemblable sous l'hypothèse de l'existence d'une population de méthanogènes tandis qu'elle ne l'est pas sous l'hypothèse d'une production abiotique liée au processus d'altération minérale lors de la circulation hydrothermale. Ce travaux ont fait l'objet d'une publication en juin 2021 dans la revue *Nature Astronomy*.

Le chapitre 4 quant à lui s'intéresse à caractériser la taille et la productivité de cet écosystème hypothétique. Nous calculons que cet écosystème serait d'une taille relativement limitée (de l'ordre de la masse d'une baleine). Nous avançons également que la quantité relative à l'estimation de la concentration d'éventuelles molécules organiques dans le panache n'est pas la taille de la population mais sa *productivité*, car celle-ci correspond à un flux de biomasse pouvant sortir de l'environnement dans lequel la population est localisée. Malgré la petite taille de la population nous calculons que la concentration de biomolécules, d'acides aminés en particulier, dans le panache pourrait être détectée par les instruments équipant les missions à destination du système saturnien actuellement à l'étude. Nous nous projetons également dans de futures mesures de concentrations d'acides aminés dans le panache, en proposant les seuils de concentrations observées qui pourrait constituer des arguments en faveur ou en défaveur de l'hypothèse d'une biosphère [b]. Ces seuils sont également considérés dans le cas où l'abondance observée de méthane dans le panache sert à informer la taille et productivité de cette biosphère hypothétique. En d'autres termes, nous produisons une prédiction de la concentration d'acides aminés dans le panache sous l'hypothèse que le méthane observé dans le panache provienne effectivement d'une population de méthanogènes. Cela ouvre la voie à considérer les biosignatures comme un ensemble cohérent de prédictions, qui peuvent chacune être évaluée à la lumière de mesures. Ces travaux font l'objet d'une publication, en cours de révision auprès de la revue *Planetary Science Journal*.

Enfin, la partie III s'intéresse à appliquer cette méthodologie quantitative des biosignatures aux exoplanètes de "type Terre", c'est à dire rocheuses et de masse similaire à celle de la Terre, situées relativement à leur étoile (de masse similaire à celle du Soleil)

---

b. précisons ici que les acides aminés peuvent être synthétisés abiotiquement.

de telle sorte que l'existence d'un océan liquide est possible (dans la "zone habitable"). Il est question dans le chapitre 5 de développer un modèle, couplant le climat, les processus géologiques d'érosion et de dégazage, la photochimie atmosphérique et la chimie océanique, laquelle pouvant inclure la participation d'un écosystème. Ce modèle prend comme point de référence la Terre primitive (il y a 3,8 milliards d'années) en ouvrant la possibilité de faire varier le "contexte", c'est à dire la distance orbitale à l'étoile et donc l'énergie lumineuse reçue ainsi que les scénarios de régimes de convection du manteau. En effet, le manteau terrestre pourrait être dans un régime particulier qui est celui permettant la tectonique des plaques. La tectonique des plaques permet à son tour la formation de croûte continentale et un cycle géologique du carbone comprenant l'érosion des silicates et des carbonates de surface ; lequel ayant un effet stabilisateur sur le climat. Un autre régime pourrait exister, appelé régime de couvercle stagnant, dans lequel la croûte n'est pas mise en mouvement et l'intérieur planétaire est refroidi par conduction à travers elle. Le modèle présenté ici, intégrant un grand nombre de processus, n'a pas vocation à reproduire *in silico* de façon exhaustive toutes les réactions chimiques et interactions à l'oeuvre dans une planète ressemblant à la Terre, mais bien d'en isoler les grands éléments relatifs à l'habitabilité. Néanmoins, le système climatique comporte une complexité inhérente et essentielle, laquelle ne peut être réduite sans perte de propriétés importantes.

Dans le chapitre 6, nous simulons la composition atmosphériques d'exoplanètes de type Terre pour différentes valeurs de flux stellaire incident, sous l'hypothèse de l'existence ou de l'absence d'érosion continentale, pour différents scénarios de dégazage volcanique en fonction de l'âge planétaire, ainsi que sous l'hypothèse de l'existence ou de l'absence d'une biosphère méthanogène. Ainsi, nous prédisons quantitativement certaines tendances dans l'abondance de dioxyde de carbone dans l'atmosphère et le flux stellaire incident sous différents scénarios. Ces tendances sont discutées dans le contexte de l'habitabilité des planètes telluriques dans le temps et dans l'espace de la zone habitable. Enfin, nous estimons de manière prospective le nombre d'exoplanètes dont l'atmosphère devrait être caractérisée afin de disposer de la puissance statistique nécessaire à la distinction entre ces tendances et donc à l'inférence de la généricité ou unicité de la Terre comme disposant d'un cycle du carbone géologique permis par la tectonique des plaques.

Cette thèse dans son ensemble propose donc non seulement la clarification à la fois d'un cadre conceptuel et d'une stratégie pour aborder l'inférence de l'habitabilité et des biosignatures, mais aussi la mise en pratique de ce cadre. Nous avons donc démontré comment cette méthodologie peut servir à considérer l'information fournie par des données existantes à propos de l'hypothèse généralement mal définie de l'habitabilité. Cette approche permet d'informer *a priori* ce qui pourrait constituer une biosignature, et donc de mieux définir le type et la quantité d'observations ou d'échantillons qui doivent être collectés afin de maximiser le retour scientifique de missions spatiales ayant trait à la recherche de vie extraterrestre.

Appendix B.

Additional theoretical developments

B.1. Scaffolding habitability over hypothetical ecosystems

Definition B.1 (Habitability scaffolding)**.** Let environment E_j contain organisms of type $i \in \{1, \cdots, n\}$ with respective abundances denoted by N_i. The habitability of such an environment to a new functional type denoted by $n+1$ is determined by:

$$\left(\frac{1}{N_i} \frac{dN_{n+1}}{dt}(E_j) \right)_{\substack{\{N_i\}, i \in \{1, \cdots, n\} \\ N_{n+1}=0}} > 0 \qquad (B.1)$$

Additionally, if this criterion is to measure the viability of the complete ecosystem, another condition needs to be fulfilled:

$$\forall i \in \{1, \cdots, n+1\}, \exists N_i^*|_{E_j, \{N_k\}} > 0 \qquad (B.2)$$

Where N_i^* denotes the steady state of N_i. It is denoted by $H_{n+1}(E_j(\{N_i\}_{i \in \{1, \cdots, n\}}))$. An additional convenient assumption is that abundances $\{N_i\}$ are set at a steady-state or at equilibrium with other environmental abiotic variables.

Definition B.1 introduces the step to evaluate the habitability of an (initially abiotic) environment E_j to an ecosystem composed of $\{N_i\}_{i \in \{1, \cdots, n\}}$ as the sequential evaluation of the criterion H over an increasing number of functional types.

Definition B.2 (σ-habitability)**.** The habitability of environment E_j to a sequence of functional types $i \in \{1, \cdots, n\}$ introduced in chronological order follows:

$$H_\sigma(E_j) = \prod_k^n H_k(E_j(\{N_i\}_{i \in \{1, \cdots, k-1\}})) \qquad (B.3)$$

where σ is a sequence (permutation) of $\{1, \cdots, n\}$. The case in which there exists at least one element σ of the set S_n of permutations of $\{1, \cdots, n\}$ for which $H_\sigma(E_j) = 1$ is σ-habitable or simply habitable if the context permits.

B.2. Proofs of some dynamical properties

Proof. Proof of the appearance of $r(B_c)$ in the biomass dynamics in eq. 1.16 is obtained by addressing conservation of mass in the system. We note the total biomass $\mathbb{B} := NB_c$. We consider the decrease rate in mean cellular biomass to be unknown, noted x. The system writes as follows

$$\begin{cases} \frac{dN}{dt} & = (r(B_c) - d)N \\ \frac{dB_c}{dt} & = (q_{growth} - x)B_c \end{cases} \tag{B.4}$$

Variation of biomass yields:

$$\begin{cases} \frac{d\mathbb{B}}{dt} & = (q_{growth} - d)NB_c \\ \frac{d\mathbb{B}}{dt} & = N\frac{dB_c}{dt} + B_c\frac{dN}{dt} = (r(B_c) - d + q_{growth} - x)NB_c \end{cases} \text{and} \tag{B.5}$$

$$\begin{aligned} \Leftrightarrow \quad r(B_c) - x & = 0 \\ \Leftrightarrow \quad x & = r(B_c) \end{aligned} \tag{B.6}$$

$\square$

B.3. Upper temperature limit for growth and nutrient availability

Rewriting equation 2.3 including substrate availability in the catabolic rate yields

$$k_g = \lambda\tau Ae^{-\frac{E_{a,c}}{RT}}\frac{S}{a+S} - Ae^{-\frac{E_{a,m}}{RT}} \tag{B.7}$$

where a is the half-saturation constant for the limiting nutrient S. Then, the maximum growth temperature writes as:

$$T_{max} = \frac{E_{a,c} - E_{a,m}}{R(\ln \lambda\tau - \ln(\frac{a+S}{S}))} \tag{B.8}$$

B.4. Equivalence in fitness gradient between yield and availability limitations

Here, we slightly change the model and consider organisms where nutrient availability is important in setting growth instead of the variation of $\delta_r G_{cat}$. We consider a fixed $\Delta_r G_{cat}$, and that k_c depends on substrate availability. The previously defined k_c would now be an equivalent of a V_{max} so that:

$$k_c = V_{max} \frac{S}{a + S} \tag{B.9}$$

where $V_{max} = \tau A \mathrm{e}^{-\frac{E_{a,c}}{RT}}$, K is the half saturation constant and C the substrate concentration (this substrate could be dissolved organic matter for heterotrophs). We thus have

$$k_g = \lambda \tau A \mathrm{e}^{-\frac{E_{a,c}}{RT}} \frac{S}{a + S} - A \mathrm{e}^{-\frac{E_{a,m}}{RT}} \tag{B.10}$$

and the steady-state is reached when :

$$k_g = 0 \iff S^* = \frac{a}{\lambda \tau \exp \frac{E_{a,m} - E_{a,c}}{RT} - 1} \tag{B.11}$$

So that

$$k_g^m(S_r^*) = A \left[\exp \left(\frac{E_{a,c}^r - E_{a,m}^r - E_{a,c}^m}{RT} \right) - \exp \left(-\frac{E_{a,m}^m}{RT} \right) \right] \tag{B.12}$$

Which yields exactly the same results as in section 2.2 where the environmental variable is the Gibbs free energy of the catabolic reaction.

B.5. Maintenance rate activation energies

In this manuscript, the model of bioenergetics inside the cell assumes a single activation energy for the function-loss reaction. But the cell is composed of many different molecules, that we here separate by type and note i, that have different building costs and also different sensitivity to temperature. In fact the specific maintenance energy rate should write

$$e_m = \sum_{i=1}^{i=n} \tau_i E_{a,i} A e^{-\frac{E_{am,i}}{RT}} \tag{B.13}$$

where τ_i expresses the molar fraction of functional biomolecule i, $E_{a,i}$ its building cost and $E_{am,i}$ the activation energy of the reaction inducing the loss of its function. Under what assumptions would this expression be equivalent or at least close to an expression with only one activation energy like those being used in other parts of this thesis? To examine this, we define the mean energies:

$$
\begin{aligned}
\bar{E}_a &= \sum_i \tau_i E_{a,i} \\
\bar{E}_{am} &= \sum_i \tau_i E_{am,i}
\end{aligned}
\tag{B.14}
$$

and express the anomalies

$$
\begin{aligned}
\eta_i &= E_{a,i} - \bar{E}_a \\
\epsilon_i &= E_{am,i} - \bar{E}_{am}
\end{aligned}
\tag{B.15}
$$

Then, equation B.13 rewrites

$$
e_m = A \bar{E}_a e^{-\frac{\bar{E}_{am}}{RT}} \sum_i \tau_i \left(1 + \frac{\eta_i}{\bar{E}_a}\right) e^{-\frac{\epsilon_i}{RT}}
\tag{B.16}
$$

Which could be equivalent to a single Arrhenius law if either (i) anomalies ϵ_i and η_i are very small (the components of the cell have homogeneous properties) or (ii) there is one component that dominates the kinetics of maintenance either because it is dominates cell content (large τ_i), a lower activation energy $E_{am,i}$, or a much larger building cost $E_{a,i}$. Another way that could translate into a single Arrhenius law for the maintenance energy is that there is a keystone cellular component, the ability of which to perform its function is required for other components to perform theirs, made vulnerable by having a lower denaturation activation energy than other components.
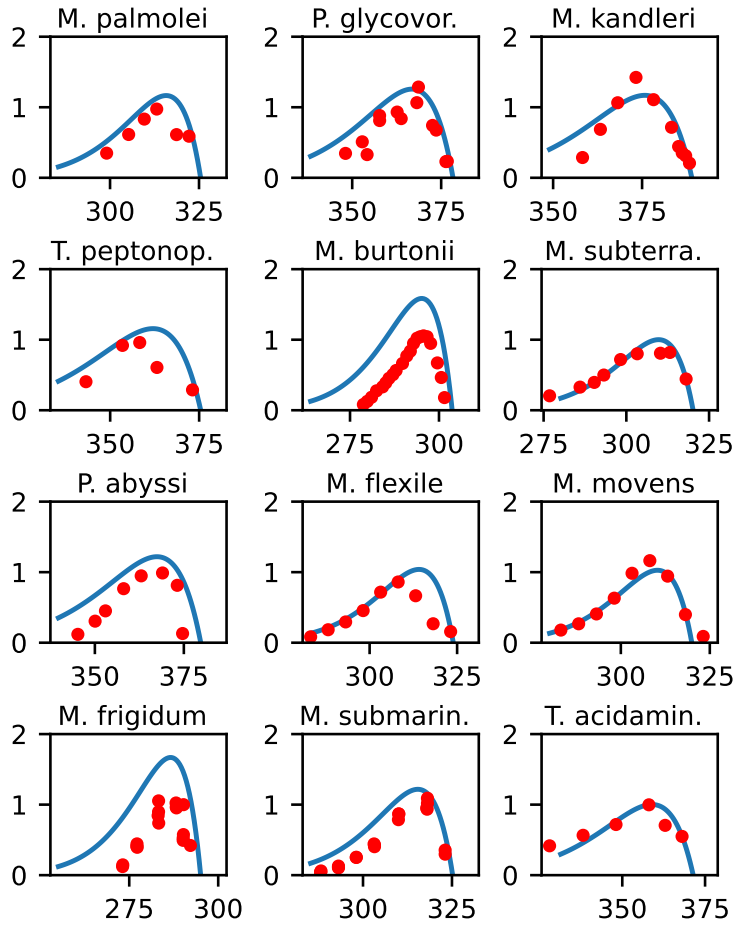
B.6. Additional figures

Figure B.1. | Simulated growth rates with estimated parameter values.
Growth rates are normalized to the maximal growth rate estimated from fitting the CTMI. Median values of the posterior distribution are used to simulate growth rates.
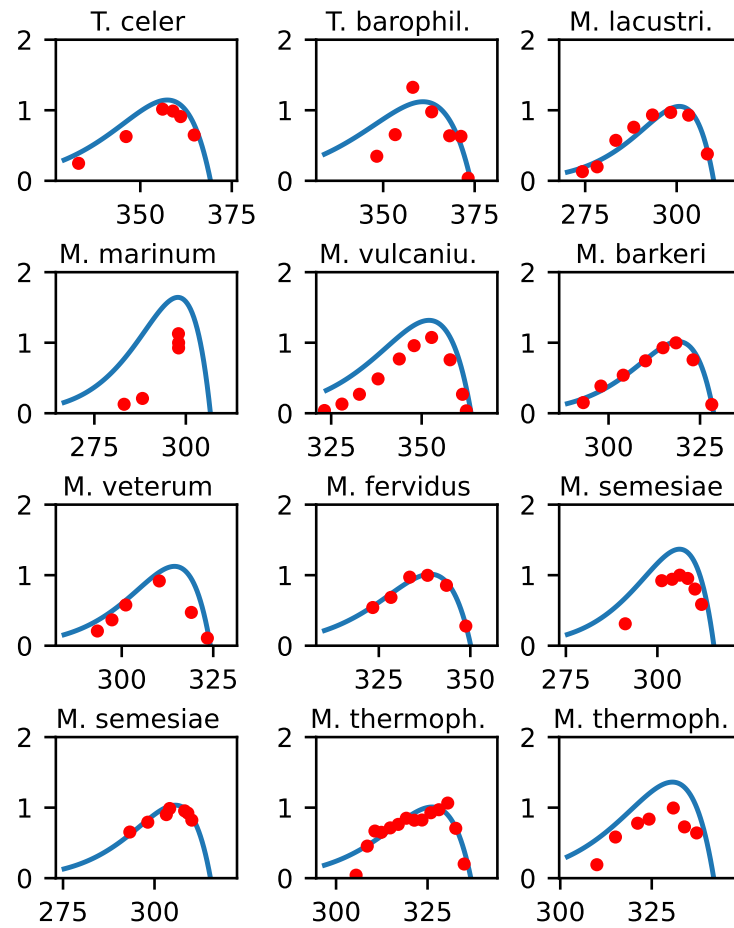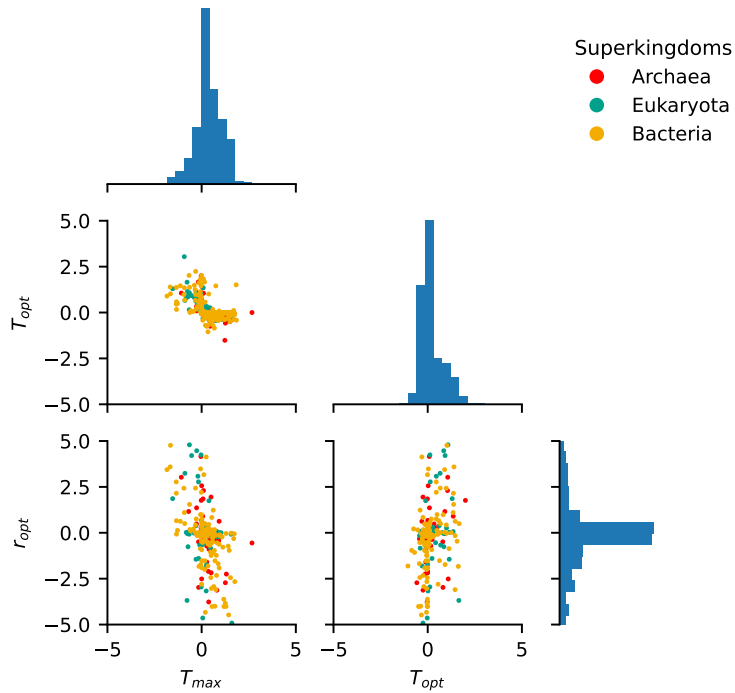
Figure B.2. | Simulated growth rates with estimated parameter values.
Growth rates are normalized to the maximal growth rate estimated from fitting the CTMI. Median values of the posterior distribution are used to simulate growth rates.

Figure B.3. | **Residuals of the ABC-SMC fit on cardinal points of the growth curve.** Difference between estimated cardinal temperatures and growth rate (median of the posterior distribution) and CTMI ground truth in percent. Note that for r_{opt}, a large proportion (29%) of the points exceed the $\pm 5\%$ range and are thus not visible on the plot. All estimates are within the $\pm 5\%$ range for both T_{opt} and T_{max}.

Appendix C.

Extended and Supplementary Data for Chapter 3

C.1. Extended Data

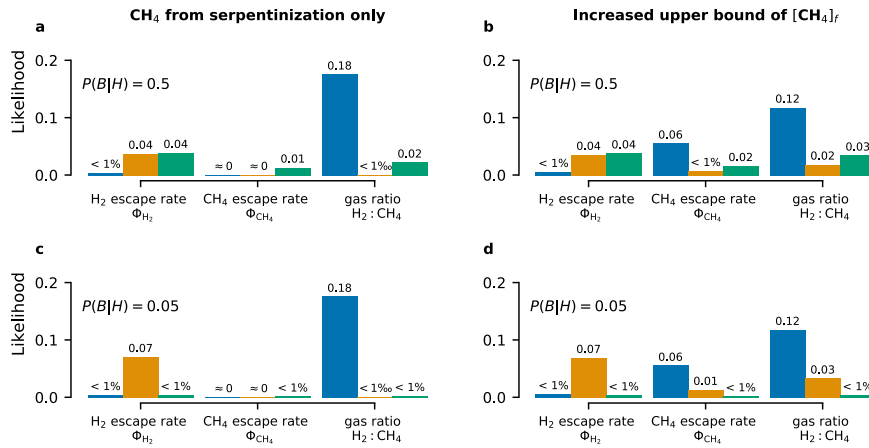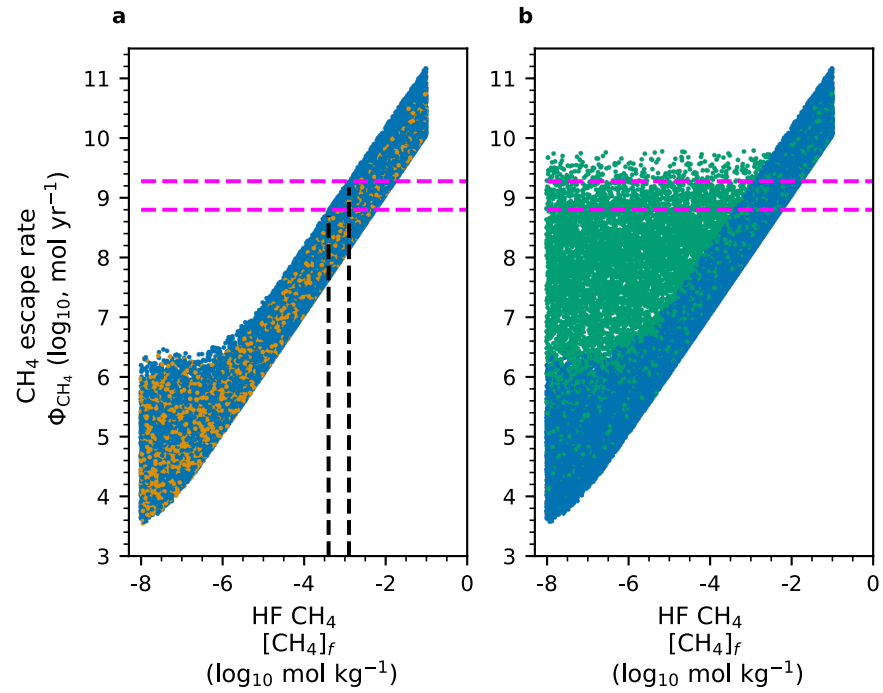### C.1.1. Extended Data Figures
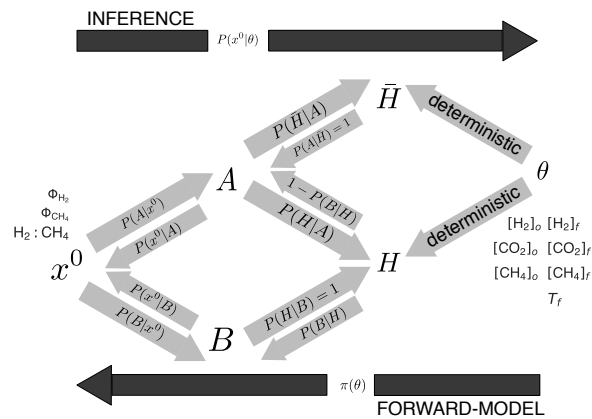
Extended Data Figure C.1. | Overview of the Bayesian inference framework as a two-directional probability tree. x^0 is an observation of system outputs, coming from the Cassini mission: Φ_{H_2} the flux of dihydrogen, Φ_{CH_4} the flux of methane, and the ratio $H_2 : CH_4$. θ denotes the set of internal parameters, namely the composition of Enceladus' putative hydrothermal fluid and ocean as well as hydrothermal fluid temperature. The modeling workflow reads from right to left: the model evaluates 'habitability' (H) from a set of parameters and produces so-called pseudo-data x when biological activity (B) contributes to shaping sea-floor waters composition (or not, A, "abiotic"); x and θ are thus related through $x = \pi(\theta)$, where π denotes a model. The inference workflow reads from left to right: the goal is to determine the posterior probability $P(B|x^0)$, which requires to compute likelihoods (e.g. $P(x^0|B)$), see Methods.
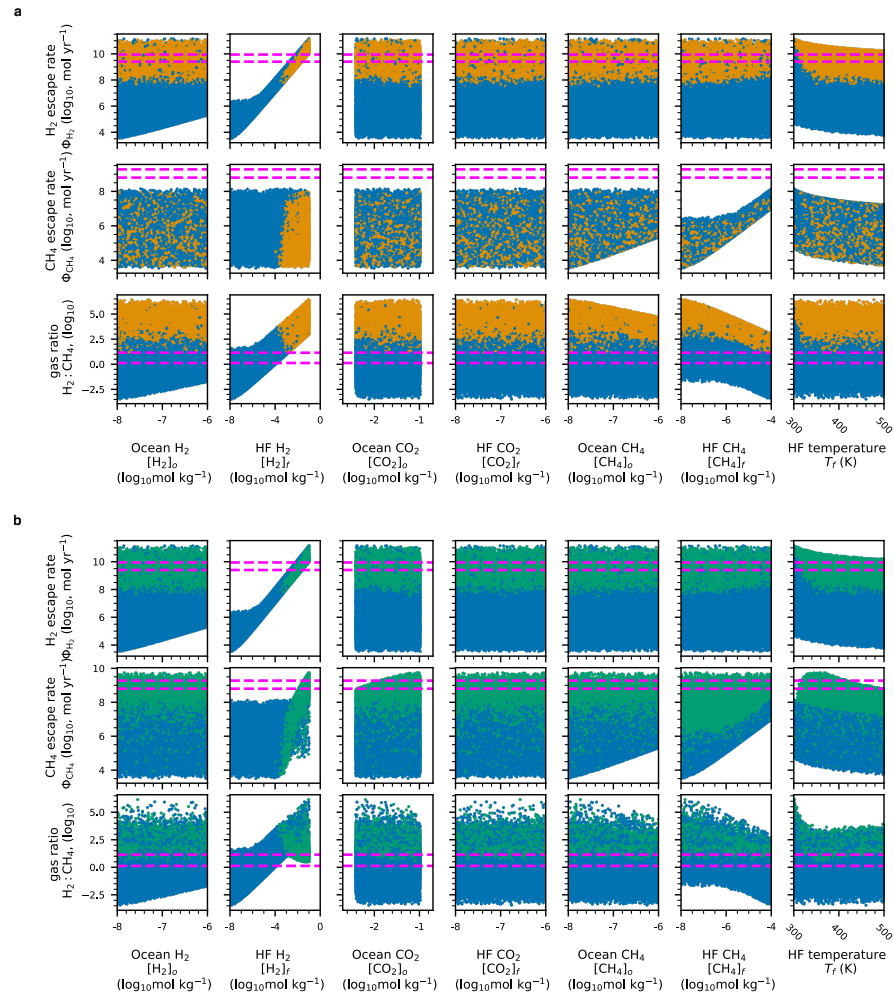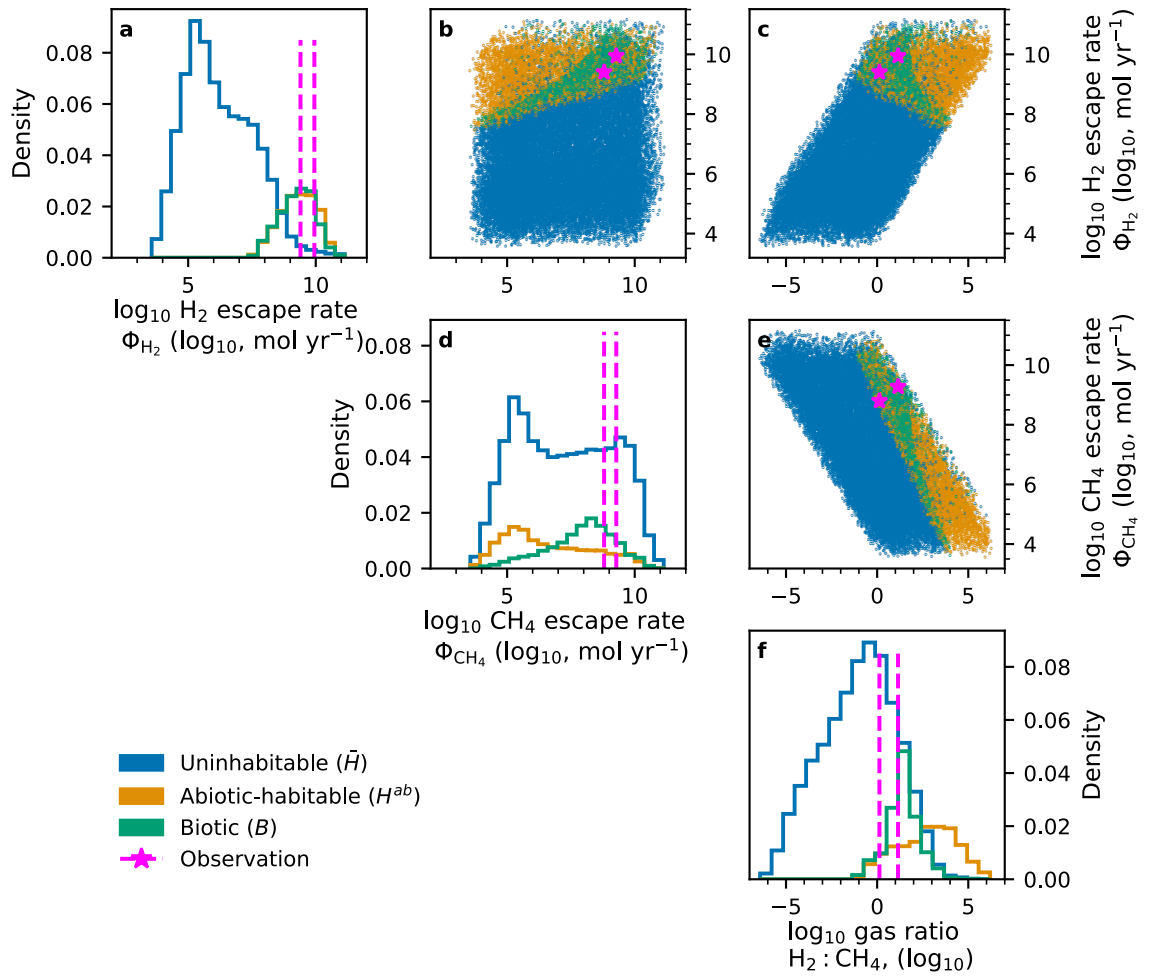
Extended Data Figure C.2. | Model outputs across the prior ranges of internal parameters. a Outputs of the purely abiotic model. Blue dots denote uninhabitable simulations, orange dots denote habitable simulations. **b** Outputs of the model including biological activity. Green dots denote habitable simulations in which biological methanogenesis occurs. Escape rates of methane and dihydrogen (Φ_{CH_4} and Φ_{H_2} respectively) are given in mol yr^{-1} while $H_2 : CH_4$ has no dimension. All concentrations are given in mol kg^{-1} and temperature is given in Kelvin. Note the $\log_{10}$ scale for every variable but the temperature. Magenta dashed lines indicate the observed values of each observable. See Methods for model equations, Extended Data Table C.1 for internal parameter ranges, and Extended Data Table C.2 for parameters values.

Extended Data Figure C.3. | Likelihood of the Cassini observations : H_2 escape rate (Φ_{H_2}, mol yr^{-1}), CH_4 escape rate (Φ_{CH_4}, mol yr^{-1}), and H_2 : CH_4 ratio under models predicting 'uninhabitability', 'abiotic habitability', and 'biotic' methane production. a,c Likelihood of the observables for the different models when serpentinization is the only modeled abiotic source of methane, for $P(B|H) = 0.5$ (**a**) and $P(B|H) = 0.05$ (**c**). **b,d** Likelihood of the observables for the different models when the abiotic methane concentration in the hydrothermal may be much higher, for $P(B|H) = 0.5$ (**b**) and $P(B|H) = 0.05$ (**d**). Blue bars denote the likelihood of the $\bar{H}$ model ('uninhabitable'), orange bars denote the likelihood of the H^{ab} model ('abiotic-habitable') and green bars denote the likelihood of B ('biotic'). Likelihood values are obtained by integrating the kernel density estimate approximation of the simulated samples (*e.g.* Fig. 3.2a, d, f) in the observation interval. The bars are labeled "≈ 0" when the likelihood was found to be $< 10^{-4}$. Internal parameters range are explained in Methods and given in Extended Data Table C.1, model parameters are given in Extended Data Table C.2.

Extended Data Figure C.4. | Abiotic and biotic methane production with an increased upper bound on $[\mathbf{CH_4}]_f$. a Outputs of the purely abiotic model. Blue dots indicate 'uninhabitable' simulations ($\bar{H}$), orange dots indicate 'abiotic-habitable' simulations (H^{ab}). **b** Outputs of the model including biological activity. Green dots indicate habitable simulations in which biological methanogenesis occurs (B). Magenta dashed lines: Cassini observations. Black dashed lines point to minimum values of CH_4 concentration in the HF to explain the lower and upper bounds of observed Φ_{CH_4}. Internal parameters ranges are explained in Methods and Extended Data Table C.1, model parameters are given in Extended Data Table C.2.

Extended Data Figure C.5. | Cassini observations and distributions of model outputs over the space of observables when higher abiotic methane concentration in the HF is allowed. a, d, f Univariate distributions for each observable. **b, c, e** Joint distributions. The color code separates the pseudo-data into simulations that were uninhabitable ($\bar{H}$, blue), abiotic-habitable (H^{ab}, orange), and biotic (B, green). Magenta dashed lines and stars indicate the observed values of each observable. See Fig. 3.2 for more details, Methods for model equations, and Extended Data Tables C.1 and C.2 for definitions of plotted parameters, prior internal parameter ranges, and model parameters.

Extended Data Tables

Extended Data Table C.1. | Summary of prior distributions. For details on
  the boundaries described here, see Methods.

| Parameter	Description	Prior distribution	Unit	Reference
$[H_2]_f$	Dihydrogen concentration in the hydrothermal fluid	$\log_e \mathbf{U}(10^{-8}, 10^{-1})$	mol kg^{-1}	Sleep et al., 200
$[H_2]_o$	Dihydrogen concentration in the ocean	$\log_e \mathbf{U}(10^{-8}, 10^{-6})$	mol kg^{-1}	
$[DIC]_f$	Dissolved inorganic carbon concentration in the hydrothermal fluid	$\log_e \mathbf{U}(4 \cdot 10^{-8}, 10^{-6})$	mol kg^{-1}	
$[DIC]_o$	Dissolved inorganic carbon concentration in the ocean	$\log_e \mathbf{U}(4 \cdot 10^{-3}, 10^{-1})$	mol kg^{-1}	Glein et al., 2015
$[CH_4]_f$	Methane concentration in the hydrothermal fluid –serpentinization only	$\log_e \mathbf{U}(10^{-8}, 10^{-4})$	mol kg^{-1}	McCollom, 2016
$[CH_4]'_f$	Methane concentration in the hydrothermal fluid with higher upper limit (unconstrained sources)	$\log_e \mathbf{U}(10^{-8}, 10^{-1})$	mol kg^{-1}	
$[CH_4]_o$	Methane concentration in the ocean	$\log_e \mathbf{U}(10^{-8}, 10^{-6})$	mol kg^{-1}	
T_f	Temperature of the hydrothermal fluid	$\mathbf{U}(300, 620)$	K	Choblet et al., 20

Extended Data Table C.2. | Biological and chemical default parameter values as well as physical and chemical constants.

Parameter	Value	Description	Unit	Ref
T_{eq}	90	Temperature at which activated and inactivated enzymes are in equal quantity	°C	Daniel et al. 2010 [84]
ΔG_{acat}	72	Activation energy of the catabolic reaction	kJ mol^{-1}	Daniel et al. 2010 [84]
ΔH_{eq}	305	Equilibrium enthalpy of enzyme deactivation	kJ mol^{-1}	Daniel et al. 2010 [84]
τ	1.73×10^{-5}	Catabolic enzymes to biomass ratio	dimensionless	Estimated from Taubner et al. 2018 [85]
d	0.03	Baseline cell death rate	d^{-1}	Connolly and Coffin 1995 [156]
NoC	1	Carbon chain length in carbon source	dimensionless	
γ	4	Number of oxidation of carbon in carbon source	dimensionless	
$\Delta_r G_{0,S}$	-32.6	Standard Gibbs energy of the catabolic reaction	kJ mol^{-1}	
$\Delta_r H_{0,S}$	-63.2	Standard enthalpy of the catabolic reaction	kJ mol^{-1}	
$e_m(T)$	$84\, e^{\frac{69,400}{R}\left(\frac{1}{298} - \frac{1}{T}\right)}$	Specific cell maintenance energy	kJ d^{-1} molC$_x^{-1}$	Tijhuis et al. 1993 [78]
T_o	275	Ocean temperature	K	
g	0.12	Enceladus gravitational acceleration	m s^{-2}	Choblet et al. 2017 [89]
F	$5 \cdot 10^9$	Hydrothermal vent heat dissipation power	W	Choblet et al. 2017 [89]
ϵ	1	ML thickness	m	
C_p	4,200	Specific heat capacity of liquid water	J K^{-1} kg^{-1}	
α	3×10^{-4}	Thermal expansion coefficient for liquid water	K^{-1}	
ρ_o	1,000	Seawater mass density	kg m^{-3}	

Extended Data Table C.3. | Parameters of the ABC inference.

| Parameter	Description
N_{trees}	Number of trees in the decision forest
max depth	Maximum tree depth (number of splits)
max features	Maximum number of features considered at a node
bootstrap	If "False", the whole data set is used to build each tree
oob score	Whether to use out-of-bag samples to estimate the generalization accuracy
min samples leaf	Minimal number of samples at the end of tree branches
min samples split	Minimum number of sample to split at a tree node

C.2. Supplementary Figures
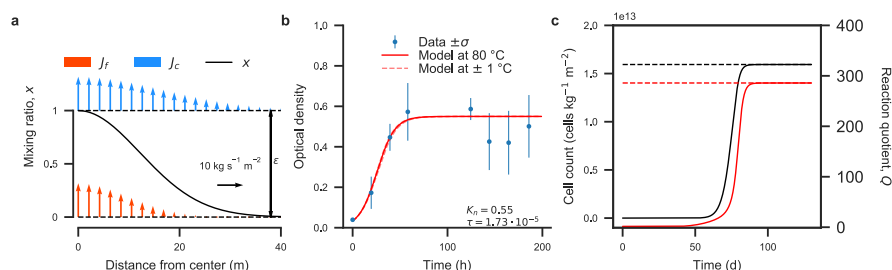
Extended Data Figure C.6. | Mixing layer model and population dynamics outputs. a Structure of the mixing layer. x is the mixing ratio of hydrothermal fluid over ocean waters. ϵ is the thickness of the mixing layer (m). Vertical arrows indicate the advection velocities of water masses, with scale indicated by the black horizontal arrow. **b** Confronting the bio-ecological model to experimental data. Red: logistic growth curve using the experimental population density at $t = 0$ as initial state $n_0 = 0.03$, an optical density $K_n = 0.55$ as carrying capacity and the growth rate predicted by the model using $\tau = 1.73 \cdot 10^{-5}$ in experimental conditions ($T = 353\ K$, $[H_2]_0 = 1.5$ mmol kg^{-1}, $[DIC]_0 = 7.7$ mmol kg^{-1} $[CH_4]_0 = 10^{-10}$ mol kg^{-1}). Red dotted lines are logistic curves using growth rates obtained with ± 1 temperature difference, corresponding to the temperature range maintained during the experiment in Taubner et al., 2018[85]. Blue: data from Taubner et al., 2018[85], error bars are standard deviation of triplicates. **c** Numerical solving of model trajectory in 1 m^3 of water for population size (N, cells kg^{-1}, black) and local reaction quotient (Q, red), and predicted steady-state (dashed lines). Initial concentrations used in this example : $[H_2] = 22$ mmol kg^{-1}, $[DIC] = 18$ mmol kg^{-1}, $[CH_4] = 0.03\ \mu$mol kg^{-1}. Temperature is 329 K. These conditions correspond to the composition found 5 m from the center of a hot spot generated with random parameters sampled in our prior distributions (described in Extended Data Fig. C.5) : $[H_2]_o = 8.0 \times 10^{-8}$ mol kg^{-1}, $[H_2]_f = 5.0 \times 10^{-6}$ mol kg^{-1}, $[CO_2]_o = 5.7 \times 10^{-7}$ mol kg^{-1}, $[CO_2]_f = 6.6 \times 10^{-8}$ mol kg^{-1}, $[CH_4]_o = 1.0 \times 10^{-4}$ mol kg^{-1}, $[CH_4]_f = 1.1 \times 10^{-5}$ mol kg^{-1} and $T_f = 421.5$ K. See Methods for model equations. Model parameters used for this example are default values given in Extended Data Fig. C.4
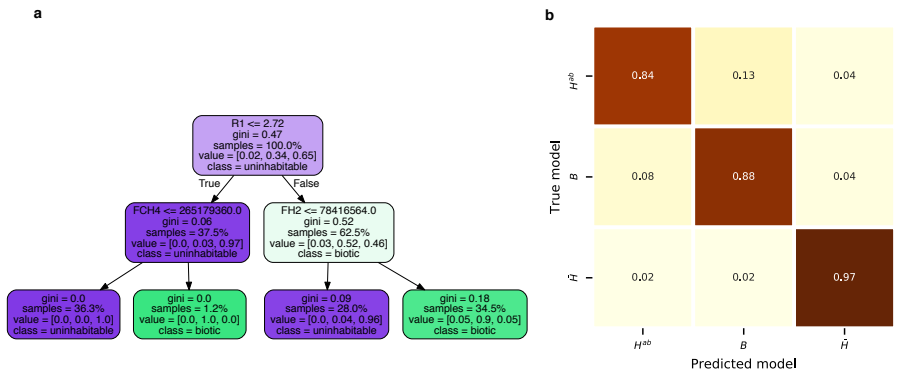
Extended Data Figure C.7. | Approximated Bayesian Computation - Random Forest (ABC-RF) classifier. a Example of a decision tree in a decision forest fitted to pseudo-data generated by our model. At each node, the left arrow is followed if the test of the node is true, the right arrow is followed if the test is false. Here, the allowed maximum depth of the tree is 2, meaning that the tree has two levels of nodes, making it easy to read. "Gini" stands for the Gini impurity, which was minimized to fit the tree to the data (Methods). "Samples" is the proportion of samples filtered at each node in the training dataset and "value" contains the probability associated with every class. In the tree, $R_1 = H_2 : CH_4$. **b** Confusion matrix of the ABC-RF classifier for our serpentinization-only dataset in which $P(B|H) = 0.5$. The confusion matrix evaluates the performance of the classifier on a set of pseudo-data on which the random forest was not fitted. The values and colors in the squares (darker means higher value) denote the proportion of simulations in the "True model" class that were classified into "Predicted model". See Methods for model equations. Model parameters used are given in Extended Data Figs. C.2 and C.3.
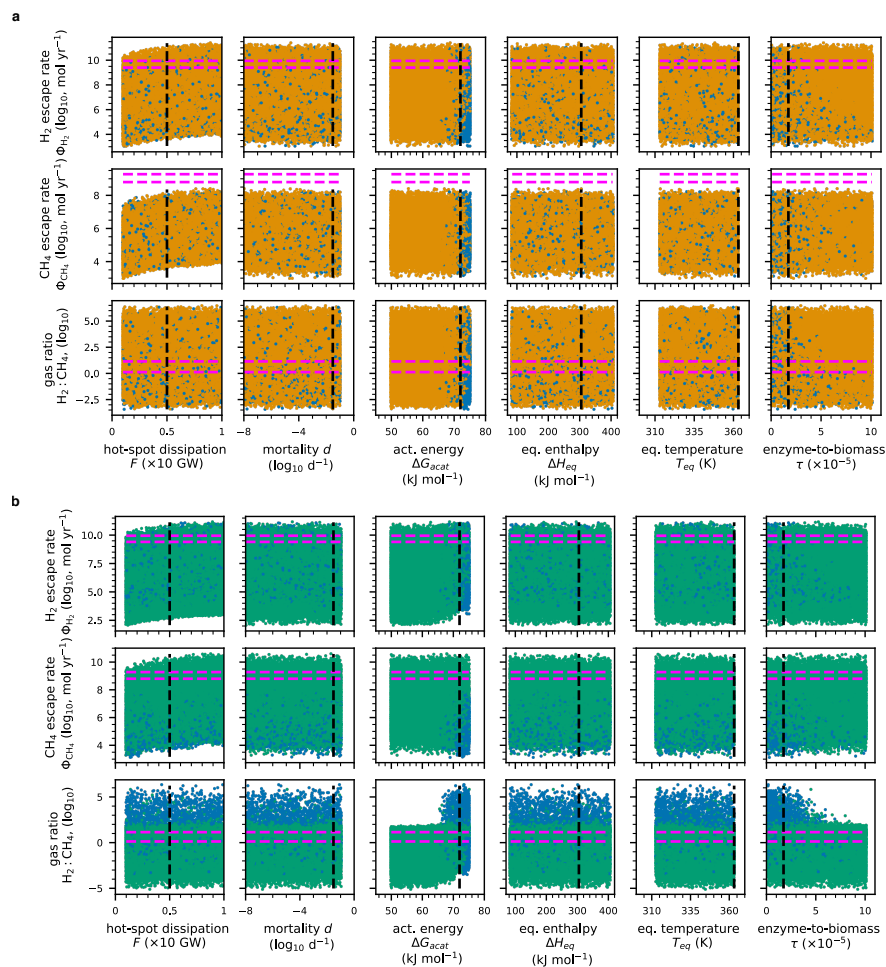
Extended Data Figure C.8. | Model outputs as a function of model parameters. a Outputs of the purely abiotic model. Blue dots indicate 'uninhabitable' simulations ($\bar{H}$), orange dots indicate 'abiotic-habitable' simulations (H^{ab}).**b** Outputs of the model including biological activity. Green dots indicate habitable simulations in which biological methanogenesis occurs (B). F is the power dissipated by the hotspot ($\times 10$ GW), d is the baseline death rate of the population (in d^{-1}, $\log_{10}$ scale), ΔG_{acat}, ΔH_{eq} and T_{eq} are parameters governing the shape of the catabolic rate as a function of temperature (in kJ, kJ and K respectively), τ is the active biomass scaling factor, in $\times 10^{-5}$ mol$_{enzyme}$ mol$_{C_x}^{-1}$ (see Methods for further detail). Black dashed lines (vertical) indicate default parameter values. Magenta dashed lines (horizontal) indicate Cassini observations[64]. Internal parameters (HF and OW compositions, HF temperature) are sampled from log-uniform distributions in ranges given in Extended Data Table C.3. See Methods for model equations. Parameters F, d, ΔG_{acat}, ΔH_{eq}, T_{eq} and τ vary as described in Supplementary Methods.
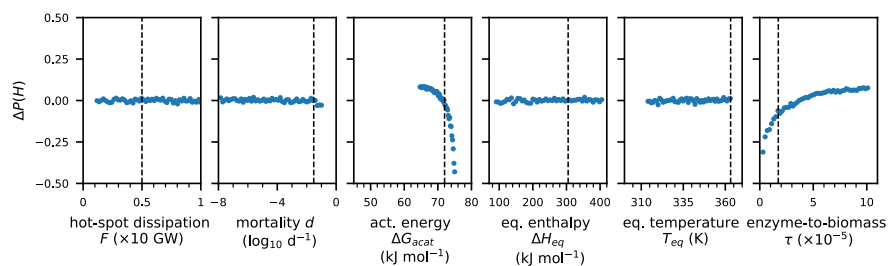
Extended Data Figure C.9. | Change in local density of the prior probability of habitability as a function of model parameters. F is the power dissipated by the hotspot ($\times 10$ GW), d is the baseline death rate of the population (in d^{-1}, $\log_{10}$ scale), ΔG_{acat}, ΔH_{eq} and T_{eq} are parameters governing the shape of the catabolic rate as a function of temperature (in kJ, kJ and K respectively), τ is the active biomass scaling factor, in $\times 10^{-5}$ mol$_{enzyme}$ mol$_{C_x}^{-1}$ (see Methods for further detail). For each point, the x coordinate is the center of a range of a model parameter's value in which the proportion of habitable simulations is computed. The y coordinate is the difference between the proportion of habitable simulations in the whole set and the local proportion. Black dashed lines (vertical) indicate default parameter values. Internal parameters (HF and OW compositions, HF temperature) are sampled from log-uniform distributions in ranges given in Extended Data Table. C.3. Parameters F, d, ΔG_{acat}, ΔH_{eq}, T_{eq} and τ vary as described in Supplementary Methods.
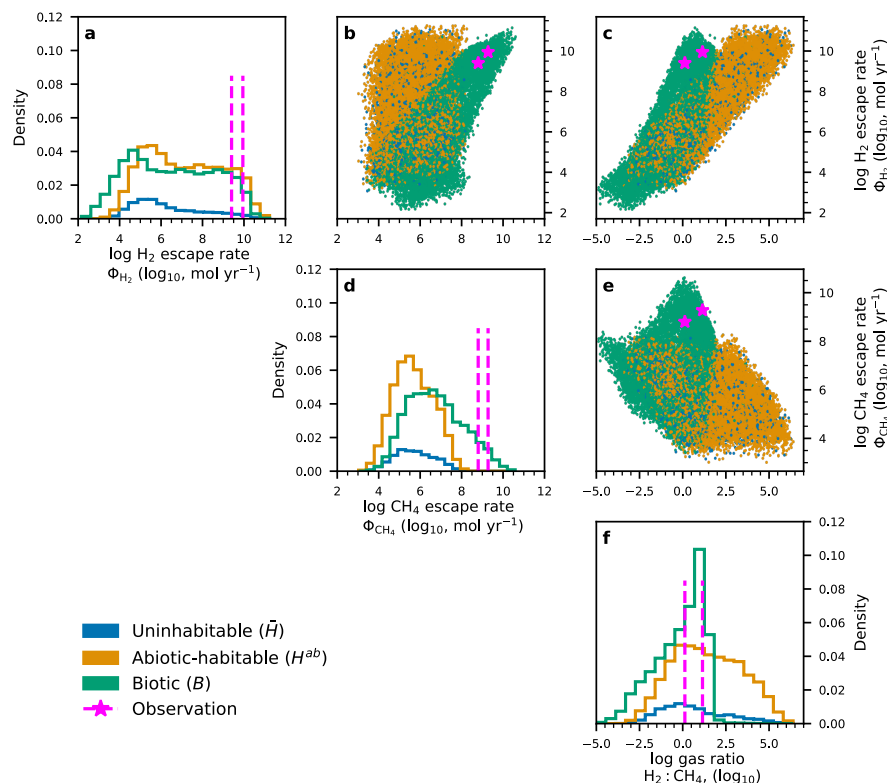
Extended Data Figure C.10. | Cassini observations and distributions of model outputs over the space of observables when model parameters vary. a, d, f Density distributions of pseudo-data generated by simulation of observables in which model parameters are drawn at random. Blue indicates the subset of simulations in which no biological methanogenesis is possible ('uninhabitable', $\bar{H}$). Orange indicates the subset of simulations in which biological methanogenesis is possible but not taken into account ('abiotic-habitable', H). Green indicates the subset of habitable simulations in which biological methanogenesis is included to generate the pseudo-data ('biotic', B). Magenta dashed lines indicate Cassini observations[64]. Note the $\log_{10}$ scale on the horizontal axis. **b, c, e** Joint distributions of observable pseudo-data generated by the model. Magenta stars indicate Cassini observations. Note the $\log_{10}$ scale on both axes. See Fig. 3.2 for more details, Methods for model equations and Extended Data Tables C.2 and C.3 for prior internal parameter ranges and model parameter values. Parameters F, d, ΔG_{acat}, ΔH_{eq}, T_{eq} and τ vary as described in Supplementary Methods.
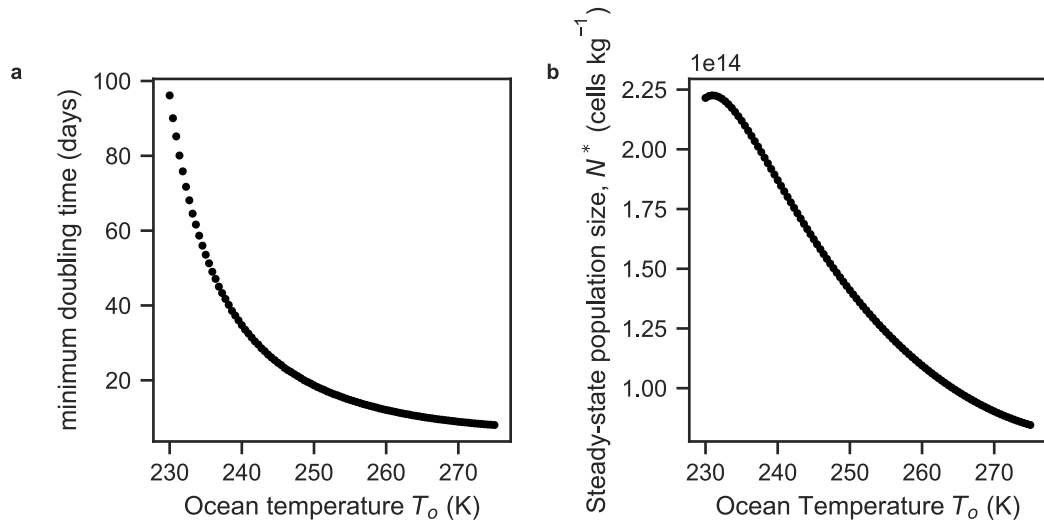
Extended Data Figure C.11. | Effect of lower ocean freezing temperature on a population of methanogens. **a** Minimum doubling time as a function of ocean temperature. **b** Steady-state population size as a function of temperature. All data points were obtained by numerically solving the differential equation system for the concentrations and population size (equation (19) in Methods) localized 5 m from the center of a hydrothermal vent with $T_f = 334\ K$, $[H_2]_f = 0.02$ mol kg^{-1}, $[DIC]_f = 0.02$ mol kg^{-1}, $[CH_4]_f = 2.9\ 10^{-8}$ mol kg^{-1}, $[H_2]_o = 3.35\ 10^{-8}$ mol kg^{-1}, $[DIC]_o = 2.8\ 10^{-6}$ mol kg^{-1} and $[CH_4]_o = 6.2\ 10^{-8}$ mol kg^{-1}. We varied T_o from 230 to 273 K to explore the consequences of a lower freezing point of water in Enceladus' ocean. Parameters for the methanogenic physiology are the standard values in Extended Data Table. C.2.

C.3. Supplementary Methods

Sensitivity analysis

We conducted a sensitivity analysis of our model by varying the parameters T_{eq}, ΔG_a, ΔH_{eq}, τ, d and F (see Extended Data Table C.2 for default values). We generated a set of 50,000 simulations using the prior distributions of internal parameters and drawing model parameters at random in the following distributions. T_{eq}, ΔG_a and ΔH_{eq}, the parameters governing the catabolic rate function, are drawn from uniform laws over ranges given in Daniel et al. (2010)[84]:

$$
\begin{array}{rcll}
T_{eq} & \sim & \mathbf{U}(313, 364) & \text{K} \\
\Delta G_a & \sim & \mathbf{U}(50, 75) & \text{kJ} \\
\Delta H_{eq} & \sim & \mathbf{U}(85, 420) & \text{kJ}
\end{array}
\tag{C.1}
$$

The power dissipated by the hotspot is taken in the range proposed in Choblet et al. (2017)[89] :

$$
F \sim \mathbf{U}(1, 10) \text{ GW}
\tag{C.2}
$$

The active biomass scaling factor is taken in a range allowing it to vary of one order of magnitude:

$$
\tau \sim \mathbf{U}(0.1, 10) \cdot 10^{-5} \text{ mol}_{enzyme} \cdot \text{mol}_{C_x}^{-1}
\tag{C.3}
$$

It has been argued[156] that the basal death rate d can be virtually 0, hence a range of very small values:

$$
d \sim \log_e \mathbf{U}(10^{-8}, 10^{-1}) \text{ d}^{-1}
\tag{C.4}
$$

Modeling the consequences of a lower freezing temperature of water

We address separately the possibility that ammonia in Enceladus' ocean might lead to a lower freezing point of water and thus a lower ocean temperature. We vary T_o linearly between 230 and 275 K and model a hot-spot with otherwise fixed parameters $T_f = 334$ K, $[\text{H}_2]_f = 0.02$ mol kg^{-1}, $[\text{DIC}]_f = 0.02$ mol kg^{-1}, $[\text{CH}_4]_f = 2.9 \; 10^{-8}$ mol kg^{-1}, $[\text{H}_2]_o = 3.35 \; 10^{-8}$ mol kg^{-1}, $[\text{DIC}]_o = 2.8 \quad 10^{-6} \quad$ mol $\quad$ kg^{-1} $\quad$ and $[\text{CH}_4]_o = 6.2 \; 10^{-8}$ mol kg^{-1}. We numerically solve the population dynamics in a localized place around the hot-spot (5 m) and measure the minimum doubling time as

$$
\min(\text{doubling time}) = \frac{N(\text{argmax}\left\{\frac{dN}{dt}\right\})}{\max\left\{\frac{dN}{dt}\right\}} \times \log_e 2
\tag{C.5}
$$

We identify the steady-state population size as the population at the end of the integration interval of 1 million days. Results are presented in Supplementary Fig. C.11 and discussed in Supplementary Discussion below.

Supplementary Results and Discussion

Sensitivity to model parameters

Perturbing the model by using randomly drawn parameter values (with distributions described in Supplementary Section C.3) shows little influence of parameter values on simulated observables (Supplementary Fig. C.8). We find that parameters ΔG_{acat} (governing the shape of the catabolic rate as a function of temperature) and τ (scaling cellular growth with enzyme function) significantly influence the distribution of observables in simulations run with parameters that allow methanogens to exist (Supplementary Fig. C.8).

Overall, variation in model parameters, and physiological parameters in particular, results in a higher fraction of habitable simulated environments ($P(H) = 0.91$, instead of $P(H) = 0.27$ with default parameter values). The ΔG_{acat} parameter is found to have great influence on $P(H)$, and higher values for this parameter, including the default value, lead to much lower $P(H)$ than the average (Supplementary Fig. C.9).

ΔG_{acat} accounts for the activation energy of catabolic enzyme and, all else being equal, increasing ΔG_{acat} limits the catabolic rate (equation (15) in main text). As a consequence, lower values of ΔG_{acat} allow methanogens to function in harsher environments due to increased q_{cat} and unchanged q_m (see Methods in main text).

Although the perturbation of model parameters decreases the overall classification power, it does not alter our inference qualitatively, that methanogenesis at Enceladus' seafloor is plausible (Supplementary Fig. C.10g). Methanogenesis under varying parameters still explains well the observed high value of methane flux, but the median value of biotic methane flux is shifted to lower values in comparison with pseudo-data produced with fixed parameters. Altogether, the higher *a priori* probability of habitability and the

lower median biotic methane production might be explained by a lower value of ΔG_{acat}, allowing harsher environments to be habitable, while colder environments, being poor in hydrothermal fluid, are also poor in nutrients, thus limiting methane production. The Φ_{CH_4} distribution might then be skewed by pseudo-data points corresponding to low availability of H_2, rendered inhabitable by the low value of ΔG_{acat} and thus producing less methane.

We stress that in order to incorporate varying parameters into the Bayesian inference, it is necessary to constrain the distribution from which parameters are drawn, so that they bring relevant information to the inference. Variation in biological parameters that measure cell 'traits' may be driven by individual plasticity or population adaptation. Our knowledge of the mechanistic relationships that may constrain plastic or adaptive variation, such as physiological and genetic trade-offs between traits, is, however, limited. Therefore we chose to interpret parameter variation as random perturbations of the model, rather than attempt at a process-based biological exploration of the parameter space.

Lower freezing temperature of water

If the freezing temperature point is lower, *e.g* due to high ammonia content in the ocean, the ocean temperature might be lower than 275 K. In the preliminary analysis described in Supplementary Methods, we find that lower ocean temperatures lead to potentially much higher doubling times in the modeled population of methanogens (Supplementary Fig. C.11a). When we generate the sets of simulations used in our statistical approach, we only use the steady state of the population dynamics, regardless of the time required to reach it (see Methods). Thus, our results are unaffected by the fact that populations of methanogens might grow exceedingly slowly in an ocean colder that 275 K. In addition, our simulations show that, in spite of extremely slow growth in a cold ocean, populations eventually reach a much larger size at steadystate (Supplementary Fig. C.11b). This may result from lower ocean temperatures increasing the volume of interfaces between hydrothermal fluid and ocean water that are cooler than the upper thermal limit of life, thus enhancing the growth of the whole population. This outcome (*i.e.* larger steady-state population size in a colder ocean) highlights the fact that ecosystems that are predicted viable at 275 K may not be imperiled by colder temperature. Fur-

thermore, larger populations at steady state might translate in a stronger environmental impact of biological methanogenesis, which might even increase the likelihood of the observations under the inhabited model.

It is worth noting that the preliminary analysis presented here uses physiological parameters of a hyperthermophilic methanogen (*e.g.* $T_{eq} = 90$ °C). In contrast, psychrophilic methanogens may have physiological adaptations that allow them to grow faster than the predicted growth of thermophilic methanogens exposed to a cold environment. For all these reasons, we expect a lower freezing point of ocean water to have limited effects on our results. This, however, warrants further investigation.

Sustainability of favorable conditions

Back-tracking rates of conversion of H_2 and DIC to methane by the modeled methanogens yields mean values of the order of 10^8 mol of H_2 and DIC consumed per year by methanogens. Waite et al. (2017)[64] estimates that the stock of minerals in Enceladus' core could support the observed outgassing rate $\approx 10^9$ mol yr^{-1} for billions of years. Estimation of DIC concentration in Glein et al. (2015)[129]
(10^{-3} to 10^{-1} mol kg^{-1}) yields a total stock of DIC in Enceladus' ocean (which mass is computed from ocean dimensions in Choblet et al. (2017)[89]) of the order of 10^{18} mol, which amounts to 50 to 500 Myr of modern outgassing rates and consumption by methanogens. Given that these estimates correspond to the modern stock of DIC, stocks in the past were probably larger. A potential methanogenic biosphere might therefore be limited in the future if no carbon recycling process is present.

Appendix D.

Additional theoretical developments for Chapter 4

D.1. Scale-free properties of the physical model

D.1.1. Abiotic quantities are insensitive to any scale parameter

The mixing layer model presented in this article has some scale-free properties that arise from the parametrization of the flux of hydrothermal fluid into the ML J_f. The shape parameters of the function $J_f(u)$ ensure that the total dissipated flux is equal to a particular value F and that the center of the mixing layer is composed of 100 % hydrothermal fluid. These assumptions alone suffice to prove that (i) the range of thermal and chemical conditions existing around the vent is always from 100% HF to 100% seawater and (ii) abiotic concentrations in the initial ocean plume are entirely determined by the concentrations and temperature of the HF and seawater. Rewriting equation (4.7) for the HF to seawater mixing ratio x^* at steady-state,

$$
\begin{aligned}
x_{OP}^* &= \frac{\int x^*(u) J_c(u) 2\pi u \, du}{\int J_c(u) 2\pi u \, du} \\
&= \frac{1}{3}
\end{aligned}
\tag{D.1}
$$

or equivalently, $C_i^{OP} = (1/3)C_i^f + (2/3)C_i^o$, which is independent from any physical parameter such as ϵ or the power dissipated by the vent, F. A consequence of the independence of abiotic concentrations from vent power F is that patchiness has no effect on the abiotic concentrations in the initial ocean plume. The range of chemical and thermal conditions existing around the plume are also unchanged since the parametrization of the function J_f ensures that $x^*(0) = 1$ and $x^*(\infty) = 0$.

Moreover, the total flux of any solute i coming out of the mixing layer (equal to $\int J_c C_i$) scales linearly with dissipated power F. As a consequence, the flux of i coming out of the hydrothermal environment is the same for a single vent dissipating F W and for the sum of an arbitrary number n of weaker vents each dissipating F/n W.

D.1.2. Relevant biological quantities are also scale-free

Equation (4.16) shows that the expression of the biomass concentration at steady state follows:

$$B^* = \frac{1}{\epsilon \rho q_{cat}}(J_f(C_f^{eD} - C_o^{eD}) + J_c(C_o^{eD} - C_{eD}^*)) \tag{D.2}$$

where eD is the electron donor (H_2 for methanogenesis) and $Y_{eD} = -1$ as a convention. Keeping in mind that both J_f and J_c scale with $\sqrt{\epsilon}$, B^* thus scales with $1/\sqrt{\epsilon}$.

At the same time, the typical volume scale of the mixing layer

$$\pi c^2 \epsilon \propto \sqrt{\epsilon} \tag{D.3}$$

so that the quantity of cells (or biomass) in the hydrothermal environment is not sensitive to the chosen vertical scale ϵ. This analytical intuition extends to all fluxes and concentrations in the initial ocean plume and is verified by numerical simulations. Like in the abiotic case, all biological absolute quantities (except concentrations) scale linearly with F, and thus again, the sum of n vents is equivalent to a single n times more powerful vent.

D.2. Dead cell entrainment

Here, we expand the equations 4.20 and 4.21 to separate dead cells in two categories. Some of the dead cells remain attached and some are entrained by the circulating fluid and may end up in the ocean plume and be ejected through the cracks. We assume that this entrainment occurs with a fixed rate (or probability) η. The concentration of the fixed dead cells N_{dfix} follows

$$\frac{dN_{dfix}}{dt} = Nd - N_{dfix}\eta \tag{D.4}$$

and the concentration of free-floating dead cells N_{dent}

$$\frac{dN_{dent}}{dt} = N_{dfix}\eta - \frac{J_c}{\rho\epsilon}N_{df} \tag{D.5}$$

At the steady-state,

$$N_{dfix}^* = N^*\frac{d}{\eta} \tag{D.6}$$

And thus,

$$N_{dent}^* = N^*\frac{\epsilon\rho d}{J_c} \tag{D.7}$$

which is the same expression as in equation 4.21, showing that the steady-state concentration of dead cells in the plume is insensitive to entrainment rate (but the total concentration of dead cells in the ML would adjust to be higher).

Appendix E.

Co-authored publication: Co-evolution of primitive methane-cycling ecosystems and the early Earth's atmosphere and climate

Co-evolution of primitive methane-cycling ecosystems and early Earth's atmosphere and climate

Boris Sauterey [1,2,3 ✉], Benjamin Charnay[4], Antonin Affholder [1,2,3], Stéphane Mazevet[3,6] & Régis Ferrière [1,2,5,6]

The history of the Earth has been marked by major ecological transitions, driven by metabolic innovation, that radically reshaped the composition of the oceans and atmosphere. The nature and magnitude of the earliest transitions, hundreds of million years before photosynthesis evolved, remain poorly understood. Using a novel ecosystem-planetary model, we find that pre-photosynthetic methane-cycling microbial ecosystems are much less productive than previously thought. In spite of their low productivity, the evolution of methanogenic metabolisms strongly modifies the atmospheric composition, leading to a warmer but less resilient climate. As the abiotic carbon cycle responds, further metabolic evolution (anaerobic methanotrophy) may feed back to the atmosphere and destabilize the climate, triggering a transient global glaciation. Although early metabolic evolution may cause strong climatic instability, a low $CO:CH_4$ atmospheric ratio emerges as a robust signature of simple methane-cycling ecosystems on a globally reduced planet such as the late Hadean/early Archean Earth.

[1] Institut de Biologie de l'Ecole Normale Supérieure (IBENS), Université Paris Sciences et Lettres, CNRS, INSERM, 75005 Paris, France. [2] International Center for Interdisciplinary Global Environmental Studies (iGLOBES), CNRS, ENS-PSL University, University of Arizona, Tucson, AZ 85721, USA. [3] Institut de Mécanique Céleste et de Calcul des Ephémérides (IMCCE), Observatoire de Paris, Université PSL, CNRS, Sorbonne Université, Univ. Lille, F-75014 Paris, France. [4] LESIA, Observatoire de Paris, Université PSL, CNRS, Sorbonne Université, Université de Paris, 5 place Jules Janssen, 92195 Meudon, France. [5] Department of Ecology & Evolutionary Biology, University of Arizona, Tucson, AZ 85721, USA. [6] These authors contributed equally: Stéphane Mazevet, Régis Ferrière. ✉email: boris.sauterey@ens.fr

By 3.5 Ga, life had emerged on Earth[1–3]. Astrophysical and geophysical data concur in showing that the planet was habitable 400 My earlier at the very least, and possibly as early as ~4.5 Gya, depending on the occurrence, magnitude, and effect of large asteroid impacts during the Hadean[3]. Early on, Earth's carbon cycle likely established and maintained temperate climatic conditions[4,5] in spite of a Sun being 20–25% dimmer than it is today[6]. The earliest microbial ecosystems evolving under these conditions, hundreds of million years before the first anoxygenic phototrophs[7] became actors of the Archean climate[8], most likely involved chemolithotrophs (i.e., unicellular organisms that use redox potential as energy source for biomass production) producing methane as a metabolic waste. Phylogenetic analyses[2,7,9,10] combined with isotopic evidence[11] and the then-time predominance[12,13] of the electron donors H_2 and CO lend weight to a very early origin of H_2-based methanogens (MG), CO-based autotrophic acetogens (AG), and methanogenic acetotrophs (AT). As CH_4 built up in the atmosphere, the evolution of anaerobic methanotrophy (MT) may have been favored. Contrary to the modern biosphere, the biomass productivity of such ecosystems was likely low and energy limited, i.e., limited by the availability of electron donors rather than nutrients such as nitrogen, phosphorus, or iron[13,14]. Whether and how the evolution of a primitive biosphere formed by these metabolisms influenced the planetary environment globally is unclear.

Previous studies[8,12,13] have addressed the productivity of primitive, chemolithotrophic ecosystems and their influence on the young Earth's equilibrium atmospheric conditions. Such studies relied on equilibrium analyses of the planetary ecosystem; they made strongly simplifying assumptions on the function of chemolithotrophic microbial metabolisms, and did not close the feedback loop linking biological activity, atmospheric composition, and climate. Although these studies showed that primitive biospheres may have had a significant impact on the planet's early atmosphere and climate, their ability to quantify this impact and estimate the underlying biomass productivity was limited. Furthermore, earlier theory based on equilibrium analyses could not address the coupled dynamics of metabolic evolution and planetary surface conditions, whereby evolutionary changes might trigger significant atmospheric and climatic events and lead to novel steady states. Thus, advancing existing models is needed to generate hypotheses on the history of atmospheric and climatic conditions that metabolic evolutionary innovation may have driven on the early Earth.

Here we ask, how constrained was the habitability of late Hadean/early Archean Earth to methane-cycling ecosystems? How productive were these ecosystems and did they have a significant impact on the atmospheric composition and climate? How did their impact change as different metabolisms evolved? To answer these questions, we lay out a new probabilistic modeling framework for an evolving microbial community coupled to early Earth surface geochemistry and climate (Fig. 1, see "Methods" and Supplementary "Results and Discussion" for further details). The mean surface temperature and the composition of the atmosphere and oceans are parameterized using a 3D climate model[4,15] and a 1D photochemical model[16], combined with a simple temperature-dependent carbon cycle model[5]. Advancing the previous studies[8,12,13], this planetary model is coupled dynamically to a biological model of cell population dynamics and evolutionary adaptation, constructed by scaling the intracellular processes of energy acquisition (i.e., catabolism), cell maintenance, and biomass production (i.e., anabolism) up to ecosystem function[17,18]. The biological model is grounded in thermodynamics and based on observations of cell size and temperature kinetic dependencies, widely and robustly shared among modern unicellular organisms[19–23]. Quantitative

validation of similar models was obtained from laboratory experiments on anoxic ecosystems in bioreactors[18].

Results

Ecosystems viability. First, we assess the viability of the methanogenic biospheres (MG, AG + AT, or MG + AG + AT) on an initially cool, lifeless Earth. The initial abiotic surface temperature T_{Geo} is assumed to be 12 °C, corresponding to $pCO_2 = 2 \times 10^5$ ppm, negligible pCH_4, and volcanic outgassing of H_2, $\varphi_{volc}(H_2)$, ranging from 5×10^9 to 2×10^{11} molecules $cm^{-2} s^{-1}$. By performing a Monte-Carlo exploration of the space of biological parameters, we generate posterior distributions of possible life-atmosphere-climate outcomes (Supplementary Figs. 1 and 2), thus providing general insights that do not depend on specific parameterizations of chemolithotrophic metabolisms. We find that all three methanogenic ecosystems are viable (i.e., they can sustain a steady, positive biomass production) in more than 50% of the simulations, regardless of the intensity of H_2 outgassing (further information on the region of viability in the space of biological parameters is provided in the Supplementary Results and Discussion). Among viable ecosystems, the posterior distributions of the planetary and ecological state variables are peaked and relatively narrow (Fig. 2). Hereafter we will focus on median values to describe model outputs.

Short-term effects of metabolic evolution. We first consider the direct effects on the early Earth's atmosphere and climate, on a relatively short timescale of ~10^6 years, of the transition from the initially cool, lifeless state to a planet populated by one of three methanogenic biospheres, MG, AG + AT, or MG + AG + AT. On such a short timescale, the carbon cycle has a negligible influence on the atmospheric CO_2. H_2 is both a metabolic substrate of MG and involved in the photochemical production of CO, the metabolic substrate of AG (Fig. 1). As a consequence, stronger H_2 volcanic outgassing always enhances biomass production and CH_4 emission (Fig. 2). The highest CH_4 emission is achieved by MG ecosystems, with pCH_4 ranging from 80 to 4000 ppm and equilibrium temperature, and T_{BioGeo}, raised by $+7°$ to $+17°$ (Fig. 2). The environmental impact of AG + AT ecosystems is similar in magnitude, with pCH_4 ranging from 50 to 1000 ppm, and temperature increases of $+6°$ to $+15°$ (Fig. 2).

The planet's abiotic surface temperature, T_{Geo}, is likely to have a strong influence on methanogenic activity (see "Methods"). Temperature influences both cell kinetics (metabolisms are slower at lower temperature) and thermodynamics (strong negative effect of high temperatures on MG, less so on AG + AT). T_{Geo} also correlates positively with pCO_2 and pCO, which are both substrates of methanogenesis. We evaluate the influence of T_{Geo} by examining bio-geo environmental feedbacks (i.e., how the change in metabolic activity due to variation in T_{Geo} feeds back to climate) for T_{Geo} ranging from −18 to 57 °C, which corresponds to pCO_2 ranging from 5×10^{-4} to 1 bar (Fig. 3). We ran simulations using a default biological parameterization for which CH_4 emissions are close to the median predictions described above. Note that we also considered T_{Geo} as varying independently of pCO_2, due to e.g. variation in stellar radiation; corresponding results are shown in Supplementary Fig. 3.

If the overall effect of T_{Geo} on methanogenic activity is positive, the methanogenic ecosystem is expected to amplify temperature fluctuations driven by external events such as variation in CO_2 outgassing. In this case, increasing T_{Geo} should enhance the biogenic emission of CH_4, further warming the planet through additional greenhouse effect; decreasing T_{Geo} should have the opposite effect. In contrast, if the overall effect of T_{Geo} on methanogenic activity is negative, methanogenic ecosystems will
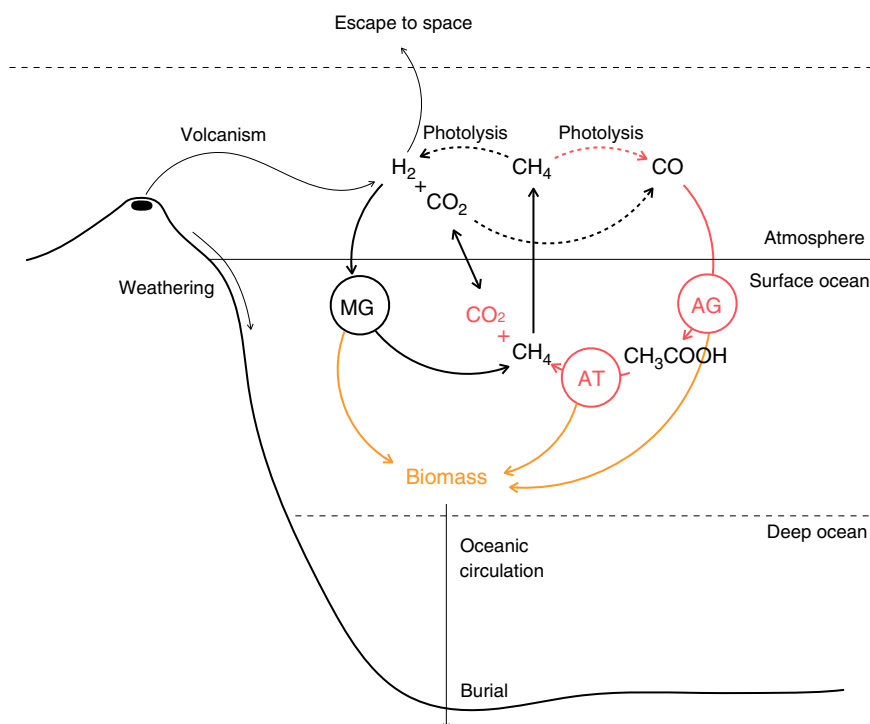
Fig. 1 Primitive methanogenic ecosystems. The ecosystem model resolves population abundance (total biomass, yellow arrows) of microbial H_2-based methanogens (MG), CO-based acetogens (AG) and methanogenic acetotrophs (AT), along with CH_4, CO, CO_2, and H_2 oceanic concentrations and atmospheric mixing ratios. Fluxes directly involved in the MG ecosystem function are indicated with black arrows. Fluxes additionally involved in the AG + AT ecosystem function are indicated in red. Key photochemical reactions are indicated with dotted arrows. The primary source of reducing power (H_2) is volcanic outgassing. Fluxes across the ocean surface are governed by a stagnant boundary layer model. Rates of H_2 escape to space and dead biomass burial in deep sediments are constant. Sulfate-based methanotrophs are not represented. See "Methods" for further details.

buffer temperature variation. For the MG ecosystem (Fig. 3), we find that there is a critical abiotic temperature $T_{Geo} \approx 5\,°C$, almost insensitive to H_2 outgassing, at which the warming effect of the ecosystem is maximum, from +5° to +17° across the range of H_2 outgassing rates. The MG ecosystem buffers fluctuations of abiotic temperature above the critical value, whereas it amplifies abiotic temperature fluctuations below the critical value. In contrast, the AG + AT ecosystem always amplifies temperature variation at all abiotic temperatures, and its influence tends to dominate when MG and AG + AT metabolisms co-occur (Fig. 3). Such amplification or buffering of temperature variations can represent up to 33% of the abiotic fluctuations (Supplementary Fig. 4). Overall, the function and evolution of methanogenic ecosystems lead to a less resilient, more variable climate.

The formation of organic hazes when the pCH_4-to-pCO_2 ratio is greater than 0.2 (ref. [24]) has been proposed as a general mechanism of climate regulation[25]. In the late Archean, pCO_2 was low[5], favoring organic haze formation that may have prevented hot runaway scenarios. In the Hadean/early Archean, however, our model predicts organic hazes to form in a limited range of conditions, at very high H_2 volcanic outgassing rates, low pCO_2, and low abiotic temperature close to or below the freezing point (Fig. 3). Under these specific conditions, the formation of organic hazes may overwhelm the warming effect of methanogenic ecosystems and leave the planet in a globally glaciated state. Under most conditions, however, it is the availability of electron donors (H_2, CO) to methanogenesis, and not organic hazes, that is expected to limit Archean climate warming by biological activity.

Biomass production. In spite of their strong impact on the planet's atmosphere and climate, primitive methanogenic

ecosystems are characterized by extremely low biomass productivity, AG + AT being the most productive pathway by far (Fig. 2). As microbial chemolithotrophs consume atmospheric electron donors, they drive the system closer to its thermodynamic equilibrium, thus gradually decreasing the thermodynamic efficiency of the metabolic coupling between energy acquisition (catabolism) and biomass production (anabolism; see "Methods equation (E2)"). As a consequence, for the highest value of abiotic H_2 outgassing, our model predicts biomass production to range from 10^6 to 10^9 molecule C cm^{-2} s^{-1}. This is 1–4 orders of magnitude below previous estimates[13] (based on models that assumed a fixed biomass yield per electron donor consumed) and 4–7 orders of magnitude below modern values[26].

Albeit extremely low, biomass production is very sensitive to the metabolic composition of the ecosystem and temperature, T_{Geo}. Supplementary Fig. 5 shows how biomass production is influenced by these two factors. For the MG ecosystem, biomass production peaks for T_{Geo} between −10 and 10 °C depending on the intensity of H_2 volcanic outgassing (slightly above 10^9 molecules C cm^{-2} s^{-1} at high rates of H_2 volcanic outgassing), and strongly decreases for higher T_{Geo}. The maximum biomass production is of the same order in the AG + AT ecosystem and reached for similar conditions (intermediate T_{Geo}, high H_2 volcanic outgassing rate), but its dependence upon T_{Geo} and the rate of H_2 volcanic outgassing is much weaker. In the MG + AG + AT ecosystem the two methanogenic pathways interact synergistically, leading to a nonlinear, multiplicative increase in biomass production at low and high temperature. The synergy involves the combination of biogeochemical recycling loops, both locally and globally. Locally, while MG consumes CO_2 to produce CH_4, AT decomposes CH_3COOH and produces CO_2. The metabolic waste of AT is, therefore, the metabolic substrate of
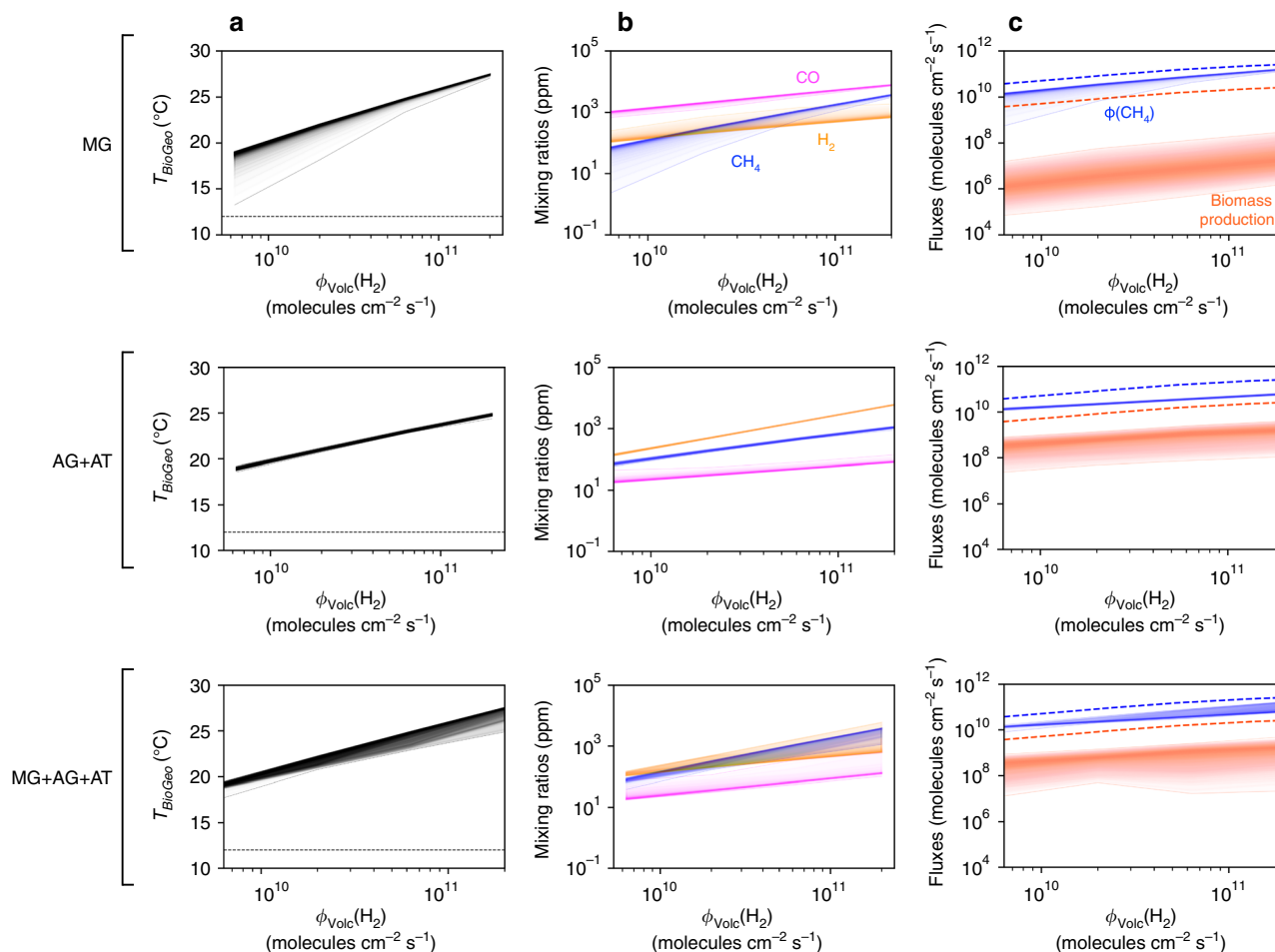
Fig. 2 Short-term biological feedback to the atmosphere and climate. Effects are computed as a function of the H2 volcanic outgassing, for each ecosystem composition. MG indicates H_2-based methanogens (MG). AG+AT indicates CO-based acetogens and methanogenic acetotrophs consortia. MG+AG+AT indicates co-occurring methanogens, acetogens, and acetotrophs. **a** Global surface temperature at ecosystem-climate equilibrium. The dotted line indicates the initial abiotic surface temperature, $T_{Geo} = 12$ °C. **b** Atmospheric composition at ecosystem-climate equilibrium. **c** Biogenic fluxes at ecosystem-climate equilibrium: CH_4 production and carbon fixation in biomass (in molecules of C cm^{-2} s^{-1}). Envelopes represent probability distributions from Monte-Carlo simulations across the biological parameter space, with each layer indicating output frequency ranging from 90 to 51%. Predictions from ref. [13] are also shown (dashed) for comparison. See "Methods" and Supplementary Tables 3 and 4 for parameter values.

MG, and the combination of the two metabolic pathways pulls the system further away from its thermodynamic equilibrium, hence an increase in the efficiency of both pathways. Globally, as the MG metabolism releases additional CH_4 in the atmosphere, the production of CO through photochemistry is accelerated; CO being the metabolic substrate of AG, its metabolic efficiency is enhanced. The synergistic effect is greatest at low abiotic temperature. In those very specific conditions and for the highest values of H_2 outgassing, biomass production can reach about 10^{10} molecules C cm^{-2} s^{-1}—about 1000 times less than estimates of modern primary production[26].

Metabolic evolution and the carbon cycle. Next, we investigate how the evolutionary process of metabolic diversification of the primitive biosphere shaped the planet atmospheric and climatic history. We consider alternate scenarios of biosphere evolutionary complexification (Fig. 4a) consistent with phylogenetic and geological inferences[2,7,9–11,27]. Our evolutionary sequences culminate with the evolution of anaerobic methanotrophy, which uses the oxidation of CH_4 as primary source of energy, based on the consumption of H_2SO_4, the main oxidative species of the globally reduced early Earth[28]. We, therefore, make the plausible

assumption that a full methane-cycling biosphere may have evolved before the advent of photosynthesis.

This evolutionary process of diversification may have spanned several hundred million years (from the origin of life 3.9–4.5 Gya, to the origin of anoxygenic phototrophy, 3.5–3.7 Gya), thus unfolding on a timescale over which the geochemical cycles interacted dynamically and reciprocally with biological activity. In particular, it has been shown[5] that on the timescale of 10^7 to 10^8 years, the carbon cycle tends to mitigate temperature variations through a negative feedback on the atmospheric CO_2 concentration. We adapted the model from ref. [5] to add a full, temperature-dependent carbon cycle to our planetary ecosystem model. The abiotic equilibrium pCO_2 is now determined by the balance between CO_2 outgassing and sequestration in the oceanic floor; $pCH4$, by the balance between serpentinization and photodissociation rates; and pH_2, by the balance between outgassing and photochemical reactions. Additionally, the H_2SO_4 oceanic concentration is determined by the balance between rainout and hydrothermal remineralization rates (taken from ref. [29]). By drawing values for the abiotic supplies in CO_2, CH_4, H_2, and H_2SO_4 from reasonable, log-uniform priors (Table 1), and starting from a lifeless primitive Earth, we evaluate the equilibrium state of the planetary system after each evolutionary
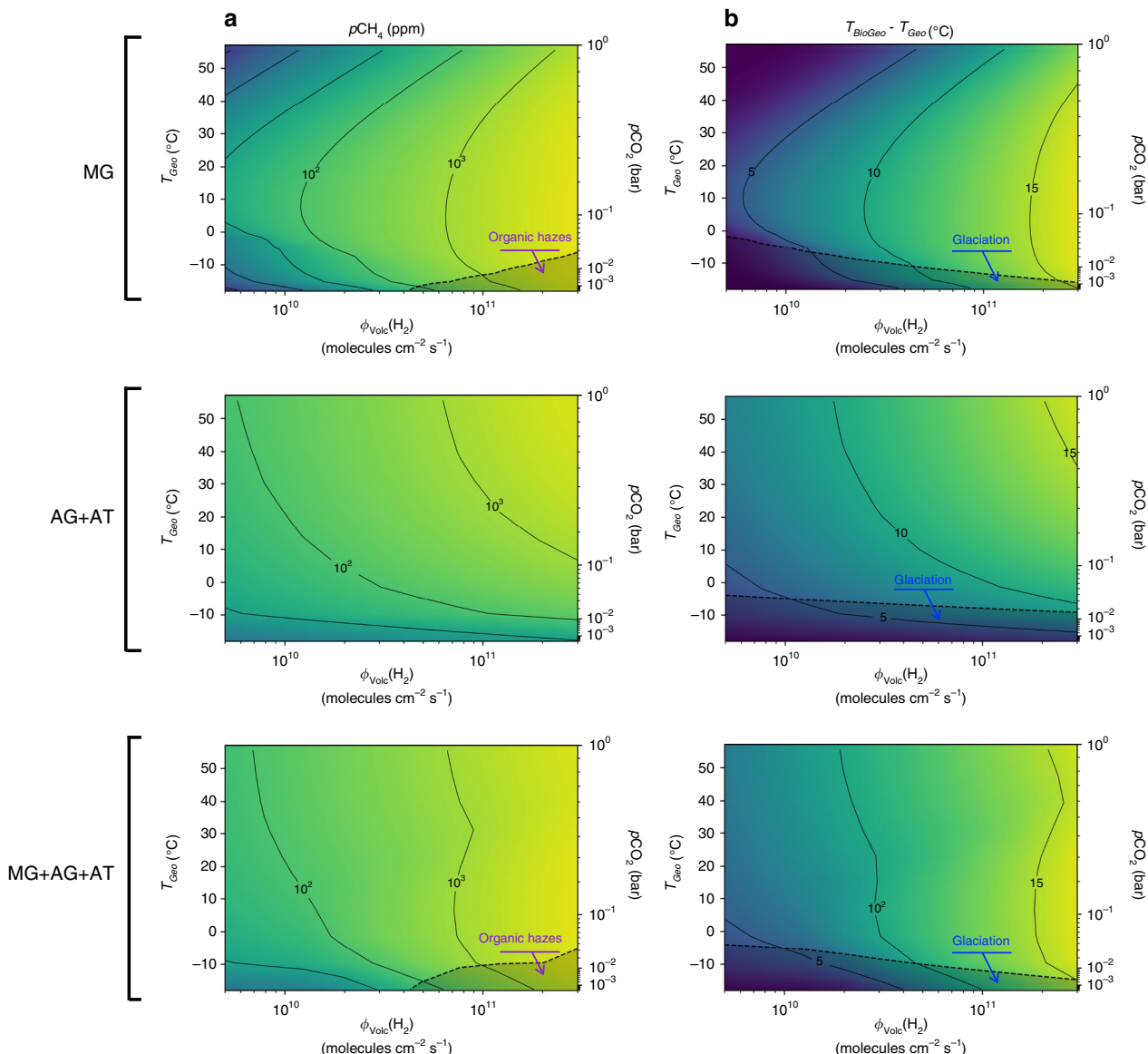
Fig. 3 Short-term biological feedback on the atmosphere and climate. Effects are computed as a function of the H_2 volcanic outgassing and abiotic surface temperature (T_{Geo}), for each ecosystem composition. MG indicates H_2-based methanogens. AG+AT indicates CO-based acetogens and methanogenic acetotrophs consortia. MG+AG+AT indicates co-occurring methanogens, acetogens, and acetotrophs. T_{Geo} is varied by changing pCO_2 in the climate model. **a** Atmospheric pCH_4 at ecosystem-climate equilibrium. Shaded areas indicate conditions for organic haze formation. **b** Temperature differential between T_{Geo} and the global surface temperature reached at ecosystem-climate equilibrium, T_{BioGeo}. Shaded areas indicate conditions leading to organic haze formation (**a**) and glaciation (**b**). Other parameters are set at their default values (Supplementary Tables 2 and 3).

metabolic transition in terms of atmospheric signatures (Fig. 4b–d) and mean surface temperature (Fig. 4e).

First, we find that a lifeless Earth is characterized by a high CO: CH_4 atmospheric ratio of 10^2–10^4 to 1, which differs markedly from the ratio predicted with a functional biosphere, regardless of its metabolic composition. As the biosphere complexifies, biological activity increases the atmospheric concentration in CH_4, decreases the atmospheric CO, or both, causing the CO:CH_4 ratio to fall. By comparing median values between the abiotic state and the most complex biosphere (MG + AG + AT + MT), the CO:CH_4 ratio is predicted to be reduced by a factor of ~5000. The earliest evolutionary events, whereby the MG, AG, or AG + AT ecosystem emerges, all cause atmospheric shifts that can be distinguished in the pCO-pH_2-pCH_4 space (Fig. 4b and c). The atmospheric shifts caused by subsequent evolutionary complexification (leading to MG + AG, MG + AG + AT, or MG + AG +

AT + MT ecosystems) are less pronounced and the corresponding atmospheric signatures are less distinctive among themselves. The evolution of anaerobic methanotrophy (MT) has for instance no effect on the equilibrium atmosphere of the planet because the influx of H_2SO_4 is sufficient for methanotrophs to survive and co-occur with methanogens, but not for them to consume a significant portion of the CH_4 produced by methanogens.

Finally, although methanogenesis can have major effects on climate on relatively short time scales (Figs. 2 and 3), the carbon cycle buffers these effects at equilibrium on longer time scales: the average temperature difference between the planet with and without a methanogenic biosphere on its surface is only 4 °C (Fig. 4d). Biological effects on temperature may be further attenuated by the formation of cooling organic hazes favored by the enhanced sequestration of CO_2 in response to methanogenesis[25]. However, the necessary conditions for organic hazes to
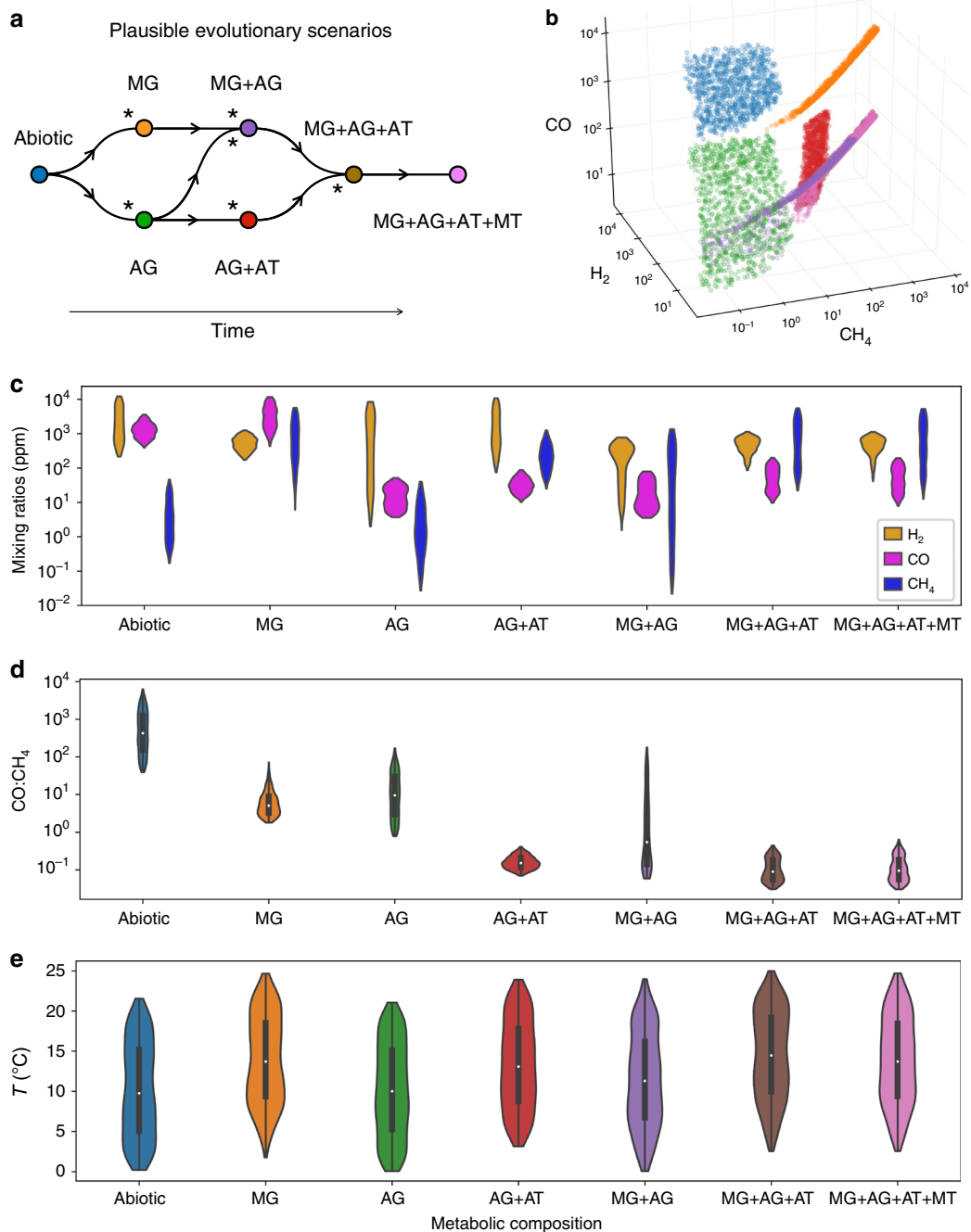
Fig. 4 Equilibrium state of the planet as the biosphere diversifies. a Plausible evolutionary sequences of metabolic innovation. Asterisks denote transitions that are very likely to cause a significant change in the atmospheric composition. **b** Scatterplot of the atmospheric compositions at equilibrium in CO, CH_4, and H_2, color-coded by the corresponding biosphere composition (1000 simulations for each ecosystem). **c** Corresponding distributions. **d** Distribution of the CO:CH_4 ratio for each scenario. **e** Distribution of the surface temperature in each scenario. The white dots in **d**, **e** represent the median of the distributions, the thick gray lines the interquartile range, and thin gray lines the rest of the distribution.

Table 1 Abiotic inputs of CO_2, H_2, CH_4 and H_2SO_4.

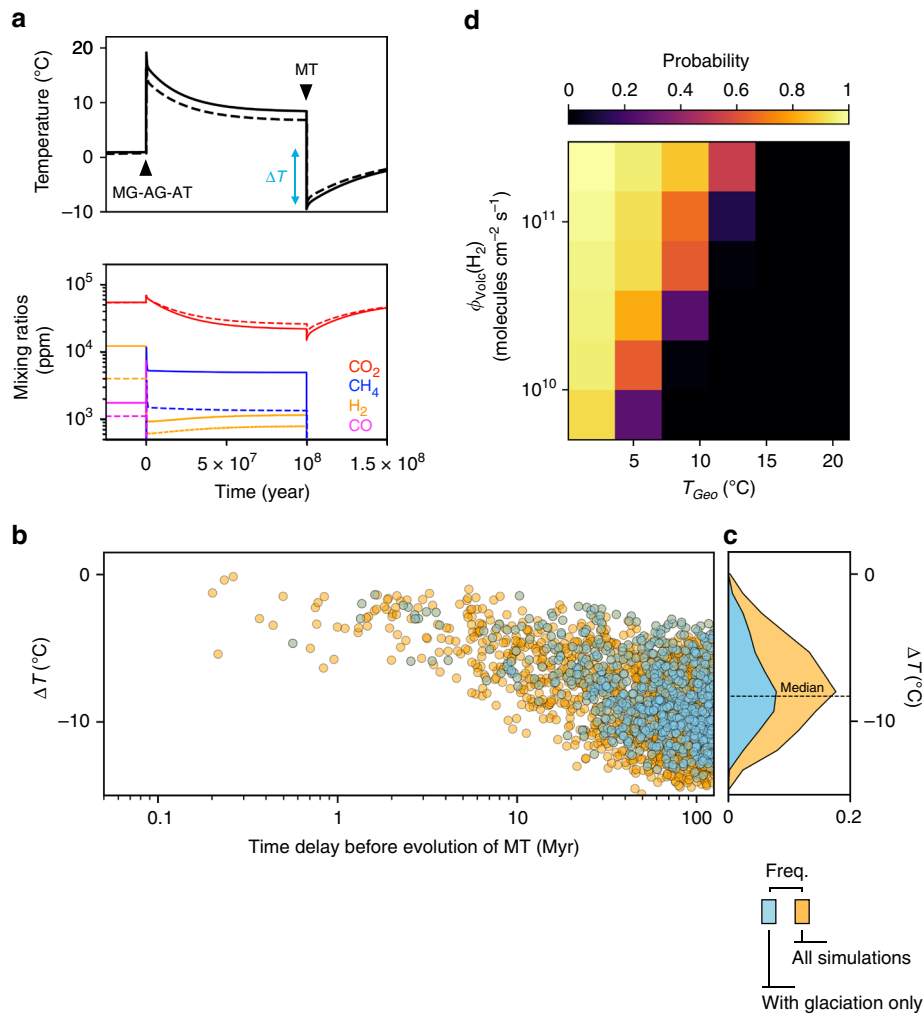| Abiotic inputs	Range (in molecules $cm^{-2} s^{-1}$)	Reference
Volcanic output of CO_2	1.2×10^{10}– 4×10^{10} (to obtain T_{Geo} ranging from 0 to 20 °C)	ref. [5]
Volcanic output of H_2	5×10^9–3×10^{11}	ref. [12]
Serpentinization rate of production of CH_4	3.7×10^8–3.7×10^9	ref. [33,42]
Deposition rate of H_2SO_4	10^7–10^9	ref. [30]

Fig. 5 Climate destabilization by evolutionary metabolic innovation. a In this example, sulfur-based methanotrophy (MT) evolves 100 million years after MG + AG + AT, i.e. after equilibration of the methanogenic biosphere (MG + AG +AT) with the atmosphere and climate mediated by the carbon cycle, with $T_{Geo} = 2\,°C$, $\varphi_{volc}(H_2) = 3 \times 10^{11}$ (plain lines) and 1×10^{11} molecules $s^{-1}\,cm^{-2}$ (dotted lines). Top, change in surface temperature. Bottom, change in atmospheric composition. **b**, **d** Distribution of outcomes across a range of abiotic temperature T_{Geo}, H_2 volcanic flux, and evolution time of MT (2000 randomly chosen combinations). **b** Amplitude of global cooling, ΔT, with respect to the evolution time of MT. **c** Frequency distribution of all temperature changes ΔT (blue) and of temperature changes conditional on glaciation outcome (yellow). **d** Estimated probability of glaciation as a consequence of MT evolution, given the abiotic temperature T_{Geo} and H_2 volcanic flux. Other parameters are set to their default values (Supplementary Tables 2 and 3).

form in this case are met in only 0.03% of the simulations including a methanogenic biosphere.

Transient climate destabilization by methanotrophy. How the planetary atmosphere-climate system responds to metabolic innovation may depend on the pace of evolution itself. The evolution of methanotrophy is a case in point. Slow evolution may delay methanotrophy after the response of the carbon cycle to methanogenesis. In this case, the oceanic stocks of H_2SO_4 are sufficient for methanotrophs to rapidly consume almost all of the atmospheric CH_4 (Supplementary Fig. 6) and the planet is temporarily characterized by an atmospheric deficit in both CO_2 and CH_4. As a result, temperature plummets below the initial abiotic temperature. In contrast, if evolution is fast enough and methanotrophs evolve before equilibration of the methanogenic biosphere with the planetary atmosphere and climate, atmospheric CH_4 may be consumed during or after the warming period (Fig. 3) but before the deficit in pCO_2 builds up; temperature then returns close to its initial value (Supplementary Fig. 6).

Figure 5a illustrates the atmospheric and climatic consequences of slow evolution, when the wait time for methanotrophy is of the order of the carbon cycle timescale. In the two examples shown, the evolution of methanotrophs causes the sharp climatic response described above, and temperature falls respectively by 8 and 10 °C below $T_{Geo} = 2\,°C$, driving the planet into a global glaciation. Among 2000 simulated planetary conditions characterized by randomly drawn abiotic characteristics (i.e., the abiotic influxes of CO_2, H_2, CH_4 and H_2SO_4, thereby setting the abiotic pCO_2, pH_2, pCH_4, initial oceanic concentration of H_2SO_4 and surface temperature T_{Geo}), and evolution time of methanotrophy (from 0 to 125 million years after methanogenesis), 50% experience a temperature drop larger than 8.3 °C below T_{Geo} (Fig. 5b), and 40% actually end up in glaciation (Fig. 5b and Supplementary Fig. 7). As expected, delayed evolution of methanotrophy makes extreme cooling more likely (Fig. 5b). Because they lead to an enhanced abiotic response of the carbon cycle, conditions for which methanogenic ecosystems have the greatest warming effect (low abiotic T_{Geo}, high H_2 outgassing rate) are also the conditions under which the evolution of

7

methanotrophy has the most dramatic effect on climate and habitability (Fig. 5a and c, Supplementary Fig. 8). Noticingly, this transient occurs irrespective of the metabolic composition of the methanogenic biosphere prior to the evolution of methanotrophy, as illustrated in Supplementary Fig. 7.

For a methane-cycling ecosystem that triggers and eventually survives global glaciation, we expect the resulting equilibrium (co-occuring methanogens and methanotrophs with low pCH$_4$) to be maintained only transitorily. We assume that during the early Archean, prior to the evolution of methanotrophy, the oceanic stock of H$_2$SO$_4$ builds up as volcanoes emit SO$_2$ photochemically transformed into H$_2$SO$_4$, which then deposits on the ocean surface. With a deposition rate corresponding to our lowest value of 10^7 molecules cm^{-2} s^{-1} (ref. [30]), and a hydrothermal removal rate of [H$_2$SO$_4$]$_{oc.}$ × 7.2×10^{12} L y^{-1} (ref. [29]), we obtain an abiotic oceanic concentration of 0.4 mM. Such a stock is sufficient for methanotrophs to consume most of the atmospheric CH$_4$, leading to the global cooling described above. Since the rate of CH$_4$ reduction by methanotrophs is faster than the deposition rate, the H$_2$SO$_4$ stock will ultimately be depleted by methanotrophs, thereby driving a new abrupt environmental shift towards the equilibrium described in Fig. 4. At this new, stable equilibrium of coexisting methanogens and methanotrophs, the atmospheric pCH$_4$ is high and the H$_2$SO$_4$ oceanic concentration is very low, below the micromolar, which aligns with the sulfur isotopic fractionation records[30–32]. This result suggests that anaerobic methanotrophy may have been the main sink of H$_2$SO$_4$ prior to the Neoarchean (2.5–2.7 Gya).

Discussion

Our initial questions were: How constrained was the habitability of late Hadean/early Archean Earth to methane-cycling ecosystems? How productive were these ecosystems and did they have a significant impact on the atmospheric composition and climate? How did their impact change as different metabolisms evolved? To address these questions, we build on the previous theory[8,12,13] by setting up a probabilistic modeling framework in which the evolution of a microbial biosphere is coupled to the dynamics of early Earth surface geochemistry and climate. We focus on four simple microbial metabolisms involved in methane cycling and likely to be some of the earliest players in Earth's ecology: hydrogenotrophic methanogenesis (MG), acetogenesis (AG), methanogenic acetotrophy (AT), and anaerobic oxidation of methane (MT). The biosphere evolves when a metabolism that was not present appears and adapts. By closing the global feedback loop between biological and planetary surface processes, the model predicts both ecosystem and atmosphere-climate states under the assumption that they reciprocally influence one another.

Our results confirm the contention that the late Hadean/early Archean planet was most likely habitable to methane-cycling chemolithotrophic biospheres and that under the assumption of high enough H$_2$ supply, these biospheres were key factors of the climatic and atmospheric evolution of the planet[8,12,13,33,34]. On short time scales (10^5–10^6 years) the evolution of methanogenic biospheres may have considerably warmed the climate and influenced its resilience, in spite of a very low ecosystem productivity. On longer timescales, commensurate with the abiotic response of the carbon cycle to temperature variation, all ecosystems converge to new stable equilibria. Under these long-term equilibrium conditions, the mean surface temperature does not differ much from the lifeless state, and the carbon cycle is the predominant mechanism of climate regulation. However, all ecosystem equilibria share a robust atmospheric signature (low CO:CH$_4$ ratio), distinctive from the lifeless state. In addition to

influencing planetary characteristics at equilibrium, metabolic evolution generates atmospheric and climatic transients. The pace of evolution thus has a strong influence on the atmosphere and climate history. In particular, fast evolution of methanotrophs has limited or no effect on climate, whereas their delayed evolution may cause strong transients leading to global glaciation.

Although the influence of chemotrophic methane-cycling ecosystems on climate has been discussed in the previous work[8,12,13,33,34], our model is the first to couple models of the Archean atmosphere, climate, and carbon cycle to an explicit eco-evolutionary model of cell population dynamics in order to quantify this effect. Our model differs from previous work primarily by addressing how climate change driven by ecological function feeds back to the biological activity of microbial populations, through the thermal dependence of the thermodynamics and kinetics of cell metabolism, and triggers an abiotic response of the carbon cycle. Closing the global feedback loop between ecological and planetary processes allows us to predict the eco-system and climate states under the assumption that they reciprocally influence one another on multiple timescales.

A general result is that MG and AG + AT ecosystems are characterized by extremely low biomass production relative to their planetary impact on the atmosphere and climate. We predict biomass production to be 1–4 orders of magnitude smaller than previous estimates[13] and 3–7 orders of magnitude below modern values[26]. Maximum global biomass production (reached for a very specific combination of biotic and abiotic conditions) is 10^{10} molecules C cm^{-2} s^{-1}, or 3×10^7 ton C year^{-1}. This is ~1000 times less than estimates of modern primary production. Both in terms of stock and fluxes, biomass has therefore very little effect on the biogeological coupling, which is a major difference with modern ecosystems.

A key assumption of our model is that nutrients N and P are not limiting; this assumption is backed up by the prediction of very low biomass production. As previously argued[13,14], primitive ecosystems with such low productivity should have been limited by the availability in electron donors rather than by N and P nutrients. More specifically, ref. [14] evaluated the most likely limitation to biomass production prior to the evolution of oxygenic photosynthesis. By assuming a fixed yield for biomass production per molecules of electron donor consumed (as in ref. [13]), they found that the N and P supplies were most likely sufficient during the Archean for electron donors to be limiting. This is even more likely given our finding of a biomass productivity far lower than the previous estimates[13,14].

Our prediction of very low biomass productivity may help better constrain the timeline of the evolution of metabolic innovation on Earth. Even in our most productive scenario and under the (extreme) assumption that 100% of the dead organic matter is buried before remineralization, the estimated biomass production is still 4–5 times lower than the level consistent with the C isotopic fractionation estimated from rocks as old as 3.5 Gy[1,35]. This suggests that more productive, likely photosynthetic life forms must have evolved more than 3.5 Gya ago.

By performing equilibrium analyses of the planetary system on longer time-scales (10^7–10^8 years), on which the carbon cycle responds to ecosystem function and sequential metabolic diversification of the biosphere, we find that the climate regulation of the planet by the abiotic carbon cycle largely buffers the influence of early methanogenic activity on climate. However, depending on the pace of evolution, metabolic transitions such as the evolution of methanotrophy can interact with the abiotic carbon cycle and trigger strong transitory climatic events such as global glaciation over 10^7–10^8 years.

Even though the timing of the origin of anaerobic oxidation of methane (AOM), by reduction of nitrate, nitrite, or sulfate, is not

well resolved, the fact that AOM proceeds enzymatically as a reversal of methanogenesis has been used to suggest that AOM may have evolved relatively soon after methanogens, i.e. before phototrophy[36,37]. Additionally, we find that the evolution of AOM prior to photosynthesis appears to be compatible with the sulfur isotopic fractionation record[30–32]. Our results thus highlight biological activity and the evolution of pre-photosynthetic methane-cycling ecosystems as a potential destabilizing factor of the early Earth climate system, alternatively or additionally to abiotic causes such as large impactors[3,4,38].

The mechanism by which the evolution of early methane-cycling ecosystems may have exposed the Earth to high risks of global glaciation—fast removal of atmospheric methane, slow response of the carbon cycle—is general. It is, therefore, tantalizing to speculate about its potential involvement in the major climatic events that paralleled the evolution of oxygenic photosynthesis. By poisoning methanogens, removing the resource limitation (oxidizing species: O_2, H_2SO_4, NO_3, NO_2) of methanotrophs, or by simply driving the abiotic oxidation of atmospheric CH_4 by outgassed O_2, oxygenic photosynthesis may have driven a dramatic decline in atmospheric CH_4 which, coupled to a delayed response of the carbon cycle, could have caused global cooling, triggering the Proterozoic glaciation ~2.3 Gya[39–41].

The substantial shifts in atmospheric composition driven by evolutionary metabolic innovation (Fig. 4) highlight the fact that simple methane-cycling ecosystems can have radically different atmospheric signatures. Thus, the atmosphere composition is shaped very early on by the course of biological evolution. We observe that the atmospheric signature of a specific metabolism is highly dependent on the ecological context set by the whole metabolic composition of the biosphere. As the biosphere evolves and complexifies, the atmospheric signature of each metabolic type becomes less identifiable, yet the state of the planet remains distinctive from the lifeless scenario. This backs up and quantifies the hypothesis that on a globally reduced planet such as the early Archean Earth, a low $CO:CH_4$ atmospheric ratio is a highly discriminant indicator of inhabitation by a primitive CH_4-based biosphere[42].
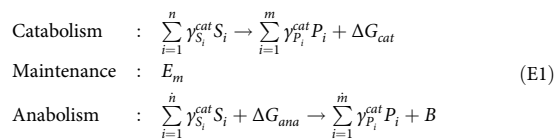
In conclusion, our results suggest that life has had a dramatic impact on the anoxic Earth's surface environment, long before phototrophy evolved. They highlight the importance of the evolutionary process and its timeline in shaping up the planet's atmosphere and climate. In spite of extremely low productivity, metabolic evolutionary innovation in primitive methane-based biospheres is predicted to cause distinctive shifts in atmospheric composition, such as a decreasing $CO:CH_4$ ratio as greater metabolic complexity evolves. The warming effect of methanogens and cooling effect of methanotrophs can be strong but they are only transient, on timescales that depend on the pace of evolution. We anticipate that the continued development of models that couple planetary processes with ecological and evolutionary dynamics of microbial biospheres will further advance our understanding of major events in the co-evolutionary history of life and Earth, and help identify detectable biosignatures for the search of life on Earth-like exoplanets.

Methods

Biological model. In the following section, we present the biological model. Parameters' definition, unit and default value are given in Supplementary Tables 1, 2, and 3.

The biological model describes the dynamics of one or several biological populations of chemotrophic organisms, driven by the growth, birth (division) and death of individual cells. The individual cell life cycle is controlled by catabolic and anabolic reactions occurring within cells[17,18,43]. Catabolism produces energy used by anabolism for biomass production, which determines cell growth and division; a fraction of energy produced by catabolism is used for cell maintenance. Energy thus flows from catabolism to maintenance and anabolism, and these processes can

be described as follows:

$$
\begin{aligned}
\text{Catabolism} \quad &: \quad \sum_{i=1}^{n} \gamma_{S_i}^{cat} S_i \rightarrow \sum_{i=1}^{m} \gamma_{P_i}^{cat} P_i + \Delta G_{cat} \\
\text{Maintenance} \quad &: \quad E_m \\
\text{Anabolism} \quad &: \quad \sum_{i=1}^{\dot{n}} \gamma_{S_i}^{cat} S_i + \Delta G_{ana} \rightarrow \sum_{i=1}^{\dot{m}} \gamma_{P_i}^{cat} P_i + B
\end{aligned}
\tag{E1}
$$

where S_i and P_i are the substrates and products of the metabolic reactions, and the γ's are the corresponding stoichiometric coefficients. We follow ref. [17] and assume that the average organic compound $CH_{1.8}O_{0.5}N_{0.2}$ is a plausible approximation for the living biomass B. The energy E_m (in kJ d^{-1}) measures the cost of maintenance for a single cell per unit of time. The ΔG terms measure the oxidative power released or consumed by the catabolic and anabolic reactions; they are given by the Nernst relationship:

$$
\Delta G(T) = \Delta G_0(T) + RT log \left(\prod_{i=1}^{n} S_i^{\gamma_{S_i}} \prod_{i=1}^{m} P_i^{\gamma_{P_i}} \right)
\tag{E2}
$$

where R is the ideal gas constant, T is the temperature (in K) and $\Delta G_0(T)$ (in kJ) is the Gibbs energy of the reaction. $\Delta G_0(T)$ is obtained from the Gibbs–Helmholtz relationship:

$$
\Delta G(T) = \Delta G_0(T_S) \frac{T}{T_S} + \Delta H_0(T_S) \frac{T_S - T}{T_S}
\tag{E3}
$$

where T_S is the standard temperature of 298.15 K. Note that equations (E2) and (E3) describes how the thermodynamics of any given metabolism (i.e., the combination of catabolism and anabolism) vary with temperature.

Michaelis–Menten kinetics apply to catabolism:

$$
q_{cat} = q_{max} \frac{min(S_i^{cat}/\gamma_{S_i}^{cat})}{min(S_i^{cat}/\gamma_{S_i}^{cat}) + K_S}
\tag{E4}
$$

where K_S is the half-saturation constant, q_{max} the maximum metabolic rate of the cell (d^{-1}), and $min(S_i^{cat}/\gamma_{S_i}^{cat})$ measures the concentration of the limiting substrate (taking stoichiometry into account). The energy produced is first directed toward maintenance. The cell energetic requirement for maintenance is:

$$
q_m = \frac{-E_m}{\Delta G_{cat}}
\tag{E5}
$$

The cell therefore meets its energy requirement only if $q_{cat} > q_m$. If the cell does not meet this requirement, the basal mortality rate of the cell, m, (in d^{-1}), is augmented by a decay-related mortality term equal to $k_d(q_m - q_{cat})$. Hence the actual mortality rate:

$$
\begin{aligned}
\text{If } q_{cat} < q_m \quad &: \quad d = m + k_d(q_m - q_{cat}) \\
\text{If } q_{cat} > q_m \quad &: \quad d = m
\end{aligned}
\tag{E6}
$$

When the energy requirements for maintenance are not met ($q_{cat} < q_m$) no energy is allocated to biomass production. Conversely, when those requirements are met ($q_{cat} < q_m$), then the energy remaining after allocation to cell maintenance can be directed to anabolism. A constant quantity of energy ΔG_{diss} (in kJ) is then lost through dissipation. Following ref. [17] we consider the following empirical relationship:

$$
\Delta G_{diss} = 200 + 18(6 - NoC)^{1.8} + e^{(-0.2-\alpha)^{2.16}(3.6+0.4NoC)}
\tag{E7}
$$

where NoC is the number of carbons in the carbon source used by the anabolic reaction, and α is its degree of oxidation. The efficiency of metabolic coupling (i.e., the number of occurrences of the catabolic reaction to fuel one occurrence of the anabolic reaction once the maintenance cost has been met) is then measured by

$$
\lambda = \frac{-\Delta G_{cat}}{\Delta G_{ana} + \Delta G_{diss}}
\tag{E}
$$

The Michaelis–Menten kinetics of anabolism is given by

$$
\begin{aligned}
\text{If } q_{cat} > q_m \quad &: \quad q_{ana} = \lambda(q_{cat} - q_m) \frac{min(S_i^{ana}/\gamma_{S_i}^{ana})}{min(S_i^{ana}/\gamma_{S_i}^{ana}) + K_S} \\
\text{If } q_{cat} < q_m \quad &: \quad q_{ana} = 0
\end{aligned}
\tag{E9}
$$

where the half-saturation constant K_S independent of the substrate, as was assumed in ref. [43]. As biomass accumulates in the cell at rate q_{ana}, cell growth may lead to cell division. The cell division rate, r, is given by:

$$
\begin{aligned}
\text{If } B < 2B_{Struct} \quad &: \quad r = 0 \\
\text{If } B > 2B_{Struct} \quad &: \quad r = r_{max} \frac{1}{1+e^{-\theta log10((B-2B_{Struct})/B_{Struct})}}
\end{aligned}
\tag{E10}
$$

This means that a cell cannot divide if its internal biomass is not at least twice its cell structural biomass so that the two daughter cells meet this structural requirement. Above this threshold value of $2B_{Struct}$, r is of sigmoidal form so that the division rate first increases exponentially with the intracellular biomass content then saturates to r_{max} when biomass is largely available.

Using the rates of catabolic and anabolic cell activity and resulting cell division and mortality rates, we derive the following system of ordinary differential equations driving the cell population dynamics (dynamics of the number of cells

and average cell biomass) and the feedback of the population on its environment (chemical composition of the ocean surface):

$$\frac{dN_i}{dt} = (r_i - d_i)N_i$$
$$\frac{dB_i}{dt} = q_{ana_i} - r_iB$$
$$\frac{dX_j}{dt} = F(X_j) + \sum_{i=1}^{MT}(q_{cat_i}\gamma_{i,X_j}^{cat} + q_{ana_i}\gamma_{i,X_j}^{ana})N_i \qquad (E11)$$

where MT denotes the ensemble of metabolic types considered, N_i is the number of individual cells in a population of a given metabolic type, B_i is the average cellular biomass of that type, and $X_1, ..., X_S$ are the concentrations of all relevant chemical species in the environment. The term $\sum_{i=1}^{MT}(q_{cat_i}\gamma_{i,X_j}^{cat} + q_{ana_i}\gamma_{i,X_j}^{ana})N_i$ describes how concentrations vary according to the biological activity of each biological population i in the microbial community. The $F(X_j)$ terms describe the environmental forcing resulting from ocean circulation and atmosphere-ocean exchanges as simulated by a stagnant boundary layer model as in ref. [13]. The system of equations (E11) is solved numerically using a forward Euler method.

The flow of energy through the cell is driven by the maximum metabolic rate, q_{max} (in d^{-1}), and the rate of energy consumption for maintenance, E_m (in kJ d^{-1}). They are both expressed as functions of temperature and cell size of the form $e^{a+b}TV^c$. Default values for parameters a, b and c entering q_{max} and E_m are given in Supplementary Table 2.

The structural cell biomass B_{Struct} increases with cell size according to $B_{Struct} = aV^b$. Both metabolic rate and maintenance cost increase with cell size, but not as fast as structural biomass. Consequently, the biomass specific rates of metabolism and energy consumption for maintenance decrease with cell size. Thus, small organisms are better at acquiring energy, but large organisms are more cost efficient due to lower maintenance requirements. A trade-off mediated by cell size thus exists between metabolic and maintenance rates, hence an optimal (intermediate) cell size, which is consistent with previous work conducted on unicellular marine organisms[22]. Both metabolic and maintenance rates increase with temperature, but the metabolic rate increases slightly faster[19,20], shifting the trade-off toward larger sizes. As a consequence, the optimal cell size increases with temperature.

To compute the evolutionarily optimal cell size for a given metabolic type at a given temperature, we run simulations across a range of cell size and measure the level of resource use at equilibrium given by $Q^* = \prod_{i=1}^{n} S_i^{\gamma_{S_i}} \prod_{i=1}^{m} P_i^{\gamma_{P_i}}$, the product of the metabolic substrates and wastes concentrations at equilibrium weighted by their stoichiometric coefficient. According to the classical principle of "pessimization" (maximization of resource use)[44–46], populations that are better at exploiting their environment have lower Q^* and evolution by natural selection will favor the cell size that minimizes Q^*, thus leading to the evolutionarily optimal cell size. Supplementary Fig. 9 shows Q^* as a function of cell size and temperature for the H_2-based methanogenesis.

The optimal cell size, S_C^*, follows a positive relationship with temperature given by $S_C^* = 10^{a+bT}$. We consider that over geological time scales, adaptive evolution acting on genetic variation among cells is fast enough so that S_C is equal to S_C^*. As temperature changes, evolutionary adaptation by natural selection tracks the temperature-dependent optimal cell size.

In contemporary Earth oceans, most of the dead biomass is recycled by fermentors (>99%), and the rest is buried into the ocean floor. Although the most general version of our model includes populations of acetogenic biomass fermentors and acetotrophs, their inclusion considerably increases simulation time (results not shown). All the results presented in the main text have been obtained without fermentors, assuming that the dead biomass accumulates in the ocean's interior. It appears that biomass productivity is so low that the effect of biomass recycling (or lack thereof) on the atmospheric composition is negligible. We verified this by testing the effect of a recycling pathway in each ecosystem (MG, AG + AT, MG + AG + AT), for an intermediate value of H_2 volcanic outgassing. Although biomass production is sufficient to sustain a population of fermentors, we found no significant effect of their biological activity on the atmospheric composition. Additionally, when we can compare the global atmospheric redox budget of the planet with and without biomass production (see Supplementary Results and Discussion, Supplementary Fig. 12), we find no significant differences. This further demonstrates that biomass production and the accumulation of dead biomass in the absence of remineralization represents a sink of C and H that is marginal compared to the other fluxes in the model. Note that the situation would be very different after the evolution of more productive, photosynthetic primary producers.

Because we do not model the fate of dead biomass explicitly, we evaluate the consistency of our predictions of biomass production with the geological record (carbon isotopic fractionation data) by taking biomass production as the upper bound for burial (in which case 100% of the produced biomass is ultimately buried) and using the modern value of burial (taken to be 0.2% as in e.g., ref. [13]) as lower bound.

Planetary model. Our computation of climate state and mean surface temperature is based on 3D simulations with the Generic LMD GCM[4,47,48]. The model includes a 2-layer dynamic ocean computing heat transport and sea ice formation[49]. The

radiative transfer is based on the correlated-k methods with k-coefficients calculated using the HITRAN 2008 molecular database. We used the simulations described in ref. [4] for the early Earth at 3.8 Ga, assuming no land, 1 bar of N_2 and a 14 h rotation period. The simulation grid covers a range of pCO_2 from 0.01 to 1 bar and pCH_4 from 0 to 10 mbar. From this grid, we derived the following simple parametrization of the mean surface temperature as a function of pCO_2 and pCH_4 (expressed in bar):

$$T(^\circ C) = -19.26 + 77.67\sqrt{pCO_2} + 5\log10\left(\frac{1 + pCH_4 10^6}{3}\right) \qquad (E12)$$

In the coupled biological-planetary model, we assume that the climate is always at equilibrium, meaning that the timescale of climate convergence is shorter than biological and geochemical timescales.

Photochemistry is computed with the 1D version of the Generic LMD GCM, which now includes a photochemistry core from ref. [50]. The chemical network includes 30 species (mostly hydrocarbons) and 114 reactions. We use the reactions from ref. [50] for H_2-H_2O-CO_2 and from ref. [51] for hydrocarbons. The photochemistry model also includes a pathway for the formation of hydrocarbon aerosol ($C_2H + C_2H_2 \rightarrow HCAER + H$)[51,52].

We use the eddy diffusion vertical profile from ref. [53] and the solar UV spectrum at 3.8 Ga from ref. [54]. Boundary conditions are set by the mixing ratios of CO_2, CH_4, and H_2O at the first atmospheric layer. The atmospheric CO is either consumed biotically by acetogens when they are present in the biosphere, or abiotically by the formation of formate in the ocean (resulting in a deposition velocity of ~10^8 cm s^{-1}) as in ref. [13,55]. This eliminates the possibility of CO-runaway, which otherwise occurs in our simulations at high level of H_2 or CO_2. In addition, we assume that H_2 undergoes diffusion-limited atmospheric escape (see for instance ref. [13]).

We performed simulations across a range of pCO_2 (10^4–10^5 ppm), pCH_4 (1–10^4 ppm), H_2 (100–10^4 ppm). For our range of atmospheric composition, photochemistry is dominated by the photolysis of CO_2 and CH_4, whose net reactions are:

$$CO_2 + H_2 = CO + H_2O \qquad (R1)$$

$$CH_4 + CO_2 = 2CO + 2H_2 \qquad (R2)$$
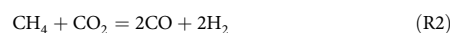
From the simulation outputs we derived simple parametrizations for the production rates and loss rates of CH_4, CO, H_2 (see Supplementary Fig. 10). The reaction rates of (R1) and (R2) can be parameterized respectively as (in molecules $cm^{-2}\,s^{-1}$):

$$F_1 = 1.8\,10^{10}\cdot\left(\frac{pCO_2}{10^{-1}}\right)\cdot\left(\frac{pH_2}{10^{-4}}\right)^{0.4} \qquad (E13)$$

$$F_2 = 2\,10^{10}\left(\frac{pCO_2}{10^{-1}}\right)^{-0.2}\cdot\left(\frac{pH_2}{10^{-4}}\right)^{-0.2}\cdot\left(\frac{pCH_4}{10^{-4}}\right)^u \qquad (E14)$$

where u (between 0.5 and 1) is given by

$$u = 0.6 + 0.1\log\left(\frac{pH_2}{10^{-4}}\right) - \frac{\log(pCH_4) + 2}{15} + 0.08\log\left(\frac{pCO_2}{10^{-1}}\right) \qquad (E15)$$

To simulate the evolution of pCO_2 with time and feedbacks between the microbial community, climate, and the carbon cycle, we use a simple carbon cycle model based on ref. [5]. The model computes the evolution of atmospheric CO_2, dissolved inorganic carbon (CO_2, HCO_3^- and CO_3^{2-}) and pH in the ocean and in seafloor pores. The model takes into account outgassing (from volcanoes and mid-oceanic ridges), continental silicate weathering, dissolution of basalts in the seafloor, and oceanic chemistry, as sources and sinks of CO_2. For all parameters in the carbon cycle model, we use the mean values given in ref. [5]. For the temperature dependences of silicate weathering and oceanic chemistry, we use the mean surface temperature from our climate model. Even though this model only computes global mean quantities and does not take into account the organic matter in carbon sources and sinks of carbon, it is computationally very fast and well suited for studying the major feedbacks between biological populations and the atmosphere and climate.

Coupled biological-planetary model. The model resolves dynamics that take place on extremely different timescales—geological processes are extremely slow (10^3–10^6 years) compared to biological dynamics (days to years). We use a time-scale separation approach and assume that the planetary environment is fixed on the biological time scale, and the biological system (population and local environment) is at ecological and evolutionary equilibrium on the geological time scale. This allows us to resolve the biological and geological dynamics separately and couple them at discrete points in time.

The biological dynamics are first resolved by the biological model for a fixed environmental forcing (equations (E11)), with microbial cells at their evolutionarily optimal size. The biological model is integrated over a sufficiently long time so that the local ecosystem reaches its equilibrium. Then we compute the biogenic fluxes between the surface ocean and the atmosphere, and between the surface ocean and the deep ocean, and feed them into the planetary model. The planetary model is then used to resolve the system's geochemical and climate dynamics, but only for a

sufficiently small change in the planetary state (1% to 1‰ variation of the state variable that changes the most) so that this change would alter the biological equilibrium only marginally. The new biological equilibrium is then computed, and the process is re-iterated. This iterative process approximates a continuous coupling between the microbial community and its planetary environment.

Monte-Carlo simulations. We explore the parameter range by stochastically varying the parameters that determine the maximum metabolic rate, the rate of energy consumption for maintenance, the metabolic half-saturation constant, the decay and mortality rates, and the maximum division rate. We also vary the values of the parameters that shape the dependencies on size, temperature, and cellular biomass (see Supplementary Table 4). Parameter values are picked uniformly or log-uniformly (to avoid making prior assumptions on the likelihood of specific regions of the parameter space) within ranges constrained by empirical data from the literature, or large enough to cover plausible empirical variation. Three thousand simulations were run for the MG ecosystem, one thousand for the AG + AT ecosystem, and one thousand for the MG + AG + AT ecosystem, under four different values of volcanic outgassing: $\phi_{Volc}(H_2) = 2 \times 10^{9.5}$, 2×10^{10}, $2 \times 10^{10.5}$, and 2×10^{11} molecules cm^{-2} s^{-1}, hence a total of 20,000 simulations. Each simulation was run to equilibrium.

The results can be divided into two subsets of roughly equivalent size, regardless of the ecosystems and volcanic activity considered: those with biological activity and those without (Supplementary Fig. 1A, B). We then verified that the number of simulations run for each of the considered scenarios was sufficient for the resulting distribution of equilibrium states to have converged. We evaluated convergence by subsampling, for each scenario, the subset of 'biologically viable' simulations with increasing sample size, and computing the average equilibrium biomass and CH$_4$ biogenic emission of the subsamples. The results are shown in Supplementary Fig. 2 for the three scenarios and for $\phi_{Volc}(H_2) = 2 \times 10^{10.5}$ molecules cm^{-2} s^{-1}.

Data availability
The data used to produce all the results presented in this study are available upon reasonable request to B.S.

Code availability
The codes used in this study to produce the data analyzed are available on a git repository upon reasonable request to B.S.

References
1. Nisbet, E. G. & Sleep., N. H. The habitat and nature of early life. *Nature* **409**, 1083 (2001).
2. Martin, W. F. & Sousa, F. L. Early microbial evolution: the age of anaerobes. *Cold Spring Harb. Perspect. Biol.* **8**, a018127 (2016).
3. Pearce, B. K. D. et al. Constraining the time interval for the origin of life on Earth. *Astrobiology* **18**, 343–364 (2018).
4. Charnay, B. et al. A warm or a cold early Earth? New insights from a 3-D climate-carbon model. *Earth Planet. Sci. Lett.* **474**, 97–109 (2017).
5. Krissansen-Totton, J. et al. Constraining the climate and ocean pH of the early Earth with a geological carbon cycle model. *Proc. Natl Acad. Sci. USA* **115**, 4105–4110 (2018).
6. Catling, D. C. & Kasting, J. F. *Atmospheric Evolution on Inhabited and Lifeless Worlds* (Cambridge University Press, 2017).
7. Battistuzzi, F. U. et al. A genomic timescale of prokaryote evolution: insights into the origin of methanogenesis, phototrophy, and the colonization of land. *BMC Evol. Biol.* **4**, 44 (2004).
8. Ozaki, K. et al. Effects of primitive photosynthesis on Earth's early climate system. *Nat. Geosci.* **11**, 55 (2018).
9. Weiss, M. C. et al. The physiology and habitat of the last universal common ancestor. *Nat. Microbiol.* **1**, 16116 (2016).
10. Marin, J. et al. The timetree of prokaryotes: new insights into their evolution and speciation. *Mol Biol Evol.* **34**, 437–446 (2016).
11. Havig, J. R. et al. Sulfur and carbon isotopic evidence for metabolic pathway evolution and a four-stepped Earth system progression across the Archean and Paleoproterozoic. *Earth-Sci. Rev.* **174**, 1–21 (2017).
12. Kasting, J. F. et al. A coupled ecosystem-climate model for predicting the methane concentration in the Archean atmosphere. *Orig. Life Evol. Biosph.* **31**, 271–285 (2001).
13. Kharecha, P., Kasting, J. & Siefert, J. A coupled atmosphere–ecosystem model of the early Archean Earth. *Geobiology* **3**, 53–76 (2005).

14. Ward, L. M., Rasmussen, B. & Fischer, W. W. Primary productivity was limited by electron donors prior to the advent of oxygenic photosynthesis. *J. GeoPhys. Res. BioGeo.* **124**, 211–226 (2019).
15. Charnay, B. et al. Exploring the faint young Sun problem and the possible climates of the Archean Earth with a 3-D GCM. *J. Geophys. Res. Atmos.* **118**, 10–414 (2013).
16. Lefèvre, F. et al. Three-dimensional modeling of ozone on Mars. *J. Geophys. Res. Planets* **109**, E7 (2004).
17. Kleerebezem, R. & Van Loosdrecht., M. C. M. A generalized method for thermodynamic state analysis of environmental systems. *Crit. Rev. Environ. Sci. Tec.* **40**, 1–54 (2010).
18. González-Cabaleiro, R., Lema, J. M. & Rodríguez, J. Metabolic energy-based modelling explains product yielding in anaerobic mixed culture fermentations. *PLoS ONE* **10**, e0126739 (2015).
19. Tijhuis, L., Van Loosdrecht, M. C. M. & Heijnen, J. J. A thermodynamically based correlation for maintenance Gibbs energy requirements in aerobic and anaerobic chemotrophic growth. *Biotechnol. Bioeng.* **42**, 509–519 (1993).
20. Gillooly, J. F. et al. Effects of size and temperature on metabolic rate. *Science* **293**, 2248–2251 (2001).
21. Litchman, E. et al. The role of functional traits and trade-offs in structuring phytoplankton communities: scaling from cellular to ecosystem level. *Ecol. Lett.* **10**, 1170–1181 (2007).
22. Ward, B. A. et al. The size dependence of phytoplankton growth rates: a trade-off between nutrient uptake and metabolism. *Am. Nat.* **189**, 170–177 (2017).
23. Aksnes, D. L. & Egge, J. K. A theoretical model for nutrient uptake in phytoplankton. *Marine Ecol. Prog. Ser. Oldendorf* **70**, 65–72 (1991).
24. Arney, G. et al. The pale orange dot: the spectrum and habitability of hazy Archean Earth. *Astrobiology* **16**, 873–899 (2016).
25. Domagal-Goldman, S. D. et al. Organic haze, glaciations and multiple sulfur isotopes in the Mid-Archean Era. *Earth Planet. Sci. Lett.* **269**, 29–40 (2008).
26. Prentice, I. C. et al. *The Carbon Cycle and Atmospheric Carbon Dioxide*, 185–237 (Cambridge University Press, 2001).
27. Moore, E. K. et al. Metal availability and the expanding network of microbial metabolisms in the Archaean eon. *Nat. Geosci.* **10**, 629–636 (2017).
28. Catling, D. C., Claire, M. W. & Zahnle, K. J. Anaerobic methanotrophy and the rise of atmospheric oxygen. *Philos. Trans. A Math. Phys. Eng. Sci.* **365**, 1867–1888 (2007).
29. Wong, M. et al. Nitrogen oxides in early Earth's atmosphere as electron acceptors for life's emergence. *Astrobiology* **17**, 975–983 (2017).
30. Ono, S. et al. New insights into Archean sulfur cycle from mass-independent sulfur isotope records from the Hamersley Basin, Australia. *Earth Planet. Sci. Lett.* **213**, 15–30 (2003).
31. Habicht, K. S. et al. Calibration of sulfate levels in the Archean ocean. *Science* **298**, 2372–2374 (2002).
32. Crowe, S. A. et al. Sulfate was a trace constituent of Archean seawater. *Science* **346**, 735–739 (2014).
33. Kasting, J. F. Methane and climate during the Precambrian era. *Precambrian Res.* **137**, 119–129 (2005).
34. Kasting, J. F. & Ono, S. Palaeoclimates: the first two billion years. *Philos. Trans. R Soc. Lond. B Biol. Sci.* **361**, 917–929 (2006).
35. Krissansen-Totton, J. et al. A statistical analysis of the carbon isotope record from the Archean to Phanerozoic and implications for the rise of oxygen. *Am. J. Sci.* **315**, 275–316 (2015).
36. Knittel, K. & Boetius, A. Anaerobic oxidation of methane: progress with an unknown process. *Ann. Revi. Microbiol.* **63**, 311–334 (2009).
37. Nitschke, W. & Russell, M. J. Beating the acetyl coenzyme A-pathway to the origin of life. *Philos. Trans. R Soc. Lond. B Biol. Sci.* **368**, 20120258 (2013).
38. Sleep, N. H. & Zahnle, K. Carbon dioxide cycling and implications for climate on ancient Earth. *J. Geophys. Res. Planets* **106**, 1373–1399 (2001).
39. Laakso, T. A. & Schrag, D. P. Methane in the Precambrian atmosphere. *Earth Planet. Sci. Lett.* **522**, 48–54 (2019).
40. Lyons, T. W., Reinhard, C. T. & Planavsky, N. J. The rise of oxygen in Earth's early ocean and atmosphere. *Nature* **506**, 307 (2014).
41. Kopp, R. E. et al. The Paleoproterozoic snowball Earth: a climate disaster triggered by the evolution of oxygenic photosynthesis. *Proc. Natl Acad. Sci. USA* **102**, 11131–11136 (2005).
42. Krissansen-Totton, J., Olson, S. & Catling, D. C. Disequilibrium biosignatures over Earth history and implications for detecting exoplanet life. *Sci. Adv.* **4**, eaao5747 (2018).
43. González-Cabaleiro, R. et al. Microbial catabolic activities are naturally selected by metabolic energy harvest rate. *ISME J.* **9**, 2630 (2015).
44. Tilman, D. *Resource Competition and Community Structure* (Princeton University Press, 1982).

45. Mylius, S. D. & Diekmann, O. On evolutionarily stable life histories, optimization and the need to be specific about density dependence. *Oikos* **74**, 218–224 (1995).

46. Metz, J. A. J., Mylius, S. D. & Diekmann, O. When does evolution optimise? *Evol. Ecol. Res.* **10**, 629–654 (2008).

47. Wordsworth, R. et al. Modelling past Mars Climates and water cycle with a thicker CO_2 atmosphere. *Mars Atmosphere: Modelling and Observation* 447–448 (2011).

48. Leconte, J. et al. Increased insolation threshold for runaway greenhouse processes on Earth-like planets. *Nature* **504**, 268 (2013).

49. Codron, F. Ekman heat transport for slab oceans. *Clim. Dyn.* **38**, 379–389 (2012).

50. Lefèvre, F., Lebonnois, S & Forget, F. A three-dimensional photochemical-transport model of the martian atmosphere. *Sixth International Conference on Mars.* (2003).

51. Giada, A. et al. Hazy Archean Earth as an Analog for Hazy Earthlike Exoplanets. *American Astronomical Society Meeting Abstracts# 225*, Vol. 225 (2015).

52. Pavlov, A. A., Brown, L. L. & Kasting, J. F. UV shielding of NH_3 and O_2 by organic hazes in the Archean atmosphere. *J. Geophys. Res. Planets* **106**, 23267–23287 (2001).

53. Zahnle, K., Claire, M. & Catling., D. The loss of mass-independent fractionation in sulfur due to a Palaeoproterozoic collapse of atmospheric methane. *Geobiology* **4**, 271–283 (2006).

54. Claire, M. W. et al. The evolution of solar flux from 0.1 nm to 160 μm: quantitative estimates for planetary studies. *Astrophys. J.* **757**, 95 (2012).

55. Hu, R., Peterson, L. & Wolf, E. T. O_2-and CO-rich atmospheres for potentially habitable environments on TRAPPIST-1 planets. *Astrophys. J.* **888**, 122 (2020).

Author contributions

R.F. and S.M. conceived the study. R.F. designed the ecosystem model. A.A. and B.S. refined the model and developed the code. B.C. provided the climate and carbon cycle modules. B.S. and S.M. designed the Monte-Carlo approach and ran the simulations. B.S. analyzed the results and wrote the first version of the paper. All authors finalized the paper.

Competing interests

The authors declare no competing interests.

Additional information

Supplementary information is available for this paper at https://doi.org/10.1038/s41467-020-16374-7.

Correspondence and requests for materials should be addressed to B.S.

Peer review information *Nature Communications* thanks Janet Siefert and other, anonymous, reviewers for their contributions to the peer review of this work. Peer review reports are available.

Reprints and permission information is available at http://www.nature.com/reprints

Publisher's note Springer Nature remains neutral with regard to jurisdictional claims in published maps and institutional affiliations.

Appendix F.

Geophysical appendices

F.1. Solubility of CO$_2$

From Krissansen-Totton and Catling (2017)[213], we use the following parameterization for the Henry's law constant of CO$_2$ solubility as a function of temperature.

$$\alpha_{\text{CO}_2} = 10^{-5} \exp\{(\frac{9345.17}{T} - 167.8108 + 23.3585 \log_e T$$
$$+ (0.023517 - 2.3656 \times 10^{-4}T + 4.7036 \times 10^{-7}T^2)35.0)\}$$

(F.1)

mol L^{-1} bar^{-1}.

F.2. Solubility product in the ocean

The solubility product of the ocean is obtained from Krissansen-Totton and Catling (2017)[213], assuming a salinity of 35 per thousand :

$$\log_{10} K_{sol} = -171.9065 - 0.077993T + 2839.319/T + 71.595 \log_{10}(T)$$
$$+ (-0.77712 + 0.0028426T + 178.34/T)35^{0.5}$$
$$- 0.0711 \times 35.0 + 0.0041249 \times 35^{1.5}$$

(F.2)

F.3. Carbonate equilibrium constants

The dissociation constants of CO$_2$ and HCO$_3$$^-$ are given as functions of temperatures (with a salinity of 35 per thousand:

$$\log_{10} K_1(T) = -17.788 + 0.073104 \times 273 + 0.0051087 \times 35 - 1.1463e - 4T^2$$

(F.3)

and

$$\log_{10} K_2(T) = -20.919 + 0.064209 \times 273 + 0.011887 \times 35 - 8.7313e - 5T^2 \tag{F.4}$$

Appendix G.

Co-authored submission: Early Mars' habitability and global cooling by hydrogenotrophic methanogenesis

Early Mars' habitability and global cooling by hydrogenotrophic methanogenesis

Authors: Boris Sauterey[1,2]*, Benjamin Charnay[3], Antonin Affholder[2], Stéphane Mazevet[4,§], Régis Ferrière[1,2,5,§]

Affiliations:

[1]Department of Ecology & Evolutionary Biology, University of Arizona; Tucson, AZ 85721, USA.

[2]Institut de Biologie de l'Ecole Normale Supérieure (IBENS), Université Paris Sciences et Lettres, CNRS, INSERM; 75005 Paris, France.

[3]LESIA, Observatoire de Paris, Université PSL, CNRS, Sorbonne Université, Université de Paris; 5 place Jules Janssen, 92195 Meudon, France.

[4]Observatoire de la Côte d'Azur; Boulevard de l'Observatoire, 06304 Nice, France.

[5]iGLOBES International Research Laboratory, CNRS, Ecole Normale Supérieure, Université Paris Sciences et Lettres, University of Arizona; Tucson, AZ 85721, USA.

§Co-senior authors

*Corresponding author. Email: boris.sauterey@biologie.ens.fr

During the Noachian Period, more than 3.7 billion years ago, Mars' crust may have provided a favorable environment for microbial life[1,2]. The porous brine-saturated regolith[3-5] would have created a physical space sheltered from UV and cosmic radiations and provided a solvent. The below-ground temperature gradient[2] and diffusion[6,7] of a dense reduced atmosphere enriched in dihydrogen and carbon dioxide[8,9] may have supported simple microbial organisms that consume H_2 for catabolic energy production and CO_2 as a carbon source, and produce methane as a waste. On Earth, such hydrogenotrophic methanogenesis was among the earliest metabolisms[10,11]. Here we present a quantitative probabilistic assessment of early Mars' habitability to H_2-based methanogens, and evaluate the biological feedback on Mars' atmosphere and climate. We find that subsurface habitability was very likely, at depths controlled primarily by then-time surface temperature, the main limit to habitability being the extent of surface ice coverage. Biomass productivity could have been as high as in early Earth's ocean. However, the atmospheric composition shift caused by methanogenesis would have triggered a global cooling event, ending potential early warm conditions, compromising surface habitability and forcing the biosphere deep into the Martian crust. Spatial projections of our predictions show that traces of this early life exposed at the surface are more likely to be found in lowlands of low-to-intermediate latitudes.

Main Text:

To assess and quantify the habitability of early Mars and the evolution of its surface conditions under the influence of methanogenic hydrogenotrophy, we use a state-of-the-art 1D photochemical-climate model of early Mars combined with a crust model to self-consistently compute the atmospheric chemical composition, climate, thermal profile of the crust, and crust-atmosphere gas exchanges (see methods, Fig. 1 and Extended Data figure 1). The geophysical-chemical model is coupled with a depth-structured model of chemoautotrophic ecosystem adapted from previous work[12,13] to (i) evaluate the habitability of the Martian subsurface to populations of methanogenic hydrogenotrophs in the context of a global environment set by the planetary model, (ii) resolve the dynamics of these populations, and (iii) quantify the corresponding biological feedback on the planet's atmosphere and climate. We run the coupled model in a probabilistic framework, by performing a Monte-Carlo exploration of likely ranges for each planetary parameter in the model (Extended Data Table 1). From the simulations of 3,000 plausible young Mars, we obtain probabilistic estimates of global properties (atmosphere compositions, climate, ice coverage, and biosphere productivity, geographical distribution and depth profile) under two scenarios: prior to biologically induced changes to the surface conditions, and after these changes (at steady state). We assume that surface ice coverage is determined by climate and the freezing point of saline brines. Only the fraction of the surface left free of ice (denoted by ϱ) allows crust-atmosphere gas exchanges since ice forming in the regolith pores blocks gas pathways into the crust[6]. The value of brines' freezing point is poorly constrained (estimates range from 203 to 273 K) as it depends on the brines composition[3-5]. We therefore evaluate initial and steady state conditions on Mars for three values of freezing point –203, 252 and 273 K– corresponding respectively to perchlorate brines, NaCl brines, and pure water[4].

To resolve Mars' initial features, we follow previous work[14-16] and assume atmospheric pressure ranging from 0.5 to 3 bars, a volume mixing ratio of H_2, f_{H_2}, from 3,000 ppm to 0.1 (Fig 2A; corresponding to a volcanic outgassing rate of 10^{10} to 2×10^{12} molecules cm^{-2} s^{-1}, see methods), and a low f_{CH_4} of 100 ppm (Fig 2B; corresponding to a production rate through serpentinization of 8×10^8 to 10^{10} molecules cm^{-2} s^{-1}, see methods). The rest of the atmosphere is 95% CO_2 and 5% N_2 (8). From our climate-atmosphere model (Fig. 1) we infer an initial distribution of average surface temperature, $\overline{T}_{surface}$, ranging from 216 to 294 K, with a median at 256 K (Fig. 2C). For brines freezing at 203, 252 and 273K, Mars is fully covered by ice (hence uninhabitable) in 0, 10 and 40% of the cases, with median ϱ of 100%, 75%, and 0.15% respectively (Fig 2D). Thus the nature of the brines would have strongly constrained the geographic extent of Mars initial habitability. Note that for the sake of simplicity and following previous studies[15,16] we do not account for ϱ feeding back on Mars climate though an increase of the planetary albedo (see

methods) while it could significantly cool Mars down[14] (see discussion below). Finally, we draw the characteristics of the crust (porosity, tortuosity and temperature profile) from the same ranges as in ref[7] and infer the posterior distributions of the depth profiles for temperature and diffusivity of the atmospheric gases (Extended Data figure 1). A general pattern is that temperature increases with depth while diffusivity drops.

The atmospheric redox disequilibrium and its accessibility in the Martian crust make the hydrogenotrophic ecosystem viable in all of our simulations in which Mars is not fully covered by ice, at a depth that is determined primarily by surface temperature (Fig. 2F). In line with what is observed in permafrost ecosystems on Earth[17] the lowest temperature for hydrogenotrophs to exist and reproduce is ~253 K. For warmer surface temperature, cells can colonize the first layer of the Martian crust. When the surface is colder, cells are limited upward at depth at which the limit temperature of 253 K is reached (see methods). The deeper end of the microbial vertical distribution is bounded *ca.* 320 K (below the maximal temperature allowing the growth of methanogenic extremophiles on Earth[18]): at such depths the atmospheric redox potential diffusing from the surface has been entirely exploited by the ecosystem laying above.

As they colonize the Martian subsurface, methanogenic hydrogenotrophs drive atmospheric CH_4 up and atmospheric H_2 down. At steady state, the biogenic rates of CH_4 production and H_2 consumption, combined with H atmospheric escape, balance out the loss rate of CH_4 by photochemistry and the production rate of H_2 by photochemistry and volcanic outgassing (Fig. 1). As a result, the median f_{H_2} drops from 5% to between 0.35% and 2.75% depending on brines' freezing points (Fig. 2A) while the median steady state atmospheric concentration in CH_4 rises to 0.075% to ~1% (Fig. 2B). Due to the respective effect of H_2 and CH_4 on climate[14-16] (Fig. 1), the global atmospheric shift driven by the microbial biosphere triggers a dramatic cooling event (Fig. 2C): even though the biological impact on Mars' surface conditions strongly depends on the freezing point of Martian brines (Fig 2A-E) and the extent of surface ice coverage, methanogenic hydrogenotrophs make a warm early Mars unlikely, as the maximum temperature plummets from 294 K to between 250 and 260 K regardless of brines' composition..

Reciprocally, global cooling feeds back to the biosphere. First, when the average surface temperature in ice-free regions drops below 253 K, methanogens are forced deeper into the Martian crust (Fig. 2F). Second, the atmospheric change also corresponds to the planet's global thermodynamic favorability to methanogenic hydrogenotrophs decreasing as the biosphere uses up the atmospheric redox potential. As a

consequence, the total biomass productivity at steady state falls by a factor of 100 (Fig. 2E). Finally, the ice-free (hence habitable) portion of Mars can significantly shrink as the climate cools down (e.g., a median drop from 83% to 2% for brines freezing at 252 K when Mars is habitable; see Fig. 3, extended Data video 1). In spite of this biologically induced reduction of Mars habitability, the predicted steady-state values of the planetary averaged biomass productivity are similar to biomass productivity estimated for the same (H_2-based methanogenic) primitive biosphere in the Archean Earth's ocean[12,19]. Note that we made the assumption, common for chemotrophic ecosystems[12,13,19], that early Martian life would have been predominantly limited either by the energetic yield of methanogenesis (determined by the redox imbalance of the atmosphere) or by the availability in a limited number of chemical elements (C, H, N and O, provided by H_2, CO_2, N_2; see methods for additional details). Other nutrients not accounted for in the present study such as P or S could nevertheless have been limiting factors to the development of life on Mars[20]. Our estimates of carbon assimilation (Fig. 2E) provide a basis to evaluate the quantities of additional nutrients necessary to sustain such a biomass production and to more precisely determine the most likely limiting factors to early life on Mars.

The best validation of our predictions would come from the discovery of fossils or of other biomarkers of ancient H_2-based methanogens. Near-surface populations are the most productive ones (Fig. 2 F-I) and therefore maximize the likelihood of preserved biomarkers existing in detectable quantities. Additionally, the first few meters of the Martian crust are presently the most easily accessible to exploration given the technology currently embarked on Martian rovers. Our results suggest that the probability of fossilized life being located at or close to the surface is strongly dependent on the composition and freezing point of Martian brines (Fig. 2, F-I). However, specific regions may exist where this probability is maximum. To identify such areas and assess current exploration sites (e.g., Isidis Planitia, Jezero crater), we performed spatial projections of our predictions (Fig. 3 and 4; see methods).

Our maps reflect the fact that the lower the freezing point of Martian brines, the larger the extent of Mars steady state ice coverage hence the lower the habitable portion of Mars (Fig 2D and 3). Temperature drops with latitude and elevation[21] (see methods). As a result and unsurprisingly, poleward regions and highlands are the most likely to be covered in ice while lowlands located at low-to-intermediate latitudes such as Isidis and Hellas planitiae as well as the Noachian lakes scattered along the North-South dichotomy[22] (including Jezero crater currently explored by the rover Perseverance) emerge as the regions maximizing the probability of having been ice-free during the Noachian. Those regions therefore constitute the best candidate sites to search for signs of Noachian methanogenic life. Note however that the fact that those regions may have been covered by more recent sediments during later stages of Mars

history[23,24] must be taken under consideration. As shown in Figure 3, high brines' freezing point would have resulted in the expansion of Mars' ice-coverage for relatively high temperature, rapidly limiting the ability of the methanogenic biosphere to cool Mars' climate further down (Fig. 2C). Because of this positive link between brines' freezing point and steady state temperatures, methanogenesis occurs at the surface ranges in the ice-free regions in only 25 to 50% of the viable simulations (median depth of 0 to 400 meters) in the 203K freezing point scenario (Fig. 4A and D), but in more than 50% of the viable cases in the 252K scenario (Fig. 4B and E), and in 100% of the viable cases in the 273K scenario (Fig. 4C and F). Paradoxically, higher freezing point of Martian brines would have made Mars less likely habitable to methanogens but the detection of signs of early Martian methanogenesis today easier. Note finally that identifying fossilized biomarkers as such is in itself a challenging task[2,25]. Although this question is out of the scope of this study it seems based on the approaches that have been efficient to identify signs of early life on Earth and of the metabolism it was based on (reviewed in[26]) that the analysis of isotope fractionation could be the most promising approach, as it is both resilient to time and as isotopic signatures are to some extent specific to metabolic pathways.

Habitability and climate feedback of hydrogenotrophic methanogens were recently quantified for the early Archean Earth[12]. The results reported here for the Noachian Mars show striking similarities and differences. On the one hand, models predict very likely habitability to hydrogenotrophic methanogens on both young planets, with similar biomass productivity. On the other hand, climate feedbacks work in opposite directions. While hydrogenotrophic methanogens may have contributed to maintaining temperate conditions on Earth[12,19], they would have cooled the early Martian surface, with a reduction of the maximal possible temperature of 33 to 45 K. Such divergence in climate evolution is the consequence of different prebiotic atmospheric compositions. For a CO_2-dominated atmosphere as on early Mars, the greenhouse effect by H_2 (from CO_2-H_2 collision-induced absorptions) is stronger than the greenhouse effect by CH_4, in contrast to a N_2-dominated atmosphere as on the early Earth[14-16]. Contrasted planetary responses of Earth and Mars to metabolic activity might have occurred repeatedly as their biospheres diversified. On Earth, the evolution of methanotrophy (biological consumption of methane) could have transiently offset the warming effect of methanogenesis[12]; instead, methanotrophy could have driven a warming event of the Noachian/Hesperian Mars. The co-evolution of Martian surface conditions with a diversifying methane cycling biosphere therefore adds up to the possible mechanisms explaining an early global cooling event as well as transient warming episodes that seem to have punctuated the early Martian climatic history[8]. This highlights how specific the planet-life interaction might be, even when considering

planetary objects as similar as early Mars and Earth (reduced telluric planets of similar size and atmosphere) and similar primitive biospheres. Note furthermore that, as we do not take into account the effect of the biologically induced increase in planetary albedo on Mars' climate, we minimize methanogens' ability to cool down Mars. This mechanism, combined with the direct effect of methanogenesis on Mars climate, could have however triggered a full glaciation of Mars, causing its status to shift from habitable (albeit partially) to fully uninhabitable. Further work is necessary to properly assess this possibility. Beyond the case of Mars, our results thus emphasize the potential for life being the cause of its own demise by feeding back to the planetary environment and ultimately leading to its uninhabitability and the potential commonality of Gaian bottleneck scenarios on once inhabited planets[27].

When run for atmospheric conditions corresponding to modern Mars our model predicts the atmosphere to be an insufficient source of electron donors for H_2-based methanogens to survive. As Mars' surface became colder and its atmosphere thinner during the Hesperian and early Amazonian and assuming that it did not go extinct during the early stages of Mars history, a putative primitive Martian biosphere would therefore have had to shift its main energy source from the vanishing atmospheric redox gradients to hydrothermal or radiolytic ones, deeper in the Martian crust. Deep chemotrophic ecosystems exist on Earth; an extant ecosystem on modern Mars would likely be of that kind[28], and could provide a plausible biological explanation to repeated[29] (yet debated[30]) detection of traces of CH_4 in the Martian atmosphere. As current and future missions gather more geochemical data on the Martian surface, our model could be adapted to quantify the habitability of modern Mars' crust to such ecosystems and constrain their depth and productivity.

Methods

Atmospheric and climate model

To evaluate the photochemical destruction/production of H_2 and CH_4 (the two main atmospheric species in our planetary ecosystem model) we ran the latest version of the 1D photochemical model of Mars developed in the Virtual Planetary Laboratory[31], on grids of atmospheric compositions. The results are in line with previous estimates[32], and based on them, we interpolated the photochemical rates as functions of the atmospheric composition (Fig. 1A-B).

Similarly, we evaluated the dependence of the Martian climate on its atmospheric composition and pressure based on the Virtual Planetary Laboratory's 1D climate model, updated to account for the latest data on the respective collision-induced warming effect of H_2 and CH_4[14-16]. Again, we used the outputs of

the model to interpolate the mean surface temperature as a function of the atmospheric composition (f_{H_2}, f_{CH_4}, f_{CO_2}) and total atmospheric pressure (Fig. 1C-E). Note that following previous work[15,16] the climate model was run assuming a constant low planetary albedo of 0.2 corresponding to a low ice coverage of Mars surface.

Because of the collision induced absorption resulting from the CO_2-saturated atmosphere of early Mars, H_2 appears to be a more potent greenhouse gas than CH_4, in line with previous studies[14-16]. Methane may even produce an anti-greenhouse effect at low atmospheric pressure and low f_{H_2}.

Crust model

Subsurface temperature is expected to increase with depth, while the availability of diffusing atmospheric gases drops. Following on ref[7], we assume a linear temperature gradient with depth, starting from the surface temperature and warming as depth increases:

$$T(z) = T_{surface} + a_T z \qquad \text{(E1)}$$

with z the depth in kilometers and a_T the rate at which temperature increases with depth ranging between 10 and 40 K km^{-1} [7]. The decrease with depth of the diffusivity (in cm^2 s^{-1}) in the water-saturated crust depends partially on the temperature depth-profile, according to ref[7]:

$$D_i(z) = \frac{\epsilon(z)r(z)}{3\tau(z)}\sqrt{\frac{8\,RT(z)}{\pi m_i}} \qquad \text{(E2)}$$
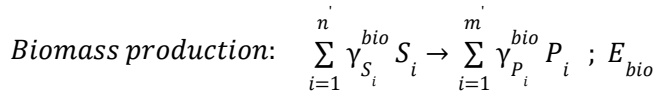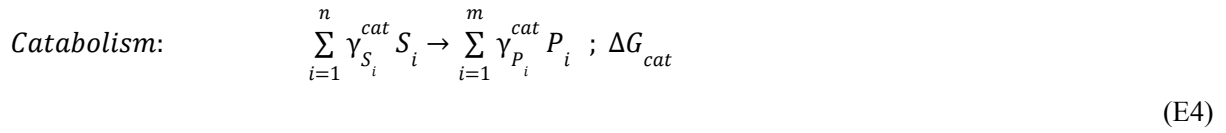
with i the considered chemical species (H_2, CO_2, CH_4, and N_2), m_i its molar mass, $\epsilon(z)$ the porosity of the crust, $r(z)$ the pores' radius (in cm), and $\tau(z)$ the tortuosity. The pore radius $r(z)$ follows a linear decrease with depth $r(z) = r(0) - a_r z$ with $a_r = \frac{r(0)}{z_{max}}$ so that $r(z) = 0$ when $z = z_{max}$, the depth of pore closure. The crust porosity and tortuosity both follow an exponential decrease with depth, respectively $\epsilon(z) = \epsilon(0)e^{-\frac{z}{z_{max}}}$ and $\tau(z) = \tau(0)e^{-\frac{z}{3\cdot z_{max}}}$. The vertical flux (in molecules cm^{-2} s^{-1}) can then be written as

$$F_i = D_i(z)\frac{\partial n_i}{\partial z} \qquad \text{(E3)}$$

n_i being the density of species i (in molecules cm^{-3}). The envelopes and distribution of depth profiles for the temperature and diffusivity of H_2 corresponding to the soil parameter ranges explored (see Extended Data Table 1) are shown in Extended Data Figure 1.

Ecological model

Our ecological model describes the dynamics of biological populations of chemotrophic cellular organisms. Equations for the growth and death of individual cells are derived from how, in each individual cell, energy flows from catabolism (energy acquisition) to anabolism (cell maintenance first, then biomass production). The individual metabolism is described by

$$\textit{Catabolism:} \qquad \sum_{i=1}^{n} \gamma_{S_i}^{cat} S_i \rightarrow \sum_{i=1}^{m} \gamma_{P_i}^{cat} P_i \;\; ; \; \Delta G_{cat}$$

$$\textit{Biomass production:} \quad \sum_{i=1}^{n'} \gamma_{S_i}^{bio} S_i \rightarrow \sum_{i=1}^{m'} \gamma_{P_i}^{bio} P_i \;\; ; \; E_{bio}$$

(E4)

where S_i and P_i are the substrates and products of the metabolic reactions that are specific to the considered metabolism and the γ's their stoichiometric coefficients, and ΔG_{cat} and E_{bio} the energy released by the catabolic reaction and necessary to biomass production, respectively. In the case of hydrogenotrophic methanogens, the catabolic reaction is $CO_2 + 4\,H_2 \rightarrow CH_4 + 2\,H_2O$. The value of ΔG_{cat} is given by the Nernst relationship

$$\Delta G(T) = \Delta G_0(T) + RT\,log(Q) \tag{E5}$$

where R stands for the ideal gas constant, T for temperature (in K), $\Delta G_0(T)$ (in kJ mol eD^{-1}) for the standard Gibbs free energy of the reaction, and Q for the reaction quotient $\dfrac{\prod_{i=1}^{n} S_i^{\gamma_{S_i}}}{\prod_{i=1}^{n} P_i^{\gamma_{S_i}}}$. The value of $\Delta G_0(T)$ is obtained from the Gibbs-Helmholtz relationship:

$$\Delta G_0(T) = \Delta G_0(T_S)\frac{T}{T_S} + \Delta H_0(T_S)\frac{T_S - T}{T_S} \tag{E6}$$

where T is the temperature of the medium, T_S the standard temperature of 298.15 K, and $\Delta H_0(T)$ the standard enthalpy. The catabolic acquisition of energy occurs at a rate q_{cat} (in mol eD cell^{-1} d^{-1}). The energy obtained is first directed toward maintenance, with E_m (in kJ cell^{-1} d^{-1}) the biomass specific energy requirements for maintenance per unit of time. The energy requirements of the cell can be expressed in terms of the rate at which the catabolic reaction must occur for the cell to function, q_m (in mol eD cell^{-1} d^{-1}), with:

$$q_m = \frac{-E_m}{\Delta G_{cat}}. \tag{E7}$$

The cell maintenance requirements are met when $q_{cat} > q_m$. If they are not (i.e., $q_{cat} < q_m$), a decay related term $k(q_m - q_{cat})$ (in d^{-1}) is added to the basal cellular mortality rate, m (in d^{-1}), with $d = k(q_m - q_{cat}) + m$ the effective mortality rate (in d^{-1}). If $q_{cat} > q_m$, the energy remaining after maintenance $(q_{cat} - q_m)\Delta G_{cat}$ (kJ cell^{-1} d^{-1}) can be allocated to biomass production. The assimilation of each mol of carbon into biomass requires a quantity of energy E_{bio} (in kJ mol C$_{org}$$^{-1}$) corresponding to the sum of the costs of producing the biomass, ΔG_{ana}, and organizing it, E_{diss}. The value of ΔG_{ana} is obtained with the Nernst equation (equation E5) and assuming the following anabolic reaction: 24 H$_2$ + 10 CO$_2$ + 1 N$_2$ $\rightarrow$ C$_{10}$H$_{18}$O$_5$N$_2$ + 15 H$_2$O. Note that we assume that Martian methanogens would have been capable of fixing N from the atmospheric N$_2$, as their terrestrial counterparts most likely were[33,34]. The term E_{diss} is a phenomenological estimate and its value the same as in ref[12] (see extended Data table 2). The efficacy of the metabolic coupling λ (i.e., the necessary number of occurrences of the catabolic reaction to fuel one occurrence of the reaction of biomass production, in mol eD mol C$_{org}$$^{-1}$) is the ratio between the energy produced by the catabolic reaction and the energetic cost of biomass production

$$\lambda = \frac{-\Delta G_{cat}}{E_{bio}}. \tag{E8}$$

Biomass is produced at a rate q_{bio} (in mol C$_{org}$ cell^{-1} d^{-1}) with

$$q_{bio} = \lambda (q_{cat} - q_m). \tag{E9}$$

The metabolic rates q_{cat} and q_{bio} depend on the concentration of the metabolic substrates through a Michaelis-Menten term:

$$q = q_{max}\frac{S_{lim}}{S_{lim}+K} \tag{E10}$$

where S_{lim} is the most limiting nutrient, q_{max} the maximum reaction rate, and K the half-saturation constant (we assume the same maximum rates and and half-saturation constants for all the reactions, their values being based on phenomenological estimates; see extended Data table 2). Rates increase with both cell size S_C (radius in μm) and temperature, which we describe with power laws. Finally the optimal cell size, i.e., the cell-size that maximizes the individual ability to exploit its environment, is itself estimated through a power law (see ref[12] for details). The default parameter values based on empirical estimates and used in the main text are given in Extended Data Table 2 (details about these values can be found in ref[12]).

A key feature of the model is that it estimates both the thermodynamic and kinetic temperature dependencies of the metabolism. Typically, high temperatures result in a decreased thermodynamic coupling between energy acquisition and biomass production – i.e., an energetic constraint. Lower temperatures on the other hand result in lower metabolic rates – i.e., a kinetic constraint. The metabolic efficiency of H_2-based methanogens is therefore optimized at intermediate temperatures, the exact value being set by the ecological context (e.g., fluxes of metabolic substrates and wastes, basal mortality[13]). Note that for the sake of simplicity, we neglect the potential effect of low water activity and osmotic constraints resulting from the high salinity of the Martian hydrosphere on the physiology of methanogens. The effect of these unaccounted constraints on Martian life are hard to evaluate as they are poorly understood on Earth; any assumption on what cellular life's adaptation to such constraints might have been on Mars would be highly speculative. Our model however could be complexified to include the thermodynamic component of these constraints.

Physiological rates can then be implemented in a model of ecological dynamics describing the variation through time of the methanogenic population abundance B (in cells) as the balance of biomass production and death, and the abundance of each chemical species in the medium X_i as the balance of the inward/outward flux $F(X_i)$ between the local ecosystem (here a given point in the crust column) and the exterior (here provided by the crust model; see equation E3) and biological consumption/production:

$$\frac{dB}{dt} = \left(\frac{q_{bio}}{Q_{C_{org}}} - d \right) B$$

$$\frac{dX_i}{dt} = F(X_i) + (q_{cat} \gamma_{X_i}^{cat} + q_{bio} \gamma_{X_i}^{bio}) B$$

(E11)

where $Q_{C_{org}}$ is the structural carbon content of a cell. From equation (E11) we obtain a quantitative criterion for habitability, which is that the initial environmental conditions must be compatible with biological population growth, i.e., $\frac{q_{bio}}{Q_{C_{org}}} > d$. By solving for the equilibrium of (E11) we also quantify (i) the biological feedback on the local chemical composition, and (ii) the ability of the local ecosystem to influence the larger scale of the environment through the value of the interaction term $F(X_i)$ at steady state (see equation E3). Although the ecological model is the same as the one used in Sauterey et al. 2020, its integration along the spatially structured environmental gradient provided by the crust model is unique to this study. This coupled model provides us with average surface fluxes at the crust-atmosphere interface corresponding to the planetary conditions set by the atmospheric and climate model. These fluxes are then integrated in the global planetary model over the ice-free surface of Mars and feedback dynamically on the atmosphere and climate, driving the evolution of Mars' surface conditions over time.

Minimum depth of the hydrogenotrophic methanogenic ecosystems

Due to the kinetic constraints on the H_2-based methanogenic metabolism, the lowest viable temperature is approximately 253 K. The minimum depth at which the ecosystem can exist in the Martian crust, z_{bio}, can be found by considering the temperature gradient of the crust:

$$z_{Bio} = max\left(\frac{253 - T_{surface}}{a_T}, 0 \right)$$

(E12)

where $T_{surface}$ is the surface temperature and a_T the temperature gradient (in K km^{-1}).

Spatial projections

To obtain spatial projections, we begin with the posterior distributions of average surface temperature $\overline{T}_{surface}$ produced by our model. Then we evaluate the probability distribution of surface temperature at any location given latitude and elevation based on Fastook and Head's model[21]. The authors used simulations from the LMD Generic Climate Model to derive empirical relationships between local surface

temperature ($T_{surface}$) and a base temperature, latitude (lat), and elevation (Z), for various scenarios of atmospheric pressure (0.008, 0.2, and 1 bar). We modified the relationship found for an atmospheric pressure of 1 bar so that the local surface temperature is expressed as a function of the average surface temperature instead of a basal temperature, and obtain

$$T_{surface} = \overline{T}_{surface} - 5\pi + 20\,cos\left(\frac{lat\,\pi}{180}\right) + 2.4Z \qquad (E13)$$

This relationship is first used to evaluate, based on a topographic map of Mars[35] and for each value of brines' freezing point, the link between the average surface temperature and the portion ice-free surface ϱ (i.e., the pourcentage of Mars' surface where $T_{surface}$ is above the freezing point of the brines; see Extended Data Figure 2A). For average surface temperatures ranging from 200 to 320K, the geographical distribution of ϱ is then projected spatially and the average surface temperature within the ice-free region evaluated (Extended Data Figure 2B). The relationships between the average surface temperature, ϱ and the average surface temperature within ϱ are then implemented in the global ecosystem model. Second, this relationship is used to compute, based on the average steady-state surface temperature distribution, the probability distribution of the ecosystem depth profile in the crust at any location and retrieve the probability that the ecosystem reaches the surface (Fig. 4B and C, Extended Data Figure 3).

References

1. C. S. Cockell *et al.*, *Astrobiology*, **16**, 89-117 (2016)

2. J. R. Michalski *et al.*, *Nature Geoscience*, **11**, 21-26 (2018)

3. A. G. Fairén *et al.*, *Nature*, **459**, 401-404 (2009)

4. S. M. Clifford *et al.*, *Journal of Geophysical Research: Planets*, **115**, E07001 (2010)

5. E. G. Rivera-Valentín, V. F. Chevrier, A. Soto, G. Martínez, *Nature astronomy*, **4**, 756-761 (2020)

6. A. H. Stevens, M. R. Patel, S. R. Lewis, *Icarus*, **250**, 587-594 (2015)

7. S. F. Sholes, J. Krissansen-Totton, D. C. Catling, *Astrobiology*, **19**, 655-668 (2019)

8. R. D. Wordsworth, *Annual Review of Earth and Planetary Sciences*, **44**, 381-408 (2016)

9. J. Liu *et al.*, *Nature Astronomy*, **5**, 503-509 (2021)

10. F. U. Battistuzzi, A. Feijao, S. B. Hedges, *BMC evolutionary biology*, **4**, 1-14 (2004)

11. W. F. Martin, F. L. Sousa, *Cold Spring Harbor perspectives in biology*, **8**, a018127 (2016)

12. B. Sauterey *et al.*, *Nature communications*, **11**, 2705 (2020)

13. A. Affholder *et al.*, *Nature Astronomy*, **5**, 805-814 (2021)

14. R. M. Ramirez, *Icarus*, **297**, 71-82 (2017)

15. R. Wordsworth *et al.*, *Geophysical Research Letters*, **44**, 665-671 (2017)

16. M. Turbet, C. Boulet, T. Karman, *Icarus*, **346**, 113762 (2020)

17. P. B. Price, T. Sowers, *Proceedings of the National Academy of Sciences*, **101**, 4631-4636 (2004)

18. R-S. Taubner *et al.*, *Nature Communications*, **9**, 1-11 (2018)

19. P. Kharecha, J. Kasting, J. Siefert, *Geobiology*, **3**, 53-76 (2005)

20. C. S. Cockell, *Astrobiology*, **14**, 182-203 (2014)

21. J. L. Fastook, J. W. Head, *Planetary and Space Science*, **106**, 82-98 (2015)

22. C. I. Fassett, J. W. Head, *Icarus*, **198**, 37-56 (2008)

23. K. L. Tanaka *et al.*, Geologic map of Mars: U.S. Geological Survey Scientific Investigations Map 3292, scale 1:20,000,000, https://dx.doi.org/10.3133/sim3292. (2014)

24. V. Z. Sun, K. M. Stack, Geologic map of Jezero crater and the Nili Planum region, Mars: U.S. Geological Survey Scientific Investigations Map 3464, scale 1:75,000, https://doi.org/10.3133/sim3464. (2020)

25. F. Westall *et al.*, *Astrobiology*, **15**, 998-1029 (2015)

26. K. Lepot, *Earth-Science Reviews*, **209**, 103296 (2020)

27. A. Chopra, C. H. Lineweaver, *Astrobiology*, **16**, 7-22 (2016)

28. J. D. Tarnas *et al.*, *Earth and Planetary Science Letters*, **502**, 133-145 (2018)

29. Y. L. Yung *et al.*, *Astrobiology*, **18**, 1221-1242 (2018)

30. E. W. Knutsen *et al.*, *Icarus*, **357**, 114266 (2021)

31. Photochemical model developed by Zahnle and Kasting (https://github.com/VirtualPlanetaryLaboratory/atmos)

32. N. Batalha *et al.*, *Icarus*, **258**, 337-349 (2015).

33. E. E. Stüeken *et al.*, *Nature*, **520**, 666-669 (2015)

34. F. Mus et al., *Free Radical Biology and Medicine*, **140**, 250-259 (2019)

35. R. L. Fergason, T. M. Hare, J. Laura, HRSC and MOLA Blended Digital Elevation Model at 200m v2. Astrogeology PDS Annex, U.S. Geological Survey. (2018) http://bit.ly/HRSC_MOLA_Blend_v0

Author contributions:

Conceptualization: BS, BC, RF, SM
Methodology: BS, AA, RF, SM
Investigation: BS
Formal analysis: BS
Visualization: BS, RF
Software: BS, SM
Supervision: RF, SM
Writing – original draft –: BS
Writing – review & editing –: BS, BC, AA, RF, SM

Competing interests: Authors declare that they have no competing interests.

Data and materials availability: The planetary ecosystem model coupling climate, atmosphere, ice-coverage and underground ecosystem will be made available upon the date of publication on a public repository. The photochemical and climate models are accessible on the Virtual Planet Laboratory's gitlab (https://github.com/VirtualPlanetaryLaboratory/atmos), the adapted versions used in this study are available upon request.
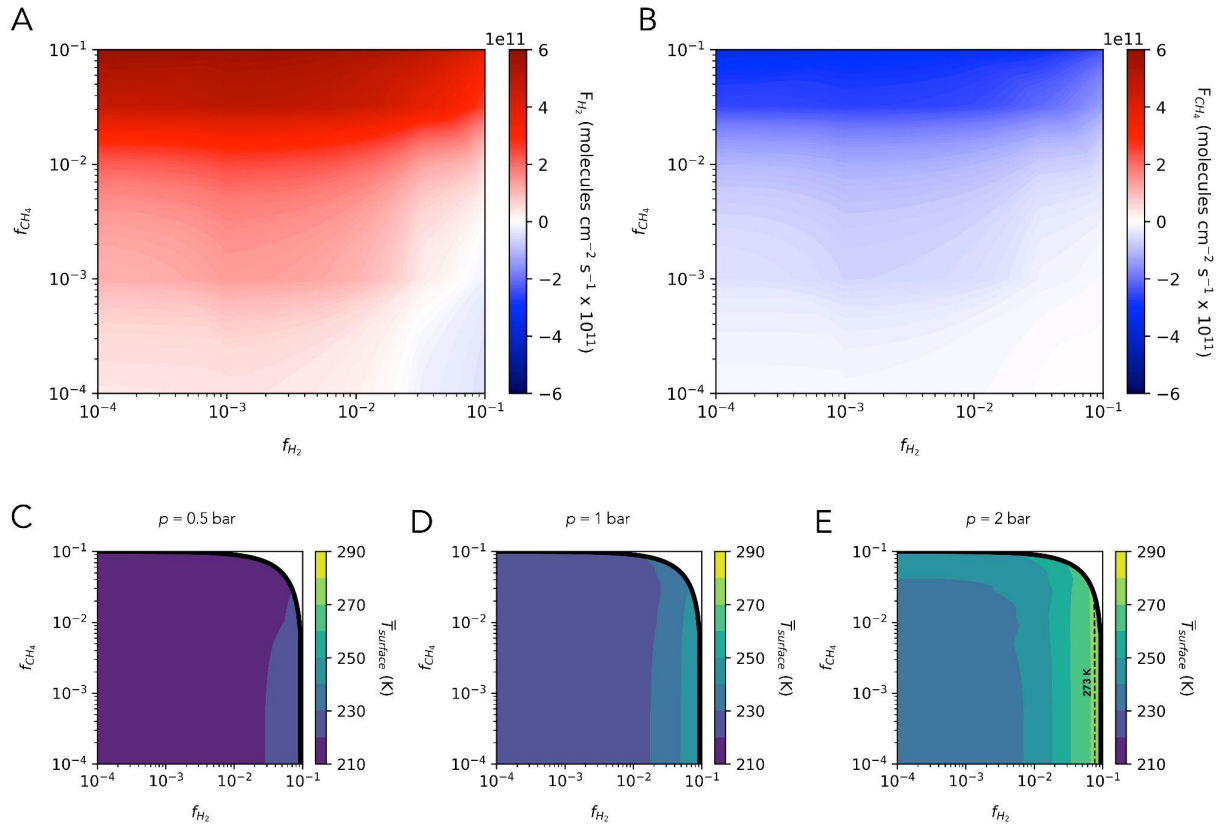
Figure 1. Modeled photochemistry (A, B) and climate (C, D, E) of early Mars. (A, B) Rates (denoted by F) of destruction/production of H_2 and CH_4 as a function of H_2 and CH_4 mixing ratios (denoted by f). (B, C, D) Average surface temperature as a function of H_2 and CH_4 mixing ratios, f_{H_2} and f_{CH_4}, for an atmospheric pressure of 0.5, 1, and 2 bars. Our simulations were constrained by $f_{H_2} + f_{CH_4} < 0.1$ (thick black boundary curve in C, D, E). Dashed black line: $\overline{T}_{surface} = 273$ K.
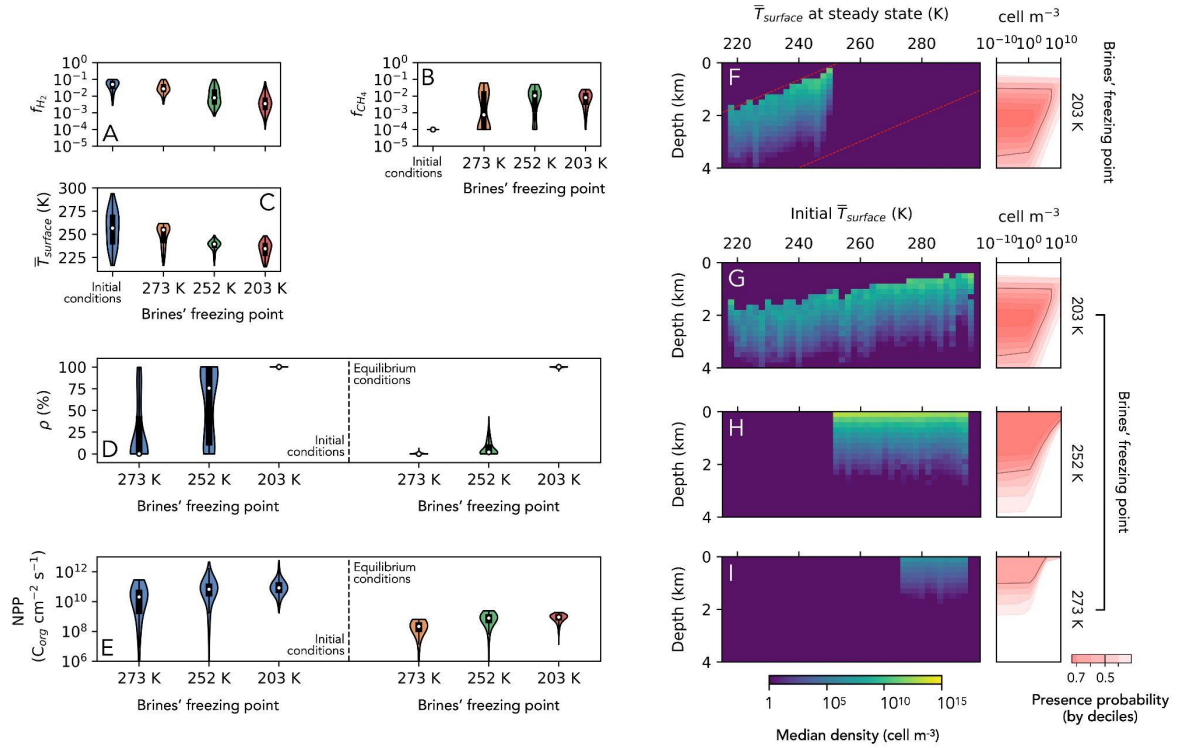
Figure 2: Initial and steady state conditions on Early Mars in terms of atmospheric composition (**A** and **B**), average surface temperature (**C**), ice-coverage (**D**) and biomass production (**E**; averaged over the whole Martian surface, only when Mars is habitable) for three values of brines' freezing point (203, 252 and 273 K). Corresponding steady-state (**F**, **G**, **H**, **I**) depth profile of the subsurface methanogenic ecosystem (median cell density in cell m-3) as a function of the steady state average surface temperature (**F**) and initial average surface temperature (**G**, **H** and **I**). The red dotted lines in **F** correspond to the median depth at which temperature equals the low and high limits to viability, 253 and 320 K.
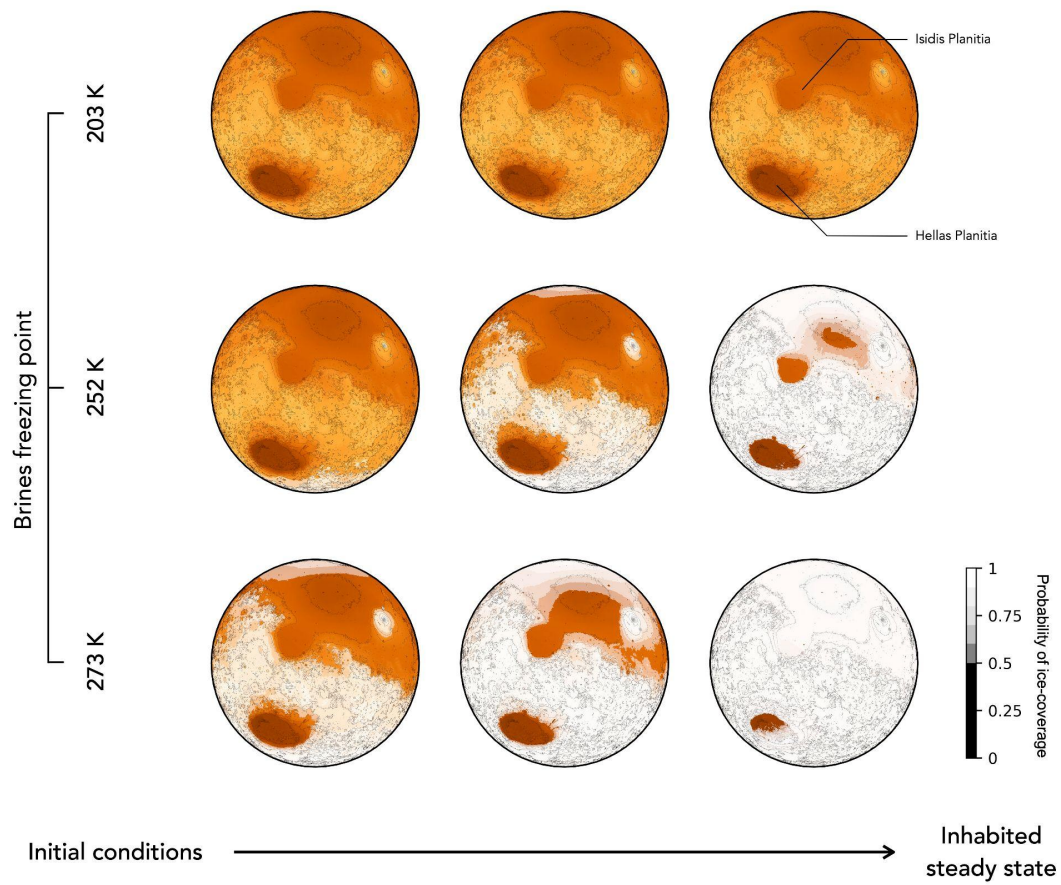
Figure 3: Scenario of ice-coverage evolution of Mars when habitable under the influence of a methanogenic biosphere for brines freezing at 203 (*top*), 252 (*middle*), and 273 K (*bottom*). The white shaded areas correspond to the probability (from 50% to 90% by steps of 10%) of ice-coverage superimposed to the maps by transparency. The closed white dots correspond to the Noachian lakes delimiting the South-North dichotomy.
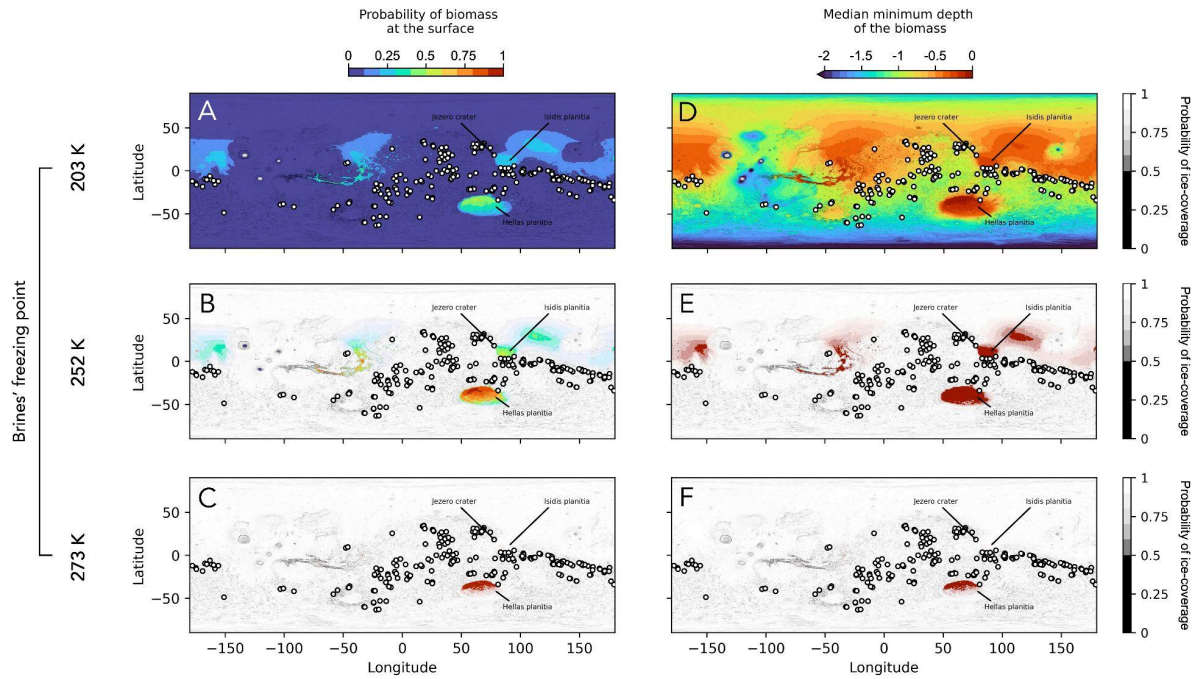
Figure 4: Maps of the steady state geographical and vertical distribution of a putative methanogenic biosphere within the Noachian Mars subsurface. Spatial projection of the probability of biomass located at the surface (**A**, **B** and **C**) and of the median minimum depth of this biomass (**D**, **E** and **F**) had methanogenesis evolved on Mars, under three scenarios of brines' freezing points of 203 K (**A** and **D**), 252 K (**B** and **E**), and 273 K (**C** and **F**). The white shaded areas correspond to the probability (from 50% to 90% by steps of 10%) of ice-coverage superimposed to the maps by transparency. The closed white dots correspond to the Noachian lakes delimiting the South-North dichotomy.
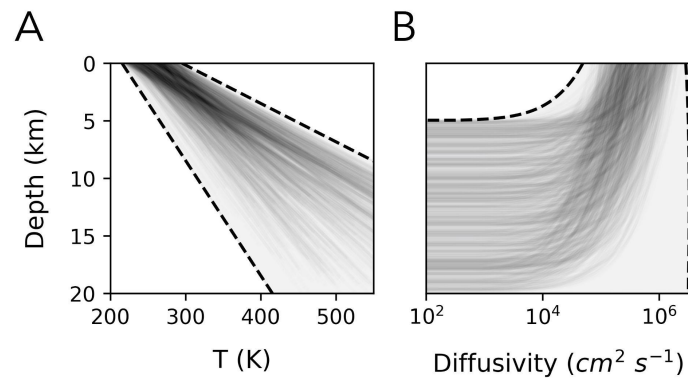
Supplementary Materials for

"Early Mars' habitability and global cooling by hydrogenotrophic methanogenesis"

Extended Data Figure 1. Simulated depth profiles of (A) temperature and (B) diffusivity in Mars' Noachian regolith. Gray areas bounded by dashed lines represent the entire space in which the depth profiles can exist. Each line (here 2,000 in total) represents one specific profile simulated for one set of parameters drawn from the ranges given in Extended Data Table 1.
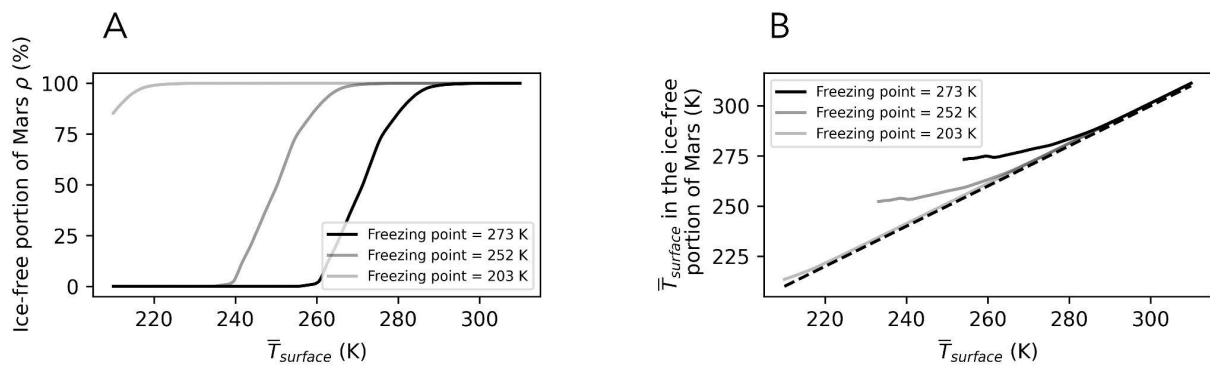
Extended Data Figure 2. Portion of ice-free surface ϱ (A) and average temperature in the corresponding region (B) as evaluated on spatial projection of Mars temperature distribution (see methods). The black dotted line in **B** is the first diagonal corresponding to the planetary averaged surface temperature $\overline{T}_{surface}$.

Extended Data Table 1. Ranges of parameter values used in the atmosphere and crust models.

Planetary features	Symbol (units)	Value or Range	Distribution type
Initial atmosphere (ref[14-16])			
Atmospheric pressure	p (bar)	$[0.5 - 3]$	uniform
H_2 mixing ratio	f_{H_2}	$[3.10^{-3} - 0.1]$	uniform
CH_4 mixing ratio	f_{CH_4}	10^{-4}	
CO_2 mixing ratio	f_{CO_2}	$[1 - (f_{H_2} + f_{CH_4})] \times 0.95$	
N_2 mixing ratio	f_{N_2}	$[1 - (f_{H_2} + f_{CH_4})] \times 0.05$	
Crust characteristics (ref[6,7])			
Surface pore radius	$r(0)$ (cm)	$[10^{-4} - 10^{-3}]$	log-uniform
Depth of pore closure	z_{max} (km)	$[5 - 20]$	uniform
Surface porosity	a_ε	$[0.2 - 0.6]$	uniform
Surface tortuosity	a_τ	$[1.5 - 2.5]$	uniform
Temperature gradient	a_T (K km^{-1})	$[10 - 40]$	uniform

Extended Data Table 2. Biological parameters.

Parameter	Notation	Value or expression	Unit	References
Cell radius	S_C	$10^{a_r + b_r \cdot T}$	μm	ref[12]
	a_r	-13.23	dimensionless	ref[12]
	b_r	0.0431	dimensionless	ref[12]
Cell volume	V_C	$\frac{4}{3}\pi S_C^{\,3}$	μm³	
Cellular carbon content	$Q_{C_{org}}$	$18\ 10^{-15} V_C$	mol C$_{org}$ cell^{-1}	ref[36]
Maximum metabolic rate	q_{max}	$e^{a_q + b_q T} V_C^{\,c_q}$	mol cell^{-1} d^{-1}	
	a_q	- 55.76	dimensionless	ref[37]
	b_q	0.1	dimensionless	ref[38]
	c_q	0.82	dimensionless	ref[39,40]
Half-saturation constant	K	10^{-8}*	mol L^{-1}	ref[41,42]
Maintenance rate	E_m	$e^{a_E + b_E T} V_C^{\,c_E}$	kJ d^{-1}	
	a_E	- 43.54	dimensionless	ref[37]
	b_E	0.08	dimensionless	ref[43]
	c_E	0.67	dimensionless	ref[44]
Decay rate	k_d	0.5	d^{-1}	
Basal mortality rate	m	0.1	d^{-1}	

Supplementary references

36. S. Menden-Deuer, E. J. Lessard, *Limnology and oceanography*, **45**, 569-579 (2000)

37. R. González-Cabaleiro, J. M. Lema, J. Rodríguez, *Plos one*, **10**, e0126739 (2015)

38. L. Tijhuis, M. C. Van Loosdrecht, J. V. Heijnen, *Biotechnology and bioengineering*, **42**, 509-519 (1993)

39. E. Litchman *et al.*, *Ecology letters*, **10**, 1170-1181 (2007)

40. B. A. Ward *et al.*, *The American Naturalist*, **189**, 170-177 (2017)

41. D. Canfield, M. Rosing, C. Bjerrum, *Philosophical Transactions of the Royal Society B: Biological Sciences*, **361**, 1819-1836 (2006)

42. K. Ozaki *et al.*, *Nature Geoscience*, **11**, 55-59 (2018)

43. J. F. Gillooly *et al.*, S*cience*, **293**(5538), 2248-2251 (2001)

44. D. L. Aksnes, J. K. Egge, *Marine ecology progress series. Oldendorf*, **70**, 65-72 (1991)